

**Physiological and Pharmacological Switches  
Combine to Uniquely Modulate the Most Common  
Cardiac Sodium Channel Mutant, E1784K**

by  
**Mena Abdelsayed**

B.Sc., Simon Fraser University, 2014

Thesis Submitted in Partial Fulfillment of the  
Requirements for the Degree of  
Doctor of Philosophy

in the  
Department of Biomedical Physiology and Kinesiology  
Faculty of Science

© Mena Abdelsayed 2018  
SIMON FRASER UNIVERSITY  
Spring 2018

# Approval

**Name:** Mena Abdelsayed

**Degree:** Doctor of Philosophy

**Title:** Physiological and Pharmacological Switches  
Combine to Uniquely Modulate the Most Common  
Cardiac Sodium Channel Mutant, E1784K

**Examining Committee:** **Chair: Dr. Will Cupples**  
Professor

**Dr. Peter C. Ruben**  
Senior Supervisor  
Professor

**Dr. Thomas Claydon**  
Supervisor  
Associate Professor

**Dr. Eric Accili**  
Supervisor  
Associate Professor  
Department of Cellular & Physiological Sciences  
University of British Columbia

**Dr. Andrew D. Krahn**  
Supervisor  
Cardiologist  
University of British Columbia

**Dr. Nadine Wicks**  
Internal Examiner  
Lecturer

**Dr. Charles Antzelevitch**  
External Examiner  
Professor  
Executive Director of Cardiovascular Research  
Lankenau Institute for Medical Research

**Date Defended/Approved:** March 8, 2018

## Abstract

The *SCN5a* gene encodes the cardiac voltage-gated sodium channel (Na<sub>v</sub>1.5) mainly expressed in cardiac muscle cells. The inward sodium current (I<sub>Na</sub>) conducted by Na<sub>v</sub>1.5 triggers depolarization in the cardiac action potential. Mutations in *SCN5a* predominantly give rise to Long-QT syndrome 3 (LQT3), Brugada syndrome 1 (BrS1), and their overlapping phenotypes (mixed syndrome). The most common *SCN5a* mutation, expressed as E1784K in the Na<sub>v</sub>1.5 C-terminal domain (CTD), mainly displays LQT3 and sometimes mixed syndromes. E1784K causes mixed channel defects by decreasing the inward peak I<sub>Na</sub> and increasing late I<sub>Na</sub>, thought to underlie BrS1 and LQT3 pathogenesises, respectively. Very little is known, however, on how physiological and pharmacological switches modulate E1784K channel properties. These triggers may often govern phenotypes in *SCN5a* mutation carriers. The goal of my thesis is to study how exercise-related physiological triggers and pharmacological agents modulate E1784K ion channel properties. I used the whole-cell patch clamp technique to study elevated temperature, elevated cytosolic calcium, and their combined effects with ranolazine, on E1784K. Ranolazine is an antianginal drug with preferential selectivity for blocking late I<sub>Na</sub> versus peak I<sub>Na</sub>. My main results show that E1784K is uniquely altered by the triggers studied, compared to other Na<sub>v</sub>1.5 mutants: (1) Elevated temperature augments late I<sub>Na</sub> in E1784K. (2) Elevated cytosolic calcium, which correlates with exercise-ameliorated LQT3, effectively blocks late I<sub>Na</sub> in most Na<sub>v</sub>1.5 mutants. However, E1784K is resistant to the native calcium-induced block on late I<sub>Na</sub>. (3) When temperature and cytosolic calcium are combined, they decrease ranolazine efficacy to suppress late I<sub>Na</sub> in E1784K. The calcium-sensitivity in E1784K is clearly affected due to the mutant-induced instability in the CTD, which may cause a steric clash between the channel and ranolazine. To predict E1784K effects on arrhythmogenesis, I simulated a dynamic action potential model to account for the frequency-dependent elevations in cytosolic calcium. Alternans is observed at high heart rates in E1784K and is exacerbated by febrile temperatures and ranolazine. This work demonstrates the importance of personalized medicine since Na<sub>v</sub>1.5 mutants like E1784K display unique sensitivity to physiological triggers that potentially govern antiarrhythmic efficacy.

**Keywords:** Mixed Syndrome; Whole-cell patch clamp; Electrophysiology; Temperature; Cytosolic Calcium; Ranolazine; Exercise

## Dedication

*To the soul of my dearest, Rowis Abdelsayed, whose blessings support me, and to my parents, without whom this thesis would not have existed, and my life would have been very different.*

The Lord makes firm the steps  
of the one who delights in him;  
though he may stumble, he will not fall,  
for the Lord upholds him with his hand.

(Psalm 37: 23-24)

## Acknowledgements

I would like to thank Dr. David Jones and Dr. Stan Sokolov who were the first to get me started on a research project at MCPG, in fall 2011. A year after, both Dave and Stan left the Ruben lab, leaving me behind with another colleague, Colin Peters. I could've never found a better teammate, mentor, and a friend than Colin, who was always a role model. Being a genius ginger and a sober researcher, Colin's research standards were stupendous. This motivated me to constantly learn and discover new knowledge in cardiac electrophysiology. Shortly after enrolling in the M.Sc. program, I met Reza Ghovanloo, who became an inspiration and a very close brother. I will never forget the fun time we spent together at the Biophysical (2016) and Gordon Research (2017) conferences, which were both held at California. The inspiring conversations we had regarding the future, motivated us to advance forward. The warm connection linking the three of us together, 'the Rubenites', made the lab my second home. I cherish the nights we all spent together patching, laughing, and challenging our intellectual abilities. Thanks also to the future physicians, Alec Yu and Manpreet Ruprai, who were both talented undergrads and made great contributions to my work.

The only reason why the Ruben lab felt this cozy was because of its intrepid leader, Dr. Peter Ruben. Besides learning electrophysiology, patch-clamp, and other technical skills, I learned many virtues from Peter. It was in BPK 205 (fall 2011) when Peter advertised job opportunities in MCPG. I was courageous to ask Peter to join the lab after his final lecture. Ever since, Peter has greatly impacted, not only my scientific career, but my life, in general. Because of Peter's genuine personality, I was able to deal with many tribulations along the way, which often threatened my continuity in the degree. Peter never lost hope. He continued to support and encourage me. If it weren't for Peter, I really couldn't have done this work. Thank you, Peter!

I would like to also thank my amazing committee. Thanks to Dr. Thomas Claydon for his support and advice on overcoming obstacles met along the way. Thanks to Dr. Eric Accili and Dr. Andrew Krahn for their time and valuable input on my research.

Thanks to all the wonderful friends I made at MCPG. Although I never drank alcohol with them, they were always fun to be with. Thank you, all!

# Table of Contents

Approval.....	ii
Abstract.....	iii
Dedication.....	iv
Acknowledgements.....	v
Table of Contents.....	vi
List of Tables.....	x
List of Figures.....	xi

## **Chapter 1. Genotype-Phenotype Correlations in Cardiac *SCN5a* Mutations ..... 1**

1.1. Introduction.....	1
1.2. Phenotypes: Clinical Diagnosis & Pathophysiology .....	3
1.2.1. Brugada Syndrome Type 1.....	3
1.2.2. Long-QT Syndrome Type 3 .....	5
1.2.3. Common Pathophysiology in BrS1 and LQT3.....	6
1.3. Phenotype Variability in BrS1 and LQT3.....	6
1.3.1. Environmental/Physiological triggers in BrS.....	7
1.3.2. Environmental/Physiological triggers in LQTS .....	9
1.4. Why Variable Phenotypic Penetrance?.....	10
1.4.1. $Na_v1.5$ and Cardiac Disease .....	11
1.4.2. Channel Function and Phenotype Correlations.....	12
1.4.3. Triggers determining channel behaviour and phenotype in some <i>SCN5a</i> mutations.....	13
1.5. Cardiac Voltage-Gated Sodium Channels (VGSC) Structure & Function Overview .....	14
1.5.1. Activation.....	15
1.5.2. Fast inactivation.....	15
1.5.3. Persistent Current.....	16
1.5.4. Slow inactivation.....	16
1.5.5. Deactivation.....	16
1.6. Extrinsic and Intrinsic $Na_v1.5$ Modifiers.....	17
1.6.1. $\beta$ subunits.....	17
1.6.2. C-terminal Domain.....	18
1.6.3. Calcium-calmodulin complex .....	19
1.6.4. $Ca^{2+}$ /calmodulin-dependent protein kinase II ( $Ca^{2+}$ -CaMKII) .....	20
1.6.5. Protein Kinases A & C .....	20
1.6.6. Temperature.....	21
1.6.7. Temperature and Calcium Interaction.....	22
1.7. Antiarrhythmic Drugs and VGSCs.....	23
1.7.1. Antiarrhythmics mode of Action .....	24
1.7.2. Arrhythmias provoked by Antiarrhythmic Drugs .....	25
1.7.3. Ranolazine .....	25
1.7.4. $Na_v$ targets exhibiting novel modes of action .....	26

1.8.	Thesis Significance.....	27
1.9.	Thesis Objectives .....	28
<b>Chapter 2. Differential Thermosensitivity in Mixed Syndrome Cardiac Sodium Channel Mutants.....29</b>		
2.1.	Abstract .....	29
2.2.	Introduction.....	30
2.3.	Methods.....	31
2.3.1.	Ethical approval .....	31
2.3.2.	Cell Culture.....	32
2.3.3.	Transfection.....	32
2.3.4.	Electrophysiology .....	32
2.3.5.	Analysis .....	34
2.3.6.	Voltage Protocols .....	34
2.3.6.1	Activation.....	34
2.3.6.2	Steady-State Fast Inactivation (SSFI).....	35
2.3.6.3	Fast Inactivation Onset.....	35
2.3.6.4	Fast Inactivation Recovery .....	35
2.3.6.5	Late Current .....	36
2.3.6.6	Use-Dependent Inactivation (1 Hz and 3 Hz).....	36
2.3.6.7	Slow Inactivation Onset .....	36
2.3.6.8	Steady-State Slow Inactivation (SSSI).....	36
2.3.6.9	Slow Inactivation Recovery.....	37
2.3.6.10	Q <sub>10</sub> Coefficients .....	37
2.3.7.	Action Potential Modeling .....	37
2.4.	Results .....	38
2.4.1.	Activation.....	38
2.4.2.	Fast Inactivation .....	42
2.4.3.	Late Sodium Current.....	45
2.4.4.	Use-dependent Inactivation .....	46
2.4.5.	Slow Inactivation.....	50
2.4.6.	Action Potential Simulations .....	51
2.5.	Discussion .....	52
2.6.	Acknowledgments .....	55
<b>Chapter 3. Differential Calcium Sensitivity in Nav1.5 Mixed Syndrome Mutants .56</b>		
3.1.	Abstracts .....	56
3.2.	Introduction.....	57
3.3.	Methods.....	59
3.3.1.	Ethical approval .....	59
3.3.2.	Cell Culture and Transfection .....	59
3.3.3.	Electrophysiology .....	59
3.3.4.	TTX-subtraction experiments.....	60
3.3.5.	Analysis and Statistics .....	61
3.3.6.	Voltage Protocols .....	61

3.3.6.1	Peak Sodium Current Density ( $I_{Na}$ ) .....	61
3.3.6.2	Maximal Peak and Late Sodium Conductance Density ( $G_{Na}$ ) .....	61
3.3.6.3	Conductance (GV) .....	61
3.3.6.4	Steady-State Fast Inactivation (SSFI) .....	62
3.3.6.5	Fast Inactivation Onset .....	62
3.3.6.6	Fast Inactivation Recovery .....	63
3.3.6.7	Late $I_{Na}$ Current .....	63
3.3.6.8	Steady-State Slow Inactivation (SSSI) .....	63
3.3.6.9	Slow Inactivation Onset .....	63
3.3.6.10	Slow Inactivation Recovery .....	64
3.3.6.11	Weighted Slow Inactivation Time Constants .....	64
3.3.6.12	Slow Inactivation $\alpha_j$ and $\beta_j$ Rates .....	64
3.3.7.	Myocardial Action Potential (AP) Modeling .....	64
3.4.	Results .....	66
3.4.1.	Peak current amplitude and conductance density .....	66
3.4.2.	Activation voltage-dependence .....	69
3.4.3.	Fast and intermediate inactivation voltage-dependence .....	69
3.4.4.	Fast inactivation recovery and onset kinetics .....	72
3.4.5.	Late current amplitude and conductance density .....	77
3.4.6.	Slow inactivation voltage-dependence .....	79
3.4.7.	Slow inactivation recovery and onset kinetics .....	81
3.4.8.	Ventricular action potential simulations .....	83
3.5.	Discussion .....	87
3.5.1.	Biophysical Implications .....	88
3.5.2.	Physiological Implications .....	90
3.5.3.	Clinical Implications .....	91
3.6.	Conclusion .....	91
3.7.	Acknowledgments .....	92
<b>Chapter 4. The efficacy of ranolazine on E1784K is altered by temperature and calcium .....</b>		<b>93</b>
4.1.	Abstract .....	93
4.2.	Introduction .....	93
4.3.	Methods .....	96
4.3.1.	Homology Modelling and Auto-Docking .....	96
4.3.2.	Ethical approval .....	97
4.3.3.	Cell Culture .....	97
4.3.4.	Electrophysiology .....	97
4.3.5.	Drug Preparation .....	99
4.3.6.	Analysis and Statistics .....	99
4.3.7.	Voltage Protocols .....	100
4.3.7.1	Current Density .....	100
4.3.7.2	Conductance Density .....	100
4.3.7.3	Activation (GV) .....	100

4.3.7.4	Steady-State Fast Inactivation (SSFI).....	101
4.3.7.5	Fast Inactivation Onset.....	101
4.3.7.6	Late $I_{Na}$ Current.....	101
4.3.7.7	Use-Dependent Inactivation (UDI, 1 Hz and 3 Hz).....	101
4.3.7.8	$Q_{10}$ Coefficients .....	102
4.3.7.9	Arrhenius Calculations.....	102
4.3.8.	Myocardial Action Potential (AP) Modeling .....	102
4.3.8.1	Simulations.....	102
4.3.8.2	Analysis.....	104
4.4.	Results .....	104
4.4.1.	Ranolazine binds to $Na_v1.5$ inner vestibule .....	104
4.4.2.	Ranolazine does not affect conductance .....	105
4.4.3.	E1784K availability is decreased in ranolazine .....	109
4.4.4.	Fast inactivation onset kinetics are not altered with ranolazine .....	109
4.4.5.	Ranolazine does not suppress thermosensitive late $I_{Na}$ in E1784K with elevated cytosolic calcium .....	112
4.4.6.	Ranolazine does not enhance UDI in E1784K with elevated cytosolic calcium .....	114
4.4.7.	E1784K-induced alternans is exacerbated with ranolazine .....	117
4.5.	Discussion .....	118
4.5.1.	Drug Binding in Mutant-Trigger Context.....	120
4.5.2.	E1784K-induced Structural Rearrangements in $Na_v1.5$ and its Impact on ranolazine .....	121
4.5.3.	Physiological and Medical Implications.....	122
4.6.	Conclusions.....	124
4.7.	Acknowledgments .....	124
<b>Chapter 5. General Discussion and Future Directions .....</b>		<b>125</b>
5.1.	What was the point? .....	125
5.2.	Possible Limitations.....	130
5.2.1.	Patching using Immortal cell lines.....	130
5.2.2.	Calcium Buffering .....	130
5.2.3.	The $\beta 1$ -Subunit.....	132
5.2.4.	Action Potential Modelling .....	135
5.2.5.	Physiological and Medical Implications.....	135
5.3.	Conclusions and Future Directions .....	137
<b>References.....</b>		<b>139</b>

## List of Tables

Table 1-1	Class I antiarrhythmics .....	24
Table 2-1	Temperature Voltage Error .....	33
Table 2-2	Temperature Peak Current Density and Time to Half peak $I_{Na}$ .....	39
Table 2-3	Temperature Conductance .....	42
Table 2-4	Temperature Steady-State Fast Inactivation .....	43
Table 2-5	Temperature -130 mV and -70 mV Fast inactivation time constants (ms) .....	45
Table 2-6	Temperature -50 mV and +10 mV Fast inactivation time constants (ms)	45
Table 2-7	Temperature Late $I_{Na}$ .....	46
Table 2-8	Temperature Use-Dependence 1Hz & 3Hz .....	49
Table 2-9	Temperature Slow Inactivation Onset.....	50
Table 2-10	Temperature Steady-State Slow Inactivation.....	51
Table 2-11	Temperature Slow Inactivation Recovery .....	51
Table 3-1	Calcium Voltage Error .....	60
Table 3-2	Calcium Peak Current and Conductance Densities .....	68
Table 3-3	Calcium Conductance .....	69
Table 3-4	Calcium Steady-State Fast and Intermediate Inactivation .....	72
Table 3-5	Calcium -130 mV to -70 mV Fast Inactivation Time Constants (ms).....	73
Table 3-6	Calcium -50 mV to +10 mV Fast Inactivation Time Constants (ms) .....	75
Table 3-7	Calcium Late $I_{Na}$ .....	79
Table 3-8	Calcium Steady-State Slow Inactivation .....	81
Table 3-9	Calcium -130 mV to -70 mV Slow Inactivation Time Constant (s).....	83
Table 3-10	Calcium -50 mV to -10 mV Slow Inactivation Time Constant (s).....	83
Table 4-1	Ranolazine Voltage Error .....	99
Table 4-2	Ranolazine Peak Current and Conductance Densities .....	107
Table 4-3	Ranolazine Conductance and Steady-State Fast Inactivation .....	108
Table 4-4	Ranolazine Fast Inactivation Onset Kinetics.....	111
Table 4-5	Ranolazine Late $I_{Na}$ .....	114
Table 4-6	Ranolazine Use-Dependence 1Hz & 3Hz.....	116
Table 5-1	Differences between $\alpha + \beta 1$ and $\alpha - \beta 1$ subunits.....	134

## List of Figures

Figure 1-1	Arrhythmia Syndromes Caused by <i>SCN5a</i> mutations .....	2
Figure 1-2	Brugada Syndrome Electrophysiological and Electrocardiographic features.....	5
Figure 1-3	Brugada Syndrome response to exercise.....	9
Figure 1-4	Trigger Effects on Inherited LQTS.....	10
Figure 1-5	The correlation between phenotype and chanotype in <i>SCN5a</i> mutations .....	13
Figure 1-6	Schematic Diagram of Sodium Channel Gating.....	17
Figure 2-1	Temperature effects on current density and activation kinetics.....	39
Figure 2-2	Temperature effects on activation and steady-state fast inactivation.....	41
Figure 2-3	Temperature effects on fast inactivation kinetics .....	44
Figure 2-4	Temperature effects on late $I_{Na}$ .....	46
Figure 2-5	Temperature effects on $I_{Na}$ use-dependence at 1Hz and 3Hz.....	48
Figure 2-6	Temperature effects on cardiac action potentials at varying $I_{Kto}$ densities .....	52
Figure 3-1	Mutants characterized in $Na_v1.5$ .....	58
Figure 3-2	Wild type and Mutant Currents and Conductance .....	67
Figure 3-3	Effects of cytosolic calcium on steady-state fast inactivation .....	71
Figure 3-4	Effects of cytosolic calcium on late $I_{Na}$ .....	79
Figure 3-5	Effects of cytosolic calcium on steady-state slow inactivation.....	80
Figure 3-6	Effects of cytosolic calcium on slow inactivation kinetics .....	82
Figure 3-7	Ventricular action potential simulations .....	84
Figure 3-8	Action potential velocity and electrical restitution curves (ERC).....	86
Figure 3-9	Sodium-calcium overload .....	87
Figure 4-1	Sodium Channel Schematic Diagram.....	95
Figure 4-2	Ranolazine docked to $Na_v1.5$ - $Na_vPas$ .....	105
Figure 4-3	Ranolazine effects on channel conductance. ....	106
Figure 4-4	Ranolazine effects on steady-state fast inactivation. ....	109
Figure 4-5	Ranolazine effects on fast inactivation onset time constants. ....	110
Figure 4-6	Ranolazine effects on late $I_{Na}$ . ....	113
Figure 4-7	Ranolazine effects on use-dependence. ....	115
Figure 4-8	Endocardial action potential simulations.....	117
Figure 4-9	Cardiac electrical restitution properties.....	118
Figure 5-1	$Na_v1.5$ - $Na_vPas$ DIII-DIV Linker and CTD Homology Model.....	127
Figure 5-2	Calmodulin C-lobe interaction with the DIII-DIV linker in $Na_v1.5$ .....	129

# Chapter 1. Genotype-Phenotype Correlations in Cardiac *SCN5a* Mutations

This chapter describes part of the work published in the journal *Channels*, “Voltage-gated sodium channels: pharmaceutical targets via anticonvulsants to treat epileptic syndromes”, with minor modifications and formatting changes to suit the thesis style.

## 1.1. Introduction

Cardiovascular disease (CD) is the most prevalent cause of morbidity and mortality worldwide (Myerburg & Junttila, 2012; Laslett *et al.*, 2012). In many cases CD results in cardiac arrest which, if not resuscitated within a few minutes, culminates in sudden cardiac death (SCD) (Modi & Krahn, 2011; Harris & Lysitsas, 2016). SCD accounts for approximately 50% of the mortality from cardiovascular disease and 15 – 20% of all deaths (Zipes & Wellens, 1998; Deo & Albert, 2012). The principle factor underlying cardiac arrest, and thus SCD, is malignant ventricular arrhythmia (Chugh *et al.*, 2008; Millar *et al.*, 2012; Harris & Lysitsas, 2016). Pathophysiological arrhythmias involve re-entering electrical impulses in the heart, which lead to ventricular tachycardia, often followed by ventricular fibrillation.

Arrhythmias are caused by genetic and/or environmental factors. Inherited arrhythmias usually arise from mutations in the main and/or auxiliary subunits of cardiac ion channels, known as ‘channelopathies’. Mutations in the *SCN5a* gene, located in chromosome 3p21, have been implicated in cardiac disease. This gene encodes the ion-conducting  $\alpha$ -subunit of the cardiac voltage-gated sodium channel (VGSC),  $Na_v1.5$ .  $Na_v1.5$  is mainly expressed in cardiac myocytes, and along with other  $Na_v$  isoforms in cardiac conduction system tissues, like Purkinje fibers (Haufe *et al.*, 2005; Qu *et al.*, 2007; Zimmer *et al.*, 2014). The  $Na^+$ -selective  $Na_v1.5$  conducts a transient inward sodium current (peak  $I_{Na}$ ), underlying phase 0 (depolarization) in the cardiac action potential (CAP). Peak  $I_{Na}$  is quickly curtailed by fast inactivation. Some fast-inactivated channels revert back into the open state, causing a late  $I_{Na}$  current, which partly contributes to phase 2 (plateau) in the CAP.

Approximately 382 *SCN5a* mutations have been discovered (See NCBI ClinVar Database and inherited arrhythmias database - Fondazione Salvatore Maugeri, <http://triad.fsm.it/cardmoc/>). *SCN5a* mutations have variable penetrance, where 98% of diagnosed probands express either a pure or a mixed clinical arrhythmogenic phenotype (**Figure 1-1**). Disease phenotypes include Long-QT syndrome 3 (LQT3), Brugada Syndrome 1 (BrS1), Progressive familial heart block 1A (PFHB1A), Sick sinus syndrome 1 (SSS1), Familial paroxysmal ventricular fibrillation 1 (VF1), Sudden infant death syndrome (SIDS), Atrial standstill 1 (ATRST1), Dilated cardiomyopathy 1E (CMD1E), and Familial atrial fibrillation 10 (ATFB10). Often the first syndrome an *SCN5a* mutation carrier may express is lethal malignant ventricular arrhythmia or sudden death.

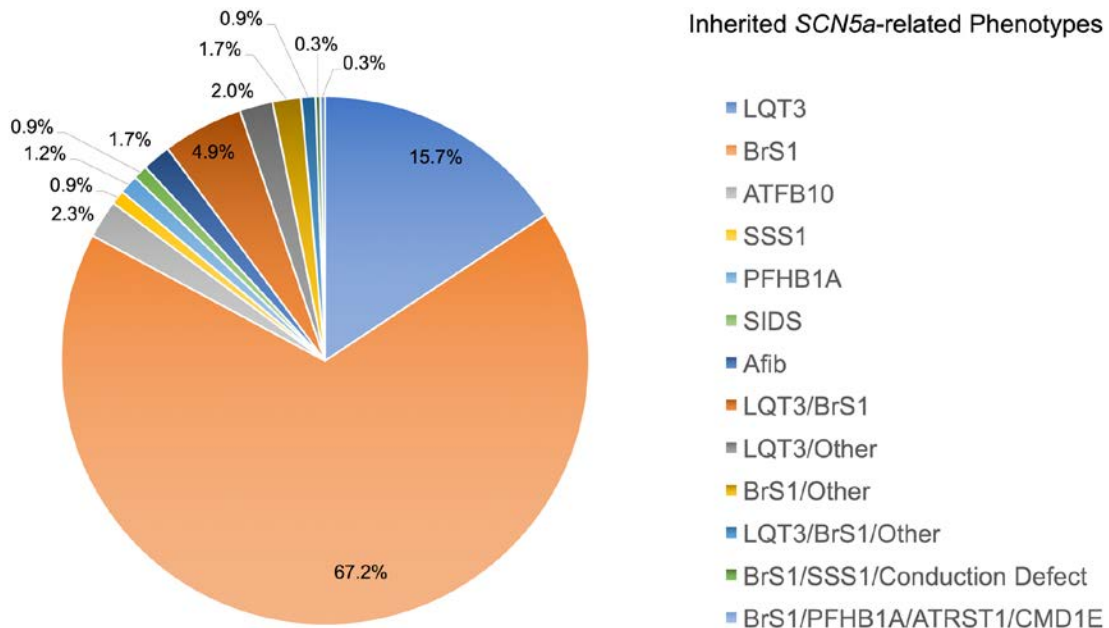


**Figure 1-1 Arrhythmia Syndromes Caused by *SCN5a* mutations**  
 Inherited *SCN5a* mutations can cause either pure or overlapping phenotypes. The pie chart includes both types.

The three most prevalent cardiac syndromes caused by *SCN5a* mutations are Brugada Syndrome 1 (BrS1), Long-QT syndrome 3 (LQT3), and their overlapping phenotype, known as mixed syndrome (**Figure 1-1**). Environmental/physiological and pharmacological triggers associated with exercise or provocative drug testing, respectively, are often required to determine the disease identity (Wu *et al.*, 2008; Serletis-Bizios *et al.*, 2009; Yuasa *et al.*, 2014).

Establishing a clear genotype-phenotype correlation in inherited *SCN5a* conditions is often difficult. Not only do mutations in the *SCN5a* gene give rise to multiple cardiac phenotypes but a single mutation can express several or overlapping phenotypes (i.e., variable expressivity). The ion channel sequence variation profile, known as “channotype”, ultimately determines the biophysical attributes imposed on the channel by the mutation, resulting in gain-of-function, loss-of-function, or both (Klassen *et al.*, 2011; Noebels, 2015). The interaction between channotype and physiological and/or pharmacological triggers may underlie the highly variable phenotypic expressivity in *SCN5a* mutation carriers.

Over the past two decades, many discoveries have linked cardiac arrhythmia pathogenesis to underlying malfunctions in ion channels (Balsler, 2002; Jones & Ruben, 2008; Pitt, 2009; Amin *et al.*, 2010*b*; Catterall, 2012; Horvath & Bers, 2014; Ahern *et al.*, 2016). This effort has elucidated the role played by ion channels as contributors, if not the primary cause behind arrhythmias and sudden cardiac death. Advances in understanding cardiac pathophysiology were mainly determined using classic electrophysiology techniques, which correlate channotype in *SCN5a* mutations with their corresponding clinical phenotypes (Bezzina *et al.*, 1999; Veldkamp *et al.*, 2000*a*; Baroudi & Chahine, 2000; Viswanathan *et al.*, 2001; Clancy & Rudy, 2002; Groenewegen *et al.*, 2003; Keller *et al.*, 2006). Nevertheless, the shortcomings in this approach are apparent from the phenotypic variability in *SCN5a* mutation carriers.

## **1.2. Phenotypes: Clinical Diagnosis & Pathophysiology**

### **1.2.1. Brugada Syndrome Type 1**

Brugada syndrome (BrS) was first described by Josep and Pedro Brugada, in 1992, who diagnosed the disease as a right bundle branch block (RBBB) accompanied with ST-elevation in V<sub>1</sub>-V<sub>3</sub> precordial leads (Brugada & Brugada, 1992). The type 1 Brugada ECG pattern is diagnostic compared to the other two ECG types (**Figure 1-2**). Brugada pattern type 1 is characterized by a coved ST-segment elevation ( $\geq 2$  mm) followed by a T-wave inversion in the right precordial leads, V<sub>1</sub>-V<sub>3</sub> (Antzelevitch, 2001*a*; Francis & Antzelevitch, 2003; Castro Hevia *et al.*, 2006; Antzelevitch & Yan, 2010; Tomita *et al.*, 2012). Type 2 and 3 patterns are characterized by an elevated J-wave ( $\geq 2$  mm) followed by a positive T-wave (**Figure 1-2**) (Francis & Antzelevitch, 2003;

Antzelevitch *et al.*, 2005; Antzelevitch, 2005). Asymptomatic BrS patients with types 2 or 3 phenotypes may express type 1 with provocative drug tests (Barajas-Martinez *et al.*, 2008; Doetzer *et al.*, 2011; Obeyesekere *et al.*, 2011; Barra *et al.*, 2013; Zhou *et al.*, 2013, 2013; Yu *et al.*, 2013). BrS is often associated with conduction abnormalities that prolong the PR interval and QRS duration (Amin *et al.*, 2009; Tomita *et al.*, 2012; Aizawa *et al.*, 2013).

Approximately 15 – 30 % of patients with congenital BrS carry an *SCN5a* mutation displaying an autosomal dominant mode of inheritance with incomplete penetrance (Antzelevitch, 2007; Modi & Krahn, 2011). BrS1 mutants cause loss-of-function in  $\text{Na}_v1.5$  by decreasing sodium channel expression and/or conduction. The resultant decrease in the depolarizing current increases the risk for arrhythmias as envisaged by the depolarizing and repolarizing hypotheses. The depolarization hypothesis suggests that the decrease in conduction velocity to the right ventricular outflow tract (RVOT) creates spatial heterogeneity in the right ventricle (RV) (Meregalli *et al.*, 2005; Wilde *et al.*, 2010). The repolarization hypothesis indicates that high  $\text{K}_v4.3$  expression (passing transient outward  $\text{K}^+$  current,  $I_{\text{Kto}}$ ) abrogates the diminished depolarizing wave in the RV epicardium, causing a loss in the action potential dome (Yan & Antzelevitch, 1999; Antzelevitch, 2001a; Di Diego, 2002; Wilde *et al.*, 2010). The transmural heterogeneity in RV creates a substrate for phase 2 re-entry (**Figure 1-2**), increasing the susceptibility for premature extrasystoles (Antzelevitch *et al.*, 2005; Di Diego *et al.*, 2005). The two mechanisms are not mutually exclusive, and both may contribute to BrS pathophysiology (Sieira *et al.*, 2016).

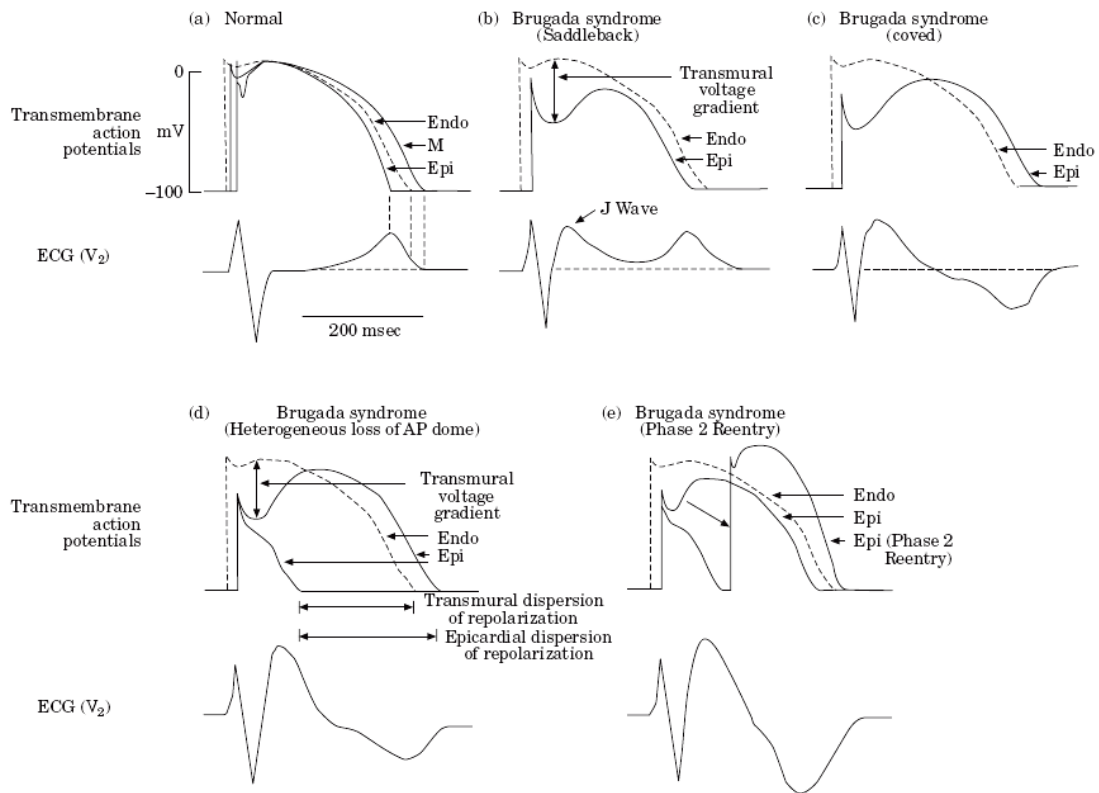


**Figure 1-2 Brugada Syndrome Electrophysiological and Electrocardiographic features**

Electrical heterogeneity exists between the three myocardial cells. The depolarization wave proceeds from the endocardium to the midmyocardium to the epicardium as shown in **panel a**. This is followed by repolarization in the opposite order. In the normal ECG,  $T_{peak}$  and  $T_{end}$  complements epicardial and midmyocardial repolarization, respectively. The difference between  $T_{peak} - T_{end}$  measures Transmural Dispersion of Repolarization (TDR). **Panel b** shows an exacerbated epicardial notch in BrS. This produces a saddleback ST-elevation with a positive T-wave. This is observed in type 2 BrS patterns while type 3 may have both saddle-back or coved type ST- elevation. **Panel c** shows the diagnostic type 1 BrS ECG pattern. In this case, there is a prolonged epicardial action potential giving rise to a negative T-wave. **Panel d** shows a loss in the epicardial action potential dome, which may lead to phase 2 reentry. The epicardial tissue recovers from the refractory period quickly conducting another action potential, thereby exacerbating the ST-elevation and the negative T-wave in **panel e**. Reproduced from Antzelevitch (2001).

### 1.2.2. Long-QT Syndrome Type 3

Long-QT syndrome (LQTS) was first described in the mid-20<sup>th</sup> century (Jervell & Lange-Nielsen, 1957). Inherited LQTS is mainly autosomal dominant (Romano-Ward Syndrome) compared to the rare autosomal recessive mode (Jervell and Lange-Nielsen Syndrome), which is accompanied with deafness (Noh *et al.*, 1995; Shimizu &

Antzelevitch, 1998, 2000). Congenital LQTS arises from 17 genes (LQT1 – 17), where the three most prevalent are *KCNQ1* (K<sub>v</sub>7.1, LQT1), *HERG* (K<sub>v</sub>11.1, LQT2), and *SCN5a* (Na<sub>v</sub>1.5, LQT3) (Schwartz *et al.*, 1995, 2001; Takenaka *et al.*, 2003). Despite its rarity, LQT3 is the most lethal inherited LQTS (Antzelevitch *et al.*, 1996; Shimizu & Antzelevitch, 1998; Yan & Antzelevitch, 1998; Shimizu & Antzelevitch, 1999).

LQTS has a prolonged QT interval with a diagnostic QT<sub>c</sub> ≥ 500 ms (Antzelevitch & Oliva, 2006; Priori *et al.*, 2013). The cellular mechanism underlying LQTS involves either a reduction in the repolarizing current or an increase in the depolarizing current, mediated by I<sub>Kr</sub>/I<sub>Ks</sub> or late I<sub>Na</sub>, respectively (Antzelevitch *et al.*, 1996; Sicouri *et al.*, 2007; Antzelevitch *et al.*, 2014). Both mechanisms delay cardiac repolarization, especially in the mid-myocardium. The augmented depolarizing current during phase 2 in the CAP can generate early after-depolarizations (EADs) or drive the sodium-calcium exchanger (NCX) in reverse mode, causing intracellular calcium and sodium overload, leading to delayed after-depolarizations (DADs) (Akar, 2002; Shimizu *et al.*, 2005; Gaur *et al.*, 2009; Antzelevitch & Burashnikov, 2011).

### 1.2.3. Common Pathophysiology in BrS1 and LQT3

A shared mechanism between BrS and LQTS is exacerbated transmural dispersion of repolarization (TDR), the primary substrate precipitating arrhythmias (Castro Hevia *et al.*, 2006; Antzelevitch *et al.*, 2007). TDR is measured as the peak – end difference in the T-wave. The T<sub>peak</sub> and T<sub>end</sub> correlate with epicardial and mid-myocardial action potential termination, respectively (**Figure 1-2**) (Antzelevitch, 2001*b*). The right epicardial action potential dome loss in BrS, as in the repolarization hypothesis, increases TDR (Lukas & Antzelevitch, 1996; Dumaine *et al.*, 1999; Antzelevitch & Patocskai, 2015). In LQTS, the relatively prolonged APD in mid-myocardium compared to the endocardium and epicardium, exacerbates the TDR (Zygmunt *et al.*, 2001). Increased TDR enlarges the vulnerable window during which premature extrasystoles may occur, leading to ventricular tachycardia/fibrillation.

## 1.3. Phenotype Variability in BrS1 and LQT3

Phenotypes resulting from *SCN5a* mutations can vary with sex, age, ethnicity, circadian rhythms, and physiological state. All these factors modify *SCN5a* transcription

and translation. The exercise stress test is a common diagnostic tool used to unmask latent arrhythmias in patients with *SCN5a* mutations. During exercise, heightened sympathetic tone elevates heart rate and contractility. Various intracellular cascades are activated in cardiomyocytes that alter  $Na_v1.5$  transcription, translation, and gating. Environmental factors, like hypoxia, acidemia (either metabolic or respiratory), or elevations in body temperature, accompany exercise.

### 1.3.1. Environmental/Physiological triggers in BrS

BrS patients may not express diagnostic phenotypes; however, they may still die from SCD. Many BrS patients require an external trigger to precipitate their latent cardiac disease (Fish & Antzelevitch, 2004a; Minoura *et al.*, 2012). Various triggers like exercise, acidemia, fever, and sodium channel blockers unmask BrS (Wakita *et al.*, 2004; Ozeke *et al.*, 2005; Peng *et al.*, 2005; García-Borbolla *et al.*, 2007; Kukla *et al.*, 2007; Grimster *et al.*, 2008; Amin *et al.*, 2009; Jayasuriya & Whitman, 2011; Kumar *et al.*, 2013; Masrur *et al.*, 2015). A large clinical group created the website, [www.brugadadrugs.org](http://www.brugadadrugs.org), to identify high risk BrS provocative drugs. Environmental and pharmacological triggers modify  $I_{Na}$  (Di Diego *et al.*, 2005; Minoura *et al.*, 2012). Other factors may modulate the extent to which external triggers unmask BrS. For instance, elevated testosterone levels in males upregulates  $K_v4.3$  expression in the RV epicardium, thereby increasing their risk for BrS (Shimizu *et al.*, 2007). Thus, BrS is predominant in males, with an 8:1 (male:female) ratio, especially in Southeastern Asian populations (Wilde, 2002; Antzelevitch *et al.*, 2002; Ackerman *et al.*, 2004; Antzelevitch *et al.*, 2005; Antzelevitch, 2005). These factors often account for complete versus incomplete penetrance in carriers of BrS1 mutations.

Exercise elevates the J-point in BrS1 patients (Amin *et al.*, 2009). Some reports show exercise-induced J-point elevation during peak exercise while others during recovery from exercise (**Figure 1-3**) (García-Borbolla *et al.*, 2007; Grimster *et al.*, 2008; Amin *et al.*, 2009; Makimoto *et al.*, 2010; Walker *et al.*, 2010; Jayasuriya & Whitman, 2011; Masrur *et al.*, 2015). This conflicting observation may be partly explained by the fact that there are controversies regarding effects of sympathetic versus parasympathetic tone in BrS. Increased sympathetic output is thought to ameliorate the syndrome by increasing the depolarizing current through  $I_{Na}$  and  $I_{Ca}$  (Makimoto *et al.*, 2010; Antzelevitch & Patocskai, 2015). Thus, medications for BrS include quinidine

(blocks  $I_{K10}$ ),  $\beta$  adrenergic agents, anticholinergic agents, and implantable cardioverter defibrillators (ICDs) (Antzelevitch & Fish, 2006). However, the elevated sympathetic tone during exercise may increase  $Na_v1.5$  use-dependence, precipitating BrS1 (Bezzina *et al.*, 1999; Veldkamp *et al.*, 2000a). Decreased  $Na_v1.5$  availability leads to conduction blocks diagnosed as prolonged QRS durations in BrS1 patients (Amin *et al.*, 2009). When challenged with flecainide, BrS1 patients also manifest a  $QT_C$  prolongation during exercise (Amin *et al.*, 2009). The reduced  $I_{Na}$  accompanying BrS1, indirectly accentuates phase 1 notch in the CAP, mediated by  $I_{to}$ . Thus, the augmented outward repolarizing current, temporarily delays  $I_{CaL}$  activation, thereby prolonging phase 2 and 3 in CAP (Krishnan & Antzelevitch, 1993).

Most BrS patients suffer from arrhythmias during sleep, such as in sudden infant death syndrome (Skinner, 2005; Makielski, 2006; Huang *et al.*, 2009; Qiu *et al.*, 2009; Andreasen *et al.*, 2013). Although sleep is a restful state, it shares some physiological properties with exercise; the rapid-eye movement (REM) phase is accompanied with elevated heart rate (HR) and blood pressure (BP) (Somers *et al.*, 1993). Whether this physiological change is sufficient to cause arrhythmias remains unknown. The relative changes in HR and BP during sleep may mimic exercise effects. High vagal input during non-REM sleep may trigger BrS in patients (Trinder *et al.*, 2001). Additionally, sleep is accompanied with decreased body temperature and sometimes increased blood acidosis due to sleep apnea, which may precipitate arrhythmias (Fish & Antzelevitch, 2004b). As with exercise, sleep physiology is complicated as physiological fluctuations occur in REM and non-REM sleep.

Even with no genetic mutations, environmental factors may induce Brugada phenocopy in non-athletes and athletes (Kovacic & Kuchar, 2004), primarily due to a reduction in the depolarizing current carried by peak  $I_{Na}$  (Di Diego *et al.*, 2005). The combined interaction between environmental and genetic factors may synergistically heighten arrhythmia lethality in patients with *SCN5a* mutations.

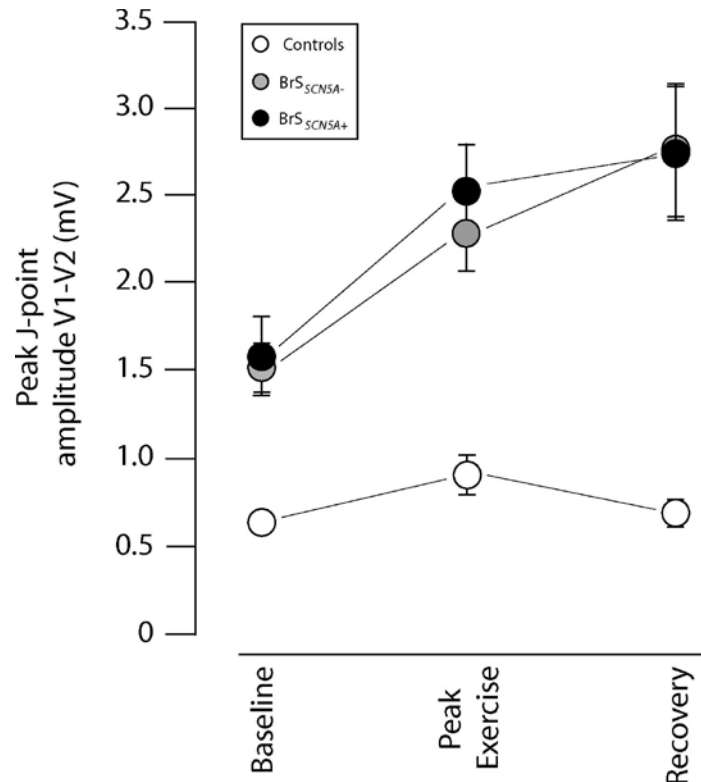


**Figure 1-3 Brugada Syndrome response to exercise**

The J-point size is plotted against the exercise stage. Control subjects have no significant variation in their J-points compared to both BrS patients with and without *SCN5a* mutations. Both patient types have elevated J-points at peak exercise, which is maintained during recovery. Reproduced from Amin *et al.* (2009).

### 1.3.2. Environmental/Physiological triggers in LQTS

Unmasking congenital LQTS depends on the genotype. The common trigger for cardiac events in LQT1 patients is exercise, especially swimming (Shimizu & Antzelevitch, 1998). Most cardiac events in LQT2 patients are provoked by emotional arousals while only a few occur with rest/sleep (Schwartz *et al.*, 1995; Shimizu & Antzelevitch, 2000; Paavonen *et al.*, 2001; Takenaka *et al.*, 2003). The latter trigger, which accompanies decreased heart rate, is very common for precipitating LQT3 (**Figure 1-4**) (Schwartz *et al.*, 1995, 2001). Only a few LQT3 patients express their syndromes during exercise or emotion (Shimizu & Antzelevitch, 2000; Aziz *et al.*, 2011). Exercise is a general therapy for LQT3 mutant carriers. Recommended therapies for LQT3 include  $\beta_1$  blockers (most common in LQT1),  $\text{Na}_v$  blockers like Mexiletine or Flecainide, or ICDs (especially in LQT3) (Haverkamp, 2000; Bennett *et al.*, 2014). The LQT3 mutant signature, however, determines the patients' response to exercise

(Veldkamp *et al.*, 2000a; Chen *et al.*, 2015). Most LQT3 patients ameliorated by exercise were screened positive for the  $\Delta$ KPQ mutant (Schwartz *et al.*, 1995).

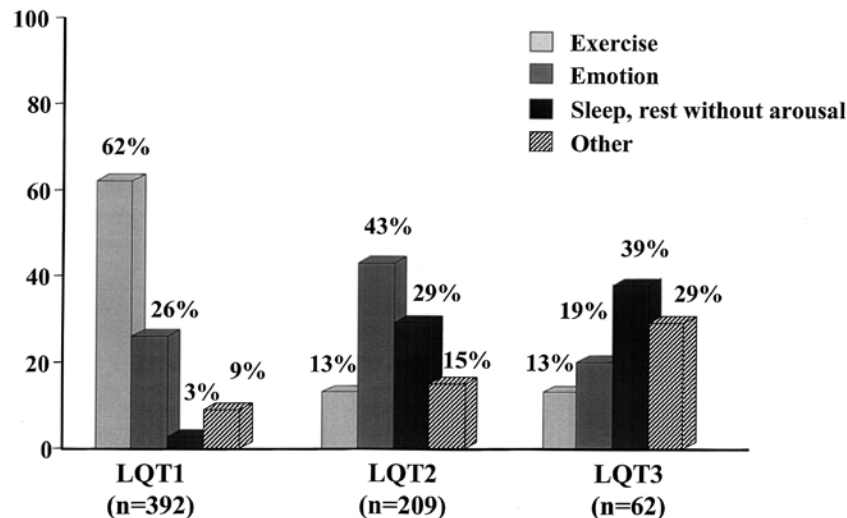


**Figure 1-4 Trigger Effects on Inherited LQTS**  
 Reproduced from Schwartz *et al.* (2001).

## 1.4. Why Variable Phenotypic Penetrance?

BrS1 and LQT3 phenotypes can be correlated with the channeltype-induced biophysical defects. The phenotypic variability observed in *SCN5a* mutation carriers can be ascribed to the various stages of modification in  $Na_v1.5$  life-cycle: *SCN5a* transcription, post-transcription by RNA processing, translation of mRNA transcript, post-translational modification, and protein degradation (Liu *et al.*, 2014). Transcription and translation modifiers ultimately downregulate or upregulate  $Na_v1.5$  expression and trafficking, which is modulated by channeltype. These factors vary with age, sex, and physiological state.

Various protein kinases, such as mitogen-activated protein kinases (MAPKs), affect  $Na_v1.5$  translation, folding, and trafficking (Muslin, 2008). Protein kinase C (PKC) and Protein kinase A (PKA) have antagonistic effects on channel trafficking (Muslin, 2008; Hallaq *et al.*, 2012). Unfortunately, few reports describe how *SCN5a* mutations impact transcription and translation. Sodium channel research was mainly directed at understanding how channeltype affects gating. This reductionist approach for studying channeltype is inadequate and may not fully explain the phenotypic heterogeneity observed in *SCN5a* mutation carriers.  $Na_v1.5$  is co-expressed and modified by various

other subunits and molecules, so channel modification sites may be altered with channel type.

### 1.4.1. Nav1.5 and Cardiac Disease

The voltage-gated sodium channel ( $Na_v$ ) exists in humans as nine different isoforms ( $Na_v1.1$ - $Na_v1.9$ ). The isoforms commonly expressed in the central nervous system include  $Na_v1.1$ ,  $Na_v1.2$ ,  $Na_v1.3$ , and  $Na_v1.6$ . Dorsal root ganglion cells in the peripheral nervous system mainly express  $Na_v1.7$ ,  $Na_v1.8$ , and  $Na_v1.9$ .  $Na_v1.4$  is predominant in skeletal muscle and is minimally expressed along with the predominant cardiac-specific isoform,  $Na_v1.5$ , in the heart (Qu *et al.*, 2007; Zimmer *et al.*, 2014). TTX-sensitive  $Na_v$ s ( $Na_v1.1$ - $1.4$ ,  $1.6$ , and  $1.7$ ) are not prevalent in mammalian hearts as confirmed by normal ECG and action potential recordings in hearts perfused with a low TTX concentration (Santarelli *et al.*, 2007; Zimmer *et al.*, 2014). However, the TTX-resistant  $Na_v1.8$  (encoded by *SCN10a*) is expressed in the heart and *SCN10a* mutations cause BrS18 (Zimmer *et al.*, 2014; Fukuyama *et al.*, 2016).

$Na_v1.5$  functions to depolarize cardiomyocytes. The inward peak  $I_{Na}$  is altered in cardiac disease. Genetic factors, such as those causing BrS1, mainly affect peak  $I_{Na}$  by modulating channel gating (Deschênes *et al.*, 2000; Di Diego, 2002; Tester *et al.*, 2005; Antzelevitch, 2007; Kapplinger *et al.*, 2010; Wilde *et al.*, 2010).  $Na_v1.5$  mainly transitions between a closed-state (deactivated), activated, and fast- or slow-inactivated states in a voltage-dependent manner. Gating defects caused by BrS1 mutants decrease  $Na_v1.5$  open probability via a voltage-dependent depolarization in activation, or hyperpolarization in fast or slow inactivation, or enhanced onset or decelerated recovery from inactivation (Wang *et al.*, 2000; Baroudi *et al.*, 2002; Wang, 2004; Huang *et al.*, 2006; Keller *et al.*, 2006; Poelzing *et al.*, 2006; Tan *et al.*, 2006; Casini *et al.*, 2007; Jones & Ruben, 2008; Makita *et al.*, 2008b; Lizotte *et al.*, 2009; Gui *et al.*, 2010). BrS1 mutants may also perturb  $Na_v1.5$  trafficking and expression, thereby suppressing peak  $I_{Na}$ .

LQT3 is mainly associated with exacerbated late  $I_{Na}$ . This non-inactivating  $I_{Na}$  serves as the pathological substrate underlying various cardiac disease states, associated with myocardial ischemia/infarction and heart failure (Schwartz & Wolf, 1978; Antzelevitch *et al.*, 1996; Yan & Antzelevitch, 1998; Shimizu & Antzelevitch, 1999;

Gimeno *et al.*, 2010; Antzelevitch *et al.*, 2014; Horvath & Bers, 2014). The increased late  $I_{Na}$  in LQT3 is caused by late re-opening of  $Na_v1.5$  due to destabilized fast inactivation. Following fast inactivation, a few  $Na_v1.5$  channels recover from fast inactivation, bursting back into the open state, thereby enhancing the depolarizing current during phase 2 in CAP (Quandt, 1987; Maltsev & Undrovinas, 2006; Maltsev *et al.*, 2009). The augmented late  $I_{Na}$  in LQT3 delays cardiac repolarization. Late  $I_{Na}$  is larger in the midmyocardium compared to endocardium and epicardium due to decreased  $K_v7.1$  ( $I_{Ks}$ ) expression and increased  $I_{NCX}$ , thereby reducing the repolarizing current causing the late depolarizing current to prevail (Liu *et al.*, 1993; Antzelevitch *et al.*, 1996; Schwartz *et al.*, 2000; Akar, 2002).

### 1.4.2. Channel Function and Phenotype Correlations

Approximately 14 % of *SCN5a* mutations have been characterized using the voltage-clamp technique. Channotype positively correlates with phenotype in the *SCN5a* variants characterized (**Figure 1-5**). A positive correlation involves LQT3 mutants expressing  $Na_v1.5$  gain-of-function, BrS1 mutants expressing  $Na_v1.5$  loss-of-function, and the mixed phenotype (BrS1 & LQT3) expressing both channel defects. Intriguingly, a mixed correlation exists between channotype and phenotype, which is as prevalent as the positive correlation in BrS1 and LQT3 (**Figure 1-5**). This mixed correlation involves either a pure phenotype accompanied with mixed channel function, or vice versa. Very few cases show a negative correlation (**Figure 1-5**).

## Channotype-Phenotype Correlation

~382 reported *SCN5a* mutations (only 14 % characterized)

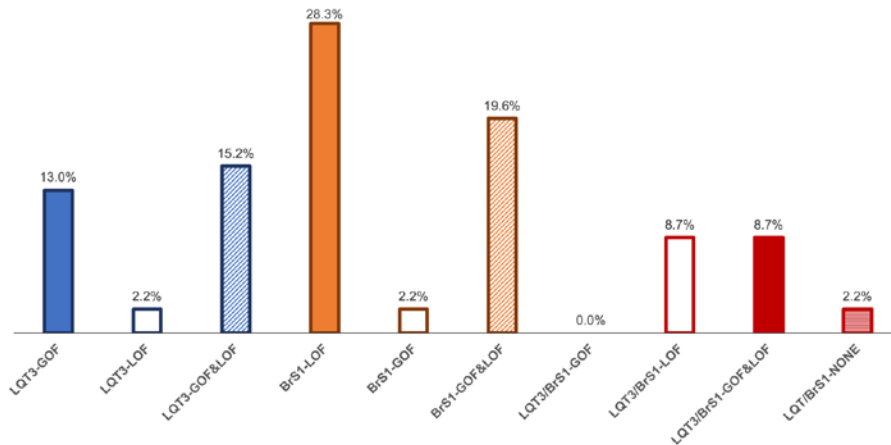


**Figure 1-5** The correlation between phenotype and channotype in *SCN5a* mutations

### 1.4.3. Triggers determining channel behaviour and phenotype in some *SCN5a* mutations

The most common *SCN5a* mutation expresses as the E1784K mutant in the Nav1.5 C-terminal Domain (CTD) (Kapplinger *et al.*, 2010; Sumitomo, 2014; Takahashi *et al.*, 2014; Veltmann *et al.*, 2016). This mutation is common in the Okinawa islands in Japan, where more than 80% of the genotype-positive children express LQTS (Nakajima *et al.*, 2011; Takahashi *et al.*, 2014). Although commonly associated with LQTS, E1784K cohorts express other phenotypes including sinus node dysfunction (SND), LQT3/SND, LQT3/BrS1, and LQT3/BrS1/SND (Wei *et al.*, 1999; Deschênes *et al.*, 2000; Makita *et al.*, 2008a). Electrophysiology data confirms that E1784K displays mixed channel behavior (Wei *et al.*, 1999; Makita *et al.*, 2008a; Sumitomo, 2014; Peters *et al.*, 2016; Veltmann *et al.*, 2016; Abdelsayed *et al.*, 2017). Very little is known, however, on how arrhythmogenic triggers alter E1784K channel behavior, which could be the reason for the differential phenotypic variability in cohorts (Makita *et al.*, 2008a).

The founder Netherlands *SCN5a* mutation expressed in Nav1.5 CTD as the 1795insD mutant, displays LQT3 at rest and BrS1 during peak exercise (Veldkamp *et al.*, 2000a; Clancy & Rudy, 2002; Veldkamp *et al.*, 2003; Remme *et al.*, 2006). Biophysical characterization reveals reduced and augmented peak and late  $I_{Na}$ , respectively, in 1795insD (Bezzina *et al.*, 1999; Rivolta, 2001; Clancy & Rudy, 2002;

Veldkamp *et al.*, 2003; Beaufort-Krol *et al.*, 2005; Remme *et al.*, 2006). These biophysical defects are modified by stimulation frequency, where high rates further reduce peak  $I_{Na}$  and low rates increase late  $I_{Na}$  percentage compared to peak  $I_{Na}$  (Veldkamp *et al.*, 2000a; Clancy & Rudy, 2002; Veldkamp *et al.*, 2003).

Beneficial effects of exercise on LQT3 patients were validated using data from patients screened positive for  $\Delta$ KPQ, the first discovered LQT3 mutant (Schwartz *et al.*, 1995). Generalizing exercise as a therapeutic for the LQT3 patient population can be misleading since  $Na_v1.5$  mutants have unique responses to exercise. The exercise-ameliorated LQT3 in  $\Delta$ KPQ carriers was correlated with reduced late  $I_{Na}$  caused by elevated cytosolic calcium, high stimulation frequency, and  $\beta_1$  adrenergic activation (Chandra *et al.*, 1998, 1999; Fredj *et al.*, 2006a; Potet *et al.*, 2015). These are amongst a multitude of factors that are upregulated in cardiomyocytes during exercise. Various protein kinases are activated during exercise and pathophysiological states (Steenbergen *et al.*, 1987; Belardinelli, 2006a; Pitt, 2009; Horvath & Bers, 2014). PKA and PKC underlie the epinephrine-induced  $QT_c$  prolongation and sinus node dysfunction in V2016M carriers ( $Na_v1.5$  CTD mutant) (Chen *et al.*, 2015).

It is notable that many CTD mutants are linked to mixed syndromes and have variable sensitivity to exercise-related factors.

## **1.5. Cardiac Voltage-Gated Sodium Channels (VGSC) Structure & Function Overview**

The heteromeric voltage-gated sodium channel is composed of four Domains (DI-DIV) consisting of six transmembrane segments (S1-S6). The voltage-sensing domain (VSD) and the pore-forming domain (PFD) is encompassed by S1-S4 and S5-S6, respectively, in each homologous Domain. The four Domains are connected by intracellular linkers, which modulate channel gating (Bennett, 1999, 2001, 2004). The PFDs and VSDs form a functional channel, which can be modified by “auxiliary”  $\beta$ -subunits (McCormick *et al.*, 1998; Bennett, 1999; Lee *et al.*, 2014; Yan *et al.*, 2017b).

### 1.5.1. Activation

Channel activation is controlled by DI, DII, and partially DIII voltage sensor movements (**Figure 1-6**) (Cha *et al.*, 1999). Changes in the membrane electric field are sensed by the peripheral VSDs and relayed by the S4-S5 linkers to the central PFDs (Yang & Horn, 1995; Payandeh *et al.*, 2011; Zhang *et al.*, 2012; Catterall *et al.*, 2012; Shen *et al.*, 2017; Yan *et al.*, 2017*b*). The S4s contain conserved arginine and lysine residues, which form salt bridges with residues in S2 and S3 segments (DeCaen *et al.*, 2009; Yarov-Yarovoy *et al.*, 2012). Upon membrane depolarization, a rearrangement occurs in the ionic bonds, and the S4s are outwardly displaced, as envisaged by the sliding-helix model (Yang & Horn, 1995; DeCaen *et al.*, 2009; Kubota *et al.*, 2017). The voltage sensor transition to the depolarized state is rapid (microsecond scale) and causes a conformational change in the PFD (Payandeh *et al.*, 2011; Zhang *et al.*, 2012). The S5 and S6 segments are thought to slide laterally, dilating the channel's inner vestibule. The PFD rearrangement results in ionic conduction passing a transient inward sodium current, rushed into the cell by a steep electrochemical driving force. Sodium ions move into the outer vestibule, where Na<sup>+</sup> is stripped from its hydration shell. This is followed by Na<sup>+</sup> passing through a selectivity filter formed by amino acid residues, DEKA, in each of the homologous Domains (i.e. D in Domain I, E in Domain II, K in Domain III, and A in Domain IV) (Payandeh *et al.*, 2011; Zhang *et al.*, 2012; Shen *et al.*, 2017). Na<sup>+</sup> is then rehydrated in the central cavity and the inner vestibule (Payandeh *et al.*, 2011).

### 1.5.2. Fast inactivation

A few milliseconds following activation, the inward sodium current is curtailed by fast inactivation. The DIV S4 movement is correlated with fast inactivation onset and is suggested to be its rate-determining step (Armstrong & Bezanilla, 1977; Bezanilla & Armstrong, 1977; Kühn & Greeff, 1999; Groome *et al.*, 2007; Capes *et al.*, 2013). Near resting potential, the DIV S4 activates in a small population of channels giving rise to closed-state fast inactivated state (**Figure 1-6**) (Groome *et al.*, 2011); therefore, only half-maximal channel availability exists at resting potential (Starkus *et al.*, 1993). The outward helical movement in DIV S4 causes hydrophobic residues in the DIII-DIV linker, the IFMT (1485-1488) motif, to bind to residues in the inner vestibule and S4-S5 linkers in DIII and DIV (Richmond *et al.*, 1997; Ulbricht, 2005; Groome *et al.*, 2007). The IFM-

QQQ mutant completely abolishes fast inactivation (Featherstone *et al.*, 1996). Positively charged residues in the DIII-DIV linker form electrostatic interactions with their counter charges in the inner vestibule, thereby stabilizing fast inactivation (Ulbricht, 2005; Groome *et al.*, 2007).

### **1.5.3. Persistent Current**

Not all channels are fast inactivated; rather, some channels recover into the open-state and conduct a small residual sodium current, referred to as the non-inactivated, persistent, or late  $I_{Na}$  (Quandt, 1987; Maltsev & Undrovinas, 2006). Late  $I_{Na}$  partially underlies phase 2 stabilization in the CAP (Maltsev *et al.*, 2009).

### **1.5.4. Slow inactivation**

With maintained or repetitive depolarizations,  $Na_v$  channels recover from fast inactivation and transition into a distinct mode of inactivation, known as slow inactivation. Slow inactivation is mechanistically and pharmacologically distinct from fast inactivation (Featherstone *et al.*, 1996; Richmond *et al.*, 1997, 1998; Vilin *et al.*, 2001; Goldin, 2003; Ulbricht, 2005). Slow inactivation occurs over several seconds and is thought to involve conformational changes in the selectivity filter, voltage sensors, and lateral pores known as fenestrations (Ruben *et al.*, 1992; Vilin *et al.*, 2001; Webb, 2009; Payandeh *et al.*, 2011, 2012, Silva & Goldstein, 2013a, 2013b). During slow inactivation, the voltage sensors adapt to an activated locked-up state in which the pore collapses (Ruben *et al.*, 1992). There is an inverse relationship between fast and slow inactivation in  $Na_v$ . More channels slow inactivate when fast inactivation is abolished with the IFM-QQQ mutant. Thus, charge immobilization in DIV S4, which impedes full recovery from fast inactivation, limits the extent of slow inactivation (Featherstone *et al.*, 1996; Nuss *et al.*, 1996; Richmond *et al.*, 1997).

### **1.5.5. Deactivation**

The membrane must sufficiently repolarize for channels to recover from fast and slow inactivation and then deactivate. Upon repolarizing, the voltage-sensors move back into their deactivated states and the channel PFD is re-orientated into the 'activation-ready' conformation. Deactivation can be measured by very short depolarization pulses

followed by abrupt hyperpolarization (Hodgkin & Huxley, 1952; Hodgkin *et al.*, 1952; Groome *et al.*, 2003). This method allows for a large inward sodium current surge, capturing the ‘tail  $I_{Na}$ ’ carried by channels which are not fast-inactivated.

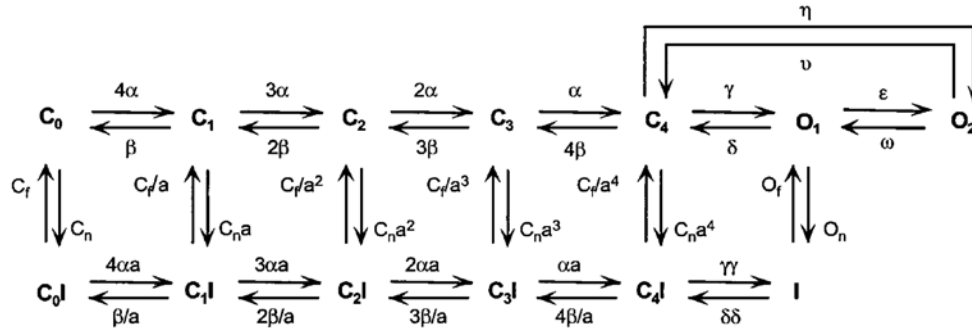


**Figure 1-6 Schematic Diagram of Sodium Channel Gating**

The Markov scheme shows the series of voltage-dependent steps required for sodium channel activation. All closed states are in equilibrium with inactivation, giving rise to closed-state inactivation. The forward and reverse rates are represented as  $\alpha$  and  $\beta$ , respectively. Reproduced from (Irvine *et al.*, 1999).

## 1.6. Extrinsic and Intrinsic $Na_v1.5$ Modifiers

### 1.6.1. $\beta$ subunits

The  $Na_v1.5$  is co-expressed in cardiomyocytes with one or two ‘‘accessory’’  $\beta$ -subunits encoded by the *SCN1B* ( $\beta_1$ ), *SCN2B* ( $\beta_2$ ), *SCN3B* ( $\beta_3$ ), and *SCN4B* ( $\beta_4$ ) genes (McCormick *et al.*, 1998; Malhotra *et al.*, 2001; Gilchrist *et al.*, 2013).  $\beta_2$  and  $\beta_4$  form covalent disulfide links with the DIV S5-S6 extracellular linker, whereas  $\beta_1$  and  $\beta_3$  form non-covalent interactions with the  $\alpha$ -subunit (Qu *et al.*, 1995; Chen *et al.*, 2012; Gilchrist *et al.*, 2013).  $\beta$ -subunits usually increase sodium channel expression and alter inactivation kinetics in an isoform-dependent or mutant-dependent fashion (Brackenbury & Isom, 2008; Aman *et al.*, 2009; Patino & Isom, 2010). The biophysical defects caused by the BrS1 mutant, T1620M, are aggravated by  $\beta_1$  co-expression (Makita *et al.*, 2000). Mutations in *SCN1B*, *SCN2B*, *SCN3B* cause BrS5, BrS7, and BrS17, respectively. *SCN4B* mutations cause LQT10, such as with  $\beta_4$ -L179F which destabilizes fast inactivation (Medeiros-Domingo *et al.*, 2007).

## 1.6.2. C-terminal Domain

The C-terminal domain (CTD) in Nav<sub>v</sub>1.5 plays a crucial role in governing fast inactivation. Both intra-CTD and inter-CTD interactions are necessary for proper channel function (Tan *et al.*, 2002; Deschenes, 2002; Cormier *et al.*, 2002; Van Petegem *et al.*, 2012). Chimera studies, interchanging Nav<sub>v</sub>1.2 and Nav<sub>v</sub>1.5 CTDs, show that Nav<sub>v</sub>1.5 CTD does not stabilize or enhance onset in fast inactivation compared to Nav<sub>v</sub>1.2 (Mantegazza *et al.*, 2001). The proximal half of the Nav<sub>v</sub>1.5 CTD, however, is important in regulating inactivation compared to the distal half (Mantegazza *et al.*, 2001). Mutants in Nav<sub>v</sub>1.5 CTD proximal half perturb the normal CTD control on fast inactivation, potentially inducing Nav<sub>v</sub>1.2 fast inactivation characterized by a hyperpolarized voltage-dependence and accelerated onset kinetics (Mantegazza *et al.*, 2001; Tan *et al.*, 2002; Cormier *et al.*, 2002; Mori *et al.*, 2003).

Fluorescence resonance energy transfer (FRET) has been used to elucidate Nav<sub>v</sub>1.5 intra-CTD interactions (Glaaser *et al.*, 2012). The CTD contains a pair of EF-like hand domains ( $\alpha_1$ – $\alpha_4$ ) composed of a helix-loop-helix, approximately 120 residues upstream from an IQ domain ( $\alpha_6$ ), which binds calmodulin (Tan *et al.*, 2002; Wingo *et al.*, 2004; Glaaser *et al.*, 2006; Chagot *et al.*, 2009; Van Petegem *et al.*, 2012; Bagn ris *et al.*, 2013). The IQ motif interacts with aromatic residues in  $\alpha_1$  (F1791 and Y1795) and with residues in  $\alpha_1$ – $\alpha_2$  and  $\alpha_2$ – $\alpha_3$  linkers via its N-terminus (Chagot *et al.*, 2009; Glaaser *et al.*, 2012; Gabelli *et al.*, 2014). The S1904L mutant, located four residues upstream from the IQ motif, causes a steric clash with the EF-like hand domain (Bankston *et al.*, 2007). Disrupting the intra-CTD interactions involves decoupling CTD from inter-connections with the DIII-DIV linker, as with S1904L, which increases late  $I_{Na}$  (Glaaser *et al.*, 2006; Wang *et al.*, 2014). Intra-CTD interactions are also crucial in Nav<sub>v</sub>1.5 heterodimers where the IQ motif of one channel interacts with the EF-like hand domain of the neighboring channel (Gabelli *et al.*, 2014).

Interconnections between the CTD and the DIII-DIV linker in Nav<sub>v</sub>1.5 are modulated by the calcium-calmodulin complex under a calcium signal (Potet *et al.*, 2009; Sarhan *et al.*, 2009). During fast inactivation, the CTD fastens like a latch on the DIII-DIV linker via electrostatic and hydrophobic interactions, stabilizing fast inactivation (Motoike, 2004; Sarhan *et al.*, 2009; Wang *et al.*, 2012; Van Petegem *et al.*, 2012; Bagn ris *et al.*, 2013; Pitt & Lee, 2016; Yan *et al.*, 2017a). A proline-rich region (PIPRP, 1509-1513) in

the DIII-DIV linker partially constitutes the intermolecular interactions with the CTD (Motoike, 2004). *SCN5a* mutations expressed in the CTD usually halt this mode of regulation, thereby destabilizing inactivation and augmenting late  $I_{Na}$  (An *et al.*, 1998; Wei *et al.*, 1999; Bezzina *et al.*, 1999; Wang *et al.*, 2007).

### 1.6.3. Calcium-calmodulin complex

Unlike in  $Na_v1.4$ , which contains an additional aspartate in the CTD EF-like hand domain,  $Na_v1.5$  does not chelate calcium (Herzog *et al.*, 2003; Kim *et al.*, 2004; Shah *et al.*, 2006; Pitt, 2007; Chagot *et al.*, 2009; Van Petegem *et al.*, 2012; Ben-Johny *et al.*, 2014; Pitt & Lee, 2016). Calmodulin initially binds to the IQ domain via its C-lobe but reverts and weakly binds via its N-lobe with a calcium signal (Chagot *et al.*, 2009; Miloushev *et al.*, 2009; Sarhan *et al.*, 2012). The calmodulin C-lobe is then free to bind to other channel regions, primarily the DIII-DIV linker  $\alpha$ -helix formed by residues 1498-1501 (Potet *et al.*, 2009; Sarhan *et al.*, 2012). The tripartite complex formed by calmodulin destabilizes and stabilizes the fast inactivation particle at resting and depolarized potentials, respectively (Sarhan *et al.*, 2012; Potet *et al.*, 2015). Thus, calcium-dependent facilitation (CDF) dominates at resting potentials, thereby sustaining rapid heart rhythms, and calcium-dependent inhibition (CDI) at depolarized potentials, which reduces EADs and DADs (Shah *et al.*, 2006; Sarhan *et al.*, 2012). There are conflicting opinions on the role of calcium-calmodulin in modulating  $Na_v1.5$ . The controversies arise from the differences in experimental conditions between the studies. Calcium-dependent facilitation in  $Na_v1.5$  is not observed under dynamic calcium influx measured using photo-uncaging or with calcium spillover from neighboring calcium channels (Ben-Johny *et al.*, 2014). Some studies suggest that  $Na_v1.5$  functions like  $Ca_v1.2$ , refuting a tripartite complex formation and localizing CDF and CDI solely to the CTD (Pitt & Lee, 2016).

Both arrhythmia and epilepsy-associated mutations expressed in  $Na_v1.5$  and  $Na_v1.2$  CTDs, weaken non-calcified calmodulin affinity, thereby destabilizing fast inactivation (Miloushev *et al.*, 2009; Yan *et al.*, 2017a). Calmodulin over-expression rescues biophysical defects in  $Na_v1.5$  CTD mutants that perturb calmodulin's binding affinity except in the EF-like hand mutant, D1790G (Yan *et al.*, 2017a).

#### 1.6.4. Ca<sup>2+</sup>/calmodulin-dependent protein kinase II (Ca<sup>2+</sup>-CaMKII)

Besides regulating Nav<sub>v</sub>1.5, calcium-calmodulin activates protein kinase II (Ca<sup>2+</sup>-CaMKII) which antagonizes CDF and CDI (Wagner *et al.*, 2006; Pitt, 2007; Scheuer, 2011; Herren *et al.*, 2013). This adaptive 'fail-safe' mechanism induced by Ca<sup>2+</sup>-CaMKII may be useful with inherited *SCN5a* mutations, especially those expressed in the CTD, and thus disrupt normal calcium-calmodulin regulation of Nav<sub>v</sub>1.5.

CaMKII $\delta$ c is the main isoform expressed in the heart and phosphorylates Nav<sub>v</sub>1.5 at S516, S571 and T594 (Wagner *et al.*, 2006; Maltsev *et al.*, 2009; Herren *et al.*, 2013; Marionneau & Abriel, 2015). Over-expression of CaMKII $\delta$ c hyperpolarizes the voltage-dependence of fast inactivation, enhances intermediate/slow inactivation, slows recovery from inactivation, and increased late I<sub>Na</sub> (Wagner *et al.*, 2006; Livshitz & Rudy, 2007; Hund *et al.*, 2008; Herren *et al.*, 2013). The biophysical shifts caused by Ca<sup>2+</sup>-CaMKII may augment mixed syndrome pathogenesis due to inherited and/or acquired cardiac disease (Herren *et al.*, 2013).

#### 1.6.5. Protein Kinases A & C

Protein kinase A (PKA) and protein kinase C (PKC) have opposing effects on Nav<sub>v</sub>1.5 conductance (Qu *et al.*, 1996; Chen *et al.*, 2006; Marionneau & Abriel, 2015). Substances known to increase PKC activity include 2-dioctanoyl-rac-glycerol (DOG), 1-oleoyl-2-acetyl-sn-glycerol (OAG), and phorbol 12-myristate 13-acetate (PMA). PKC phosphorylates S1505 (in rodent Nav<sub>v</sub>1.5, S1503 in human Nav<sub>v</sub>1.5) in the DIII-DIV linker, which stabilizes closed-state fast inactivation (Qu *et al.*, 1996; Chen *et al.*, 2006). An alanine scan to the consensus PKC binding residues abolishes the PKC-induced reduction in peak I<sub>Na</sub> caused by voltage shifts in closed-state fast inactivation (Qu *et al.*, 1996). PKC effects on open-state fast inactivation and late I<sub>Na</sub> remain unknown.

The cAMP-dependent PKA phosphorylates S525 and S528 in the DI-DII linker (Murphy *et al.*, 1996; Frohnwieser *et al.*, 1997; Tateyama *et al.*, 2003). *In vitro*, *in silico*, and proteomic analyses suggest the presence of additional PKA phosphorylation sites in Nav<sub>v</sub>1.5 (Marionneau & Abriel, 2015). However, the extent to which these sites are phosphorylated is unknown. PKA increases Nav<sub>v</sub>1.5 trafficking and hyperpolarizes the voltage-dependence of activation and fast inactivation (Murphy *et al.*, 1996; Frohnwieser

*et al.*, 1997; Tateyama *et al.*, 2003; Chen *et al.*, 2006; Scheuer, 2011). The D1790G mutant has a unique response to PKA compared Y1795C and Y1795H (Tateyama *et al.*, 2003). Late  $I_{Na}$  in D1790G is markedly increased by PKA (Tateyama *et al.*, 2003). Although this charge-neutralizing mutant is located in the CTD, it enhances PKA activity which binds to S36 and S525 residues, suggesting that the CTD may have direct or indirect interactions with the N-terminus and/or the DI-DII linker. A crosstalk mechanism may exist between  $Na_v1.5$  inter-linkers, and the N- and C-termini, thereby modulating PKA activity. The R526H mutant, however, found adjacent to the PKA phosphorylation site, inhibits PKA and exacerbates loss-of-function in  $Na_v1.5$  (Marionneau & Abriel, 2015).

### 1.6.6. Temperature

Temperature plays an important role in regulating channel behavior and kinetics (Collins & Rojas, 1982; Matteson & Armstrong, 1982; Smeets *et al.*, 1986). A major caveat in the electrophysiology studies is the temperature at which patch-clamp recordings are performed. Most experiments are conducted at room temperature (22 °C). Patch-clamp recordings become unstable at elevated temperatures. Reports of  $Q_{10}$  coefficients for the different  $Na_v1.5$  states are limited, and extrapolating biophysical data using a uniform  $Q_{10}$  coefficient cannot be generalized since  $Na_v1.5$  variants are differentially altered by temperature (Mohammadi *et al.*, 2003; Mok *et al.*, 2003; Keller *et al.*, 2006; Trip *et al.*, 2007; Egri *et al.*, 2012; Holzherr *et al.*, 2014).

Governed by anabolism and catabolism, body temperature is usually around 37 °C. Body temperature varies with sex, age, time of the day, and the physiological state. During sleep, body temperature generally decreases (~ 36 °C) but may increase during REM sleep. Elevations in body temperature accompany exercise, reaching as high as 40 °C. Body temperature may drop below 35 °C or rise to 45 °C under extreme hypothermia or hyperthermia, respectively. Hyperthermia may serve as an arrhythmogenic trigger, unmasking BrS1 (Wakita *et al.*, 2004; Peng *et al.*, 2005; Makaryus *et al.*, 2009).

One case study reported a 54 year-old man displaying BrS1 patterns during a fever (41 °C) which recovered during the afebrile state (Mok *et al.*, 2003). The man carried the H681P  $Na_v1.5$  mutant. This mutant stabilizes activation and inactivation

states leading to a decrease in window current, reducing the net  $I_{Na}$  (Mok *et al.*, 2003). H681P was not characterized at elevated temperature, however.

Elevated temperatures depolarized the voltage-dependence of activation in the BrS1 mutant, T1620M, located in DIV S3-S4 linker (Dumaine *et al.*, 1999). Decreased  $Na_v1.5$  availability explains the decelerated cardiac conduction velocity resulting in right bundle branch block and H-R interval prolongation in T1620M carriers (Dumaine *et al.*, 1999). Similarly, hyperthermia destabilizes the voltage-dependence of activation and enhances fast inactivation recovery kinetics in the F1344S mutant. The former biophysical shift overrides the latter thereby unmasking BrS1 in F1344S carriers (Keller *et al.*, 2006).

Hyperthermia-induced LQTS was mainly reported in LQT1 and LQT2 patients (Amin *et al.*, 2008; Burashnikov *et al.*, 2008; Amin *et al.*, 2010a; Elbey *et al.*, 2012; Nakajima *et al.*, 2015). Less is known about LQT3 patients' response to hyperthermia. The LQT3 mutant,  $\Delta$ KPQ, was functionally characterized at elevated temperature and was not thermosensitive (Nagatomo *et al.*, 1998). Nevertheless, no clinical data correlate with this biophysical finding.

### **1.6.7. Temperature and Calcium Interaction**

Hypothermia elevates cytosolic calcium by mainly increasing RyR open probability (more leaky), thereby increasing heart contracture in hibernators (Hannon, 1958; Johansson, 1996; Nolan, 2003; Shutt & Howlett, 2008; El-Sayed *et al.*, 2012; Polderman, 2013; Nielsen *et al.*, 2013). Hypothermia slows  $Ca_v1.2$  kinetics and the turnover rate of other transporters such as SERCA and NCX, and reduces troponin C and calmodulin's binding affinities to calcium (Pelzmann *et al.*, 1998; da Silva *et al.*, 2002; Fu *et al.*, 2005).

Shifts in cytosolic calcium caused by hyperthermia have not been studied extensively as hypothermia. Elevated temperature increases L-type  $I_{Ca}$  amplitude and  $Ca_v1.2$  kinetics in cardiomyocytes, and also increase NCX's and SERCA's turnover rates (Elias *et al.*, 2001; Ferrier *et al.*, 2003). However, it is difficult to determine cytosolic calcium levels from the large amplitude and short lasting  $I_{Ca}$  transients. A hyperthermia stimulus to human colon cancer cells initially reduces cytosolic calcium but is followed by

a marked rise in cytosolic calcium with maintained stimulation (Mikkelsen *et al.*, 1991). Other confounding variables may contribute to the rise in cytosolic calcium, falsely attributed to elevated temperature in physiological settings (Marks, 2003).  $\beta_1$  adrenergic agonists indirectly modulate cytosolic calcium. PKA activation increases L-type  $I_{Ca}$  influx and the open-probability of RyR (Marks, 2003). PKA phosphorylates Troponin I, thereby reducing Troponin C's affinity for cytosolic calcium, causing a faster attenuation to the calcium spark (Peña & Wolska, 2004). PKA also phosphorylates phospholamban, increasing calcium uptake into the sarcoplasmic reticulum (Song *et al.*, 2001). Thus, the overall net increase in cytosolic calcium accompanying exercise is complex and governed by many factors modulating the inflow and outflow of cytosolic calcium.

## 1.7. Antiarrhythmic Drugs and VGSCs

Voltage gated sodium channels are a target for many antiarrhythmics, anticonvulsants, and local anesthetics. Various toxins and pharmacological modulators bind to different channel modes (Hille, 1977; Tikhonov & Zhorov, 2017). The modulated receptor hypothesis relates the functional state of VGSC with pharmacodynamics (Ragsdale *et al.*, 1996; Li *et al.*, 1999; Denac *et al.*, 2000). Although the hypothesis was originally based on local anesthetics, it is applicable to antiarrhythmics and postulates that  $Na_V$  blockers bind to the activated/inactivated states versus the deactivated state.

The Food and Drug Administration (FDA) approved 12 class I a-c antiarrhythmics (**Table 1-1**). Other antiarrhythmics function as  $\beta_1$  blockers (slow heart rate, class II), potassium channel blockers (class III), calcium channel blockers (class IV), and ones with variable pharmacological mechanisms (class V). The yellow-highlighted class I antiarrhythmics in **Table 1-1** are no longer prescribed in the clinic due to their dangerous effects.

**Table 1-1 Class I antiarrhythmics**

Class Name	Generic Name	Brand Name
Class Ia	Quinidine	Cardioquin
	Ajmaline	Gilurytmal
	Procainamide	Pronestyl
	Disopyramide	Norpace
Class Ib	Lidocaine	Anestacaine
	Phenytoin	Dilantin
	Mexiletine	Mexitil
	Tocainide	Tonocard
Class Ic	Encainide	Enkaid
	Flecainide	Tambocor
	Propafenone	Rythmol
	Moricizine	Ethmozine

### 1.7.1. Antiarrhythmics mode of Action

Most class I antiarrhythmics share common molecular determinants with other local anesthetics and anticonvulsants (Ragsdale *et al.*, 1996; Ragsdale & Avoli, 1998; Clare *et al.*, 2000; Czapiński *et al.*, 2005; Sheets *et al.*, 2010; Lipkind & Fozzard, 2010; O'Reilly *et al.*, 2012; Lee *et al.*, 2012). Residues F1760 and Y1767 in the inner vestibule of Na<sub>v</sub>1.5 form the binding sites for class I antiarrhythmics (Ragsdale *et al.*, 1996; Fredj *et al.*, 2006b; Lipkind & Fozzard, 2010; Huang *et al.*, 2011; O'Reilly *et al.*, 2012). The location of these residues indicates that these drugs adopt an intracellular binding mode in Na<sub>v</sub>1.5. In the open-state conformation, the C-termini of S6 in DI to DIV form a wide opening, which exposes the two receptor sites in the pore. In this high affinity conformational state, small class I antiarrhythmics and anesthetics like Lidocaine and Phenytoin, form interactions with F1760 and Y1767 aromatic rings, thereby blocking the pore (Fredj *et al.*, 2006b; Sheets *et al.*, 2010; Lipkind & Fozzard, 2010; O'Reilly *et al.*, 2012). Phenytoin forms a non-polar aromatic-aromatic interaction with the Y1767 residue, while the other amide containing branch (hydantoin ring) forms a polar bond between the electron-donating π electron in F1760 aromatic residue (Lipkind & Fozzard, 2010). Phenytoin partially interacts with residues near the IFM motif, thereby stabilizing the fast-inactivated state. F1760 and Y1767 form thermodynamically favourable interactions with the IFM motif and also stabilize fast inactivation (Ulbricht, 2005).

Lidocaine has similar effects as Phenytoin. Alanine scans to the receptors sites reduce Lidocaine binding affinity to Na<sub>v</sub>1.5, which reduces the drug's voltage-dependent and frequency-dependent block (Li *et al.*, 1999).

Minimal research has been devoted to drug effects on channel trafficking or expression. The M1766L is the only Nav1.5 mutant where the expression defect is rescued by Mexiletine (Valdivia *et al.*, 2002).

### **1.7.2. Arrhythmias provoked by Antiarrhythmic Drugs**

Antiarrhythmics do not always ameliorate arrhythmias, rather they may be clinically used to provoke, and hence test for positive *SCN5a* mutation carriers (Haverkamp, 2000; Fenichel *et al.*, 2004; Fish & Antzelevitch, 2004a). E1784K carriers express BrS more preferentially when administered with Ajmaline compared to Flecainide or Pilsicainide (Makita *et al.*, 2008a). Flecainide has proven to be therapeutic in certain *SCN5a* mutations; however, it induces a large tonic peak  $I_{Na}$  block in certain Nav1.5 mutants, posing a pro-arrhythmic threat for BrS1 and mixed syndrome mutants (Viswanathan *et al.*, 2001; Moss *et al.*, 2005). Arrhythmias may occur with enhanced peak  $I_{Na}$  tonic-block, inducing channel loss-of-function. Flecainide is therapeutic compared to lidocaine in treating LQT3-induced phenotypes in D1790G by increasing channel use-dependence (Benhorin *et al.*, 2000; Abriel *et al.*, 2000; Zhu *et al.*, 2006). Similarly, lidocaine is effective in treating LQT3, but augments channel use-dependence in V232I+L1308F, which unmasks BrS (Balsler *et al.*, 1996; Sheets & Hanck, 2007; Barajas-Martinez *et al.*, 2008).

Acquired BrS and LQTS are usually caused by class I antiarrhythmics and class III antiarrhythmics, respectively (Day *et al.*, 1990; Shimizu & Antzelevitch, 1999; Fenichel *et al.*, 2004). Quinidine is implicated in acquired LQTS due to its high potency for blocking HERG (Paul *et al.*, 2002). To selectively target LQT3 in *SCN5a* mutations and prevent the occurrence of BrS, the pharmaceutical industry has developed LQT3-specific drugs: ranolazine and new compounds like aryl sulfonamides selectively block late  $I_{Na}$  compared to peak  $I_{Na}$  (Antzelevitch, 2004; Antzelevitch *et al.*, 2004; Belardinelli, 2006b; Ahuja *et al.*, 2015).

### **1.7.3. Ranolazine**

Ranolazine is used to treat angina pectoris, cardiac instability, arrhythmias, and reduced contractility due to improper sodium balance within myocytes caused by augmented late  $I_{Na}$  (Antzelevitch *et al.*, 2004; Belardinelli, 2006a). Sodium overload

reverses NCX function causing calcium overload, thereby increasing the risk for electrical and mechanical abnormalities. Ranolazine preferentially blocks late  $I_{Na}$ , thereby reducing intracellular sodium and calcium overload.

A Cysteine substitution to the second receptor site in  $Na_V1.5$ , Y1767, abolishes the inhibitory effects of Quinidine, Mexiletine, and Flecainide on late  $I_{Na}$  (Huang *et al.*, 2011). Ranolazine, however, is not affected by Y1767C and effectively suppresses late  $I_{Na}$ , suggesting that ranolazine adapts a different binding mode compared to classic antiarrhythmics (Ahern *et al.*, 2008; Huang *et al.*, 2011). Replacing the large aromatic group in Y1767 with a smaller cysteine side chain may reduce the steric hindrance experienced by ranolazine while accessing its binding site at the inner pore (Huang *et al.*, 2011; Kaczmarek & Corry, 2014). Ranolazine binding mode is not limited, however, to the inner pore; the fenestrations are an accessory route for large and bulky  $Na_V$  blockers (Kaczmarek & Corry, 2014). Thus, it is plausible for ranolazine to regulate  $Na_V$  inactivation at the fenestrations or at the interphase between the inner vestibule drug binding sites and the fenestrations.

In addition to its inhibitory effects on  $Na_V1.5$ , ranolazine also blocks neuronal  $Na_V$  isoforms. Ranolazine reduces pathological late  $I_{Na}$  caused by epilepsy-associated  $Na_V1.1$  mutants (Kahlig *et al.*, 2010). In most  $Na_V$  isoforms, ranolazine stabilizes the slow inactivated state by accelerating onset and decelerating recovery kinetics of slow inactivation (Peters *et al.*, 2013). Acidosis accentuates these drug effects in both  $Na_V1.2$  and  $Na_V1.5$ , which is correlated with attenuated late  $I_{Na}$  (Sokolov *et al.*, 2013; Peters *et al.*, 2013). Ranolazine, may thus adopt a different binding mode from that of the receptor modular hypothesis. Ranolazine is structurally similar to Lidocaine. Movement of DIII and DIV S4s stabilizes Lidocaine binding (Sheets & Hanck, 2007). Thus, ranolazine may stabilize slow inactivation by interacting with DIII or DIV segments and not necessarily bind to the inner vestibule.

#### **1.7.4. $Na_V$ targets exhibiting novel modes of action**

Lacosamide is a novel anticonvulsant that effectively treats partial seizures. Lacosamide, like ranolazine, stabilizes the slow-inactivated state compared to other anticonvulsants that primarily affect fast inactivation. By increasing channel use-dependence, Lacosamide is able to reduce long-lasting neuronal repetitive firing spikes

elicited by prolonged depolarizations (Errington *et al.*, 2007). Phenytoin, Carbamazepine, and Lamotrigine exert their action over substantially shorter time scale (Ragsdale *et al.*, 1996; Errington *et al.*, 2007; Yang *et al.*, 2010).

As opposed to drugs binding to the inner vestibule or through the fenestrations, recent drug design attempts to target  $\text{Na}_v$  extracellularly. Ionic compounds, such as aryl sulfonamides like GX-936, form salt bridges with the fourth arginine (R4) residue in DIV S4 (Ahuja *et al.*, 2015). This ionic bond stabilizes the activated fast inactivation segment (DIV S4), thereby reducing late  $I_{\text{Na}}$  (Sheets & Hanck, 2007; Ahuja *et al.*, 2015). Although a breakthrough, further modifications to aryl sulfonamide compounds is required to achieve higher  $\text{Na}_v$ -isoform selectivity.

## 1.8. Thesis Significance

The most common *SCN5a* mutation, expressed as the E1784K mutant, is very well characterized. Functional data support a correlation between channel type and phenotype in E1784K. However, the high phenotype heterogeneity in E1784K carriers must be further elucidated. The cardiac conduction abnormalities manifesting as BrS1 or heart block accompanied by prolonged QT intervals in E1784K carriers may ultimately trickle down to the effects of external triggers on channel type. E1784K distorts  $\text{Na}_v1.5$  CTD integrity. Despite E1784's presence prior to the EF-like hand domain, it forms electrostatic interactions with downstream residues in the IQ domain, establishing an intact CTD (Chagot *et al.*, 2009; Yan *et al.*, 2017a). The charge reversal mutant distorts the normal salt bridges required for CTD maintenance, thereby eliminating the adaptive roles adopted by several CTD-interacting molecules like calmodulin, in rescuing biophysical defects (Yan *et al.*, 2017a). Various CTD mutants disrupt calmodulin's inherent role in limiting pathogenic late  $I_{\text{Na}}$  either by directly or indirectly affecting the molecule's binding affinity for the CTD. Furthermore, both the dependent and independent calcium-calmodulin interactions between the CTD and the DIII-DIV linker may be affected in E1784K. I hypothesize that exercise-related factors like elevated temperature and cytosolic calcium affect channel type expressivity in E1784K. Temperature enhances channel kinetics, thereby augmenting E1784K biophysical defects. Cytosolic calcium, although is known to be therapeutic for LQT3 mutants, is not effective in ameliorating E1784K since the mutant deprives  $\text{Na}_v1.5$  from calcium-calmodulin regulation. The disintegration in intra-CTD interactions caused by E1784K

may decouple the CTD and the DIII-DIV linker, further reducing calcium-calmodulin regulation. I hypothesize that ranolazine is an effective therapy for E1784K since it preferentially blocks augmented late  $I_{Na}$ .

## 1.9. Thesis Objectives

My thesis objectives are to study the effect of **(1)** elevated temperature, **(2)** elevated cytosolic calcium, and **(3)** their combined triggering effects on E1784K when screened against ranolazine. An in-depth biophysical characterization of wild type and mutant channel gating is done using the whole-cell patch clamp technique. Chinese Hamster Ovary (CHOK1) or Human Embryonic Kidney (HEK293) cells, with varying calmodulin levels, are used to control for temperature and cytosolic calcium effects, separately. Temperature effects are studied on E1784K along with a reference mixed syndrome mutant, R1193Q, expressed in the DII-DIII linker. Cytosolic calcium effects are studied on E1784K and other DIII-DIV linker and CTD mutants like  $\Delta$ KPQ, 1795insD, and Q1909R. These mutants are chosen specifically for comparative reasons since their position may uniquely modify calcium-calmodulin regulation in  $Na_v1.5$ . Ranolazine is screened against E1784K at elevated temperature and cytosolic calcium. *In-silico* cardiac action potentials are simulated using modified ten Tüßscher (2006) and O'Hara-Rudy (2011) models. A dynamic simulation is included using the latter model in objectives **(2)** and **(3)** to account for the positive-staircase phenomenon of cytosolic calcium. Thus, I am able to account for modifications in sodium currents caused by cytosolic calcium. Molecular docking is used to understand ranolazine binding to  $Na_v1.5$ . Ranolazine was auto-docked against the  $Na_v1.5$  homology model based on the new American cockroach  $Na_vPas$  structure.

## Chapter 2. Differential Thermosensitivity in Mixed Syndrome Cardiac Sodium Channel Mutants

This chapter describes the work published in (Abdelsayed *et al.*, 2015) with minor modifications and formatting changes to suit the thesis style.

### 2.1. Abstract

**Introduction:** Cardiac arrhythmias are often associated with mutations in *SCN5a*, the gene that encodes the cardiac paralog of the voltage-gated sodium channel,  $Na_v1.5$ . The  $Na_v1.5$  mutants R1193Q and E1784K give rise to both Long QT and Brugada syndromes. Various environmental factors, including temperature, may unmask arrhythmia. We sought to determine whether temperature might be an arrhythmogenic trigger in these two mixed syndrome mutants.

**Methods:** Whole-cell patch-clamp was used to measure the biophysical properties of  $Na_v1.5$  WT, E1784K and R1193Q mutants. Recordings were performed using Chinese Hamster Ovary (CHOK1) cells transiently transfected with the  $Na_v1.5$   $\alpha$  subunit (wild type, E1784K, or R1193Q),  $\beta_1$  subunit, and eGFP. The channels' voltage-dependent and kinetic properties were measured at three different temperatures: 10 °C, 22 °C, and 34 °C.

**Results:** The E1784K mutant is more thermosensitive than either WT or R1193Q channels. When temperature is elevated from 22 °C to 34 °C, there is a greater increase in late  $I_{Na}$  and use-dependent inactivation in E1784K than WT or R1193Q. However, when temperature is lowered to 10 °C, the two mutants show a decrease in channel availability. Action potential modeling using  $Q_{10}$  fit values, extrapolated to physiological and febrile temperatures, show a larger transmural voltage gradient in E1784K compared to R1193Q and WT with hyperthermia.

**Conclusions:** The E1784K mutant is more thermosensitive than WT or R1193Q channels. This enhanced thermosensitivity may be a mechanism for arrhythmogenesis in patients with E1784K sodium channels.

## 2.2. Introduction

Voltage-gated sodium channels are responsible for the upstroke of action potentials in most cardiac, skeletal, and neuronal tissue. In this study, we focus on  $\text{Na}_v1.5$ , the sodium channel most prevalent in the cardiac conduction system and cardiomyocytes (Remme *et al.*, 2009). Mutations in *SCN5a*, the gene encoding  $\text{Na}_v1.5$ , give rise to a large spectrum of potentially arrhythmogenic disorders including Brugada and Long QT-3 syndromes.

Long QT syndrome 3 (LQT3) is due to gain-of-function mutants of  $\text{Na}_v1.5$ , in which the S4 voltage sensor, the DIII-DIV linker segment, and the C-terminus are most commonly affected (Glaaser *et al.*, 2012). These mutants hinder fast inactivation and lead to an increase in late  $I_{\text{Na}}$  which disrupts the normal balance between outward and inward currents that maintain the plateau phase of the cardiac action potential (AP). An increase in late  $I_{\text{Na}}$  delays cardiomyocyte repolarization and prolongs the cardiac action potential. In contrast, loss-of-function  $\text{Na}_v1.5$  mutants that diminish peak  $I_{\text{Na}}$  can cause Brugada syndrome 1 (BrS1). Many of the mechanisms underlying BrS1 involve stabilizing inactivated states and/or destabilizing the activated state (Grant *et al.*, 2002). Due to heterogeneous channel expression in the heart tissue, BrS1 preferentially affects the right epicardial AP. Relatively high levels of  $I_{\text{K,to}}$  (transient outward potassium current), found in the right ventricular epicardium, can cause the loss of the AP plateau in myocytes with decreased  $I_{\text{Na}}$ . This loss generates a transmural voltage gradient causing ST segment elevation, visible in the right precordial leads. This phenomenon is also known as “phase 2 reentry” (Chen *et al.*, 1998; Antzelevitch, 2005). There are three different manifestations of this phenomenon in the ECG: Type I is characterized by a J-point elevation, a coved ST-segment, and an inverted T wave in  $V_1$ - $V_3$ ; Type II shows a saddleback-type ST-segment elevation; Type III shows an ST-segment elevation accompanied by a J-point elevation. Types II and III are not diagnostic of BrS (Antzelevitch, 2005).

BrS1 and LQT3 have been reported to precipitate ventricular tachycardia and ventricular fibrillation leading to sudden death in men and women, and sudden infant death syndrome in young children (Priori *et al.*, 2000; García-Borbolla *et al.*, 2007; Makaryus *et al.*, 2009). BrS1 may be unmasked by decreases in plasma pH, changes in body core temperatures, and pharmacological agents that block sodium channels (Mok

*et al.*, 2003; Makaryus *et al.*, 2009; Doetzer *et al.*, 2011). Elevated temperatures exacerbate the decrease in channel function in the BrS1 mutant T1620M by causing a larger destabilization of the activated state (Dumaine *et al.*, 1999). Additionally, there is an enhanced onset into inactivation at elevated temperatures (Dumaine *et al.*, 1999). In another thermosensitive-mutant, F1344S, the conductance is further destabilized at elevated temperatures (Keller *et al.*, 2006).

Interestingly, some Nav1.5 mutants, including R1193Q and E1784K, can cause both LQT3 and BrS1 and are referred to as mixed syndromes (Bezzina *et al.*, 1999; Veldkamp *et al.*, 2000a; Grant *et al.*, 2002). Molecular genetic screening revealed that a heterozygous mutation, in which a guanine was replaced with an adenine in the 3578<sup>th</sup> position in exon 20 of *SCN5a*, results in the R1193Q mutant (Huang *et al.*, 2006). R1193Q is located in the intracellular DII-DIII linker region. This mutant stabilizes the fast-inactivated state (Wang, 2004; Huang *et al.*, 2006). Enhanced inactivation may lead to a decrease in sodium currents, consistent with the phenotype of BrS1. However, the mutant increases late I<sub>Na</sub>, associated with LQT3 (Sun *et al.*, 2008). A guanine to an adenine mutation in the 5349<sup>th</sup> position of *SCN5a* results in the E1784K mutant in the C-terminus of Nav1.5 (Splawski *et al.*, 2000; Tester *et al.*, 2005). E1784K tends to stabilize steady-state inactivation but also increases late I<sub>Na</sub> (Wei *et al.*, 1999; Makita *et al.*, 2008a).

Our study focused on the effects of temperature on wild-type (WT), R1193Q, and E1784K channels. Our results suggest differential thermosensitivity in the E1784K and R1193Q mutants. E1784K is most strongly affected by temperature changes. Action potential simulations suggest that increasing temperature may attenuate the epicardial AP dome in cardiomyocytes expressing the E1784K mutant. Temperature increases may therefore be arrhythmogenic in E1784K.

## **2.3. Methods**

### **2.3.1. Ethical approval**

The research was approved by Biohazards review 251-2012 issued by the office of the Environmental Health and Safety at Simon Fraser University, Burnaby, BC, Canada.

### **2.3.2. Cell Culture**

Chinese hamster ovary (CHOK1) cells (Sigma-Aldrich) were grown at pH 7.4 in filter sterile F12 (Ham) nutrient medium (Life Technologies, NY, USA), supplemented with 5% FBS and maintained in a humidified environment at 37°C with 5% CO<sub>2</sub>. Twenty-four hours prior to electrophysiology experiments, cells were transfected with cDNA for the sodium channel  $\alpha$  and  $\beta$  subunits as well as green fluorescent protein (eGFP). Eight hours after transfection, cells were dissociated with 0.25% trypsin-EDTA (Life Technologies, NY, USA) and then plated on sterile cover slips. These time intervals were used to control for channel expression.

### **2.3.3. Transfection**

Transfection followed the procedures suggested by Qiagen. Briefly, 1  $\mu$ g of the Na<sub>v</sub>1.5  $\alpha$  subunit, 0.5  $\mu$ g of the sodium channel  $\beta$ 1 subunit, and 1  $\mu$ g of eGFP were allowed to incubate with 15  $\mu$ l of polyfect transfection reagent (Qiagen) and 147  $\mu$ l of unsupplemented medium for 10 minutes. The cDNA mixture was then allowed to incubate with the CHOK1 cells for 8 hours before plating on coverslips. Na<sub>v</sub>1.5 mutations were generously provided by Dr. Charles Antzelevitch (E1784K) and Dr. Mohamed Chahine (R1193Q).

### **2.3.4. Electrophysiology**

Whole-cell recordings were performed in extracellular solution containing (mM): 140 NaCl, 4 KCl, 2 CaCl<sub>2</sub>, 1 MgCl<sub>2</sub>, and 10 HEPES (pH 7.4). Solutions were titrated with CsOH to pH 7.4. Pipettes were fabricated with a P-1000 puller using borosilicate glass (Sutter Instruments, CA, USA), dipped in dental wax to reduce capacitance, then thermally polished to a resistance of 1.0-1.5 M $\Omega$ . Low resistance electrodes were used to minimize series resistance between pipette and intracellular solution resulting in typical access resistances of 3.5 M $\Omega$  or less, thereby minimizing voltage measurement error. Pipettes were filled with intracellular solution, containing (mM): 130 CsF, 10 NaCl, 10 HEPES, and 10 EGTA titrated to pH 7.4.

All recordings were made using an EPC-9 patch-clamp amplifier (HEKA Elektronik, Lambrecht, Germany) digitized at 20 kHz using an ITC-16 interface (HEKA

Elektronik, Lambrecht, Germany). Data were acquired and low-pass-filtered (5 kHz) using PatchMaster/FitMaster software (HEKA Elektronik, Lambrecht, Germany) running on an Apple iMac (Apple Computer, Cupertino, CA). Leak subtraction was performed online using a P/4 procedure. Bath solution temperature was controlled using a Peltier device driven by a TC-10 Temperature Controller (Dagan, Minneapolis, MN). Bath temperature was maintained at 10 °C, 22 °C or 34 °C. Experiments were not performed at physiological temperatures because of the inherent instability of cells at temperatures above 34 °C. Using a Q<sub>10</sub> relationship we extrapolated data to physiological temperatures (described below). After a Giga-ohm seal-resistance was achieved, the whole-cell configuration was attained. Currents were then allowed to stabilize such that currents measured by successive trains of five 10 ms depolarizations at 1 Hz to 0 mV were similar. Run-down was assessed by comparing peak current amplitudes before and after each protocol. With the exception of use-dependent inactivation protocols only protocols with less than 5% run-down were used. Use-dependent protocols showing more than 5% rundown were corrected post hoc. The holding potential between protocols was -110 mV. We recorded I<sub>Na</sub> from cells that expressed currents no greater than -5 nA. Cells with larger currents were not used since they gave rise to voltage-error issues. The average voltage error calculated for all cells used in this study is 6.15 mV obtained from a total of 114 cells (**Table 2-1**). There are no differences between the voltage-errors in the different conditions (p>0.05).

**Table 2-1      Temperature Voltage Error**

Condition	Voltage Error	N
WT-10	6.59 ± 0.95	14
WT-22	5.15 ± 0.95	11
WT-34	6.49 ± 1.08	9
RQ-10	6.95 ± 1.12	14
RQ-22	6.58 ± 1.37	6
RQ-34	7.10 ± 0.86	15
EK-10	6.23 ± 1.47	10
EK-22	6.75 ± 1.08	14
EK-34	8.73 ± 0.81	21

### 2.3.5. Analysis

Analysis and graphing were done using FitMaster software (HEKA Elektronik, Lambrecht, Germany) and Igor Pro (Wavemetrics, Lake Oswego, OR, USA) with statistical information derived using JMP statistical software. All data acquisition and analysis programs were run on an Apple iMac (Apple Computer, Cupertino, CA). Statistical significance was accepted at  $p < 0.05$  using a two-factor completely randomized design (CRD) ANOVA test followed by a post-hoc Tukey test. We used a post hoc Student's t test to analyze temperature effect on late current (22 °C and 34 °C) and steady-state slow inactivation (10 °C and 22 °C). Statistical analysis was performed on the averages between three variables: channel variant (WT, R1193Q, E1784K), temperature (10 °C, 22 °C, 34 °C), and channel variant  $\times$  temperature. The latter represented the statistical significance of a change in channel variants as a result of temperature changes. All values reported are given as means  $\pm$  standard error of means.

### 2.3.6. Voltage Protocols

#### 2.3.6.1 Activation

To determine the voltage dependence of activation, we measured the peak current amplitude at test pulse potentials ranging from -100 mV to +80 mV in increments of +10 mV for 19 ms. Prior to the test pulse, channels were allowed to recover from fast inactivation at -130 mV for 197 ms. Channel conductance was calculated from peak  $I_{Na}$ .

$$1. G_{Na} = I_{Na}/V - E_{rev}$$

where  $G_{Na}$  is sodium channel conductance,  $I_{Na}$  is peak sodium current in response to the command potential  $V$ , and  $E_{rev}$  is the reversal potential. Calculated values for conductance were fit with the Boltzmann function:

$$2. G/G_{max} = 1/(1 + \exp[-ze_0[V_m - V_{1/2}]/kT])$$

where  $G/G_{max}$  is the normalized conductance amplitude,  $V_m$  is the command potential,  $z$  is the apparent valence,  $e_0$  is the elementary charge,  $V_{1/2}$  is the midpoint voltage,  $k$  is the Boltzmann constant, and  $T$  is temperature in °K.

### **2.3.6.2 Steady-State Fast Inactivation (SSFI)**

The voltage-dependence of SSFI was measured by preconditioning the channels to a hyperpolarizing potential of -130 mV and then eliciting prepulse potentials that range from -130 or -150 to +10 mV in increments of 10 mV for 200 ms. Channel availability was assessed by a test pulse to 0 mV. Different hyperpolarizing prepulse potentials (-130 mV or -150 mV) were used to obtain a plateau for the SSFI curve. Normalized current amplitude as a function of voltage was fit using the Boltzmann function:

$$3. \quad I/I_{\max} = 1/(1 + \exp(-ze_0 (V_M - V_{1/2})/kT))$$

where  $I/I_{\max}$  is the normalized current amplitude,  $z$  is apparent valence,  $e_0$  is the elementary charge,  $V_m$  is the prepulse potential,  $V_{1/2}$  is the midpoint voltage of SSFI,  $k$  is the Boltzmann constant, and  $T$  is temperature in °K.

### **2.3.6.3 Fast Inactivation Onset**

Time constants for open-state fast inactivation were derived by fitting a single exponential function to the decay of current obtained from the activation protocol. To measure onset into fast inactivation, channels were preconditioned at -130 mV prior to a prepulse at -50 mV, -70 mV, or -90 mV for 0 – 0.256 s. Current amplitude was measured during a test pulse to 0 mV for 20 ms. Normalized current amplitudes as a function of time were fit using a single exponential equation:

$$4. \quad I = I_{ss} + \alpha \exp(-(t-t_0)/\tau)$$

where  $I$  is the current amplitude,  $I_{ss}$  is the plateau amplitude,  $\alpha$  is the amplitude at time 0 for time constant  $\tau$ , and  $t_0$  is initial time. Rates of recovery from and onset into fast inactivation were calculated from the reciprocal of the time constants ( $\tau$ ) obtained from the single-exponential fits.

### **2.3.6.4 Fast Inactivation Recovery**

Channels were fast-inactivated during a 200 ms depolarizing step to 0 mV. Recovery was measured during a 19 ms test pulse to 0 mV following 0 – 1.024 s conditioning pulses at -130 mV, -110 mV, or -90 mV. Time constants of fast inactivation recovery as a function of time were fit using a single exponential equation, as above.

### **2.3.6.5 Late Current**

Late current was measured between 45 – 50 ms during a 50 ms depolarizing pulse to 0 mV from a holding potential of –130 mV. An average of 60 pulses was used to increase the signal-to-noise ratio.

### **2.3.6.6 Use-Dependent Inactivation (1 Hz and 3 Hz)**

Channels accumulated into a use-dependent inactivated state during either a series of 300 380 ms depolarizing pulses to 0 mV followed by a 615 ms – 90 mV recovery pulse at a frequency 1 Hz, or 500 220 ms depolarizing pulses to 0 mV followed by a 110 ms – 90 mV recovery pulse at a frequency 3 Hz. Normalized current amplitude as a function of time was fit with a double exponential.

$$5. I = I_{ss} + \alpha_1 \exp(-t/\tau_1) + \alpha_2 \exp(-t/\tau_2)$$

where  $I$  is the current amplitude,  $I_{ss}$  is the plateau amplitude,  $\alpha_1$  and  $\alpha_2$  are the amplitudes at time 0 for time constants  $\tau_1$  and  $\tau_2$ , and  $t$  is time.

### **2.3.6.7 Slow Inactivation Onset**

To measure onset into slow inactivation, channels were preconditioned at -130 mV for 30 s prior to a prepulse at 0 mV for 0 – 64 s. A test pulse to 0 mV followed a -130 mV recovery pulse from fast inactivation for 20 ms. Normalized current amplitudes as a function of time were fit using a double exponential equation.

### **2.3.6.8 Steady-State Slow Inactivation (SSSI)**

The voltage-dependence of SSSI was measured by preconditioning the channels to a hyperpolarizing potential of -150 mV for 30 s and then eliciting prepulse potentials that range from -150 to -10 mV in increments of 20 mV for 60 s. Channel availability was assessed by a test pulse to 0 mV following a -130 mV recovery pulse from fast inactivation at 20 ms. Normalized current amplitude as a function of voltage was fit using a modified Boltzmann function:

$$6. I/I_{max} = (I_1 - I_2)/(1 + \exp(-ze_0 (V_M - V_{1/2})/kT)) + I_2$$

where  $I_1$  and  $I_2$  are maximum and minimum values of fit. The other symbols are as previously stated.

### 2.3.6.9 **Slow Inactivation Recovery**

To measure recovery from slow inactivation, channels were preconditioned at -130 mV for 30 s prior to a prepulse at 0 mV for 60 s, followed by series of test pulses to 0 mV for 20 ms between increasing incremental recovery durations at -130 mV for 0 – 32s. Normalized current amplitudes as a function of time were fit using a double exponential equation with the plateau equal to 1.00.

### 2.3.6.10 **Q<sub>10</sub> Coefficients**

To determine an appropriate fit for the kinetic or thermodynamic parameters plotted as a function temperature, we used the Q<sub>10</sub> formula:

$$7. \quad Q_{10} = (R_2/R_1)^{10/(T_2-T_1)}$$

where R is the rate and T is temperature (1 and 2 refer to initial and secondary, respectively). Rate was calculated by the inverse of the  $\tau$  value. Q<sub>10</sub> fits for steady-state midpoints and slopes were calculated by replacing the Rs with V<sub>1/2</sub> and z values. Fits for y<sub>0</sub> were calculated based of the 1/y<sub>0</sub> to yield optimal Q<sub>10</sub> values. The best fit was used with three points obtained at 10 °C, 22 °C and 34 °C to increase the accuracy of the Q<sub>10</sub> fit. The fit was extrapolated to physiological and febrile temperatures.

### 2.3.7. **Action Potential Modeling**

Cardiac action potential modeling was based on a modified ten Tüßscher 2006 model, previously described (ten Tüßscher *et al.*, 2004; ten Tüßscher, 2006; Jones *et al.*, 2011). All action potentials were programmed and run in the Python language. The I<sub>to</sub> formulation and maximal conductance were modified as suggested by Dumaine *et al.* 1999 (Dumaine *et al.*, 1999). The epicardial L-type calcium current was decreased by 50% to obtain a more realistic action potential length (Dumaine *et al.*, 1999; Xia *et al.*, 2006). Simulations were run at 1 Hz. The 34 °C data were incorporated into the model to account for hypothermic conditions. Predicted channel kinetics and steady state properties at 37 °C (normothermia) and 41 °C (hyperthermia) temperatures were obtained from the Q<sub>10</sub> extrapolations. Our model only accounted for current density, activation, steady-state fast inactivation, fast inactivation kinetics, and late I<sub>Na</sub>. The slow inactivation parameters were excluded from the model since we did not have a full slow inactivation kinetics profile. As described earlier, it is challenging to patch at elevated

temperatures because of a loss of patch stability. Temperature shifts affect the kinetics of other channels that contribute to the maintenance of the cardiac action potential, thus changes in temperature will have other effects on cardiac action potential morphology, for which we are unable to account. We used the ten Tüschler model to determine the effects of temperature on cardiac action potential based only on shifts occurring in  $I_{NaV1.5}$ . We modeled epicardial action potentials with increasing  $I_{K,to}$  to simulate changes across the heart wall and between the right and left ventricles.

## 2.4. Results

### 2.4.1. Activation

We measured current density from the ratio of peak current amplitude to the cell membrane capacitance (pA/pF). Representative raw current traces are shown for the different channel variants at the three temperatures studied (**Figure 2-1**). Peak  $I_{Na}$  density was higher in WT and E1784K when temperature was elevated from 22 °C to 34 °C ( $p < 0.05$ , **Table 2-2**). The  $Q_{10}$  values are consistent with temperature insensitivity in R1193Q compared to WT and E1784K (**Table 2-2**).

We measured activation rate by fitting the rise phase of  $I_{Na}$  at 0 mV, from the beginning of the test pulse to the half peak  $I_{Na}$ . Both mutants, E1784K and R1193Q, were slower to reach half peak  $I_{Na}$  than WT channels at 10 °C ( $p < 0.0001$ , **Table 2-2**). Time to half peak  $I_{Na}$  was reduced ( $p < 0.0001$ ) in E1784K ( $550.2 \mu s \pm 52.4 \mu s$ ) and R1193Q ( $525.4 \mu s \pm 60.0 \mu s$ ) compared to WT ( $270.3 \mu s \pm 47.0 \mu s$ ) when temperature was elevated from 10 °C to 22 °C (**Figure 2-1** and **Table 2-2**). With further elevations in temperature (22 °C to 34 °C) time to half peak  $I_{Na}$  was further reduced ( $p > 0.05$ ) in E1784K ( $124.4 \mu s \pm 49.0 \mu s$ ) compared to smaller changes in WT and R1193Q (**Figure 2-1** and **Table 2-2**). **Table 2-2** includes  $Q_{10}$  fit values which are consistent with overall trends in which E1784K exhibits higher thermosensitivity compared to WT and R1193Q.

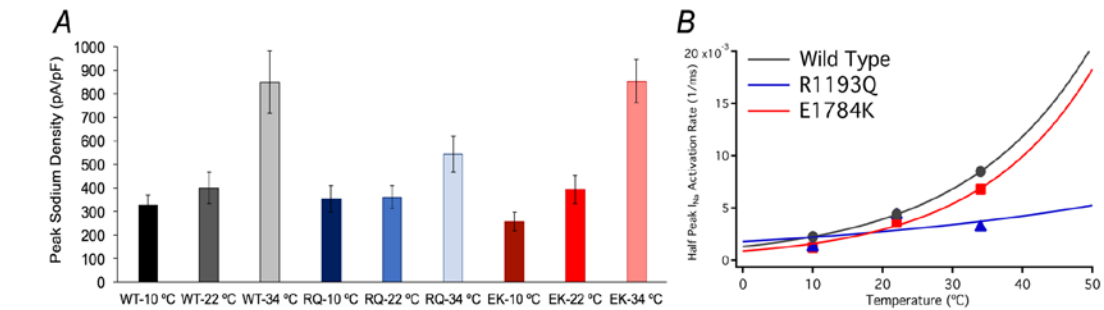
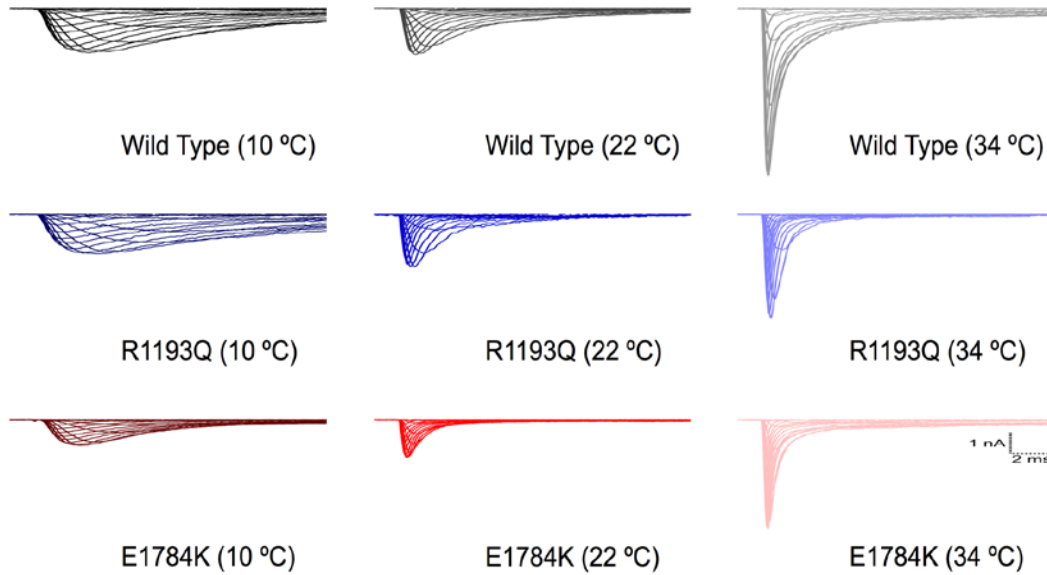


**Figure 2-1 Temperature effects on current density and activation kinetics**  
 Current recordings of the channel variants are shown at three temperatures. Panel A shows peak current density for the different channel variants as a function of temperature. Panel B shows the time to half peak of maximal  $I_{Na}$  measured at 0 mV.

**Table 2-2 Temperature Peak Current Density and Time to Half peak  $I_{Na}$**

Condition	Peak $I_{Na}$ Density (pA/pF)	N	Time to half peak $I_{Na}$ ( $\mu$ s)	N
WT-10	328.11 $\pm$ 40.61	16	530 $\pm$ 56 <sup>2</sup>	16
WT-22	399.70 $\pm$ 65.83	11	260 $\pm$ 26	11
WT-34	848.80 $\pm$ 132.77 <sup>1</sup>	9	230 $\pm$ 42	10
WT-Q <sub>10</sub>	1.61		1.7	
RQ-10	351.96 $\pm$ 56.84	15	810 $\pm$ 24 <sup>2</sup>	8
RQ-22	360.60 $\pm$ 48.20	8	280 $\pm$ 50	8
RQ-34	543.18 $\pm$ 76.47	17	320 $\pm$ 9.0	14
RQ-Q <sub>10</sub>	1.22		1.2	
EK-10	255.93 $\pm$ 40.43	11	830 $\pm$ 35 <sup>2</sup>	11
EK-22	394.22 $\pm$ 60.13	16	280 $\pm$ 16	10
EK-34	853.23 $\pm$ 91.86 <sup>1</sup>	22	160 $\pm$ 9.2	15
EK-Q <sub>10</sub>	1.75		1.8	

<sup>1</sup>p<0.05 vs. 22 °C of same channel variant, <sup>2</sup>p<0.0001 vs. 22 °C and 34 °C of same channel variant

We show conductance as a function of membrane potential in **Figure 2-2**. The conductance midpoint ( $GV-V_{1/2}$ ) was depolarized ( $p < 0.0001$ ) in E1784K compared to WT and R1193Q (**Figure 2-2** and **Table 2-3**).  $GV-V_{1/2}$  in both E1784K and R1193Q was hyperpolarized ( $p < 0.0001$ ) by approximately 10 mV when temperature was increased from 10 °C to 22 °C compared to WT channels. Further elevations in temperature did not significantly shift  $GV-V_{1/2}$  in the mutants. The  $Q_{10}$  fit values are reported in **Table 2-3** and are consistent with a slightly higher  $Q_{10}$  value for E1784K compared to R1193Q and WT.

The conductance slope ( $GV-z$ ) was significantly different between the channel variants in which E1784K had a lower slope value compared to WT and R1193Q ( $p < 0.01$ , **Figure 2-2**).  $GV-z$  increased when temperature was elevated ( $p < 0.0001$ , **Table 2-3**). The changes in slope due to temperature were not significantly different between the channel variants ( $p > 0.05$ ). The  $Q_{10}$  fit values reported in **Table 2-3** are relatively equal between the channel variants.

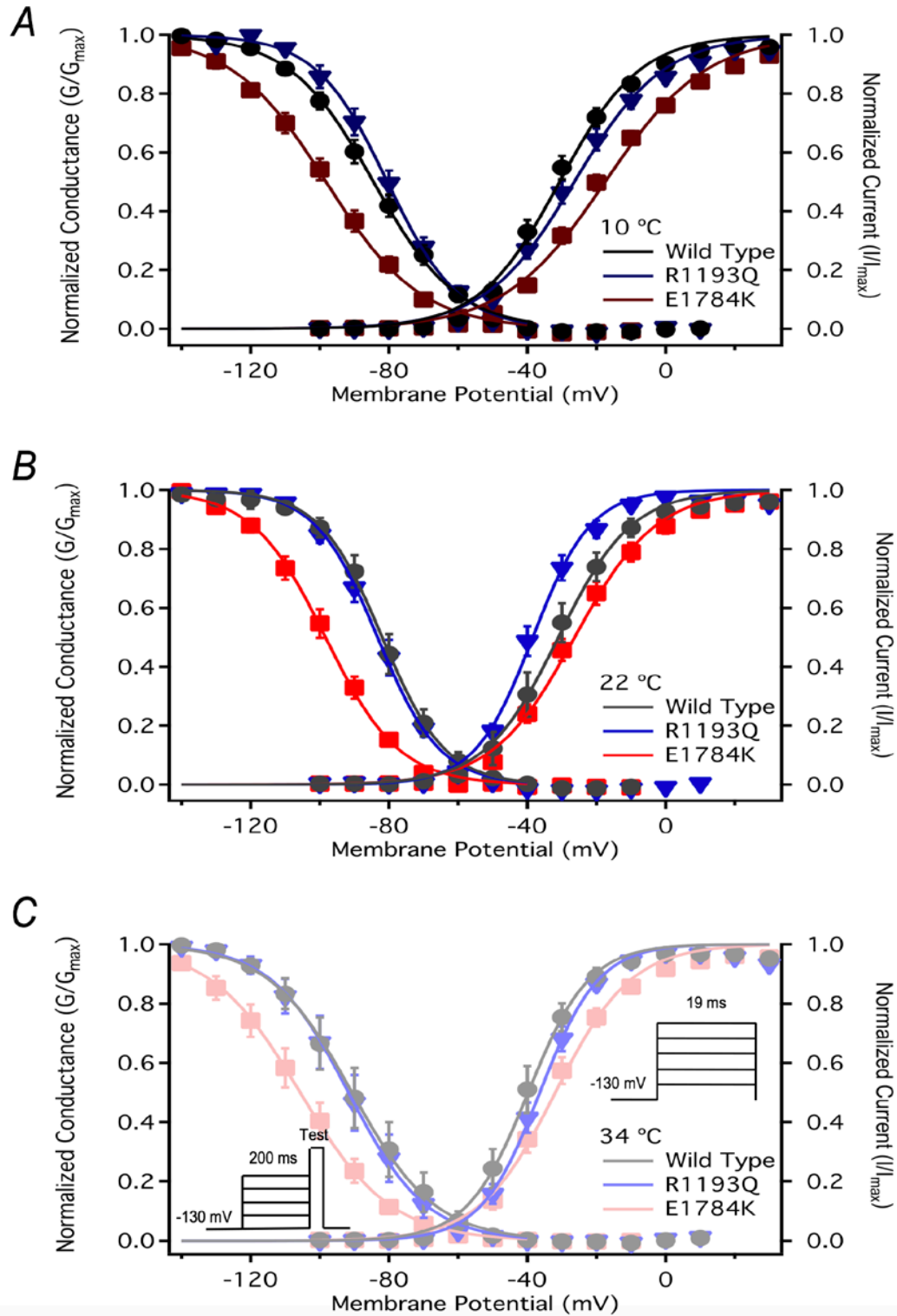


**Figure 2-2 Temperature effects on activation and steady-state fast inactivation**

Panels A-C show the voltage-dependence of activation and fast inactivation as normalized conductance and normalized current, respectively, plotted against membrane potential. The insets in panel C show pulse protocols used to measure GV and SSFI.

**Table 2-3 Temperature Conductance**

Condition	GV-V <sub>1/2</sub>	GV-z	N
WT-10	-30.56 ± 1.99	2.33 ± 0.11	14
WT-22	-31.22 ± 3.12	2.88 ± 0.20	9
WT-34	-40.22 ± 2.39	3.97 ± 0.33	10
WT-Q <sub>10</sub>	1.13	1.26	
RQ-10	-25.82 ± 2.14 <sup>*1</sup>	2.05 ± 0.09	15
RQ-22	-38.12 ± 1.58	3.34 ± 0.32	7
RQ-34	-36.56 ± 1.69	3.70 ± 0.15	18
RQ-Q <sub>10</sub>	1.13	1.24	
EK-10	-17.22 ± 1.82 <sup>*1</sup>	1.76 ± 0.07	11
EK-22	-25.85 ± 2.09	2.40 ± 0.13	16
EK-34	-32.46 ± 1.79	3.28 ± 0.23	23
EK-Q <sub>10</sub>	1.28	1.30	

<sup>\*1</sup>p<0.0001 vs. 22 °C and 34 °C of same channel variant

### 2.4.2. Fast Inactivation

Normalized currents obtained from the SSFI protocols are plotted as a function of membrane potential (**Figure 2-2**). The E1784K SSFI-V<sub>1/2</sub> was hyperpolarized (p<0.0001) compared to WT and R1193Q at all temperatures measured (**Figure 2-2** and **Table 2-4**). At 34 °C, SSFI-V<sub>1/2</sub> was hyperpolarized (p<0.01) compared to 22 °C and 10 °C (**Figure 2-2** and **Table 2-4**). The differences in SSFI-V<sub>1/2</sub> due to temperature were not significantly different between the channel variants (p>0.05, **Figure 2-2**). The Q<sub>10</sub> values reported in **Table 2-4** are almost identical between the different channel variants.

The E1784K mutant had a lower (p<0.0001) steady-state fast inactivation slope (SSFI-z) than R1193Q and WT (**Table 2-4**). The WT SSFI-z was increased (p<0.0001) when temperature was elevated from 10 °C to 22 °C (**Table 2-4**). In R1193Q, the SSFI-z was increased (p<0.0001) between 10 °C and 34 °C (**Table 2-4**). Q<sub>10</sub> fit values are relatively consistent between the different channel variants reported in **Table 2-4**.

**Table 2-4 Temperature Steady-State Fast Inactivation**

Condition	SSFI-V <sub>1/2</sub>	SSFI-z	N
WT-10	-84.46 ± 1.96	-2.11 ± 0.09 <sup>*1</sup>	8
WT-22	-82.01 ± 2.45	-2.95 ± 0.23	5
WT-34	-90.21 ± 4.55	-2.99 ± 0.21	8
WT-Q <sub>10</sub>	<b>1.03</b>	<b>1.14</b>	
RQ-10	-80.67 ± 1.89	-2.49 ± 0.15 <sup>*1</sup>	7
RQ-22	-83.34 ± 1.81	-3.03 ± 0.23	5
RQ-34	-91.65 ± 4.12	-3.16 ± 0.12	9
RQ-Q <sub>10</sub>	<b>1.06</b>	<b>1.10</b>	
EK-10	-98.27 ± 2.07	-1.82 ± 0.06	5
EK-22	-98.47 ± 1.99	-2.52 ± 0.10	7
EK-34	-106.13 ± 3.23	-2.45 ± 0.08	12
EK-Q <sub>10</sub>	<b>1.03</b>	<b>1.11</b>	

\*1 p<0.0001 vs 22 °C and 34 °C of same channel variant

Time constants measured from single exponential fits to the recovery from fast inactivation at -130 mV are shown in **Figure 2-3**. Insets in **Figure 2-3** show time constants plotted against the membrane potential. The values of the time constants (ms) are reported in **Table 2-5** and **Table 2-6**, for time constants between -130 mV to -70 mV, and -50 mV to +10 mV, respectively. E1784K had enhanced fast inactivation kinetics between -90 mV to +10 mV compared to R1193Q and WT (p<0.01, **Figure 2-3**). Fast inactivation kinetics of all channel variants between -130 mV to -90 mV, and -30 mV to -10 mV had a significantly larger (p<0.01) time constant (decelerated kinetics) at 10 °C compared to 22 °C and 34 °C, which were not significantly different (**Table 2-5** and **Table 2-6**). At -70 mV, both WT and R1193Q fast inactivation time constants decrease significantly from 10 °C to 34 °C (p<0.01) compared to a minor (p>0.05) change in E1784K. At -50 mV, WT and E1784K channels had reduced time constants when temperature increased from 10 °C to 34 °C compared to R1193Q which decreased from 10 °C to 22 °C (p<0.01). The Q<sub>10</sub> fit values for the different channel variants are reported in **Table 2-5** and **Table 2-6**.

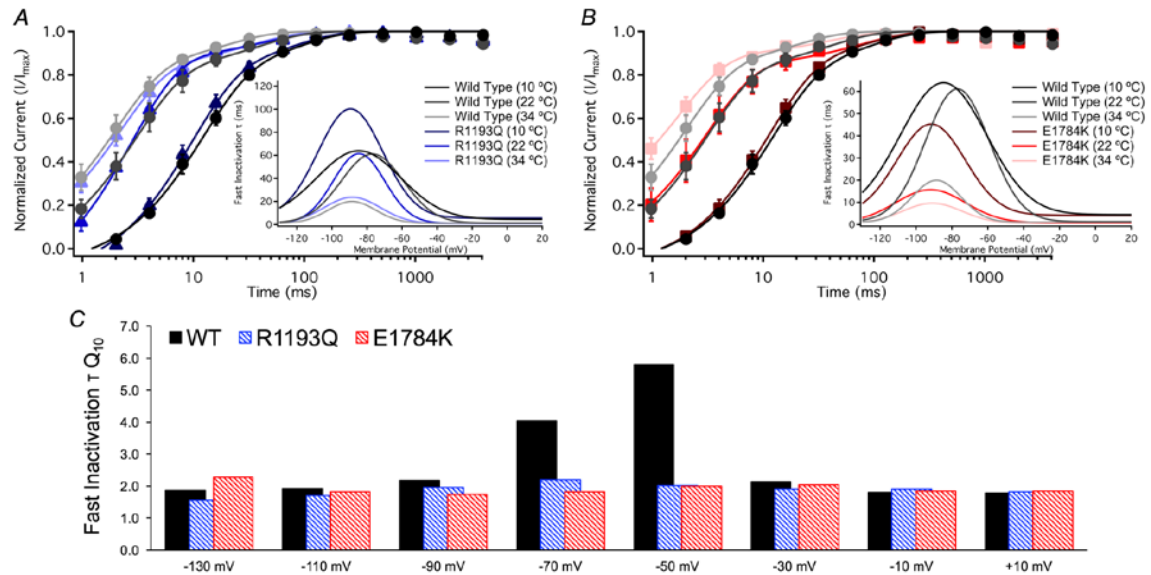


### Figure 2-3 Temperature effects on fast inactivation kinetics

Panels A-B show the recovery from fast inactivation at -130 mV as normalized currents versus recovery time duration. The insets show the fast inactivation single-exponential time constants ( $\tau$ , ms) plotted against the membrane potential. Panel C shows fast inactivation  $Q_{10}$ s for all three channel variants plotted against the membrane potential.

**Table 2-5 Temperature -130 mV and -70 mV Fast inactivation time constants (ms)**

Condition	-130 mV $\tau$	n	-110 mV $\tau$	n	-90 mV $\tau$	n	-70 mV $\tau$	n
WT-10	18.0 ± 1.8	5	36.4 ± 5.2	5	176.0 ± 52.5	4	55.0 ± 10.0	4
WT-22	5.5 ± 1.3	6	12.4 ± 2.6	5	46.5 ± 8.3	4	57.2 ± 3.1	5
WT-34	3.0 ± 0.5	5	6.2 ± 0.8	5	19.9 ± 2.5	5	8.2 ± 2.1	5
WT-Q <sub>10</sub>	<b>1.86</b>		<b>1.92</b>		<b>2.18</b>		<b>4.03</b>	
RQ-10	15.4 ± 1.8	7	54.4 ± 6.8	4	103.2 ± 19.2	4	55.5 ± 6.2	4
RQ-22	4.4 ± 0.2	5	14.7 ± 4.4	5	57.2 ± 6.2	5	38.5 ± 10.5	5
RQ-34	3.4 ± 0.6	5	9.6 ± 2.2	5	23.7 ± 4.2	4	12.6 ± 3.0	4
RQ-Q <sub>10</sub>	<b>1.56</b>		<b>1.71</b>		<b>1.96</b>		<b>2.19</b>	
EK-10	16.0 ± 1.8	5	25.7 ± 1.9	6	47.8 ± 7.5	6	23.8 ± 2.8	6
EK-22	5.5 ± 1.5	5	8.9 ± 1.1	5	16.6 ± 2.3	5	8.3 ± 1.8	5
EK-34	2.1 ± 0.3	5	4.8 ± 0.9	4	9.8 ± 2.2	5	4.5 ± 1.4	4
EK-Q <sub>10</sub>	<b>2.27</b>		<b>1.82</b>		<b>1.74</b>		<b>1.83</b>	

**Table 2-6 Temperature -50 mV and +10 mV Fast inactivation time constants (ms)**

Condition	-50 mV	n	-30 mV	n	-10 mV	n	+10 mV	n
WT-10	24.40 ± 4.86	4	7.39 ± 0.48	9	4.96 ± 0.29	9	4.34 ± 0.29	9
WT-22	20.10 ± 5.11	5	1.98 ± 0.29	8	0.96 ± 0.10	8	0.67 ± 0.09	8
WT-34	2.09 ± 0.59	5	0.88 ± 0.16	8	0.61 ± 0.13	8	0.45 ± 0.09	8
WT-Q <sub>10</sub>	<b>5.80</b>		<b>2.13</b>		<b>1.80</b>		<b>1.79</b>	
RQ-10	23.60 ± 3.69	4	7.08 ± 0.42	10	4.49 ± 0.35	10	3.76 ± 0.24	10
RQ-22	3.34 ± 0.54	6	1.29 ± 0.10	6	0.73 ± 0.03	6	0.53 ± 0.04	6
RQ-34	1.80 ± 0.27	11	0.75 ± 0.12	11	0.43 ± 0.07	11	0.35 ± 0.04	11
RQ-Q <sub>10</sub>	<b>2.02</b>		<b>1.89</b>		<b>1.90</b>		<b>1.82</b>	
EK-10	8.59 ± 0.71	6	4.42 ± 0.36	8	3.47 ± 0.26	8	3.20 ± 0.21	8
EK-22	1.73 ± 0.23	10	0.90 ± 0.12	10	0.58 ± 0.06	10	0.49 ± 0.05	10
EK-34	0.91 ± 0.18	10	0.45 ± 0.07	10	0.36 ± 0.05	10	0.31 ± 0.05	10
EK-Q <sub>10</sub>	<b>1.99</b>		<b>2.03</b>		<b>1.84</b>		<b>1.84</b>	

### 2.4.3. Late Sodium Current

We show representative normalized current traces of late  $I_{Na}$  for the channel variants only at 22 °C and 34 °C in **Figure 2-4**. **Figure 2-4** includes bar graphs of late  $I_{Na}$  percent along with the  $Q_{10}$  values. We eliminated 10 °C late current traces since currents at 10 °C took a longer time to reach plateau. The late  $I_{Na}$  percentage was larger in E1784K compared to WT and R1193Q ( $p < 0.0001$ , **Table 2-7**). This effect is only present at 34 °C compared to 22 °C ( $p < 0.0001$ , **Figure 2-4** and **Table 2-7**). Late  $I_{Na}$  percent was increased by 2.67 % ± 0.46% in E1784K compared to a minor change in WT and R1193Q when temperature was elevated from 22 °C to 34 °C (**Figure 2-4** and **Table 2-7**). Late  $I_{Na}$  density was also increased in E1784K in a temperature-dependent fashion

(Table 2-7). The  $Q_{10}$  fit values reported in Table 2-7 are consistent with a higher thermosensitivity in E1784K compared to WT and R1193Q. At febrile temperatures (41 °C) E1784K has 9.24% late current.

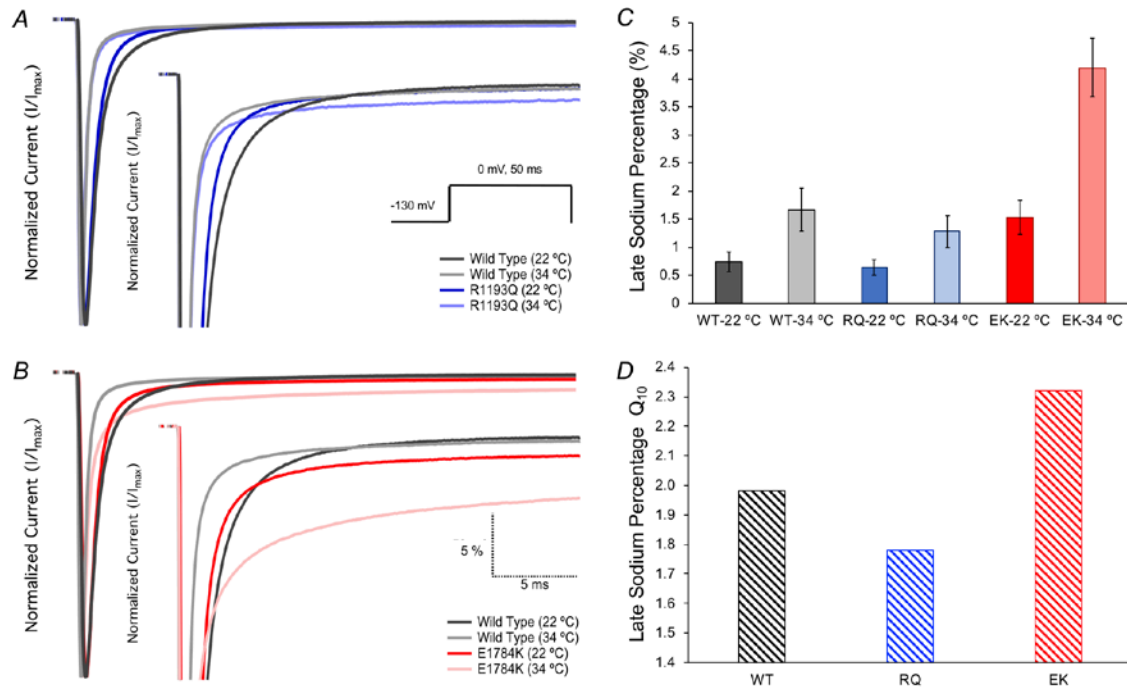


**Figure 2-4 Temperature effects on late  $I_{Na}$**

Panels A-B show normalized current plotted as a function of time with insets that focus on narrower current window to show late  $I_{Na}$ . The pulse protocol inset is shown in Panel A. Panel C shows the late  $I_{Na}$  percent as a function of channel variant and temperature. Panel D shows the  $Q_{10}$  values for late  $I_{Na}$  of all the channel variants.

**Table 2-7 Temperature Late  $I_{Na}$**

Condition	Late (%)	N	Late Density (pA/pF)	N
WT-22	0.74 ± 0.18	8	7.55 ± 1.92	7
WT-34	1.67 ± 0.39	6	13.28 ± 2.60	6
WT- $Q_{10}$	<b>1.98</b>		<b>1.60</b>	
RQ-22	0.64 ± 0.14	6	6.35 ± 2.15	6
RQ-34	1.28 ± 0.29	5	13.17 ± 4.28	5
RQ- $Q_{10}$	<b>1.78</b>		<b>1.84</b>	
EK-22	1.53 ± 0.30	9	12.06 ± 3.32	8
EK-34	4.20 ± 0.52 <sup>*1</sup>	10	39.12 ± 7.13 <sup>*1</sup>	10
EK- $Q_{10}$	<b>2.32</b>		<b>2.67</b>	

<sup>\*1</sup>  $p < 0.05$  vs. 22 °C of same conditions

#### 2.4.4. Use-dependent Inactivation

Normalized currents from use-dependent inactivation (1 Hz) are plotted against time in Figure 2-5. The decay of current was best fit by a double exponential equation.

The  $\tau_1$  was unaffected by the channel variant or temperature, separately (**Figure 2-5** and **Table 2-8**); however, there was an interaction effect on  $\tau_1$  ( $p < 0.05$ ). When temperature increased from 10 °C to 34 °C,  $\tau_1$  decreased in E1784K by  $8.21 \text{ s} \pm 2.47 \text{ s}$  compared to WT and R1193Q (**Figure 2-5** and **Table 2-8**). The  $\tau_2$  value significantly decreased in E1784K ( $p < 0.05$ ) by  $82.8 \text{ s} \pm 26.5 \text{ s}$  when temperature was increased from 10 °C to 34 °C (**Figure 2-5** and **Table 2-8**). The UDI plateau ( $y_0$ ) decreased by  $0.21 \pm 0.07$  in E1784K when temperature was increased from 10 °C to 34 °C ( $p < 0.05$ ) as opposed to minor shifts in WT and R1193Q (**Figure 2-5** and **Table 2-8**). The reported  $Q_{10}$  fit values in **Table 2-8** are consistent with a markedly heightened thermosensitivity in E1784K  $\tau_1$ ,  $\tau_2$  and  $y_0$  compared to R1193Q and WT.

To indirectly measure elevated heart rate effects on channel function, we elicited use-dependent inactivation at 3 Hz. Normalized currents from 3 Hz use-dependent inactivation protocols are plotted against time in **Figure 2-5**. The  $\tau_1$  was not significantly affected by channel variants or temperature, separately. However, when temperature was elevated from 10 °C to 34 °C,  $\tau_1$  increased and decreased ( $p < 0.01$ ) in WT and E1784K, respectively compared to a non-significant change in R1193Q (**Figure 2-5** and **Table 2-8**). Similar shifts were observed in  $\tau_2$  ( $p < 0.01$ ) when temperature was elevated from 10 °C to 34 °C. The UDI (3 Hz)  $y_0$  was not significantly affected by channel variant, temperature, and the interaction between both factors ( $p > 0.05$ , **Figure 2-5**).

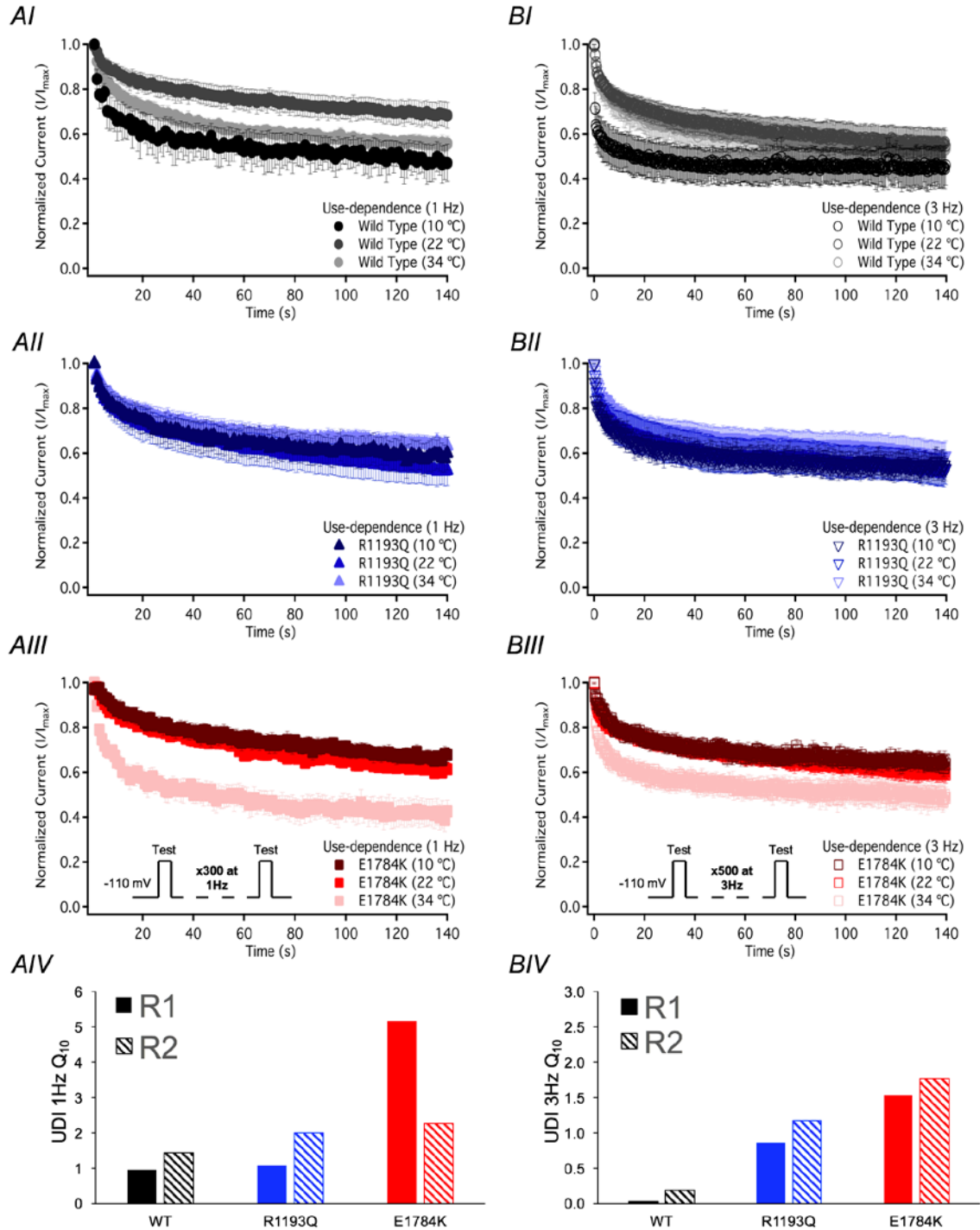


**Figure 2-5 Temperature effects on  $I_{Na}$  use-dependence at 1Hz and 3Hz**  
 Panels AI-AIII show normalized current plotted as a function of time measured at 1Hz. The inset in panel AIII includes the pulse protocols used to measure UDI 1 Hz. Panel AIV shows the UDI 1Hz  $Q_{10}$ s of both the fast and slow rates as a function of channel variants. Panels BI-BIII show normalized current plotted as a function of time measured at 3Hz. The inset in panel BIII includes the pulse protocols used to measure UDI 3 Hz. BIV shows the UDI 3Hz  $Q_{10}$ s of both the fast and slow rates as a function of channel variants.

**Table 2-8 Temperature Use-Dependence 1Hz & 3Hz**

Condition	1Hz- $y_0$	1Hz- $\tau_1$ (s)	1Hz- $\tau_2$ (s)	N	3Hz- $y_0$	3Hz- $\tau_1$ (s)	3Hz- $\tau_2$ (s)	N
WT-10	0.44 ± 0.07	4.52 ± 1.31	96.33 ± 8.77	4	0.45 ± 0.07	0.55 ± 0.39 <sup>2</sup>	11.30 ± 4.86	6
WT-22	0.62 ± 0.07	7.01 ± 0.74	105.30 ± 12.92	5	0.55 ± 0.07	2.91 ± 0.43	49.24 ± 7.04	6
WT-34	0.52 ± 0.05	7.59 ± 2.76	66.83 ± 18.32	5	0.47 ± 0.05	3.52 ± 0.99	69.22 ± 21.03 <sup>3</sup>	6
WT-Q <sub>10</sub>	<b>1.06</b>	<b>0.97</b>	<b>1.44</b>		<b>1.06</b>	<b>0.03</b>	<b>0.19</b>	
RQ-10	0.52 ± 0.07	8.27 ± 2.22	115.16 ± 28.17	6	0.54 ± 0.06	1.33 ± 0.21	31.77 ± 4.65	6
RQ-22	0.45 ± 0.05	5.16 ± 0.87	112.23 ± 9.27	6	0.53 ± 0.07	2.22 ± 0.42	50.54 ± 9.43	6
RQ-34	0.58 ± 0.05	5.41 ± 1.26	75.96 ± 22.01	7	0.63 ± 0.06	2.42 ± 0.67	25.61 ± 4.63	6
RQ-Q <sub>10</sub>	<b>1.05</b>	<b>1.07</b>	<b>2.00</b>		<b>1.07</b>	<b>0.86</b>	<b>1.17</b>	
EK-10	0.58 ± 0.03 <sup>1</sup>	10.66 ± 2.82 <sup>1</sup>	125.85 ± 23.32 <sup>1</sup>	5	0.62 ± 0.04	4.82 ± 1.53 <sup>2</sup>	68.37 ± 17.76	5
EK-22	0.51 ± 0.03	7.98 ± 2.17	116.01 ± 15.02	4	0.56 ± 0.03	2.45 ± 0.29	81.27 ± 11.88	7
EK-34	0.37 ± 0.07	2.44 ± 0.70	43.05 ± 10.37	6	0.51 ± 0.05	1.28 ± 0.28	27.23 ± 7.74 <sup>3</sup>	6
EK-Q <sub>10</sub>	<b>0.84</b>	<b>5.18</b>	<b>2.28</b>		<b>0.92</b>	<b>1.54</b>	<b>1.77</b>	

<sup>1</sup> p<0.05 vs EK 34 °C, <sup>2</sup> p<0.01 vs. 34 °C of same channel variant, <sup>3</sup> p<0.01 vs. 22 °C of same channel variant

## 2.4.5. Slow Inactivation

Slow inactivation onset was measured with a double-pulse protocol and fit with a double exponential curve. The  $\tau_2$  and  $y_0$  values were not affected by channel variant, temperature or both interactions ( $p>0.05$ ). The  $\tau_1$  value was affected significantly by temperature ( $p<0.01$ ), where the slow inactivation onset kinetics was enhanced at 10 °C compared to 22 °C and 34 °C in all channel variants (**Table 2-9**).

**Table 2-9 Temperature Slow Inactivation Onset**

Condition	Slonset- $y_0$	Slonset- $\tau_1$ (s)	Slonset- $\tau_2$ (s)	N
WT-10	0.29 ± 0.04	0.16 ± 0.04 <sup>*1</sup>	21.27 ± 3.73	6
WT-22	0.25 ± 0.05	3.89 ± 1.28	23.83 ± 8.57	4
WT-34	0.32 ± 0.05	2.49 ± 0.84	19.31 ± 6.30	5
RQ-10	0.31 ± 0.04	0.12 ± 0.04 <sup>*1</sup>	17.29 ± 3.63	7
RQ-22	0.29 ± 0.05	2.14 ± 1.00	14.97 ± 3.96	6
RQ-34	0.21 ± 0.03	1.68 ± 0.35	17.61 ± 2.33	5
EK-10	0.31 ± 0.06	1.33 ± 1.07 <sup>*1</sup>	21.95 ± 4.29	6
EK-22	0.23 ± 0.05	4.02 ± 1.73	13.71 ± 2.38	5
EK-34	0.23 ± 0.04	2.99 ± 0.84	11.78 ± 4.63	6

<sup>\*1</sup>  $p<0.01$  vs 22 °C and 34 °C of same channel variant

SSSI measurement and ANOVA analysis were only limited to the channel variant (3 levels) and the temperature factor with only two levels (10 °C and 22 °C). The 34 °C data were excluded from the analysis since we were not able to record a full steady-state slow inactivation for E1784K at 34 °C. The SSSI midpoint (SSSI- $V_{1/2}$ ) for E1784K (34 °C) was hyperpolarized. To obtain a full plateau the prepulse potential was reduced to potentials like -170 mV. With cellular instability at patch temperatures of 34 °C, cells did not survive this protocol. The SSSI- $V_{1/2}$  in all channel variants were unaffected by temperature ( $p>0.05$ , **Table 2-10**). The SSSI slope and plateau were unaffected by channel variant, temperature, or their interaction ( $p>0.05$ ).

**Table 2-10 Temperature Steady-State Slow Inactivation**

Condition	SSSI-V <sub>1/2</sub>	SSSI-z	SSSI-y0	N
WT-10	-105.35 ± 3.18	-2.70 ± 0.07	0.27 ± 0.04	8
WT-22	-95.27 ± 4.04	-2.27 ± 0.57	0.26 ± 0.04	4
WT-34	-85.76 ± 5.90	-1.97 ± 0.58	0.40 ± 0.06	4
RQ-10	-100.86 ± 5.21	-2.89 ± 0.64	0.34 ± 0.04	7
RQ-22	-94.76 ± 6.57	-1.85 ± 0.24	0.30 ± 0.02	5
RQ-34	-89.03 ± 7.45	-1.95 ± 0.28	0.32 ± 0.06	4
EK-10	-117.02 ± 1.90	-2.27 ± 0.22	0.26 ± 0.04	6
EK-22	-104.39 ± 7.21	-1.89 ± 0.29	0.32 ± 0.03	9
EK-34	n/a	n/a	n/a	

The  $\tau_1$  values of slow inactivation recovery were not affected by channel variant, temperature, or both interactions ( $p > 0.05$ ). The  $\tau_2$  value was decreased at 10 °C compared to 22 °C and 34 °C ( $p < 0.01$ ).

**Table 2-11 Temperature Slow Inactivation Recovery**

Condition	Slrec- $\tau_1$ (s)	Slrec- $\tau_2$ (s)	N
WT-10	0.05 ± 0.02	3.30 ± 0.69 <sup>1</sup>	5
WT-22	0.04 ± 0.02	1.37 ± 0.41	5
WT-34	0.02 ± 0.00	0.85 ± 0.06	4
RQ-10	0.05 ± 0.02	2.93 ± 0.93	4
RQ-22	0.03 ± 0.02	1.11 ± 0.19	5
RQ-34	0.04 ± 0.01	2.19 ± 0.43	5
EK-10	0.02 ± 0.01	2.36 ± 0.35 <sup>1</sup>	3
EK-22	0.04 ± 0.02	1.73 ± 0.43	5
EK-34	0.04 ± 0.01	0.94 ± 0.29	6

<sup>1</sup>  $p < 0.01$  vs 22 °C and 34 °C of same channel variant

## 2.4.6. Action Potential Simulations

We used a modified the ten Tüschler model to simulate epicardial and endocardial action potentials. We focused specific attention on the transmural voltage gradient between both walls of the heart. **Figure 2-6** shows the 1999<sup>th</sup> and 2000<sup>th</sup> simulated APs for the different channel variants at three different physiological temperatures (34 °C, 37 °C, 41 °C). The transient outward potassium current conductance was varied in the epicardium of the heart (0.400 pA/pF to 0.700 pA/pF) since its expression is heterogeneous. Across all the temperatures, the E1784K channel had a less negative resting membrane potential (RMP) compared to R1193Q and WT. The E1784K mutant cardiomyocytes showed a decrease in the initial depolarization. The decrease in E1784K AP plateau is not constant across all the temperatures. At 34 °C the

loss of AP plateau in E1784K alternates with the second AP at 0.700 pA/pF of  $I_{Kto}$  current relative to the lower 0.400 pA/pF (**Figure 2-6**). At 37 °C there is a loss of AP plateau which is exacerbated at 41 °C.

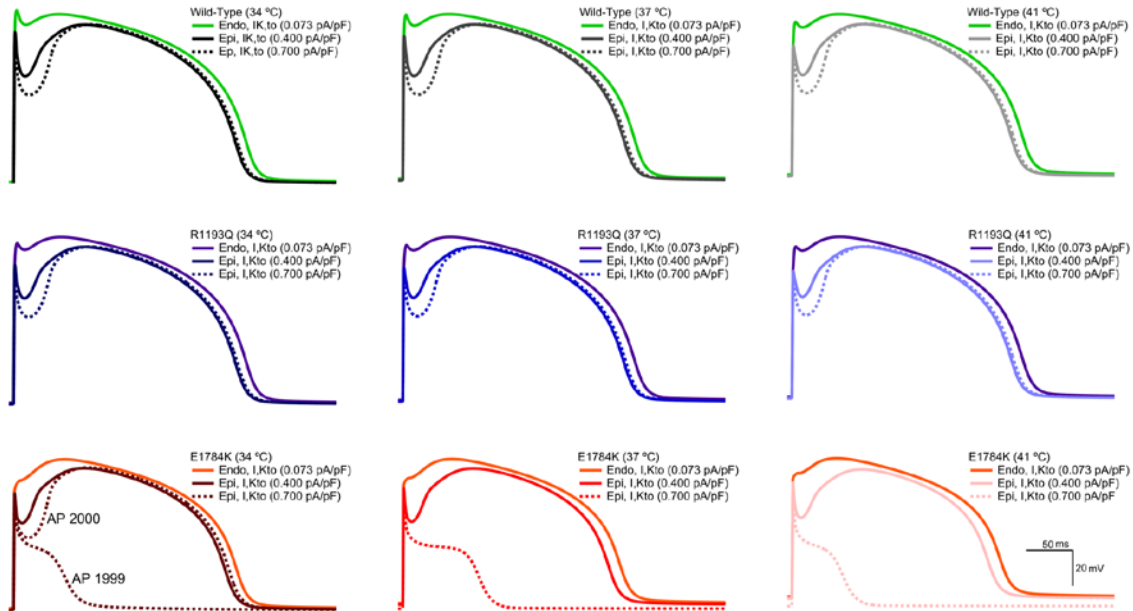


**Figure 2-6** Temperature effects on cardiac action potentials at varying  $I_{Kto}$  densities

## 2.5. Discussion

Febrile temperatures are known to unmask Brugada Syndrome (Meggiolaro *et al.*, 2013; Salinski & Worrlow, 2014). We characterized the temperature sensitivity of two mixed syndrome mutants, E1784K and R1193Q in the cardiac sodium channel  $Na_v1.5$ . Long lasting recordings at physiological temperatures are difficult to obtain due to membrane instability. Thus, channel behavior was assessed at three different, albeit non-physiological, temperatures to allow data to be extrapolated to physiologically-relevant temperatures. We found the E1784K mutant to be more temperature-sensitive than WT  $Na_v1.5$  or R1193Q in ways that suggest temperature could be an arrhythmogenic trigger.

Previous studies on the E1784K and R1193Q mutants have shown either no effect or a decrease in channel current density (Wei *et al.*, 1999; Huang *et al.*, 2006; Makita *et al.*, 2008a). These inconsistencies may be due to differences in the expression

systems used in different studies or to the variability in current amplitudes in transiently transfected heterologous expression systems. One previous study quantifying E1784K expression using fluorescence showed no difference in cell surface expression between E1784K and WT (Makita *et al.*, 2008a). Our results using CHOK1 cells also suggest that the E1784K mutant does not affect channel expression compared to WT.

Arrhythmogenesis in the E1784K mutant may thus be related to changes in channel gating rather than expression. Current density in E1784K was, however, acutely sensitive to temperature. This result should be interpreted with caution due to the variability in currents as mentioned above. In contrast to E1784K, we show no change in WT conductance midpoints even with a greater than 10 °C change in temperature, consistent with previous studies (Nagatomo *et al.*, 1998).

The greater temperature sensitivity of E1784K is reflected in the AP model, in which E1784K mutant decreases the rise of the initial upstroke of AP and also attenuates the epicardial AP plateau. This effect is exacerbated with elevated temperatures and with larger  $I_{K,t0}$ . This is not the case with R1193Q as expected from the relatively lower  $Q_{10}$  values for both current density and time to half peak  $I_{Na}$ . The increase in late current in E1784K has the greatest temperature sensitivity, suggesting temperature has the potential to be arrhythmogenic in this mixed syndrome mutant. Although the data suggest the AP should be prolonged at greater temperature, consistent with LQT3, the predominate effect in our AP model was a loss-of-function due to decreased epicardial E1784K sodium currents. Decreased sodium current in E1784K could lead to a failure to activate L-type  $Ca^{2+}$  channels and a subsequent loss of the epicardial AP plateau, causing a transmural voltage-gradient between endocardium and epicardium typical of BrS1. In addition, greater use-dependent inactivation in the E1784K mutant, which was not accounted for within the model, is predicted to further exacerbate loss-of-function in  $I_{Na}$ , *in vivo*. Our *in vitro* data show that with higher heart rates the stabilization in use-dependent inactivation in E1784K compared to WT is no longer apparent. Thus, higher frequencies may partially ameliorate the biophysical defects associated with E1784K.

At high stimulation frequencies, we observed a fast rate of entry into use-dependent inactivation in WT below 22 °C and above 34 °C, yielding a U-shaped temperature dependence. This is consistent with the slow inactivation onset kinetics measured. Previous literature shows that both fast inactivation (with prepulses of at least

500 ms) and slow inactivation are stabilized in Nav1.5 and Nav1.4 channels as temperature decreases, as observed in different heterologous expression systems (Murray *et al.*, 1990; Ruff, 1999; Carle *et al.*, 2009). Murray *et al.* (1990) suggests this effect may be due to disturbances in lipid-channel interactions or metabolic disturbances affecting charge transfer across the membrane (Murray *et al.*, 1990). Although biophysically curious, the U-shaped temperature dependence of WT channels does not appear in the range of physiological temperatures extrapolated in this study.

The effects of E1784K on activation, fast inactivation and use-dependent inactivation confirm previous studies that highlight the role of the C-terminus in sodium channel gating (Shah *et al.*, 2006; Sarhan *et al.*, 2012). With a  $Ca^{2+}$  signal, the C-terminus interacts with the DIII-DIV linker through the actions of calmodulin. This interaction was reported to shift the inactivation curve and decrease late currents with increased  $[Ca^{2+}]_i$  (Shah *et al.*, 2006; Sarhan *et al.*, 2012). We limited our study, however, to the apo- $Ca^{2+}$  condition, using intracellular EGTA to chelate  $[Ca^{2+}]_i$ . Other studies reported a direct interaction between the C-terminus and the DIII-DIV linker under apo- $Ca^{2+}$  conditions (Cormier *et al.*, 2002; Motoike, 2004). In those studies, a series of residues following the IFM motif, PIPR (non-alpha helical structure), was thought to interact with the C-terminus. In this interpretation, the C-terminus does not affect the extent of inactivation but rather ensures that the IFM motif latch is in place upon occluding the pore. The 1885stop mutation (truncation of helix VI of C-terminus) in Nav1.5 causes a large increase in late current compared to 1921stop (intact C-terminus including helix VI) (Motoike, 2004). Helix VI, the IQ motif, plays an essential role in maintaining inactivation, preventing increases in late  $I_{Na}$ . The E1784K mutant is in a region prior to helix I in the C-terminus (EF-hand domain). The E1784K charge reversal mutation may disrupt the interaction between helix VI and helices I-IV, thus altering the mechanism by which helix VI modulates inactivation via the DIII-DIV linker, which could explain the large increase in late  $I_{Na}$ . Chimera studies on the DI-DII and DII-DIII linkers, as well as the C-terminus, have shown that these regions modulate channel activation and account for many isoform-specific differences (Bennett, 1999, 2001; Choi *et al.*, 2004). Slow inactivation is stabilized when fast inactivation is removed (Featherstone *et al.*, 1996; Richmond *et al.*, 1998). Late current and use-dependent inactivation increases are largest in the E1784K mutant when temperature is elevated to 34 °C, consistent with the previously reported inverse relationship between fast and slow inactivation.

In conclusion, we show that the E1784K mutant shows enhanced thermosensitivity compared to WT channels and another mixed syndrome mutant, R1193Q. Heightened thermosensitivity in E1784K may play a role in arrhythmogenesis during a fever or intense exercise by prolonging the cardiac action potential or causing loss-of function.

## **2.6. Acknowledgments**

The authors thank Dr. David Jones and Dr. Stanislav Sokolov for their contribution and their support.

## Chapter 3. Differential Calcium Sensitivity in $Na_v1.5$ Mixed Syndrome Mutants

This chapter describes the work published in (Abdelsayed *et al.*, 2017) with minor modifications and formatting changes to suit the thesis style.

### 3.1. Abstracts

**Introduction:** Inherited arrhythmias may arise from mutations in the *SCN5a* gene, which encodes the cardiac voltage-gated sodium channel,  $Na_v1.5$ . Mutants in  $Na_v1.5$  result in Brugada Syndrome (BrS1), Long-QT Syndrome (LQT3), or mixed syndromes (an overlap of BrS1/LQT3). Exercise is a potential arrhythmogenic trigger in mixed syndromes. We sought to determine the effects of elevated cytosolic calcium, common during exercise, in mixed syndrome  $Na_v1.5$  mutants.

**Methods:** We used whole-cell patch-clamp to assess the biophysical properties of  $Na_v1.5$  wild-type (WT),  $\Delta$ KPQ, E1784K, 1795insD, and Q1909R mutants in Human Embryonic Kidney (HEK293) cells transiently transfected with the  $Na_v1.5$   $\alpha$  subunit (WT or mutants),  $\beta$ 1 subunit, and eGFP. Voltage-dependence and kinetics were measured at approximately 0 nM, 500 nM, and 2500 nM cytosolic calcium levels. *In silico*, action potential (AP) model simulations were performed using a modified O'Hara-Rudy model.

**Results:** Elevated cytosolic calcium attenuates the late sodium current in  $\Delta$ KPQ, 1795insD, and Q1909R but not in E1784K. Elevated cytosolic calcium restores steady-state slow inactivation (SSSI) to the WT-form in Q1909R, but depolarized SSSI in E1784K. Our AP simulations showed a frequency-dependent reduction of action potential duration (APD) in  $\Delta$ KPQ, 1795insD, and Q1909R carriers. In E1784K, APD is relatively prolonged at both low and high heart rates, resulting in a sodium overload.

**Conclusions:** Cellular perturbations during exercise may affect BrS1/LQT3 patients differently depending on their individual genetic signature. Thus, exercise may be therapeutic or may be an arrhythmogenic trigger in some patients with *SCN5a* mutations.

## 3.2. Introduction

Inherited arrhythmias may arise from mutations in the *SCN5a* gene, which encodes the cardiac voltage-gated sodium channel (Nav1.5) (Jones *et al.*, 2011; Priori *et al.*, 2013). These mutations result in gain-of-function (Long QT Syndrome, LQT3) or loss-of-function (Brugada Syndrome, BrS1) in Nav1.5. Although BrS1 and LQT3 are clinically distinct, a subset of mutations simultaneously trigger both syndromes (BrS1/LQT3, Mixed Syndromes) Rivolta *et al.*, 2001; Clancy & Rudy, 2002; Makita *et al.*, 2008).

BrS1 and LQT3 patients have differential expressivities depending on the physiological triggers, such as exercise (Shimizu & Antzelevitch, 2000; Veldkamp *et al.*, 2000*b*; Schwartz *et al.*, 2001; Masrur *et al.*, 2015). BrS1 patients manifest the diagnostic ST-elevation during both exercise and recovery from exercise (Amin *et al.*, 2009; Masrur *et al.*, 2015). In contrast, LQT phenotype manifestation during exercise is genotype-dependent (Schwartz *et al.*, 2001). Whereas LQT1 patients have cardiac events during exercise, LQT3 is mainly associated with arrhythmia during sleep (Schwartz *et al.*, 1995; Shimizu & Antzelevitch, 2000). Although sleep is primarily a restful physiological state, the REM phase includes exercise-like physiological properties (Somers *et al.*, 1993). A small proportion of LQT3 patients have lethal cardiac events during exercise (Schwartz *et al.*, 1995).

Studies showing exercise-induced QT<sub>c</sub> shortening in LQT3 patients have focused on cases positive for the  $\Delta$ KPQ mutation (Schwartz *et al.*, 1995; Chandra *et al.*, 1998). In  $\Delta$ KPQ patients, the exercise-induced QT<sub>c</sub> shortening was linked to reductions in late sodium current (late I<sub>Na</sub>) caused by elevated cytosolic calcium (Potet *et al.*, 2015). To assume that the LQT3 phenotype is rescued by exercise is highly controversial since *SCN5a* mutation responses to exercise-induced triggers vary (Abdelsayed *et al.*, 2015; Chen *et al.*, 2015). For example, the C-terminal mutant, E1784K, has greater channel availability with elevated temperature and stimulation frequencies (Abdelsayed *et al.*, 2015), both of which are associated with exercise. E1784K carriers generally have a high phenotypic gain-of-function (LQT3) expressivity, as in the Okinawa islands, where the mutation is most prevalent, whereas a minority of patients display sinus node dysfunction, BrS1, or mixed syndrome phenotypes (Makita *et al.*, 2008*a*; Takahashi *et al.*, 2014). Another C-terminal mutant, V2016M, expresses protein kinase-induced gain-

and loss-of-function translating to epinephrine-induced LQT3 and sinus node dysfunction (Chen *et al.*, 2015). Unfortunately, little is known regarding the response of *SCN5a* mutations to physiological factors accompanying exercise. To better understand the variability in response to exercise among *SCN5a*-mutation patients, it is critical to study  $\text{Na}_v1.5$  mutants with cellular perturbations that mimic exercise.

With elevated heart rates, a rise in sympathetic tone triggers multiple cellular cascades which elevate cytosolic calcium (Song *et al.*, 2001; Baartscheer *et al.*, 2003). The  $\text{Na}_v1.5$  C-terminus contains a pair of EF-hand domains and an IQ motif (Kim *et al.*, 2004). Calcium effects are mediated via calmodulin binding to the IQ motif (Chagot *et al.*, 2009; Miloushev *et al.*, 2009; Van Petegem *et al.*, 2012). The calcium-calmodulin complex interacts with the DIII-DIV linker, destabilizing inactivation, and increasing  $\text{Na}_v1.5$  channel availability during elevated heart rates (Shah *et al.*, 2006). The presence of intact intra- and inter-C-terminal interactions are essential for calcium binding (Shah *et al.*, 2006). We hypothesized that mixed syndrome mutants located in intracellular linkers or the C-terminus may either strengthen or weaken the calcium-calmodulin modulation of  $\text{Na}_v1.5$ . Thus, elevated cytosolic calcium may alleviate or exacerbate gain/loss-of-function properties in mutants, and consequently rescuing or unmasking the phenotype. The BrS1/LQT3 mutants we studied include the DIII-DIV linker mutant,  $\Delta\text{KPQ}$ , and C-terminal mutants, E1784K, 1795insD, and Q1909R (**Figure 3-1**). All these mutants are located in calcium-sensitive regions known to modulate  $\text{Na}_v1.5$  fast and slow inactivation.

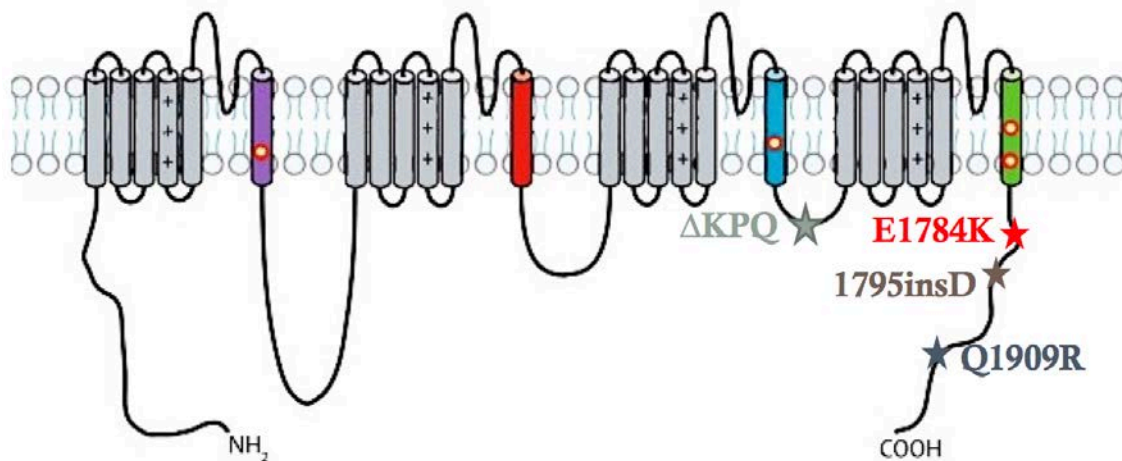


**Figure 3-1** Mutants characterized in  $\text{Na}_v1.5$

### **3.3. Methods**

#### **3.3.1. Ethical approval**

The research was approved by Biohazards review 251-2012 issued by the office of the Environmental Health and Safety at Simon Fraser University, Burnaby, BC, Canada.

#### **3.3.2. Cell Culture and Transfection**

Human Embryonic Kidneys (HEK293) cells were grown at pH 7.4 in a DMEM (1×) nutrient medium (Life Technologies, NY, USA), supplemented with 10 % FBS and maintained in a humidified environment at 37 °C with 5 % CO<sub>2</sub>. To preserve calcium-calmodulin effects on Na<sub>v</sub>1.5, HEK293 cells were selected for this study since they contain a relatively high [calmodulin]<sub>free</sub> level compared to other cell lines (Black *et al.*, 2004).

Transfection followed the procedures suggested by Qiagen. Briefly, 1.5 µg of the Na<sub>v</sub>1.5  $\alpha$  subunit, 0.75 µg of the sodium channel  $\beta_1$  subunit, and 1.5 µg of eGFP were allowed to incubate with 15 µl of polyfect transfection reagent (Qiagen) and 146 µl of un-supplemented medium for 10 minutes. The cDNA mixture was then allowed to incubate with the HEK293 cells for 8 hours before plating on coverslips.

#### **3.3.3. Electrophysiology**

Whole-cell patch clamp recordings were performed in extracellular solution containing (mM): 96 NaCl, 4 KCl, 2 CaCl<sub>2</sub>, 1 MgCl<sub>2</sub>, and 10 HEPES (pH 7.4). Solutions were titrated with CsOH. Pipettes were fabricated with a P-1000 puller using borosilicate glass (Sutter Instruments, CA, USA), dipped in dental wax to reduce capacitance, then thermally polished to a resistance of 1.0-1.5 M $\Omega$ . Voltage measurement error were minimized by using low resistance electrodes to limit series resistance between pipette and intracellular solution to 3.5 M $\Omega$  or less. Pipettes were filled with intracellular solution. For minimal cytosolic calcium levels, reported below as 0 nM, pipettes contained (mM): 130 CsF, 9.6 NaCl, 10 HEPES, and 10 EGTA titrated to pH 7.4. To mimic average and peak systolic cytosolic calcium we calculated, using the Ca-EGTA Calculator TS v1.3 –

Maxchelator, the amount of CaCl<sub>2</sub> added to bring cytosolic calcium to 500 nM and 2500 nM: 8.04 mM and 9.5 mM CaCl<sub>2</sub>, respectively (Steenbergen *et al.*, 1987; Kirschenlohr *et al.*, 2000).

All recordings were made using an EPC-9 patch-clamp amplifier (HEKA Elektronik, Lambrecht, Germany) digitized at 20 kHz using an ITC-16 interface (HEKA Elektronik, Lambrecht, Germany). Data were acquired and low-pass-filtered (5 kHz) using PatchMaster/FitMaster software (HEKA Elektronik, Lambrecht, Germany) running on an Apple iMac (Apple Computer, Cupertino, CA). Leak subtraction was performed online using a P/4 procedure. Recordings were performed at room temperature (22 °C). After a giga ohm resistance seal was achieved, the whole-cell configuration was attained. The holding potential between protocols was -110 mV. We recorded I<sub>Na</sub> from cells that expressed currents no greater than -5 nA. The average voltage error calculated for all cells used in this study (n=362) is 5.16 mV ± 0.24 mV obtained (**Table 3-1**). There are no differences between the voltage-errors in the different conditions (p>0.05).

**Table 3-1 Calcium Voltage Error**

Condition	Voltage Error	N
WT - 0 nM	4.45 ± 0.42	26
WT - 500 nM	5.10 ± 0.81	14
WT - 2500 nM	7.17 ± 1.21	13
ΔKPQ - 0 nM	7.18 ± 0.82	33
ΔKPQ - 500 nM	5.98 ± 0.83	24
ΔKPQ - 2500 nM	7.67 ± 0.99	12
EK - 0 nM	6.63 ± 0.63	33
EK - 500 nM	4.49 ± 0.55	31
EK -2500 nM	5.98 ± 0.56	20
1795insD - 0 nM	2.56 ± 0.32	28
1795insD - 500 nM	2.97 ± 0.51	21
1795insD - 2500 nM	2.98 ± 0.29	23
QR - 0 nM	5.35 ± 0.46	36
QR - 500 nM	4.33 ± 0.83	27
QR - 2500 nM	5.02 ± 0.69	21

### 3.3.4. TTX-subtraction experiments

To confirm the mutant-induced increases in late I<sub>Na</sub>, we performed TTX-subtraction experiments at 0 nM cytosolic calcium, where the late I<sub>Na</sub> in mutant channels

was the largest. The concentration of TTX used was 40  $\mu\text{M}$  in extracellular solution. The 40  $\mu\text{M}$  TTX current trace was subtracted from the control (non-TTX) current trace in all conditions, to calculate the TTX-sensitive late  $I_{\text{Na}}$ .

### 3.3.5. Analysis and Statistics

Analysis and graphing were done using FitMaster software (HEKA Elektronik, Lambrecht, Germany) and Igor Pro (Wavemetrics, Lake Oswego, OR, USA) with statistical information derived using JMP statistical software. Statistical significance was accepted at  $p < 0.05$  using a two-factor completely randomized design (CRD) ANOVA test followed by a post-hoc Tukey test. Statistical results were obtained for the channel variant, calcium, and channel variant  $\times$  calcium factors. We report the statistical results for the mutants and the interaction between mutants and calcium. All values reported are given as means  $\pm$  standard error of means.

### 3.3.6. Voltage Protocols

#### 3.3.6.1 *Peak Sodium Current Density ( $I_{\text{Na}}$ )*

We measured current density from the ratio of peak current amplitude in pA to the cell membrane capacitance in pF.

#### 3.3.6.2 *Maximal Peak and Late Sodium Conductance Density ( $G_{\text{Na}}$ )*

Maximal conductance density relates to membrane channel trafficking and expression. We could not directly measure maximal peak or late conductance density, rather we indirectly calculated it from the conductance at 0 mV, measured by a test pulse described under *Conductance (GV)*:

$$1. G_{\text{Na}} = g_{\text{Na}}/C_{\text{M}}$$

where  $G_{\text{Na}}$  is the conductance at 0 mV,  $g_{\text{Na}}$  is the conductance at 0 mV (calculated using equation 2) and  $C_{\text{M}}$  is the membrane capacitance in pF.

#### 3.3.6.3 *Conductance (GV)*

To determine the voltage dependence of activation, we measured the peak current amplitude at test pulse potentials ranging from -100 mV to +80 mV in increments

of +10 mV for 19 ms. Prior to the test pulse, channels were allowed to recover from fast inactivation at -130 mV for 197 ms. Channel conductance was calculated from peak  $I_{Na}$ .

$$2. \quad g_{Na} = I_{Na}/V - E_{rev}$$

where  $g_{Na}$  is sodium channel conductance,  $I_{Na}$  is peak sodium current in response to the command potential  $V$ , and  $E_{rev}$  is the reversal potential. Calculated values for conductance were fit with the Boltzmann function:

$$3. \quad G/G_{max} = 1/(1 + \exp[-ze_0[V_m - V_{1/2}]/kT])$$

where  $G/G_{max}$  is the normalized conductance amplitude,  $V_m$  is the command potential,  $z$  is the apparent valence,  $e_0$  is the elementary charge,  $V_{1/2}$  is the midpoint voltage,  $k$  is the Boltzmann constant, and  $T$  is temperature in °K.

#### **3.3.6.4 Steady-State Fast Inactivation (SSFI)**

The voltage-dependence of SSFI was measured by preconditioning the channels to a hyperpolarizing potential of -130 mV and then eliciting prepulses between -150 mV and +10 mV in increments of 10 mV for 500 ms. Channel availability was assessed during a test pulse to 0 mV. Different hyperpolarizing prepulse potentials (-130 mV or -150 mV) were used to obtain a plateau for the SSFI curve. Normalized current amplitude as a function of voltage was fit using the Boltzmann function:

$$4. \quad I/I_{max} = 1/(1 + \exp(-ze_0 (V_m - V_{1/2})/kT))$$

where  $I/I_{max}$  is the normalized current amplitude,  $z$  is apparent valence,  $e_0$  is the elementary charge,  $V_m$  is the prepulse potential,  $V_{1/2}$  is the midpoint voltage of SSFI,  $k$  is the Boltzmann constant, and  $T$  is temperature in °K.

#### **3.3.6.5 Fast Inactivation Onset**

Time constants for open-state fast inactivation were derived by fitting a double exponential function to the decay of current obtained from the activation protocol. To measure closed-state fast inactivation onset, channels were preconditioned at -130 mV prior to a prepulse at -50 mV, -70 mV, or -90 mV for 0 – 0.256 s. Current amplitude was measured during a test pulse to 0 mV for 20 ms. Normalized current amplitudes as a function of time were fit using a double exponential equation:

$$5. I = I_{ss} + \alpha_1 \exp(-t/\tau_1) + \alpha_2 \exp(-t/\tau_2)$$

where  $I$  is current amplitude,  $I_{ss}$  is the plateau amplitude,  $\alpha_1$  and  $\alpha_2$  are the amplitudes at time 0 for time constants  $\tau_1$  and  $\tau_2$ , and  $t$  is time.

### **3.3.6.6 Fast Inactivation Recovery**

Channels were fast-inactivated during a 500 ms depolarizing step to 0 mV. Recovery was measured during a 19 ms test pulse to 0 mV following 0 – 1.024 s conditioning pulses at -130 mV, -110 mV, or -90 mV. Time constants of fast inactivation recovery as a function of time were fit using a double exponential equation, as above.

### **3.3.6.7 Late $I_{Na}$ Current**

Late  $I_{Na}$  current was measured between 450 – 500 ms during a 500 ms depolarizing pulse to 0 mV from a holding potential of -130 mV. An average of 30 pulses was used to increase the signal-to-noise ratio.

### **3.3.6.8 Steady-State Slow Inactivation (SSSI)**

The voltage-dependence of SSSI was measured by preconditioning the channels to -150 mV for 30 s and then eliciting prepulse potentials that range from -150 to -10 mV in increments of 20 mV for 60 s. Channel availability was assessed during a test pulse to 0 mV following a -130 mV recovery pulse from fast inactivation at 20 ms. Normalized current amplitude as a function of voltage was fit using a modified Boltzmann function:

$$6. I/I_{max} = (I_1 - I_2)/(1 + \exp(-ze_0 (V_M - V_{1/2})/kT)) + I_2$$

where  $I_1$  and  $I_2$  are maximum and minimum values of fit. The other symbols are as previously stated.

### **3.3.6.9 Slow Inactivation Onset**

To measure onset into slow inactivation, channels were preconditioned at -130 mV for 30 s prior to a prepulse at 0 mV for 0 – 64 s. A test pulse to 0 mV followed a -130 mV fast inactivation recovery pulse for 20 ms. Normalized current amplitude as a function of time was fit with a double exponential.

### **3.3.6.10 Slow Inactivation Recovery**

To measure recovery from slow inactivation, channels were preconditioned at -130 mV for 30 s prior to a prepulse at 0 mV for 60 s, followed by series of test pulses to 0 mV for 20 ms between increasing incremental recovery durations at -130 mV for 0 – 32s. Normalized current amplitudes as a function of time were fit using a double exponential equation with the plateau equal to 1.00.

### **3.3.6.11 Weighted Slow Inactivation Time Constants**

The weighted slow inactivation time constant at each voltage was calculated using the double  $\tau$  values obtained from equation 5:

$$7. \tau_{\text{slow-weighted}} = ((\alpha_1 \times \tau_1) + (\alpha_2 \times \tau_2)) / (\alpha_1 + \alpha_2)$$

### **3.3.6.12 Slow Inactivation $\alpha_j$ and $\beta_j$ Rates**

The recovery from slow inactivation (forward,  $\alpha_j$ ) and the onset into slow inactivation (reverse,  $\beta_j$ ) rates were calculated using Hodgkin-Huxley formulations:

$$8. \alpha_j = j_{\infty} / \tau_j$$

$$9. \beta_j = (1 - j_{\infty}) / \tau_j$$

where  $j_{\infty}$  is channel availability obtained from equation 6 and  $\tau_j$  is the weighted slow inactivation time constant obtained from equation 7, at a given voltage. The slow inactivation  $\alpha_j$  rates versus voltage were fit using a single exponential curve and beta rates were fit with a line with a slope of 0.

## **3.3.7. Myocardial Action Potential (AP) Modeling**

Action potentials were simulated using a modified version of the O'Hara-Rudy (O'Rd) model at 37 °C programmed in Python (O'Hara *et al.*, 2011). The sodium data were extrapolated to physiological temperatures using previously reported  $Q_{10}$  values for WT,  $\Delta$ KPQ, and E1784K variants (Nagatomo *et al.*, 1998; Abdelsayed *et al.*, 2015). The thermosensitivity of 1795insD and Q1909R mutants was never reported; thus, we used the WT temperature-dependence for these mutants. The maximal  $G_{\text{Na}}$  density was 75 mS/ $\mu$ F across all channel variants in the O'Rd model. We modified the gating  $I_{\text{Na}}$

parameters data in accordance with our biophysical data for the various channel variants. The GV, SSFI, and SSSI midpoints and slopes of the channel variants extrapolated to 37 °C were normalized to the original O’Rd parameters. The normalized midpoint and slope values for GV and SSFI were then incorporated into the Boltzmann curve (equation 4) and SSSI into the modified Boltzmann curve (equation 6). The original O’Rd SSSI ( $j_{\infty}$ ) curve was equated to the SSFI curve ( $h_{\infty}$ ), which had no plateau. Our experimental SSSI plateaus were subtracted from the original O’Rd value of 0, to compensate for this caveat. The phosphorylated steady-state fast inactivation midpoints in all channel variants were equally hyperpolarized by 6.2 mV. Late  $I_{Na}$  density was normalized to the original O’Rd value and multiplied by the percentage of late to peak  $I_{Na}$  calculated above. The relationship between fast inactivation time constants versus voltage was calculated using an inverse double exponential distribution at 37 °C. The O’Rd slow inactivation time constant equation was used for all the channel variants since it encompassed a comprehensive range of voltages.

To model the calcium-dependence of our  $I_{Na}$  data, we fit the extrapolated biophysical parameters to 37 °C with a Hill equation:

$$10. Z = Y_0 + (Y_M - Y_0) / (1 + (X_{1/2}/X)^b)$$

where Z is the biophysical parameter of interest,  $Y_0$  is the minimum value,  $Y_M$  is the maximum value,  $X_{1/2}$  is the midpoint of the curve, X is the intracellular cytosolic calcium, b is the rate.

Subspace calcium was not accounted for due to the lack of experimental data. Thus, the modified O’Rd model is a dynamic simulation of the calcium-induced shifts which are observed with increasing intracellular calcium levels as a function of pacing frequency, comprising the positive staircase phenomenon.

Simulations were run on endocardial and epicardial ventricular myocytes using a 0.5 ms stimulus pulse with an amplitude of -80  $\mu A/\mu F$ . The stimulus protocol was designed accordingly to step up the frequency gradually from 0.5 Hz to 2.5 Hz. The stimulus protocol had a cycle length of 2000 ms for the first 75 APs, 1000 ms for the following 75 APs, 667 ms for the following 75 APs, 500 ms for the following 75 APs, 400 ms for the following 100 APs.

Analysis of APs only included those that fully recovered and were restored to baseline. Action potential duration (APD) was measured at 30 %, 60 %, and 90 % of repolarization by multiplying these percentages by the resting membrane potential (RMP) value prior to the current stimulus pulse. The  $APD_x$  ( $X=30, 60, 90$ ) values were plotted versus the diastolic interval ( $DI = BCL - APD_x$ ), where BCL is the basic cycle length, creating electrical restitution curves. The curves were fitted with a double-exponential equation 5. Action potential velocity was calculated from initiation of the current stimulus to the maximal peak.

## 3.4. Results

### 3.4.1. Peak current amplitude and conductance density

Raw  $I_{Na}$  traces are shown in **Figure 3-2** for all the channel variants at 0 nM and 2500 nM. The current density of 1795insD was smaller ( $p < 0.0001$ , **Table 3-2**) compared to WT and the rest of the mutants. Elevations in cytosolic calcium had no effect on current density in any of the channel variants ( $p > 0.05$ , **Figure 3-2** and **Table 3-2**). Peak conductance density was also reduced in 1795insD compared to WT and the mutants ( $p < 0.0001$ , **Figure 3-2** and **Table 3-2**). In  $\Delta$ KPQ, peak conductance density was larger ( $p < 0.01$ , **Table 3-2**) by  $4.59 \text{ pA/pF} \pm 1.06 \text{ pA/pF}$  with 500 nM to 2500 nM elevations in cytosolic calcium. No other mutants were affected by elevations in cytosolic calcium ( $p > 0.05$ , **Table 3-2**).

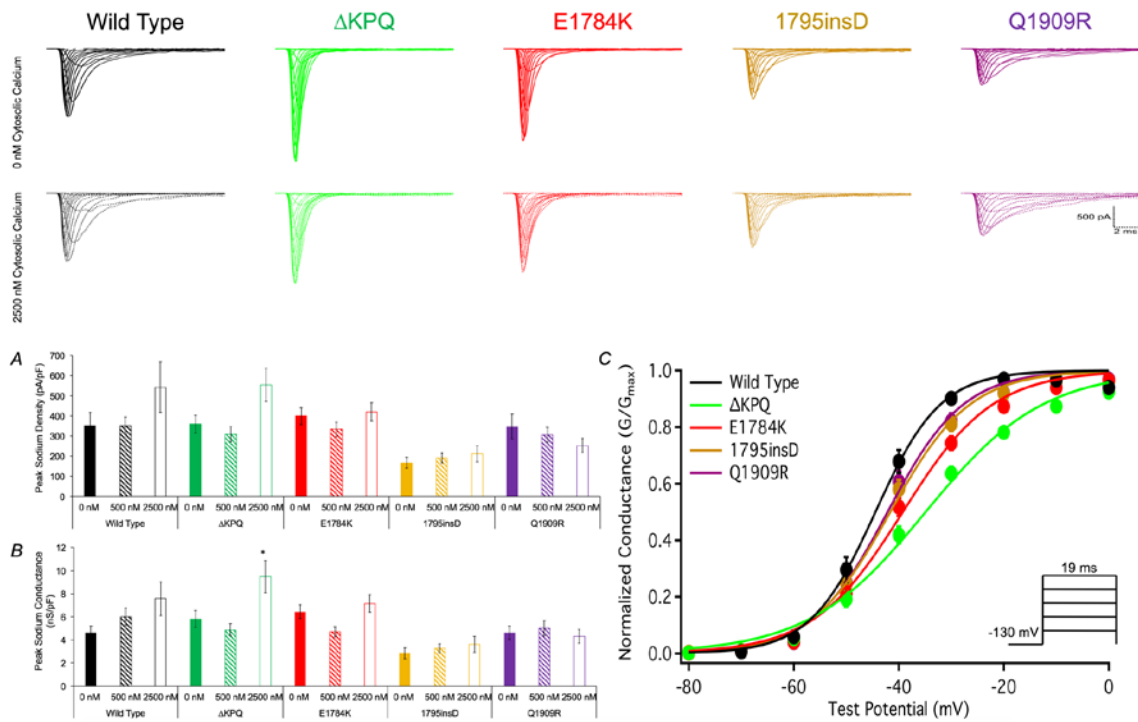


**Figure 3-2 Wild type and Mutant Currents and Conductance**

Raw current traces for the wild-type and mutant channels at 0 nM and 2500 nM cytosolic calcium. Panels A and B show bar graphs of peak  $I_{Na}$  current density and peak  $I_{Na}$  conductance density, respectively, as a function of the three cytosolic calcium levels. Panel B includes an asterisk indicating a significant rise in  $\Delta$ KPQ conductance density with 500 nM to 2500 nM elevations in cytosolic calcium. Panel C shows normalized conductance versus membrane potential for the mutant effect at 0 nM cytosolic calcium.

**Table 3-2 Calcium Peak Current and Conductance Densities**

Condition	Peak I <sub>Na</sub> Density (pA/pF)	N	Peak GV Density (nS/pF)	N
WT - 0 nM	352.99 ± 62.86	21	4.66 ± 0.57	19
WT - 500 nM	351.68 ± 44.06	13	6.01 ± 0.75	13
WT - 2500 nM	542.91 ± 124.29	8	7.58 ± 1.47	7
ΔKPQ - 0 nM	358.88 ± 44.00	28	5.83 ± 0.71	27
ΔKPQ - 500 nM	308.51 ± 37.56	20	4.88 ± 0.53	19
ΔKPQ - 2500 nM	554.2 ± 81.95	11	9.47 ± 1.40 <sup>*1</sup>	11
EK - 0 nM	399.15 ± 40.85	23	6.44 ± 0.61	22
EK - 500 nM	333.65 ± 35.27	26	4.70 ± 0.46	29
EK - 2500 nM	419.13 ± 45.16	13	7.16 ± 0.77	13
1795insD - 0 nM	166.90 ± 27.14	17	2.85 ± 0.46	17
1795insD - 500 nM	191.35 ± 24.73	19	3.27 ± 0.42	19
1795insD - 2500 nM	211.93 ± 39.87	12	3.62 ± 0.68	12
QR - 0 nM	346.55 ± 61.56	25	4.62 ± 0.57	23
QR - 500 nM	306.78 ± 36.87	19	5.00 ± 0.64	20
QR - 2500 nM	253.19 ± 34.58	15	4.33 ± 0.59	15

<sup>\*1</sup> p<0.01 versus ΔKPQ (0 nM and 500 nM)

### 3.4.2. Activation voltage-dependence

Normalized conductance is plotted as a function of membrane potential in **Figure 3-2**. Activation midpoint ( $GV-V_{1/2}$ ) was depolarized in all mutants compared to WT ( $p < 0.0001$ , **Table 3-3**). The mutants depolarized  $GV-V_{1/2}$  in an increasing order compared to WT: Q1909R, 1795insD, E1784K, and  $\Delta$ KPQ, respectively. In all channel variants,  $GV-V_{1/2}$  was not affected by elevations in cytosolic calcium ( $p > 0.05$ , **Table 3-3**). Activation slope ( $GV-z$ ) was reduced in the same order as the mutant-induced  $GV-V_{1/2}$  shifts ( $p < 0.0001$ , **Table 3-3**). Elevations in cytosolic calcium did not affect  $GV-z$  in any channel variant ( $p > 0.05$ , **Table 3-3**).

**Table 3-3 Calcium Conductance**

Condition	$GV-V_{1/2}$ (mV)	$GV-z$	N
WT - 0 nM	$-44.42 \pm 1.20$	$4.87 \pm 0.25$	19
WT - 500 nM	$-41.45 \pm 1.66$	$3.79 \pm 0.24$	13
WT - 2500 nM	$-46.95 \pm 1.88$	$4.89 \pm 0.38$	8
$\Delta$ KPQ - 0 nM	$-34.98 \pm 1.30$	$2.56 \pm 0.10$	30
$\Delta$ KPQ - 500 nM	$-34.94 \pm 1.69$	$2.89 \pm 0.13$	16
$\Delta$ KPQ - 2500 nM	$-38.46 \pm 1.09$	$3.54 \pm 0.16$	11
EK - 0 nM	$-39.03 \pm 1.21$	$3.28 \pm 0.13$	23
EK - 500 nM	$-38.20 \pm 1.52$	$3.29 \pm 0.16$	30
EK - 2500 nM	$-38.38 \pm 1.11$	$3.71 \pm 0.22$	13
1795insD - 0 nM	$-41.51 \pm 1.08$	$3.72 \pm 0.21$	17
1795insD - 500 nM	$-39.43 \pm 1.02$	$3.81 \pm 0.22$	19
1795insD - 2500 nM	$-39.02 \pm 1.38$	$3.29 \pm 0.17$	12
QR - 0 nM	$-41.89 \pm 1.20$	$4.14 \pm 0.18$	25
QR - 500 nM	$-42.96 \pm 1.12$	$4.03 \pm 0.23$	22
QR - 2500 nM	$-43.18 \pm 1.63$	$4.38 \pm 0.16$	16

### 3.4.3. Fast and intermediate inactivation voltage-dependence

Normalized current versus membrane potential is shown in **Figure 3-3**. The steady-state fast inactivation midpoint ( $SSFI-V_{1/2}$ ) was hyperpolarized by  $\Delta$ KPQ, E1784K, and 1795insD compared to WT ( $p < 0.0001$ , **Table 3-4**). The  $SSFI-V_{1/2}$  of  $\Delta$ KPQ was depolarized ( $p < 0.01$ ) by elevations in cytosolic calcium compared to the other channel variants ( $p > 0.05$ , **Figure 3-3** and **Table 3-4**). When cytosolic calcium was elevated from 0 nM to 500 nM, the  $SSFI-V_{1/2}$  of  $\Delta$ KPQ depolarized by  $8.98 \text{ mV} \pm 2.35 \text{ mV}$  ( $p < 0.01$ , **Table 3-4**). Additional elevations in cytosolic calcium to 2500 nM did not further depolarize the  $SSFI-V_{1/2}$  of  $\Delta$ KPQ ( $p > 0.05$ , **Figure 3-3** and **Table 3-4**). The steady-state fast inactivation slope ( $SSFI-z$ ) was reduced in E1784K, 1795insD, and

Q1909R compared to WT ( $p=0.0005$ , **Table 3-4**). Elevations in cytosolic calcium had no effects on SSFI-z in any channel variant ( $p>0.05$ , **Table 3-4**). Steady-state intermediate inactivation (SSII) was measured using a similar protocol to SSFI, except with 1000 ms prepulse durations (**Table 3-4**). The SSII- $V_{1/2}$  of E1784K and 1795insD are hyperpolarized compared to WT ( $p<0.0001$ , **Table 3-4**). Both mutants also reduced SSII-z ( $p<0.0001$ , **Table 3-4**) compared to WT. Elevations in cytosolic calcium had no effect on both SSII- $V_{1/2}$  and SSII-z in any channel variant ( $p>0.05$ , **Table 3-4**).

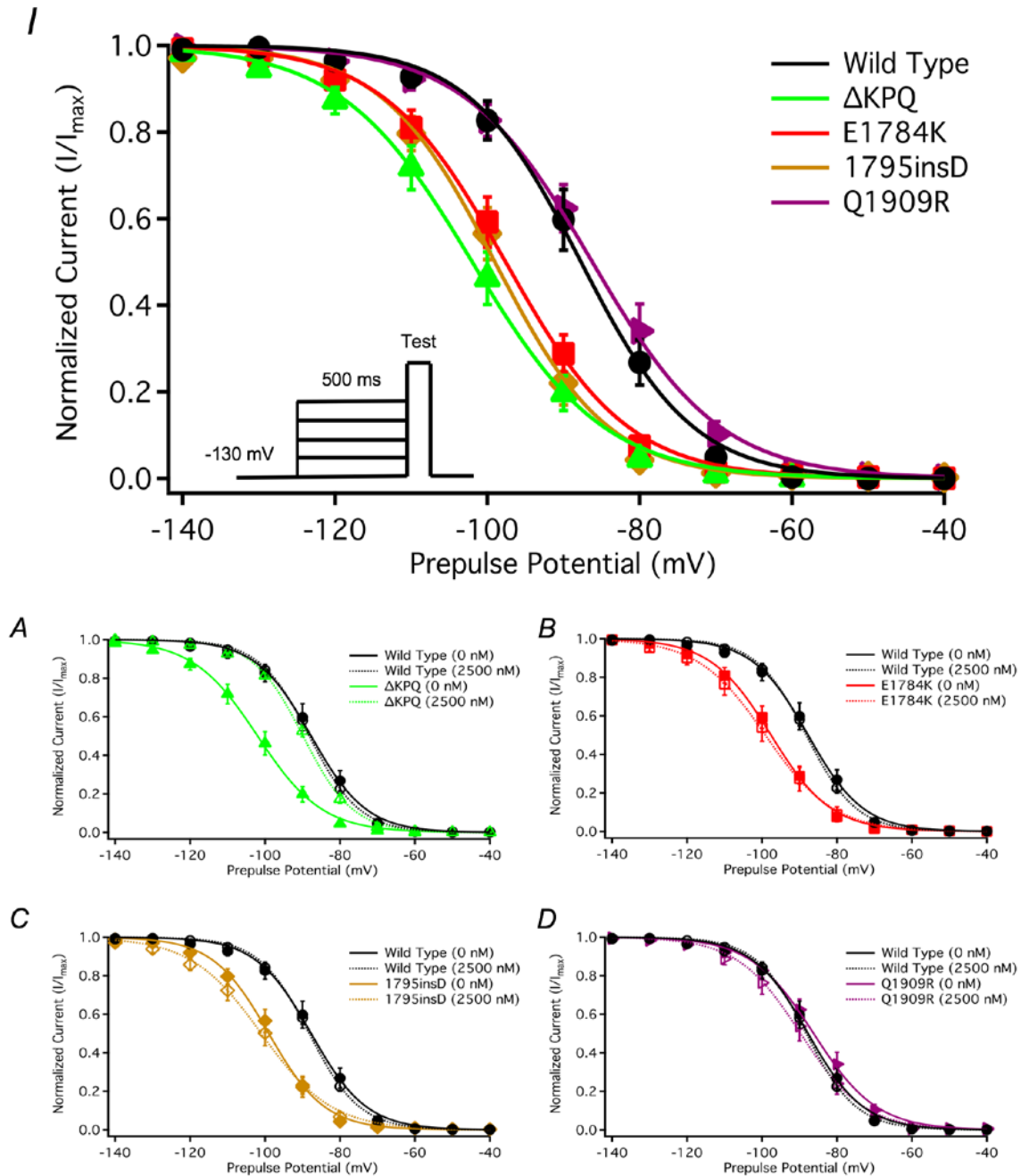


**Figure 3-3 Effects of cytosolic calcium on steady-state fast inactivation**  
 Panels I shows the mutant effect at 0 nM cytosolic calcium and contains a voltage pulse inset. Panels A-D show the calcium effect on each individual mutant compared to WT. Normalized current versus membrane potential was fit with a Boltzmann fit.

**Table 3-4 Calcium Steady-State Fast and Intermediate Inactivation**

Condition	SSFI-V <sub>1/2</sub> (mV)	SSFI-z	N	SSII-V <sub>1/2</sub> (mV)	SSII-z	N
WT - 0 nM	-87.95 ± 2.06	-3.84 ± 0.27	7	-86.17 ± 2.21	-4.24 ± 0.11	9
WT - 500 nM	-89.73 ± 0.79	-3.91 ± 0.23	8	-90.97 ± 2.99	-3.87 ± 0.20	6
WT - 2500 nM	-88.24 ± 0.89	-3.92 ± 0.17	8	-90.56 ± 0.68	-3.90 ± 0.14	8
ΔKPQ - 0 nM	-102.15 ± 2.07 <sup>**1</sup>	-3.71 ± 0.12	17	-97.19 ± 2.68	-3.70 ± 0.19	7
ΔKPQ - 500 nM	-93.17 ± 1.06	-3.58 ± 0.18	13	-95.12 ± 2.64	-4.02 ± 0.13	9
ΔKPQ - 2500 nM	-89.83 ± 0.76	-3.91 ± 0.08	8	-90.98 ± 0.80	-3.86 ± 0.09	8
EK - 0 nM	-97.62 ± 1.84	-3.38 ± 0.07	7	-99.33 ± 1.34	-3.08 ± 0.11	8
EK - 500 nM	-97.82 ± 2.98	-3.32 ± 0.11	8	-98.70 ± 1.97	-3.10 ± 0.10	8
EK -2500 nM	-99.06 ± 2.82	-3.25 ± 0.13	8	-100.73 ± 2.98	-3.27 ± 0.13	8
1795insD - 0 nM	-99.03 ± 1.95	-3.71 ± 0.11	7	-100.64 ± 1.78	-3.78 ± 0.10	8
1795insD - 500 nM	-95.70 ± 2.03	-3.37 ± 0.21	13	-100.53 ± 2.45	-3.55 ± 0.16	12
1795insD - 2500 nM	-101.01 ± 2.37	-3.22 ± 0.16	12	-102.81 ± 2.24	-3.18 ± 0.15	12
QR - 0 nM	-86.28 ± 2.16	-3.28 ± 0.17	7	-90.53 ± 2.37	-3.53 ± 0.17	8
QR - 500 nM	-89.30 ± 1.89	-3.46 ± 0.16	7	-88.00 ± 2.34	-3.98 ± 0.37	7
QR - 2500 nM	-89.78 ± 2.51	-3.56 ± 0.15	9	-90.18 ± 2.33	-3.49 ± 0.10	7

<sup>\*\*1</sup> p<0.01 versus ΔKPQ (500 nM and 2500 nM)

### 3.4.4. Fast inactivation recovery and onset kinetics

Double-pulse protocols were used to measure onset ( $\tau_{on}$ ) and recovery ( $\tau_{off}$ ) kinetics of fast inactivation. The time constant ( $\tau$ ) obtained from the fits to the recovery and onset curves equals the inverse of the sum of both the forward (recovery) and reverse (onset) rates. At voltages hyperpolarized relative to SSFI-V<sub>1/2</sub>, recovery from fast inactivation predominates. At voltages depolarized relative to SSFI-V<sub>1/2</sub>, onset into fast inactivation predominates. At SSFI-V<sub>1/2</sub>, both onset and recovery are in equilibrium.

Fast inactivation time constants as a function of voltage are reported in **Table 3-5** and **Table 3-6**. At -10 mV, the slow component ( $\tau_2$ ) of the fast inactivation onset in ΔKPQ decreased when cytosolic calcium was elevated from 0 nM to 500 nM. 1795insD fast inactivation time constant ( $\tau_2$ ) is increased at -30 mV when cytosolic calcium was elevated from 500 nM to 2500 nM. Q1909R fast inactivation kinetics were decelerated at both open-state and closed-state voltages with elevations in cytosolic calcium (**Table 3-5** and **Table 3-6**).

**Table 3-5 Calcium -130 mV to -70 mV Fast Inactivation Time Constants (ms)**

Condition	-130 $\tau_1$	-130 $\tau_2$	n	-110 $\tau_1$	-110 $\tau_2$	n	-90 $\tau_1$	-90 $\tau_2$	n	-70 $\tau_1$	-70 $\tau_2$	n
WT – 0 nM	3.94 ± 0.58	113.21 ± 36.03	7	13.92 ± 2.04	288.74 ± 83.60	5	70.37 ± 11.48	91.75 ± 5.50	10	43.21 ± 10.94	155.03 ± 27.72	10
WT – 500 nM	4.33 ± 0.49	200.90 ± 89.52	7	12.50 ± 0.45	170.05 ± 73.01	5	56.26 ± 7.92	177.29 ± 37.91	9	20.70 ± 4.16 <sup>ns</sup>	91.38 ± 17.83	9
WT – 2500 nM	5.28 ± 0.44	115.34 ± 24.52	7	17.25 ± 0.86	119.10 ± 14.30	7	75.67 ± 5.82	94.14 ± 8.63	7	17.93 ± 1.54	82.97 ± 15.41	7
$\Delta$ KPQ – 0 nM	3.10 ± 0.26	77.18 ± 6.61	7	7.96 ± 0.71	203.23 ± 17.35	7	8.47 ± 1.05	29.45 ± 8.37	8	3.80 ± 0.65	24.97 ± 12.37	6
$\Delta$ KPQ – 500 nM	3.00 ± 0.25	76.08 ± 13.39	7	7.16 ± 0.45	167.46 ± 16.23	8	8.67 ± 1.04	29.21 ± 10.68	8	3.44 ± 0.41	10.51 ± 6.88	8
$\Delta$ KPQ – 2500 nM	3.33 ± 0.23	74.02 ± 12.93	7	8.37 ± 0.71	207.65 ± 36.71	7	10.02 ± 0.88	52.00 ± 19.54	6	6.41 ± 0.38	28.55 ± 15.48	6
EK – 0 nM	3.04 ± 0.30	158.21 ± 70.23	7	7.48 ± 0.47	105.84 ± 23.74	5	9.17 ± 1.02	31.89 ± 7.28	7	3.76 ± 0.48	16.85 ± 5.46	7
EK – 500 nM	3.25 ± 0.53	86.18 ± 24.57	7	7.89 ± 1.25	211.05 ± 58.34	6	7.45 ± 1.06	20.34 ± 5.41	7	3.60 ± 0.82	20.19 ± 7.54	7
EK – 2500 nM	5.06 ± 0.86	159.22 ± 56.86	7	12.90 ± 1.88	60.28 ± 17.81	7	11.02 ± 2.06	61.37 ± 22.90	7	3.81 ± 0.56	13.38 ± 2.92	7
1795insD – 0 nM	8.60 ± 1.23	248.96 ± 32.04	7	24.90 ± 3.65	227.89 ± 84.10	6	21.87 ± 5.41	79.80 ± 12.43	5	10.44 ± 2.10	29.19 ± 5.89	5
1795insD – 500 nM	6.37 ± 1.00	484.91 ± 156.73	12	19.95 ± 3.54	225.55 ± 39.38	7	16.37 ± 2.67	78.86 ± 9.55	15	10.95 ± 1.98	37.08 ± 5.40	14
1795insD – 2500 nM	6.44 ± 0.44	130.28 ± 27.90	10	17.68 ± 2.29	170.47 ± 46.22	8	37.03 ± 15.64	91.95 ± 21.14	6	3.54 ± 1.08	22.99 ± 5.19	5

QR – 0 nM	3.43 ± 0.40	68.023 ± 11.15	6	9.92 ± 2.10	145.74 ± 26.44	5	58.39 ± 12.43	80.10 ± 14.21	6	26.72 ± 6.32	89.13 ± 11.00	5
QR – 500 nM	4.72 ± 0.84	116.14 ± 31.40	7	10.86 ± 2.23	227.29 ± 39.76	10	51.69 ± 19.72	48.62 ± 6.98	9	18.96 ± 5.03	74.54 ± 10.70	9
QR – 2500 nM	5.85 ± 0.59	128.70 ± 28.24	6	20.74 ± 1.82	160.05 ± 45.20	6	83.22 ± 35.21	136.73 ± 35.41 * <sup>1</sup>	7	33.25 ± 10.01	102.47 ± 27.95	8

\*<sup>1</sup> p<0.001 versus 0 nM and 500 nM Q1909R, \*<sup>2</sup> p<0.05 versus 0 nM WT

**Table 3-6 Calcium -50 mV to +10 mV Fast Inactivation Time Constants (ms)**

Condition	-50 $\tau_1$	-50 $\tau_2$	n	-30 $\tau_1$	-30 $\tau_2$	n	-10 $\tau_1$	-10 $\tau_2$	n	+10 $\tau_1$	+10 $\tau_2$	n
WT – 0 nM	6.32 ± 1.00	14.05 ± 6.12	10	0.88 ± 0.07	3.23 ± 0.23	21	0.50 ± 0.02	2.56 ± 0.44	21	0.39 ± 0.02	4.19 ± 1.80	18
WT – 500 nM	3.09 ± 0.2	3.45 ± 0.47	5	0.93 ± 0.10	3.36 ± 0.35	16	0.55 ± 0.05	3.25 ± 0.36	15	0.39 ± 0.05	1.97 ± 0.37	14
WT – 2500 nM	4.41 ± 0.47	4.51 ± 0.58	7	0.93 ± 0.10	6.35 ± 2.85	8	0.58 ± 0.03	1.99 ± 0.46	8	0.44 ± 0.02	2.68 ± 0.75	8
$\Delta$ KPQ –0 nM	1.41 ± 0.22	1.42 ± 0.22	6	0.48 ± 0.02	3.68 ± 0.62	34	0.45 ± 0.02 * <sup>3</sup>	5.46 ± 1.35	33	0.46 ± 0.02	4.95 ± 1.98	32
$\Delta$ KPQ –500 nM	1.00 ± 0.09	2.16 ± 0.85	8	0.58 ± 0.05	3.38 ± 0.68	19	0.50 ± 0.03	3.99 ± 1.01	19	0.45 ± 0.02	3.89 ± 0.70	14
$\Delta$ KPQ –2500 nM	1.47 ± 0.30	1.93 ± 0.24	6	0.61 ± 0.02	5.00 ± 0.90	11	0.58 ± 0.02	4.34 ± 0.80	11	0.59 ± 0.03 * <sup>5</sup>	3.15 ± 0.71	11
EK – 0 nM	0.75 ± 0.30	1.55 ± 0.35	5	0.46 ± 0.03	6.62 ± 3.34	22	0.33 ± 0.02	4.17 ± 1.24	22	0.27 ± 0.02	2.31 ± 0.75	21
EK – 500 nM	1.09 ± 0.24	1.21 ± 0.15	7	0.50 ± 0.03	2.13 ± 0.48	29	0.34 ± 0.01	3.29 ± 1.43	29	0.26 ± 0.02	2.01 ± 0.67	27
EK –2500 nM	1.59 ± 0.19	1.79 ± 0.22	7	0.53 ± 0.03	3.80 ± 1.38	13	0.40 ± 0.01	2.13 ± 0.34	13	0.34 ± 0.01	1.46 ± 0.26	14
1795insD –0 nM	3.53 ± 0.37	3.54 ± 0.40	6	0.81 ± 0.03	4.62 ± 0.85	15	0.46 ± 0.02	3.15 ± 0.67	15	0.31 ± 0.02	2.49 ± 0.84	15
1795insD –500 nM	4.74 ± 0.65	4.69 ± 0.62	5	0.90 ± 0.06	9.18 ± 4.16	19	0.51 ± 0.03	5.50 ± 1.91	18	0.41 ± 0.02	3.93 ± 1.19	15
1795insD –2500 nM	4.22 ± 0.38	4.23 ± 0.40	6	0.96 ± 0.10	18.72 ± 5.98 * <sup>2</sup>	13	0.56 ± 0.03	4.63 ± 1.15	12	0.41 ± 0.02	5.99 ± 1.48	11

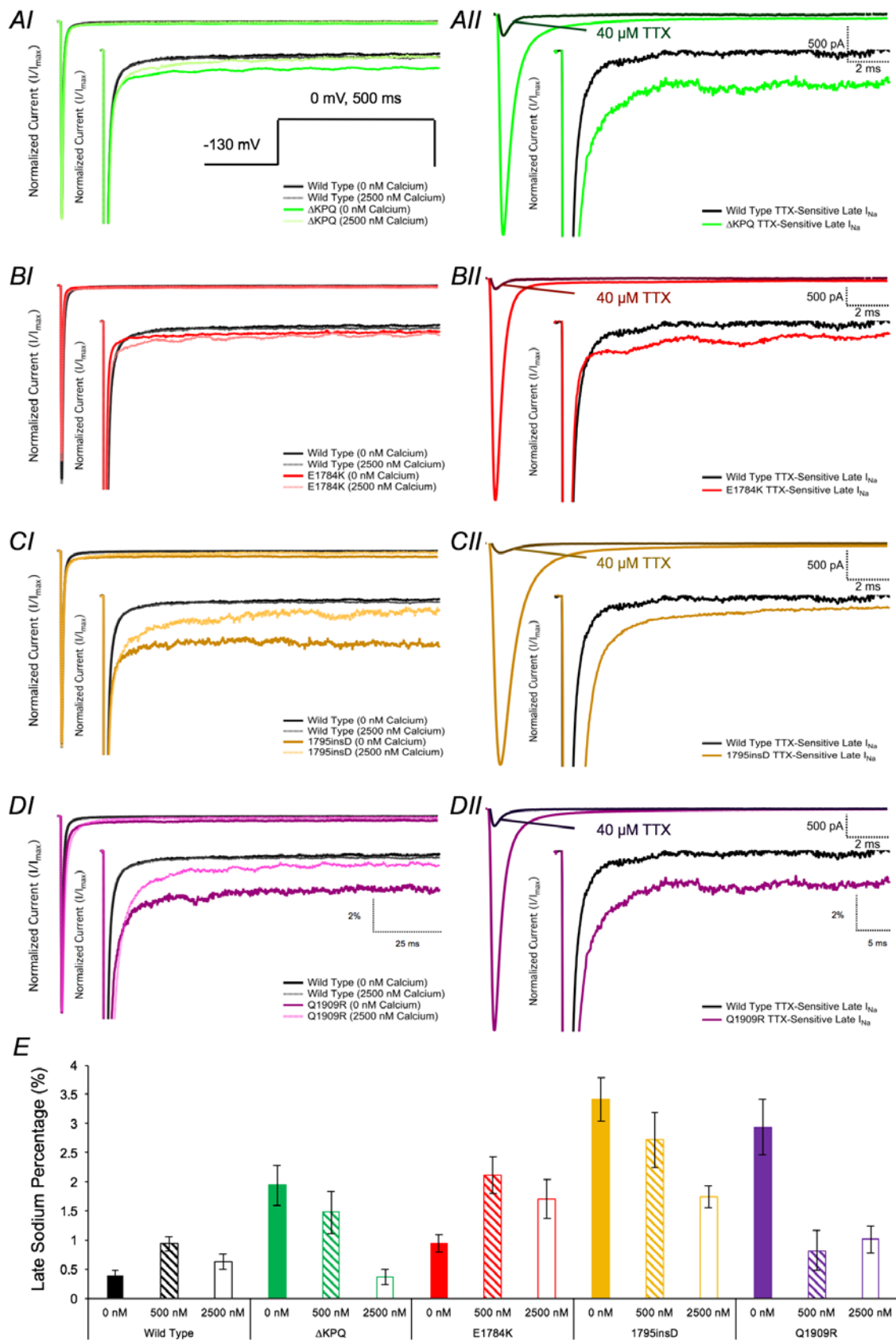
QR – 0 nM	5.90 ± 0.89	21.73 ± 4.74	5	0.99 ± 0.08	9.12 ± 2.81	27	0.60 ± 0.02	3.06 ± 0.31	28	0.46 ± 0.02	2.45 ± 0.26	27
QR – 500 nM	5.37 ± 1.24	20.44 ± 4.78	7	0.88 ± 0.07	4.63 ± 0.54	24	0.53 ± 0.02	3.15 ± 0.29	23	0.38 ± 0.02	2.23 ± 0.34	22
QR – 2500 nM	7.86 ± 0.74	34.01 ± 9.82	7	1.33 ± 0.13 <sup>*1</sup>	7.18 ± 1.55	14	0.75 ± 0.04 <sup>*4</sup>	5.11 ± 1.27	14	0.62 ± 0.024 <sup>*6</sup>	4.74 ± 0.93	12

<sup>\*1</sup> p<0.05 vs. 0 nM and 500 nM Q1909R, <sup>\*2</sup> p<0.05 vs. 0 nM 1795insD, <sup>\*3</sup> p<0.05 vs. 500 nM and 2500 nM ΔKPQ, <sup>\*4</sup> p<0.05 vs. 0 nM and 500 nM Q1909R, <sup>\*5</sup> p<0.05 vs 0 nM and 500 nM ΔKPQ, <sup>\*6</sup> p<0.05 vs 0 nM and 500 nM Q1909R

### 3.4.5. Late current amplitude and conductance density

Late  $I_{Na}$  conductance density was measured similarly to peak conductance density. Elevations in cytosolic calcium had no effect on late conductance density in any of the channel variants ( $p>0.05$ , **Table 3-7**).

Raw  $I_{Na}$  current records emphasizing late  $I_{Na}$  are shown in **Figure 3-4: AI-DI**. Traces of TTX-sensitive late  $I_{Na}$  in all mutants compared to WT are shown in **Figure 3-4: AII-DII**. The current traces were normalized to peak  $I_{Na}$ . Late  $I_{Na}$  was larger in the mutants compared to WT ( $p<0.0001$ , **Table 3-7**). Late  $I_{Na}$  was lower by  $1.58\% \pm 0.49\%$  in  $\Delta$ KPQ and by  $1.68\% \pm 0.47\%$  in 1795insD when cytosolic calcium was elevated from 0 nM to 2500 nM ( $p<0.0001$ , **Figure 3-4** and **Table 3-7**). In Q1909R, late  $I_{Na}$  was lower by  $2.11\% \pm 0.44\%$  when cytosolic calcium was elevated from 0 nM to 500 nM ( $p<0.0001$ , **Figure 3-4** and **Table 3-7**). Further elevations in cytosolic calcium did not affect late  $I_{Na}$  of Q1909R ( $p>0.05$ , **Table 3-7**). Late  $I_{Na}$  of E1784K was not affected by elevations in cytosolic calcium ( $p>0.05$ , **Table 3-7**).



(Previous page)

**Figure 3-4 Effects of cytosolic calcium on late  $I_{Na}$**

Panels AI-DI show the effects of cytosolic calcium on the mutants compared to WT. The voltage pulse used to measure late  $I_{Na}$  is shown in panel AI. Panels AII-DII show TTX-subtracted late  $I_{Na}$  for all channel variants at 0 nM cytosolic calcium. Panel E shows a bar graph of late  $I_{Na}$  as a percentage of peak  $I_{Na}$  versus the three cytosolic calcium concentrations.

**Table 3-7 Calcium Late  $I_{Na}$**

Condition	Late GV Density (nS/pF)	N	Late Percent (%)	N
WT - 0 nM	0.07 ± 0.02	16	0.40 ± 0.08	9
WT - 500 nM	0.08 ± 0.01	5	0.94 ± 0.12	6
WT - 2500 nM	0.05 ± 0.02	8	0.62 ± 0.13	6
$\Delta$ KPQ - 0 nM	0.12 ± 0.02	13	1.94 ± 0.35 <sup>*1</sup>	9
$\Delta$ KPQ - 500 nM	0.18 ± 0.05	9	1.48 ± 0.36	5
$\Delta$ KPQ - 2500 nM	0.12 ± 0.04	10	0.36 ± 0.13	6
EK - 0 nM	0.07 ± 0.02	11	0.95 ± 0.15	11
EK - 500 nM	0.13 ± 0.02	19	2.11 ± 0.32	14
EK - 2500 nM	0.09 ± 0.01	15	1.71 ± 0.34	14
1795insD - 0 nM	0.07 ± 0.02	11	3.42 ± 0.37 <sup>*1</sup>	7
1795insD - 500 nM	0.12 ± 0.02	6	2.72 ± 0.48	5
1795insD - 2500 nM	0.07 ± 0.02	13	1.74 ± 0.18	9
QR - 0 nM	0.11 ± 0.02	14	2.94 ± 0.48 <sup>*2</sup>	10
QR - 500 nM	0.04 ± 0.02	5	0.82 ± 0.34	8
QR - 2500 nM	0.08 ± 0.01	7	1.01 ± 0.24	6

<sup>\*1</sup> p<0.0001 versus same mutant (2500 nM), <sup>\*2</sup> p<0.0001 versus Q1909R (500 nM and 2500 nM)

### 3.4.6. Slow inactivation voltage-dependence

Normalized current versus membrane potential is shown in **Figure 3-5**. The steady-state slow inactivation midpoint (SSSI- $V_{1/2}$ ) was not different in any of the channel variants ( $p>0.05$ , **Table 3-8**). The SSSI- $V_{1/2}$  of E1784K was depolarized by  $23.9 \text{ mV} \pm 6.61 \text{ mV}$  when cytosolic calcium was elevated from 500 nM to 2500 nM ( $p<0.01$ , **Figure 3-5** and **Table 3-8**). The steady-state slow inactivation slope (SSSI-z) was not affected by the mutants ( $p>0.05$ , **Table 3-8**). SSSI-z of 1795insD was larger by  $0.85 \pm 0.19$  with 0 nM to 2500 nM elevations in cytosolic calcium ( $p<0.05$ , **Table 3-8**). The steady-state slow inactivation plateau (SSSI- $y_0$ ) was higher in E1784K by  $20.0 \% \pm 4.9 \%$  when cytosolic calcium was elevated from 0 nM to 500 nM ( $p<0.01$ , **Figure 3-5** and **Table 3-8**). Further elevations in cytosolic calcium did not have an effect on SSSI- $y_0$  in E1784K. The SSSI- $y_0$  of Q1909R was higher by  $18.0\% \pm 0.05\%$  with 0 nM to 500 nM elevations in cytosolic calcium ( $p<0.01$ , **Figure 3-5** and **Table 3-8**).

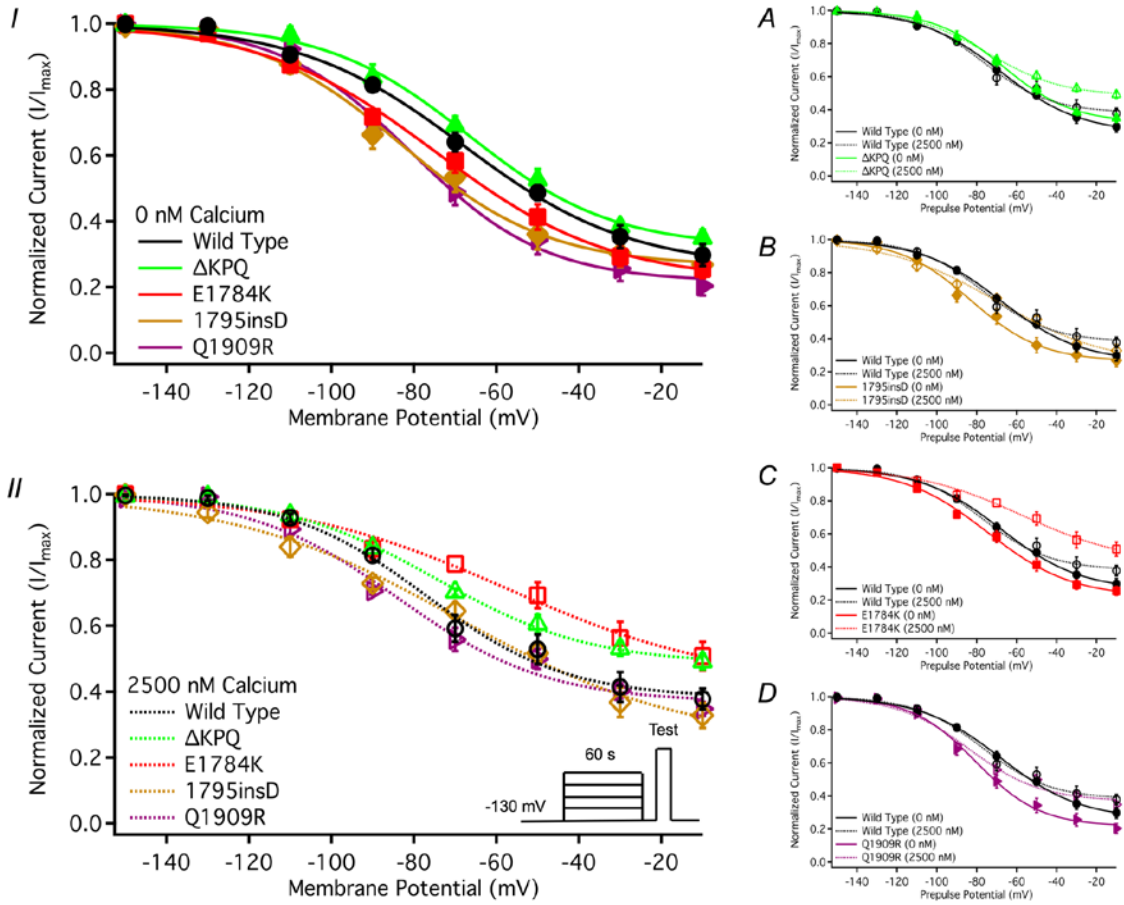


**Figure 3-5 Effects of cytosolic calcium on steady-state slow inactivation**

Panels I-II show the mutant effects at 0 nM and 2500 nM cytosolic calcium. Panel II shows a voltage pulse inset. Panels A-D show the calcium effect on each individual mutant compared to WT. Normalized current versus membrane potential was fit with a modified Boltzmann fit.

**Table 3-8 Calcium Steady-State Slow Inactivation**

Condition	SSSI- $V_{1/2}$ (mV)	SSSI-z	SSSI- $y_0$	N
WT - 0 nM	-69.26 ± 2.43	-1.33 ± 0.06	0.27 ± 0.04	7
WT - 500 nM	-69.99 ± 2.67	-1.56 ± 0.16	0.35 ± 0.01	3
WT - 2500 nM	-68.86 ± 2.47	-1.33 ± 0.14	0.34 ± 0.03	8
$\Delta$ KPQ - 0 nM	-66.16 ± 2.18	-1.50 ± 0.20	0.32 ± 0.03	5
$\Delta$ KPQ - 500 nM	-74.75 ± 8.18	-1.63 ± 0.19	0.37 ± 0.03	6
$\Delta$ KPQ - 2500 nM	-73.17 ± 2.05	-1.57 ± 0.16	0.48 ± 0.03	6
EK - 0 nM	-73.44 ± 2.41	-1.22 ± 0.10	0.21 ± 0.02	6
EK - 500 nM	-80.60 ± 5.18	-1.41 ± 0.24	0.41 ± 0.03	5
EK -2500 nM	-56.66 ± 4.48 <sup>*1</sup>	-1.02 ± 0.06	0.43 ± 0.04 <sup>*1</sup>	4
1795insD - 0 nM	-84.92 ± 3.88	-1.86 ± 0.21	0.28 ± 0.03	8
1795insD - 500 nM	-75.10 ± 6.65	-1.25 ± 0.21	0.30 ± 0.02	6
1795insD - 2500 nM	-72.72 ± 3.58	-1.00 ± 0.06 <sup>*2</sup>	0.26 ± 0.05	8
QR - 0 nM	-76.67 ± 2.82	-1.51 ± 0.14	0.20 ± 0.02 <sup>*3</sup>	7
QR - 500 nM	-73.10 ± 1.55	-1.40 ± 0.10	0.38 ± 0.02	5
QR - 2500 nM	-77.47 ± 2.66	-1.27 ± 0.08	0.33 ± 0.02	7

<sup>\*1</sup>  $p < 0.01$  ( $V_{1/2}$ ) and  $p < 0.05$  ( $y_0$ ) versus E1784K (0 nM and 500 nM), <sup>\*2</sup>  $p < 0.05$  versus 1795insD (0 nM), <sup>\*3</sup>  $p < 0.05$  versus Q1909R (500 nM and 2500 nM)

### 3.4.7. Slow inactivation recovery and onset kinetics

The weighted slow inactivation time constants are plotted as a function of the membrane potential in **Figure 3-6**. Slow inactivation recovery ( $\alpha$ ) rates are plotted against voltage in **Figure 3-6** and slow inactivation onset ( $\beta$ ) rates in **Figure 3-6**. Mutant effects on  $\tau$  are reported in **Table 3-9** and **Table 3-10**. At -130 mV and -110 mV, recovery kinetics of Q1909R are accelerated ( $p < 0.0001$ , **Table 3-9**) when cytosolic calcium was elevated from 0 nM to 500 nM. Slow inactivation recovery kinetics were also accelerated in E1784K, at -110 mV ( $p < 0.0001$ , **Table 3-9**). The other channel variants had no significant changes in recovery. At voltages greater than -70 mV, slow inactivation kinetics were not affected by elevations in cytosolic calcium in any channel variant (**Table 3-9** and **Table 3-10**).

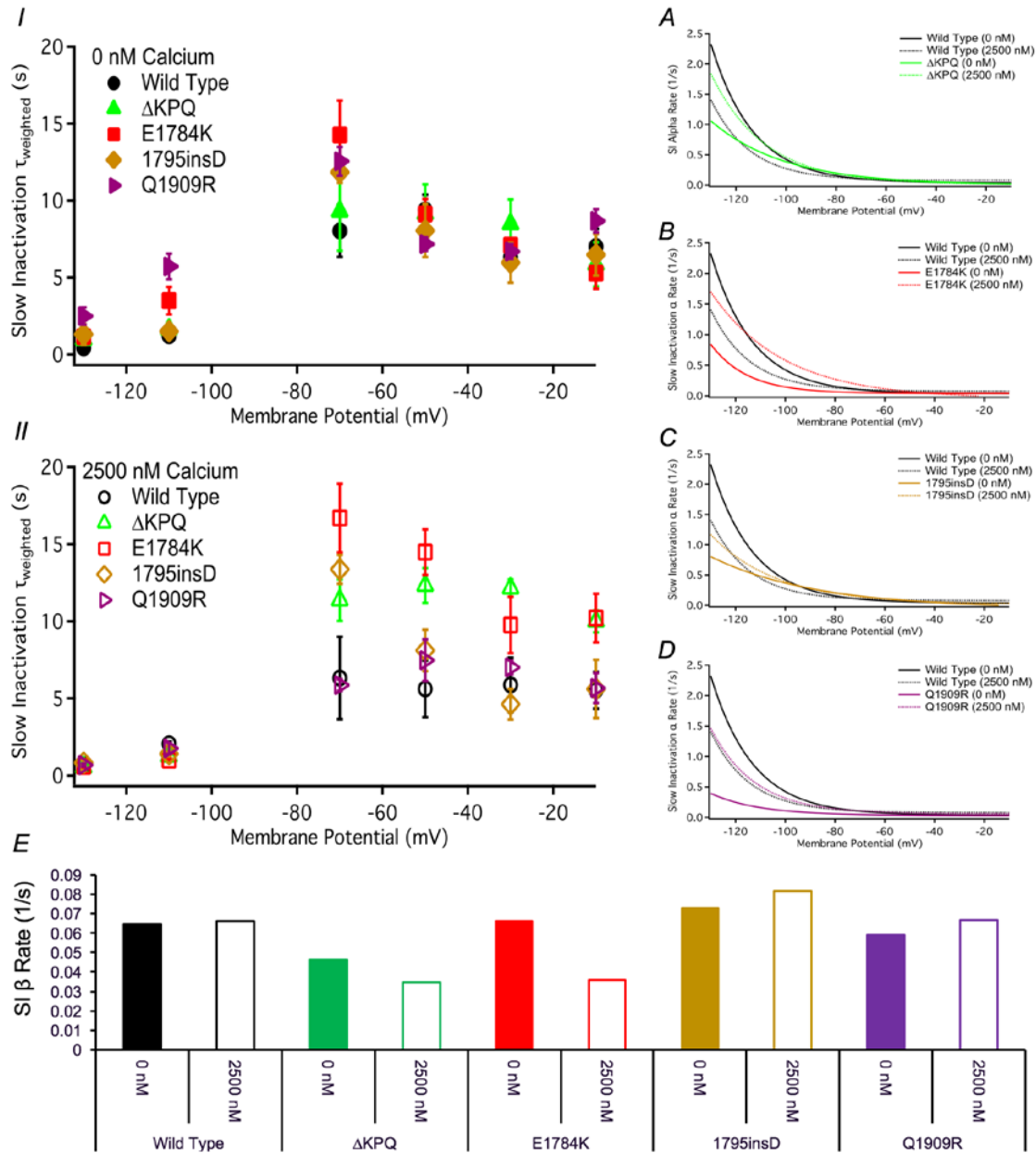


**Figure 3-6 Effects of cytosolic calcium on slow inactivation kinetics**

Panels I-II show the mutant effects on the weighted slow inactivation time constant at 0 nM and 2500 nM cytosolic calcium. Panels A-D show the calcium effects on the slow inactivation  $\alpha$ -rate for the mutants compared to WT. The bar graph below shows the slow inactivation  $\beta$ -rate as a function of calcium and channel variant. Voltage pulse protocols of recovery and onset were not shown for clarity. Please refer to Methods.

**Table 3-9 Calcium -130 mV to -70 mV Slow Inactivation Time Constant (s)**

Condition	-130 mV $\tau_{weight}$	n	-110 mV $\tau_{weight}$	n	-70 mV $\tau_{weight}$	n
WT - 0 nM	0.43 ± 0.06	6	1.22 ± 0.19	5	8.03 ± 1.69	8
WT - 500 nM	0.40 ± 0.07	5	1.41 ± 0.12	5	9.25 ± 0.99	5
WT - 2500 nM	0.70 ± 0.05	7	2.06 ± 0.15	7	6.32 ± 2.67	5
$\Delta$ KPQ - 0 nM	0.97 ± 0.12	7	1.64 ± 0.29	6	9.31 ± 2.56	4
$\Delta$ KPQ - 500 nM	0.58 ± 0.04	7	0.98 ± 0.08	6	6.41 ± 0.96	4
$\Delta$ KPQ - 2500 nM	0.54 ± 0.07	5	1.25 ± 0.18	6	11.4 ± 1.35	5
EK - 0 nM	1.15 ± 0.27	5	3.50 ± 0.89 <sup>*1</sup>	6	14.3 ± 2.23	5
EK - 500 nM	0.95 ± 0.24	6	1.37 ± 0.23	6	18.9 ± 4.31	5
EK - 2500 nM	0.60 ± 0.09	8	1.00 ± 0.12	5	16.7 ± 2.22	4
1795insD - 0 nM	1.30 ± 0.42	3	1.50 ± 0.37	2	11.8 ± 0.69	5
1795insD - 500 nM	1.78 ± 0.28	5	2.92 ± 0.55	4	11.2 ± 0.53	4
1795insD - 2500 nM	0.83 ± 0.17	5	1.40 ± 0.16	5	13.4 ± 0.94	4
QR - 0 nM	2.49 ± 0.56 <sup>*1</sup>	5	5.72 ± 0.84 <sup>*1</sup>	4	12.6 ± 0.94	5
QR - 500 nM	0.68 ± 0.08	6	1.36 ± 0.25	6	6.98 ± 1.29	6
QR - 2500 nM	0.68 ± 0.10	5	1.76 ± 0.36	5	5.86 ± 0.38	5

<sup>\*1</sup> p<0.0001 versus same mutant (500 nM and 2500 nM)

**Table 3-10 Calcium -50 mV to -10 mV Slow Inactivation Time Constant (s)**

Condition	-50 mV $\tau_{weight}$	n	-30 mV $\tau_{weight}$	n	-10 mV $\tau_{weight}$	n
WT - 0 nM	9.38 ± 1.00	5	6.32 ± 0.27	4	7.01 ± 1.15	5
WT - 500 nM	10.9 ± 0.83	5	7.17 ± 0.30	6	5.91 ± 0.65	6
WT - 2500 nM	5.62 ± 1.83	5	5.88 ± 1.77	5	5.53 ± 1.19	4
$\Delta$ KPQ - 0 nM	9.15 ± 1.90	6	8.48 ± 1.59	5	5.86 ± 1.44	5
$\Delta$ KPQ - 500 nM	14.6 ± 1.77	5	10.4 ± 1.39	4	10.7 ± 1.76	5
$\Delta$ KPQ - 2500 nM	12.3 ± 1.13	5	12.1 ± 0.56	5	10.0 ± 0.72	5
EK - 0 nM	9.12 ± 0.98	5	7.10 ± 0.39	5	5.27 ± 1.02	4
EK - 500 nM	15.5 ± 2.81	5	9.36 ± 1.06	5	9.23 ± 1.07	5
EK - 2500 nM	14.5 ± 1.48	5	9.76 ± 1.83	5	10.2 ± 1.58	4
1795insD - 0 nM	8.05 ± 1.72	6	5.96 ± 1.30	5	6.48 ± 1.35	5
1795insD - 500 nM	7.82 ± 1.93	5	5.56 ± 1.59	5	6.48 ± 1.52	5
1795insD - 2500 nM	8.11 ± 1.34	5	4.62 ± 1.00	5	5.61 ± 1.89	5
QR - 0 nM	7.17 ± 0.43	5	6.69 ± 0.49	5	8.68 ± 0.76	5
QR - 500 nM	7.56 ± 0.88	5	5.17 ± 0.30	5	5.48 ± 0.78	5
QR - 2500 nM	7.47 ± 1.35	6	7.02 ± 0.44	5	5.67 ± 0.97	5

### 3.4.8. Ventricular action potential simulations

With increasing pacing frequency stimulations, intracellular calcium naturally increases inside the cell, known as the positive stair-case phenomenon. To simulate dynamic properties of the experimentally observed calcium-induced  $I_{Na}$  shifts, we used a modified version of the O'Rd model to generate action potentials in the endocardial and epicardial cells. The  $I_{Na}$  gating parameters were held uniform across all the three cell

types. The last action potential (AP) simulated at each frequency is shown in **Figure 3-7** for all the channel variants at bradycardia, normal, and tachycardia heart rates. In E1784K, AP is lost with every other beat at elevated heart rates. Thus, both the final two E1784K APs at each frequency are shown in **Figure 3-7**.

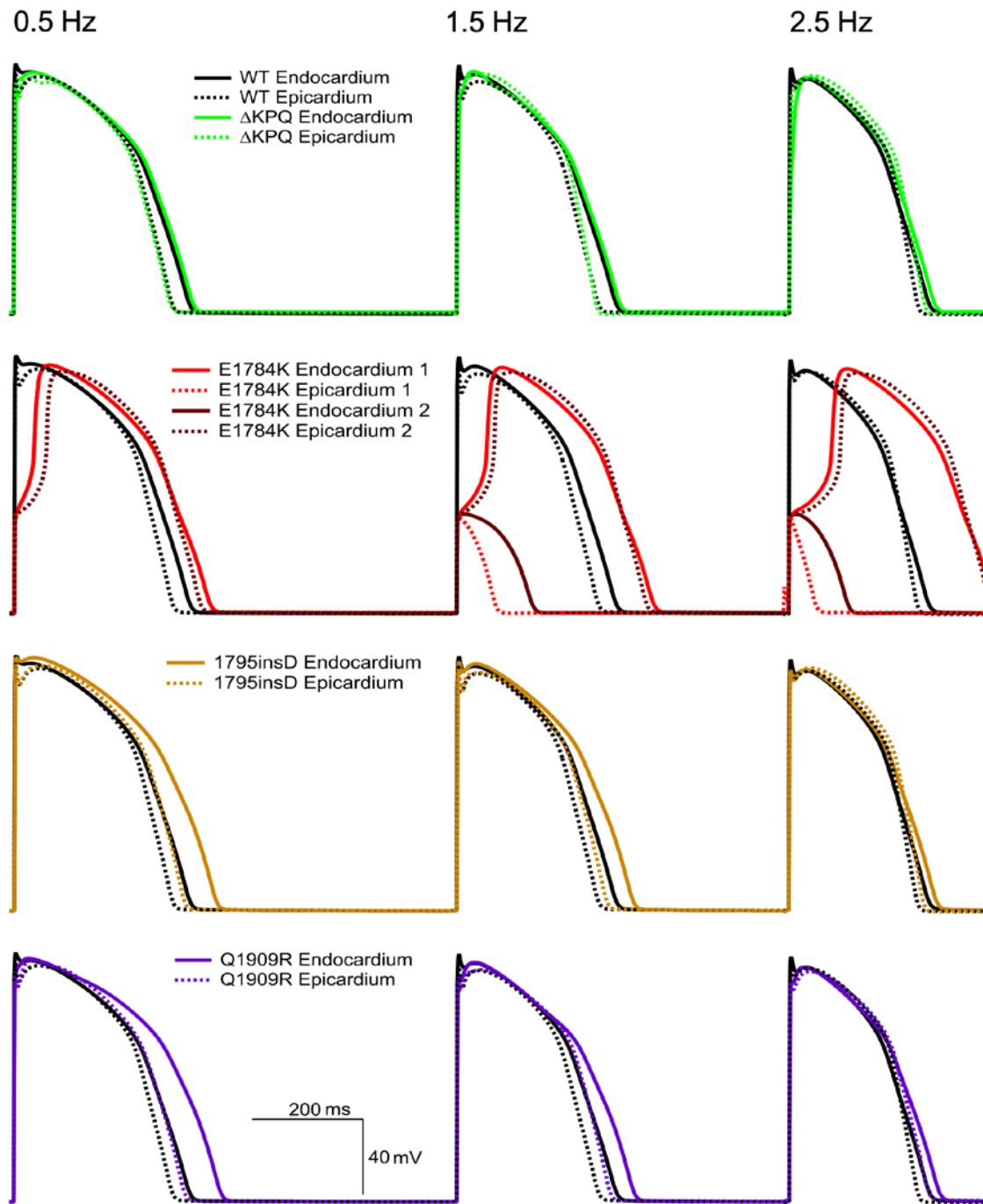


**Figure 3-7 Ventricular action potential simulations**

The AP simulations are shown for endocardial and epicardial cells as a function of frequencies (0.5 Hz, 1.5 Hz, and 2.5 Hz).

Action potential upstroke velocity and action potential duration at 30 %, 60 %, and 90 % of repolarization were measured and are shown in **Figure 3-8**. Action potential upstroke velocity was substantially reduced in  $\Delta$ KPQ, E1784K, and 1795insD compared to WT and Q1909R (**Figure 3-8: A-B**). With decreasing BCLs, particularly below 600 ms, the Q1909R upstroke velocities are reduced. AP upstroke velocity in the remaining mutants seemed to be insensitive to any BCL shortening.

Action potential durations ( $APD_x$ ,  $X=30,60,90$ ) are plotted versus the diastolic interval in **Figure 3-8: C** to create electrical restitution curves (ERCs). The plateaus of the ERC curves were increased with increasing  $APD_x$ . The greatest change in ERC as function of repolarization time was evident in E1784K compared to other variants, which displays prolonged APD at reduced diastolic intervals. In addition, the ERC slope is greatest in E1784K ( $APD_{90}$ ), suggesting heightened arrhythmogenicity.

The shifts observed in APD as a function of heart rate in all the mutants can be ascribed to the positive-staircase rise in cytosolic calcium. When the calcium-dependent gating in  $I_{Na}$  was disabled (*results not shown*),  $APD_{90}$  was less sensitive to higher pacing frequencies, suggesting a calcium-mediated effect on AP morphology in the mutants studied.

To further investigate the frequency-dependent shortening of APD, we calculated the difference in  $APD_{90}$  between successive frequencies shown in **Figure 3-8: D**. In the endocardial cell, the  $APD_{90}$  shortening displays a relatively U-type frequency dependence. E1784K exacerbates the U-type frequency dependence by prolonging greatly (**Figure 3-8: D**). This result suggests a frequency-dependent APD prolongation in E1784K.

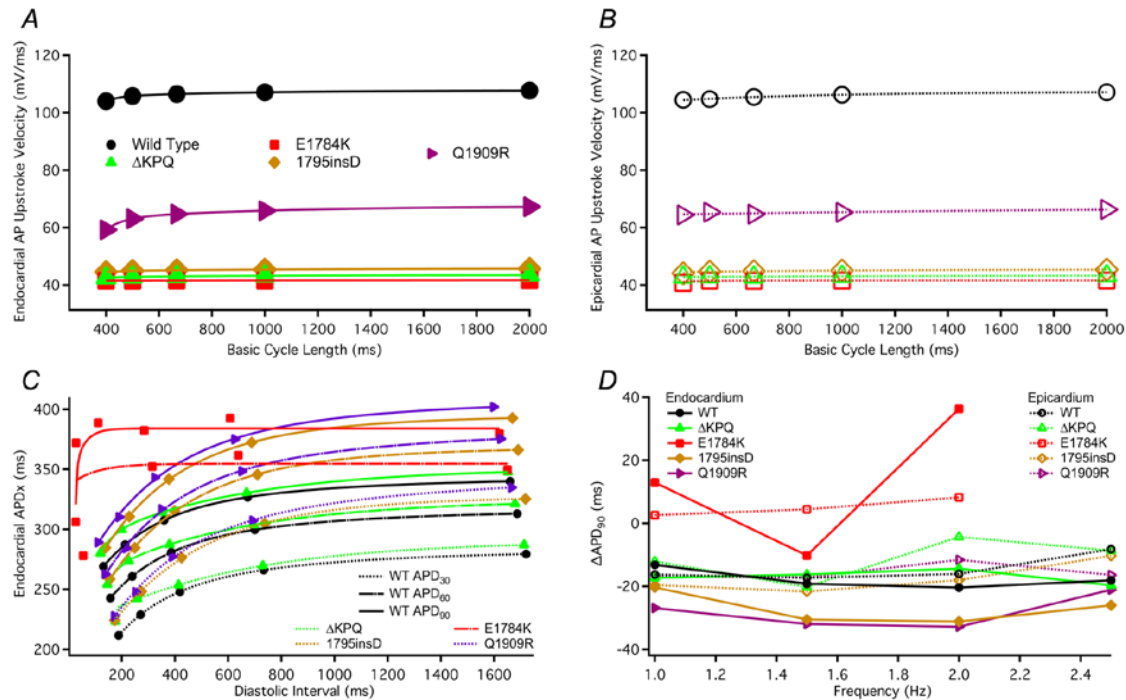


**Figure 3-8 Action potential velocity and electrical restitution curves (ERC)**  
 Panels A and B show the action potential velocity as a function of BCL. Panel C shows the ERC curve in the endocardium and Panel D shows the difference ( $\Delta$ ) in APD<sub>90</sub> as a function of frequency.

Each of the mutants characterized in this study increases the late  $I_{Na}$  compared to WT. Increases in intracellular sodium,  $[Na]_i$ , known as sodium overload, causes the sodium-calcium exchanger (NCX) to function in reverse-mode inducing a calcium-overload, which underlies cardiac diastolic dysfunction. The rise in intracellular calcium ( $[Ca^{2+}]_i$ ) during the action potential time course is shown in **Figure 3-9: A-D**. All mutants affect  $[Ca^{2+}]_i$  similar to WT, except in E1784K, which has relatively suppressed  $[Ca^{2+}]_i$  during the AP plateau and elevated  $[Ca^{2+}]_i$  during the refractory period (**Figure 3-9: A-D inset**). The  $[Na]_i^3:[Ca^{2+}]_i$  ratio was calculated for all channel variants at all frequencies and plotted against the APD<sub>90</sub> for the endocardial (**Figure 3-9: E**). The  $[Na]_i^3:[Ca^{2+}]_i$  ratio decreased in WT,  $\Delta$ KPQ, 1795insD, and Q1909R as a function of frequency. E1784K displays differential sensitivity to frequency-induced  $[Na]_i^3:[Ca^{2+}]_i$  shifts. In E1784K, the perturbations in  $[Na]_i^3:[Ca^{2+}]_i$  follow a helter-skelter manner resulting in a sodium overload at bradycardia and near tachycardia frequencies. Analysis of sodium-calcium levels at frequencies higher than 2.0 Hz in E1784K was difficult due to presence of alternans. Elevated  $[Na]_i^3:[Ca^{2+}]_i$  were sufficient to induce NCX reverse mode in the presence of alternans in E1784K (*results not shown*).

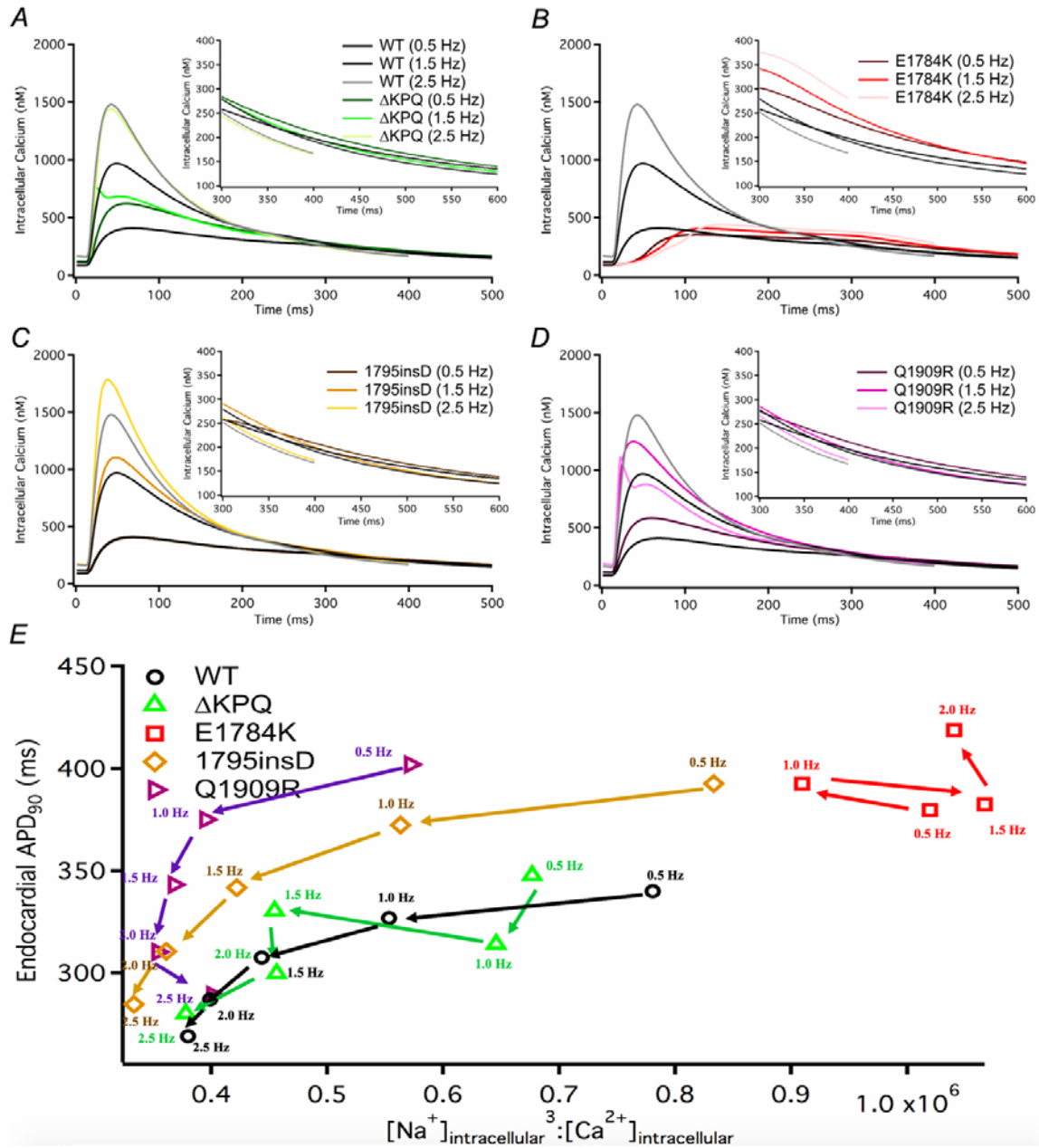


**Figure 3-9 Sodium-calcium overload**

Panels A-D show the intracellular calcium in all the channel variants at 0.5 Hz, 1.5 Hz, and 2.5 Hz simulated in endocardial cells. Panel E shows the intracellular sodium-calcium ratio as function of APD<sub>90</sub> in the endocardium.

### 3.5. Discussion

Elevated cytosolic calcium, induced by sympathetic stimulation during exercise, may serve as a potential arrhythmogenic trigger in patients with *SCN5a* mutations. The goal of our study was to explore the response of mixed syndrome mutants to elevated

cytosolic calcium. The mutants studied here have differential cytosolic calcium sensitivities. We found biophysical defects becoming either ameliorated or exacerbated by elevated cytosolic calcium in a mutant-dependent fashion.

Elevated cytosolic calcium clearly attenuates late  $I_{Na}$  in  $\Delta$ KPQ, 1795insD, and Q1909R. Since late  $I_{Na}$  is a key pathophysiological substrate in LQT3, elevated cytosolic calcium rescues the gain-of-function phenotype in those  $Na_v1.5$  mutants. In contrast, the therapeutic effect of cytosolic calcium is hampered in E1784K, suggesting carriers may express LQT3 properties under elevated heart rates. Although our experiments were performed at room temperature, we predict our results, and their phenotypic sequelae, may be exacerbated at higher temperatures since E1784K is also highly thermosensitive (Abdelsayed *et al.*, 2015). Our action potential modelling confirms that the most arrhythmogenic mutant is E1784K and predicts a large dispersion of repolarization across the ventricular wall. E1784K was the only mutant which was predicted to cause a  $[Na^+]_i$ -overload under both bradycardia and tachycardia by our model. The other mutants characterized showed decreases in  $[Na^+]_i$  with elevated heart rates. The model also predicts  $[Na^+]_i$ -overload, exacerbating E1784K arrhythmogenicity by driving NCX to run in reverse mode, further increasing cytosolic calcium. Increased cytosolic sodium and calcium results in electrical and mechanical cardiac abnormalities (Antzelevitch *et al.*, 2014).

### 3.5.1. Biophysical Implications

The DIII-DIV linker and C-terminus are crucial for both fast and slow inactivation in sodium channels. Mutations in these regions perturb their normal interaction both under diastolic calcium levels and upon a calcium signal, causing a defect in  $Na_v1.5$  inactivation. The C-terminus contains indirect binding sites for calcium (Mori *et al.*, 2003; Biswas *et al.*, 2009), including a pair of EF-hand domains composed of a helix-loop-helix, from Glu1773 to Asp1852 (comprising helices 1-4, H1-H4) Wingo *et al.*, 2004; Shah *et al.*, 2006). Approximately 120 residues downstream, an IQ domain binds to calmodulin (Tan *et al.*, 2002; Cormier *et al.*, 2002; Wingo *et al.*, 2004). The influence of calcium on inactivation has been studied using electrophysiology and isothermal titration calorimetry (ITC) experiments (Shah *et al.*, 2006; Sarhan *et al.*, 2012). Under low calcium conditions, calmodulin binds via the C-lobe to the IQ domain of the C-terminus (Chagot *et al.*, 2009). When cytosolic calcium levels rise, the calmodulin N-lobe binds to

the IQ domain and the C-lobe binds to the DIII-DIV linker, as in the tripartite complex (Shah *et al.*, 2006; Biswas *et al.*, 2009; Gaudioso *et al.*, 2011; Sarhan *et al.*, 2012).

Previous studies report intra C-terminal interactions, observed by fluorescence resonance energy transfer. The IQ motif (H6) in the C-terminus interacts with the aromatic residues of H1 (F1791 and Y1795) and the N-terminal residues of H6 interact with residues in H1-H2 and H2-H3 linkers (Glaaser *et al.*, 2006; Chagot *et al.*, 2009). Proximity of the EF-hand domain to the IQ motif is required for proper inactivation (Glaaser *et al.*, 2012). The intra C-terminal interaction associates with the DIII-DIV linker, modulating inactivation (Bankston *et al.*, 2007).

Studies supporting the tripartite complex show that residues 1498-1501 in the DIII-DIV linker form an alpha helix that interacts with the C-lobe of calmodulin, whereas the rest of the residues within the linker (1502-1522) are disordered (Sarhan *et al.*, 2012). Deletion of residues 1505-1507 in  $\Delta$ KPQ normally increases late  $I_{Na}$  and stabilizes steady-state fast inactivation at RMP (Chandra *et al.*, 1998). Stabilized inactivation may occur due to a tighter association between the truncated DIII-DIV linker and its binding site in the inner vestibule of  $Na_v1.5$ . Shortening the DIII-DIV linker in  $\Delta$ KPQ may increase the affinity for calmodulin binding upon a calcium signal. This further destabilizes fast inactivation and increases channel availability as evident in the calcium-induced depolarized shift in SSFI midpoint.

We predict the charge-reversal in E1784K disrupts crucial electrostatic interactions linking the IQ motif to the EF-hand domain, resulting in an abnormally structured C-terminus. The positive lysine may form electrostatic interactions with downstream negative charges in H1, altering the IQ-EF-hand interaction, and resulting in a loosely bound IQ. Consequently, the IQ-calmodulin complex may be more mobile and unable to modulate fast inactivation via the DIII-DIV linker, as IQ-calmodulin requires anchorage to H1 (Pitt & Lee, 2016). Since the IQ-EF-hand interaction is destabilized, calcium affinity might decrease (Shah *et al.*, 2006; Chagot *et al.*, 2009). As a result, elevations in cytosolic calcium may be unable to attenuate increases in late  $I_{Na}$  in E1784K. The fast inactivation mechanism elicited by the DIII-DIV linker is thought to function in synchrony with the C-terminus, affecting slow inactivation (Motoike, 2004). A charge-reversal mutant may uncouple both structures and thus affect the interaction between fast and slow inactivation. Consequently, the increase in E1784K late  $I_{Na}$  with

elevations in cytosolic calcium accompany destabilized slow inactivation at depolarized potentials (Featherstone *et al.*, 1998; Richmond *et al.*, 1998).

The 1795insD mutant in the EF-hand domain (H1) adds a negative charge to the region. Chagot *et al.* (2009) show that Y1795 is a key residue, establishing hydrophobic interactions with the IQ motif. Adding a negative charge may stabilize the EF-hand domain and preserve the intactness of the C-terminal interactions yielding greater sensitivity by Na<sub>v</sub>1.5 to calcium-calmodulin effects. The Q1909R mutation is in the initial segment of the IQ motif, the region that calmodulin associates with via its N-terminus during a calcium signal and via its C-lobe during diastolic calcium levels. In the IQ motif, Arginine-3 and Arginine-6 are bound by hydrogen bonds to different calmodulin residues. Thus, the introduction of an additional Arginine residue in Q1909R should enhance calmodulin binding. Fast inactivation  $\tau_{\text{onset}}$  in both 1795insD and Q1909R was decelerated at depolarized potentials in a calcium-dependent fashion, agreeing with past data showing calcium-induced deceleration of fast inactivation  $\tau_{\text{onset}}$  in WT Na<sub>v</sub>1.5 (Biswas *et al.*, 2009).

### 3.5.2. Physiological Implications

Accentuated gain-of-function in E1784K by elevated cytosolic calcium increases [Na<sup>+</sup>]<sub>i</sub>-overload. The O'Rd model simulations suggested that prolonged APDs are ameliorated by elevated pacing in  $\Delta$ KPQ, 1795insD, and Q1909R. E1784K APD is relatively prolonged, even during tachycardia. Furthermore, in all mutants except E1784K, the [Na<sup>+</sup>]<sub>i</sub>: [Ca<sup>2+</sup>]<sub>i</sub> ratio is adjusted or minimized. In E1784K, a discordant curve develops, in which the sodium overload is observed at different heart rates. Sodium overload induces multiple cellular cascades including the reverse mode in NCX, a factor known to shorten APD at elevated heart rates (Faber & Rudy, 2000; Moreau *et al.*, 2013). Reverse mode NCX causes a rise in intracellular calcium, which threatens diastolic stability resulting in diastolic dysfunction. In addition to those mechanical abnormalities, calcium overload disturbs the electrical stability of myocardial tissue by inducing DADs, increasing the likelihood of lethal cardiac events including ventricular tachycardia/fibrillation.

### 3.5.3. Clinical Implications

The effect of exercise on LQT3 is an unsettled controversial matter. Schwartz *et al.* (1995) reported a marked reduction in QT<sub>C</sub> during exercise in LQT3 patients. This effect is lost during recovery from exercise. Most of the patients in that study carried the  $\Delta$ KPQ mutation. A reduced QT<sub>C</sub> in  $\Delta$ KPQ may be explained by frequency- or calcium - dependent attenuation of late I<sub>Na</sub>. Nevertheless, a relatively minor percentage of LQT3 patients develop cardiac events during exercise. Questions remain as to whether sleep or rest without arousal (i.e. low heart rates) fully explains arrhythmogenesis in LQT3, since the REM phase of sleep is accompanied by high sympathetic tone. Thus, both sleep and exercise share some common physiological properties and may share a mechanism of arrhythmogenesis in some LQT3 cases. These commonalities raise questions about the utility of  $\beta$ -blockers as potential therapeutics for all LQT3 patients, regardless of the causative mutation. The variance seen in BrS1/LQT3 response to exercise depends, at least in part, on the exact *SCN5a* mutation. Thus, genetic screening is a critical diagnostic tool to determine whether exercise may be therapeutic or an arrhythmogenic trigger in patients with *SCN5a* mutations.

### 3.6. Conclusion

Greater calcium sensitivity in E1784K is reflected by the AP model, in which E1784K prolongs the APD. Compared to the other mutants, E1784K results in the largest transmural voltage gradient. Our results may lead to further refined treatments for BrS1/LQT3. Antiarrhythmics, potent for LQT3, should be tested in mixed syndrome cases since the propensity to be phenotypically LQT3 and/or BrS1 may be affected by triggers such as exercise. Cellular cascades, such as activation of the Ca<sup>2+</sup>/CaMKII and other protein kinases, may determine the mutant-specific biophysical effects of arrhythmogenic mutations (Herren *et al.*, 2013). This study is likely biased to the effects of calcium on predominantly phosphorylated Nav1.5 due to the use of internal fluoride, which inhibits phosphatases (Proud, 1994). Future assays should measure phosphorylation-induced shifts on gating and channel expression to further elucidate how physiological changes impact the arrhythmogenicity of these mutants. Our results support the case for more detailed biophysical analysis of all mutants underlying sudden cardiac death.

### **3.7. Acknowledgments**

The authors thank Dr. David Jones, Dr. Sam Goodchild, Mr. Colin Peters, and Mr. Mohammed-Reza Ghovanloo for their valuable input and support.

## Chapter 4. The efficacy of ranolazine on E1784K is altered by temperature and calcium

The content of this chapter has been submitted for publication in the journal of Scientific Reports.

### 4.1. Abstract

E1784K is the most common mixed syndrome *SCN5a* mutation underpinning both Brugada syndrome type 1 (BrS1) and Long-QT syndrome type 3 (LQT3). The charge reversal mutant enhances the late sodium current ( $I_{Na}$ ) passed by the cardiac voltage-gated sodium channel ( $Na_v1.5$ ), delaying cardiac repolarization. Exercise-induced triggers, like elevated temperature and cytosolic calcium, exacerbate E1784K late  $I_{Na}$ . In this study, we tested the effects of ranolazine, the late  $I_{Na}$  blocker, on voltage-dependent and kinetic properties of E1784K at elevated temperature and cytosolic calcium. We used whole-cell patch clamp to measure  $I_{Na}$  from wild type and E1784K channels expressed in HEK293 cells. At elevated temperature, ranolazine attenuated gain-of-function in E1784K by decreasing late  $I_{Na}$ , hyperpolarizing steady-state fast inactivation, and increasing channel use-dependent inactivation. Both elevated temperature and cytosolic calcium hampered the capacity of ranolazine to suppress E1784K late  $I_{Na}$ . *In-silico* action potential (AP) simulations were done using a modified O'Hara-Rudy (O'Rd) cardiac model. Simulations showed that ranolazine failed to shorten AP duration, an effect augmented at febrile temperatures. The channel/drug interaction is clearly affected by external triggers, as reported previously with ischemia. Determining drug efficacy under various physiological states in *SCN5a* cohorts is crucial for accurate management of arrhythmias.

### 4.2. Introduction

The alpha subunit of the cardiac voltage-gated sodium channel,  $Na_v1.5$ , is encoded by the *SCN5a* gene. Mutations in this gene usually cause long-QT syndrome type 3 (LQT3), Brugada syndrome type 1 (BrS1), or both (mixed syndromes) (Bezzina et al., 1999; Shimizu & Antzelevitch, 2000; Rivolta, 2001; Antzelevitch et al., 2005;

Kapplinger et al., 2010). These clinical conditions are elicited by expression of gating dysfunctions in Nav1.5 (Dumaine et al., 1996; Baroudi & Chahine, 2000; Baroudi et al., 2002; Makita et al., 2008b; Sun et al., 2011). Gain- and loss-of-function mutations can modify the inward sodium current ( $I_{Na}$ ). Gain-of-function (GoF) in Nav1.5 arises from loss in channel fast inactivation, thereby increasing the non-inactivating, late  $I_{Na}$ , underlying LQT3 (Dumaine et al., 1996, 1996; Chandra et al., 1998; Wei et al., 1999; Groenewegen et al., 2003; Bankston et al., 2007; Kwon et al., 2012; Moreau et al., 2013). Loss-of-function (LoF) mainly arises from decreased peak  $I_{Na}$  resulting in BrS1 (Bezzina et al., 1999; Veldkamp et al., 2000a; Wang et al., 2000; Baroudi & Chahine, 2000; Mok et al., 2003; Hwang et al., 2005). Interestingly, both GoF and LoF defects can occur simultaneously in a number of mutants (Wei et al., 1999; Veldkamp et al., 2000a; Baroudi & Chahine, 2000; Huang et al., 2006; Makita et al., 2008a; Postema et al., 2009; Chen et al., 2015).

A guanine to an adenine substitution at position 5349 in *SCN5a* expresses the charge reversal mutant, E1784K, in the Nav1.5 C-terminal domain (CTD) (Splawski et al., 2000; Tester et al., 2005). E1784K is the most common mixed syndrome mutant, particularly prevalent in the Okinawa Islands in Japan, where carriers mainly express diagnostic LQT3 (Takahashi et al., 2014). Clinical studies reveal differential phenotypic expressivity in E1784K cohorts (Wei et al., 1999; Deschênes et al., 2000; Makita et al., 2008a; Sumitomo, 2014).

E1784 is located directly upstream of the acidic globular EF-like hand domain ( $\alpha_1$ – $\alpha_4$ ). The residue contributes to the electrostatic interactions formed between the acidic domain and the downstream basic IQ domain ( $\alpha_6$ , **Figure 4-1** compares WT to E1784K structure) (Mantegazza et al., 2001; Cormier et al., 2002; Kim et al., 2004; Glaaser et al., 2006; Chagot et al., 2009). The proximal CTD, in which E1784K resides, has the largest effects on kinetics and steady-state inactivation (Mantegazza et al., 2001; Motoike, 2004; Glaaser et al., 2006, 2012). The charge reversal mutant, E1784K, is thought to disturb the integrity of the CTD, causing the  $\alpha_6$  to become more mobile (**Figure 4-1**) (Abdelsayed et al., 2017). A disturbance to  $\alpha_6$  integrity has been correlated with elevations in late  $I_{Na}$  and enhanced slow inactivation (Mori et al., 2003; Bankston et al., 2007; Glaaser et al., 2012; Van Petegem et al., 2012; Yan et al., 2017a), which are key biophysical attributes in E1784K (Wei et al., 1999; Deschênes et al., 2000; Makita et al., 2008a).

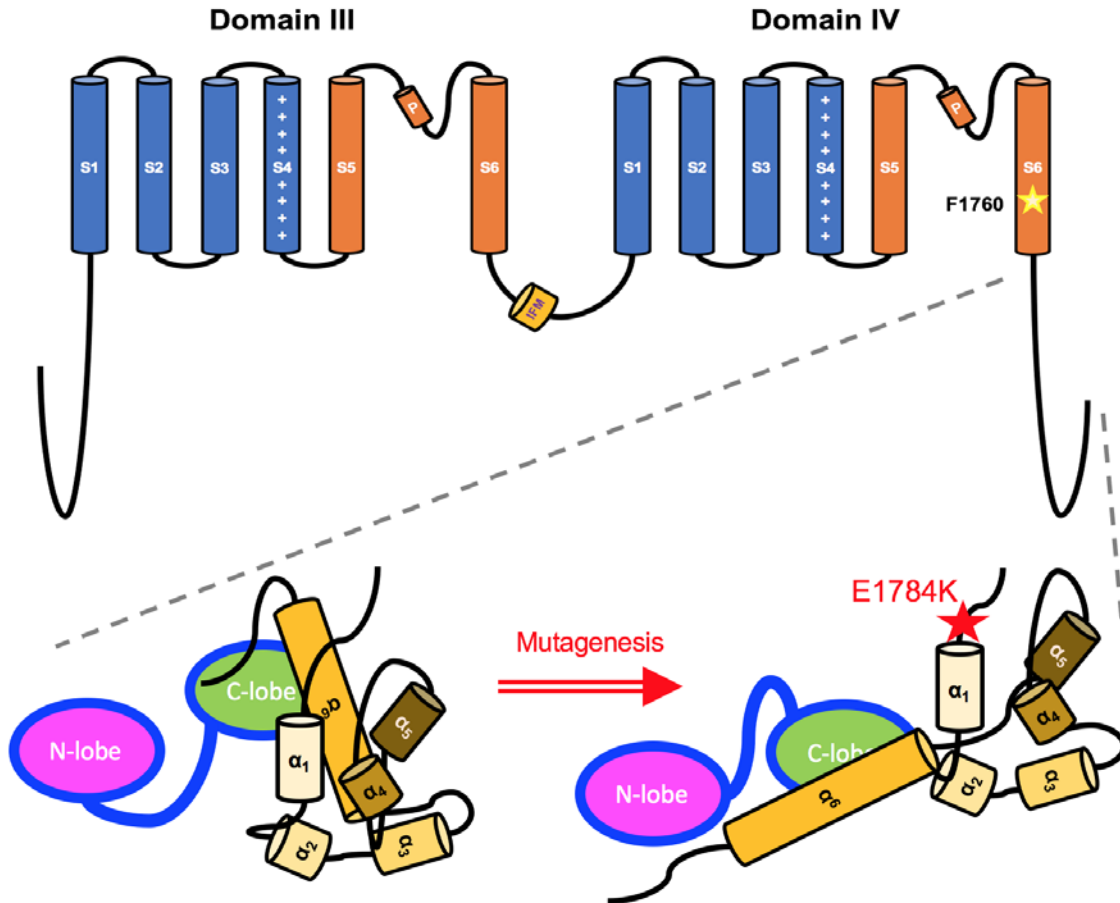


**Figure 4-1 Sodium Channel Schematic Diagram**

Domain III and Domain IV along with their inter-linker and the CTD are important in regulating channel function and calcium sensitivity. The DIII-DIV linker has the fast inactivation particle (IFM motif). DIV-S6 contains the putative drug-binding residue, F1760, which is key for binding ranolazine. The enlarged CTD contains six  $\alpha$ -helices which aggregate to form an intact domain for calmodulin binding. Calmodulin binds to the IQ-domain ( $\alpha_6$ ) under low cytosolic calcium conditions (structure adapted from Chagot *et al.*, 2009 and Gabelli *et al.*, 2014). We speculate that a disarrangement occurs in the CTD upon mutagenesis to E1784K, which may affect calmodulin interaction with other channel sites, such as the DIII-DIV linker.

Recent studies characterized the effects of exercise-induced triggers on E1784K. These triggers include acidosis, elevated temperatures and cytosolic calcium. Acidosis and elevated temperatures augment late  $I_{Na}$  and decrease peak  $I_{Na}$  in E1784K (Abdelsayed *et al.*, 2015; Peters *et al.*, 2016, 2017). Use-dependence in E1784K is reduced with high stimulation frequencies at elevated temperatures (Abdelsayed *et al.*, 2015). Compared to other mutants, E1784K tends to hamper the native potency of cytosolic calcium to block late  $I_{Na}$  in  $Na_v1.5$  (Potet *et al.*, 2015; Abdelsayed *et al.*, 2017). Elevated cytosolic calcium augments channel availability in E1784K by depolarizing the voltage-dependence of slow inactivation (Abdelsayed *et al.*, 2017). Dynamic *in silico*

action potential (AP) simulations in cardiac cells show E1784K-induced alternans at sinus rhythm and with tachycardia (Abdelsayed et al., 2015, 2017).

We hypothesize that ranolazine, which preferentially blocks late  $I_{Na}$ , is suitable for ameliorating the thermal and calcium-induced defects in E1784K. Although prescribed as an anti-anginal drug for diastolic dysfunction treatment (Antzelevitch, 2004; Antzelevitch et al., 2004; Sossalla et al., 2008), Ranolazine has antiarrhythmic efficacy proven to be useful in treating *SCN5a* inherited conditions (Moss et al., 2008; Rajamani et al., 2009; Huang et al., 2011; Sokolov et al., 2013). Ranolazine efficacy is enhanced with *SCN5a* mutations or channel triggers, such as acidosis, which augment late  $I_{Na}$  (Belardinelli, 2006a; Fredj et al., 2006b; Huang et al., 2011; Sokolov et al., 2013; Peters et al., 2013). We predicted that the channel mutation-trigger interaction may alter drug efficacy. Our goal is to study the effects of ranolazine on E1784K under conditions of elevated temperature and cytosolic calcium levels.

## 4.3. Methods

### 4.3.1. Homology Modelling and Auto-Docking

Homology modeling was performed using the Swiss-Model server (<https://swissmodel.expasy.org>) (Bordoli et al., 2008). The newly cryo-EM solved American cockroach voltage-gated sodium channel ( $Na_VPas$ ) structure (3.8-Å resolution) was used as a template against the  $Na_V1.5$  sequence. Modeling was done according to the protocol established by Bordoli et al., (2008). Sequence alignment was performed using Uniprot Align (<http://www.uniprot.org/align/>) for *SCN5A\_HUMAN* ( $Na_V1.5$ ) and *SCNA1\_PERAM* ( $Na_VPas$ ).

Ranolazine was virtually docked using AutoDock4 against the  $Na_V1.5$  homology model built on  $Na_VPas$  ( $Na_V1.5$ - $Na_VPas$ ) (Morris et al., 2009). PyMOL-pdb viewer was used for optimization and visualization of the auto-docking results.

### 4.3.2. Ethical approval

The research was approved by Biohazards review 251-2012 issued by the office of the Environmental Health and Safety at Simon Fraser University, Burnaby, BC, Canada.

### 4.3.3. Cell Culture

HEK293 cells were grown at pH 7.4 in a DMEM (1×) nutrient medium (Life Technologies, NY, USA), supplemented with 10 % FBS and maintained in a humidified environment at 37 °C with 5 % CO<sub>2</sub>. The  $\alpha$  subunits (WT or E1784K) were co-transfected with the  $\beta$ 1 subunit and green fluorescent protein, eGFP (1.50  $\mu$ g: 0.75  $\mu$ g: 1.50  $\mu$ g, respectively). The cDNA mixture was then allowed to incubate with the HEK293 cells before plating on coverslips. The HEK293 cells were selected for this study since they contain a relatively elevated [calmodulin]<sub>free</sub> level compared to other cell lines, thereby controlling for calcium-calmodulin effects on Na<sub>v</sub>1.5 (Black et al., 2004).

### 4.3.4. Electrophysiology

Whole-cell patch clamp recordings were performed in extracellular solution containing (mM): 96 NaCl, 4 KCl, 2 CaCl<sub>2</sub>, 1 MgCl<sub>2</sub>, and 10 HEPES (pH 7.4). Solutions were titrated with CsOH to pH 7.4. Pipettes were fabricated with a P-1000 puller using borosilicate glass (Sutter Instruments, CA, USA), dipped in dental wax to reduce capacitance, then thermally polished to a resistance of 1.0-1.5 M $\Omega$ . Low resistance electrodes were used to minimize series resistance between pipette and intracellular solution resulting in typical access resistances of 3.5 M $\Omega$  or less, thereby minimizing voltage measurement error. Pipettes were filled with intracellular solution. For minimal cytosolic calcium levels, pipettes contained (mM): 130 CsF, 9.6 NaCl, 10 HEPES, and 10 EGTA titrated to pH 7.4. The intracellular pipette solution was manipulated to mimic peak systolic cytosolic calcium (Steenbergen et al., 1987; Kirschenlohr et al., 2000). To do so, we calculated, using the Ca-EGTA Calculator v1.3, the amount of CaCl<sub>2</sub> (in mM) added to bring cytosolic calcium to 2500nM at both 22 °C and 34 °C: 9.53 and 9.60, respectively.

All recordings were made using an EPC-9 patch-clamp amplifier (HEKA Elektronik, Lambrecht, Germany) digitized at 20 kHz using an ITC-16 interface (HEKA Elektronik, Lambrecht, Germany). Data were acquired and low-pass-filtered (5 kHz) using PatchMaster/FitMaster software (HEKA Elektronik, Lambrecht, Germany) running on an Apple iMac (Apple Computer, Cupertino, CA). Leak subtraction was performed online using a P/4 procedure. Bath solution temperature was controlled using a Peltier device driven by a TC-10 Temperature Controller (Dagan, Minneapolis, MN). Bath temperature was maintained at 22 °C or 34 °C. Experiments were not performed at physiological temperatures because of the inherent instability of cells at temperatures above 34 °C. Using a  $Q_{10}$  relationship, which were confirmed with Arrhenius calculations, we extrapolated data to physiological temperatures (described below). After a giga-ohm seal resistance was achieved, the whole-cell configuration was attained. The holding potential between protocols was -110 mV. We recorded  $I_{Na}$  from cells that expressed currents no greater than -5 nA. The average voltage error calculated for all cells used in this study ( $n = 250$ ) is  $6.06 \text{ mV} \pm 0.40 \text{ mV}$  obtained (**Table 4-1**). There are no differences between the voltage-errors in the different conditions ( $p > 0.05$ ).

**Table 4-1 Ranolazine Voltage Error**

Condition	Voltage Error (mV)	N
WT - 22 °C - 0 nM Ca <sup>2+</sup> - 0 Ran	3.52 ± 0.97	9
WT - 22 °C - 0 nM Ca <sup>2+</sup> - 10 Ran	7.83 ± 1.47	8
WT - 22 °C - 0 nM Ca <sup>2+</sup> - 100 Ran	5.70 ± 2.05	6
WT - 22 °C - 2500 nM Ca <sup>2+</sup> - 0 Ran	4.89 ± 1.29	9
WT - 22 °C - 2500 nM Ca <sup>2+</sup> - 10 Ran	6.54 ± 1.30	11
WT - 22 °C - 2500 nM Ca <sup>2+</sup> - 100 Ran	3.12 ± 0.88	10
WT - 34 °C - 0 nM Ca <sup>2+</sup> - 0 Ran	8.35 ± 1.56	11
WT - 34 °C - 0 nM Ca <sup>2+</sup> - 10 Ran	9.08 ± 1.32	9
WT - 34 °C - 0 nM Ca <sup>2+</sup> - 100 Ran	7.18 ± 1.16	19
WT - 34 °C - 2500 nM Ca <sup>2+</sup> - 0 Ran	8.64 ± 0.98	7
WT - 34 °C - 2500 nM Ca <sup>2+</sup> - 10 Ran	8.53 ± 1.79	9
WT - 34 °C - 2500 nM Ca <sup>2+</sup> - 100 Ran	8.14 ± 1.57	6
EK - 22 °C - 0 nM Ca <sup>2+</sup> - 0 Ran	4.41 ± 0.65	19
EK - 22 °C - 0 nM Ca <sup>2+</sup> - 10 Ran	5.99 ± 1.22	10
EK - 22 °C - 0 nM Ca <sup>2+</sup> - 100 Ran	4.28 ± 0.72	14
EK - 22 °C - 2500 nM Ca <sup>2+</sup> - 0 Ran	3.01 ± 0.71	6
EK - 22 °C - 2500 nM Ca <sup>2+</sup> - 10 Ran	4.49 ± 1.04	9
EK - 22 °C - 2500 nM Ca <sup>2+</sup> - 100 Ran	4.63 ± 1.21	10
EK - 34 °C - 0 nM Ca <sup>2+</sup> - 0 Ran	6.50 ± 1.09	19
EK - 34 °C - 0 nM Ca <sup>2+</sup> - 10 Ran	6.74 ± 1.73	10
EK - 34 °C - 0 nM Ca <sup>2+</sup> - 100 Ran	5.52 ± 0.98	12
EK - 34 °C - 2500 nM Ca <sup>2+</sup> - 0 Ran	5.63 ± 1.32	8
EK - 34 °C - 2500 nM Ca <sup>2+</sup> - 10 Ran	8.95 ± 1.97	8
EK - 34 °C - 2500 nM Ca <sup>2+</sup> - 100 Ran	3.67 ± 0.69	11

### 4.3.5. Drug Preparation

Ranolazine was obtained from Gilead Sciences (Foster City, CA) in powder form, diluted to 100 mM stock in 0.1 M HCl, aliquoted at 10 mM and stored at -20°C. Working concentrations of 10 µM (therapeutic concentration) or 100 µM (non-therapeutic) were freshly prepared in bath solution. pH was readjusted before performing electrophysiological experiments. Due to the large number of experimental conditions and the challenges of maintaining whole-cell recordings at elevated temperature, we performed unmatched pair experiments.

### 4.3.6. Analysis and Statistics

Analysis and graphing were done using FitMaster software (HEKA Elektronik, Lambrecht, Germany) and Igor Pro (Wavemetrics, Lake Oswego, OR, USA) with statistical information derived using JMP statistical software. Statistical significance was

accepted at  $p < 0.05$  using a four-factor completely randomized design (CRD) ANOVA test followed by a post-hoc Tukey test. Our statistical model was a full factorial in which all the factors were allowed to interact together yielding multiple effect tests: Ranolazine, Channel Variant, Ranolazine  $\times$  Channel Variant, Temperature, Ranolazine  $\times$  Temperature, Channel Variant  $\times$  Temperature, Ranolazine  $\times$  Channel Variant  $\times$  Temperature, Calcium, Ranolazine  $\times$  Calcium, Channel Variant  $\times$  Calcium, Ranolazine  $\times$  Channel Variant  $\times$  Calcium, Temperature  $\times$  Calcium, Ranolazine  $\times$  Temperature  $\times$  Calcium, Channel Variant  $\times$  Temperature  $\times$  Calcium, Ranolazine  $\times$  Channel Variant  $\times$  Temperature  $\times$  Calcium. All values reported in the results sections are given as means  $\pm$  standard error of means.

### **4.3.7. Voltage Protocols**

#### **4.3.7.1 Current Density**

We measured current density from the ratio of current amplitude to the cell membrane capacitance (pA/pF).

#### **4.3.7.2 Conductance Density**

Channel conductance was calculated from peak  $I_{Na}$  using ohm's law at 0 mV.

$$1. G_{Na} = I_{Na} / V - E_{rev}$$

where  $G_{Na}$  is sodium channel conductance,  $I_{Na}$  is peak sodium current in response to the command potential  $V=0$  mV, and  $E_{rev}$  is the reversal potential. We measured conductance density from the ratio of conductance to the cell membrane capacitance (nS/pF).

#### **4.3.7.3 Activation (GV)**

To determine the voltage dependence of activation, we measured the peak current amplitude at test pulse potentials ranging from -100 mV to +80 mV in increments of +10 mV for 19 ms. Prior to the test pulse, channels were allowed to recover from fast inactivation at -130 mV for 197 ms. Channel conductance was calculated from peak  $I_{Na}$  using Formula (1). Calculated values for conductance were normalized to the maximal conductance and fit with the Boltzmann function:

$$2. \quad G/G_{\max} = 1/(1 + \exp[-ze_0[V_m - V_{1/2}]/kT])$$

where  $G/G_{\max}$  is the normalized conductance amplitude,  $V_m$  is the command potential,  $z$  is the apparent valence,  $e_0$  is the elementary charge,  $V_{1/2}$  is the midpoint voltage,  $k$  is the Boltzmann constant, and  $T$  is temperature in °K.

#### **4.3.7.4 Steady-State Fast Inactivation (SSFI)**

The voltage-dependence of SSFI was measured by preconditioning the channels to a hyperpolarizing potential of -130 mV and then eliciting prepulses from -130 or -150 to +10 mV in increments of 10 mV for 500 ms. Channel availability was assessed during a test pulse to 0 mV. Normalized current amplitude as a function of voltage was fit using the Boltzmann function:

$$3. \quad I/I_{\max} = 1/(1 + \exp(-ze_0 (V_M - V_{1/2})/kT))$$

where  $I/I_{\max}$  is the normalized current amplitude,  $z$  is apparent valence,  $e_0$  is the elementary charge,  $V_m$  is the prepulse potential,  $V_{1/2}$  is the midpoint voltage of SSFI,  $k$  is the Boltzmann constant, and  $T$  is temperature in °K.

#### **4.3.7.5 Fast Inactivation Onset**

Time constants for open-state fast inactivation were derived by fitting a single exponential function to the decay of current obtained from the activation protocol.

$$4. \quad I = I_{ss} + \alpha \exp(-(t-t_0)/\tau)$$

where  $I$  is current amplitude,  $I_{ss}$  is the plateau amplitude,  $\alpha$  is the amplitude at time 0 for time constant  $\tau$ , and  $t$  is time.

#### **4.3.7.6 Late $I_{Na}$ Current**

Late  $I_{Na}$  was measured between 40 – 50 ms during a 50 ms depolarizing pulse to 0 mV from a holding potential of -130 mV. An average of 10 pulses was used to increase the signal-to-noise ratio.

#### **4.3.7.7 Use-Dependent Inactivation (UDI, 1 Hz and 3 Hz)**

Channels accumulated into a use-dependent inactivated state during either a series of 300 380 ms depolarizing pulses to 0 mV followed by a 615 ms – 110 mV

recovery pulse at a frequency 1 Hz, or 500 220 ms depolarizing pulses to 0 mV followed by a 110 ms – 110 mV recovery pulse at a frequency 3 Hz. Normalized current amplitude as a function of time was fit with a double exponential.

$$5. I = I_{ss} + \alpha_1 \exp(-t/\tau_1) + \alpha_2 \exp(-t/\tau_2)$$

where I is current amplitude,  $I_{ss}$  is the plateau amplitude,  $\alpha_1$  and  $\alpha_2$  are the amplitudes at time 0 for time constants  $\tau_1$  and  $\tau_2$ , and t is time.

#### **4.3.7.8 $Q_{10}$ Coefficients**

The temperature coefficient for kinetic and thermodynamic parameters plotted as a function temperature was calculated in Igor:

$$6. Q_{10} = (R_2/R_1)^{10/(T_2-T_1)}$$

where R is the rate and T is temperature (1 and 2 are the two temperatures measured). Rate was calculated by the inverse of the  $\tau$  value.  $Q_{10}$  fits for steady-state midpoints and slopes were calculated by replacing the  $R_x$  with  $V_{1/2}$  and z values. Fits for  $y_0$  were calculated based of the  $1/y_0$  to yield optimal  $Q_{10}$  values. The fit was extrapolated to physiological (37 °C) and febrile (41 °C) temperatures.

#### **4.3.7.9 Arrhenius Calculations**

The Arrhenius linear relationship for the natural exponent of kinetic or thermodynamic parameters as a function of inverse temperature was calculated in Igor:

$$7. \ln(k) = \ln(A) - (E_a/R) \times (1/T)$$

where k is the rate constant, steady-state midpoint, or slope, A is the pre-exponential factor,  $E_a$  is the activation energy, R is the universal gas constant, and T is temperature in °K.

### **4.3.8. Myocardial Action Potential (AP) Modeling**

#### **4.3.8.1 Simulations**

Action potentials were simulated using a modified version of the O'Hara-Rudy (O'Rd) model at 37 °C and 41 °C programmed in Matlab (O'Hara et al., 2011). The

sodium data were extrapolated to physiological and febrile temperatures  $Q_{10}$  values for WT and E1784K at 0  $\mu$ M and 10  $\mu$ M ranolazine. The maximal  $G_{Na}$  density was 150 mS/ $\mu$ F in all conditions simulated. We modified the gating  $I_{Na}$  parameters data in accordance with our biophysical data for the various conditions. The GV and SSFI midpoints and slopes were extrapolated to 37 °C and 41 °C and normalized to the original O’Rd parameters. The phosphorylated steady-state fast inactivation midpoints in all channel variants were equally hyperpolarized by 6.2 mV. Late  $I_{Na}$  density was normalized to the original O’Rd value and multiplied by the percentage of late to peak  $I_{Na}$  calculated above.

To model the calcium-dependence of our late  $I_{Na}$  data, we fit the biophysical parameters extrapolated to 37 °C and 41 °C with a Hill equation:

$$8. \quad Z = Y_0 + (Y_M - Y_0) / (1 + (X_{1/2}/X)^b)$$

where Z is the biophysical parameter of interest,  $Y_0$  is the minimum value,  $Y_M$  is the maximum value,  $X_{1/2}$  is the midpoint of the curve, X is the intracellular cytosolic calcium, b is the rate.

Subspace calcium was not accounted for due to the lack of experimental data. Thus, the modified O’Rd model is a dynamic simulation of the calcium-induced shifts which are observed with increasing intracellular calcium levels as a function of pacing frequency, comprising the positive staircase phenomenon (Kort et al., 1985; Song et al., 2001).

Simulations at febrile temperature (41 °C) included modifications to the major ionic currents,  $I_{Kto}$  (Yang & Zheng, 2014),  $I_{CaL}$  (ten Tüsscher, 2003; Radzicki et al., 2013),  $I_{Kr}$  (Mauerhöfer & Bauer, 2016), and  $I_{Ks}$  (G. et al., 2001), in the O’Rd model based on previously published  $Q_{10}$  values.

Simulations were run on endocardial, midmyocardial, and epicardial ventricular myocytes using a 0.5 ms stimulus pulse with an amplitude of -80  $\mu$ A/ $\mu$ F. The stimulus protocol was designed to step up the frequency gradually from 0.5 Hz to 2.5 Hz, with 1000 beats per frequency step to ensure attainment of steady-state.

#### 4.3.8.2 Analysis

Analysis of APs only included those that fully recovered and were restored to baseline. Action potential duration (APD) was measured at 90 % of repolarization by multiplying the resting membrane potential (RMP) value, prior to the current stimulus pulse, by 0.9. The APD<sub>90</sub> of the final two beats in the frequency step were plotted versus the diastolic interval (DI = BCL – APD<sub>90</sub>), where BCL is the basic cycle length, creating electrical restitution curves.

### 4.4. Results

#### 4.4.1. Ranolazine binds to Nav1.5 inner vestibule

The Nav<sub>v</sub>1.5 homology model based on Nav<sub>v</sub>Pas (Nav<sub>v</sub>1.5-Nav<sub>v</sub>Pas) is shown in **Figure 4-2**. The side view of the channel shows the four domains and their putative voltage and pore-forming segments (including the p-helices, extracellular and intracellular linkers). Nav<sub>v</sub>Pas shares about 32 % sequence identity with Nav<sub>v</sub>1.5. The aligned the DIII-DIV linker and the CTD are shown in **Figure 4-2**. Ranolazine was auto-docked against Nav<sub>v</sub>1.5-Nav<sub>v</sub>Pas using AutoDock4. The highest affinity (-7.7 kcal/mol) binding mode is enlarged in **Figure 4-2**. The compound formed polar and Van der Waals interaction with various residues located in all four domains: S401, V405, C896, N927, F1418, S1458, L1462, N1463, I1466, F1760, V1764, I1768. The aromatic residue, F1760, is outlined in **Figure 4-2** as it is a key putative binding site for many anti-arrhythmics, local anesthetics, and anticonvulsants (Fredj et al., 2006b; Lipkind & Fozzard, 2010). F1760 orientation with respect to ranolazine confirms its critical role in drug binding.

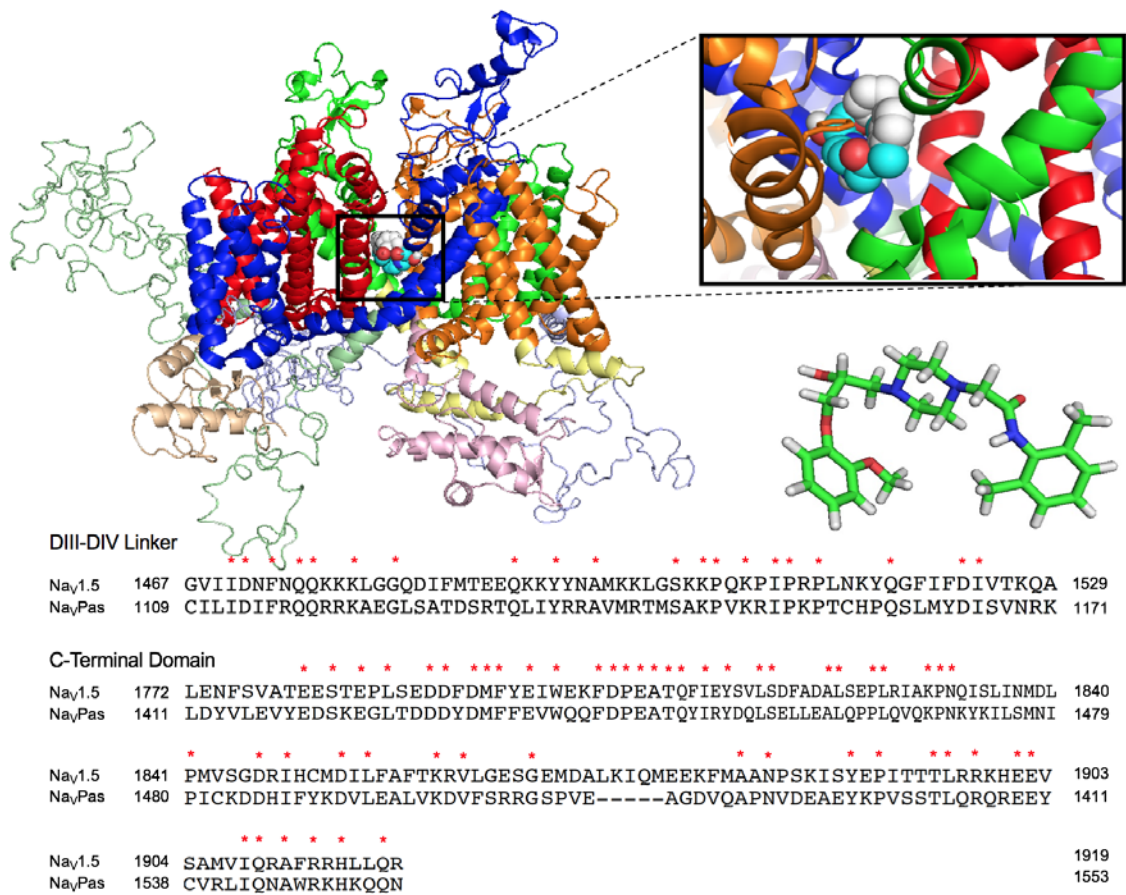


**Figure 4-2 Ranolazine docked to Nav1.5-NaVPas**

The side view of Nav1.5-NaVPas homology model is shown docked to ranolazine. The enlarged inset shows the cartoon structure of the drug binding to the central domains of the channel. The aromatic F1760 residue is outlined. Below the inset is a 3D-structure of ranolazine (Nitrogen is blue, Oxygen is red, Carbon is green, and Hydrogen is grey). Conserved residues in the DIII-DIV linker and the CTD between Nav1.5 and NaVPas are indicated by a red asterisk.

**4.4.2. Ranolazine does not affect conductance**

Raw current traces in **Figure 4-3** show the effects of 0  $\mu$ M and 100  $\mu$ M ranolazine on WT and E1784K at 0 nM and 2500 nM cytosolic calcium (only 34  $^{\circ}$ C shown). E1784K reduced ( $p < 0.0001$ ) the peak current and conductance density compared to WT. Elevated temperature (34  $^{\circ}$ C) increased ( $p < 0.0001$ ) peak current and conductance density in WT but not in E1784K. Ranolazine had no effect ( $p > 0.05$ ) on peak current or conductance density (**Table 4-2 and Figure 4-3: B**).

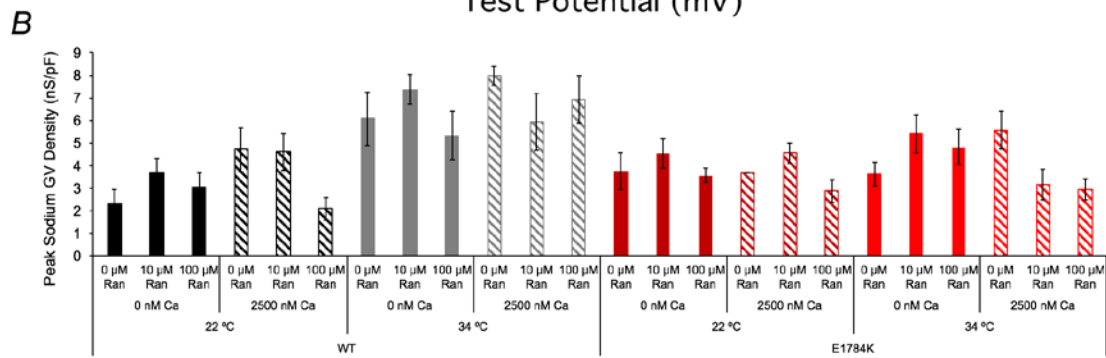
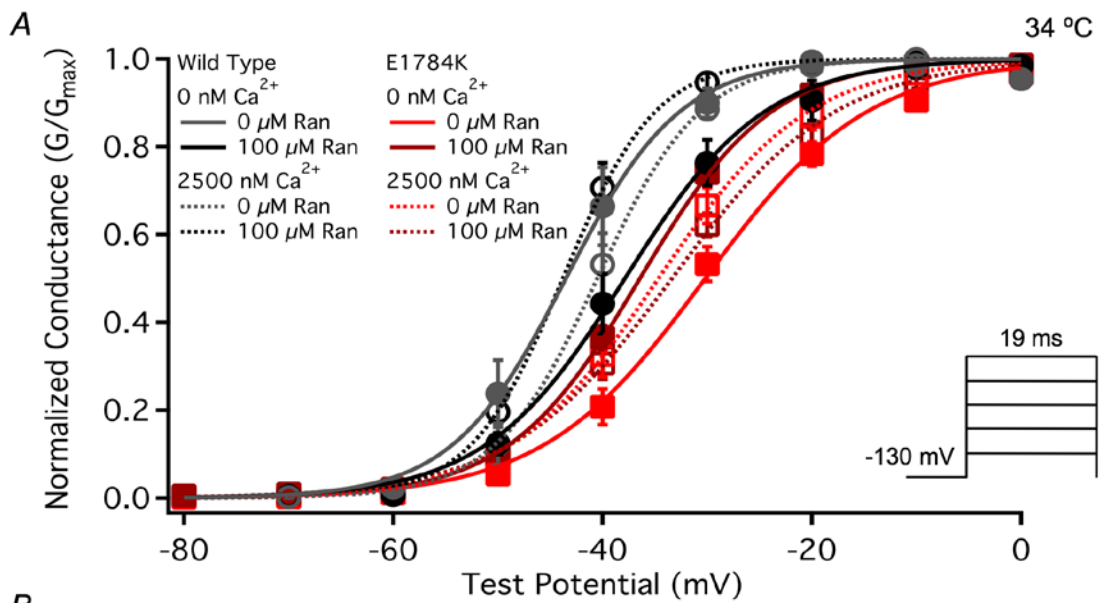
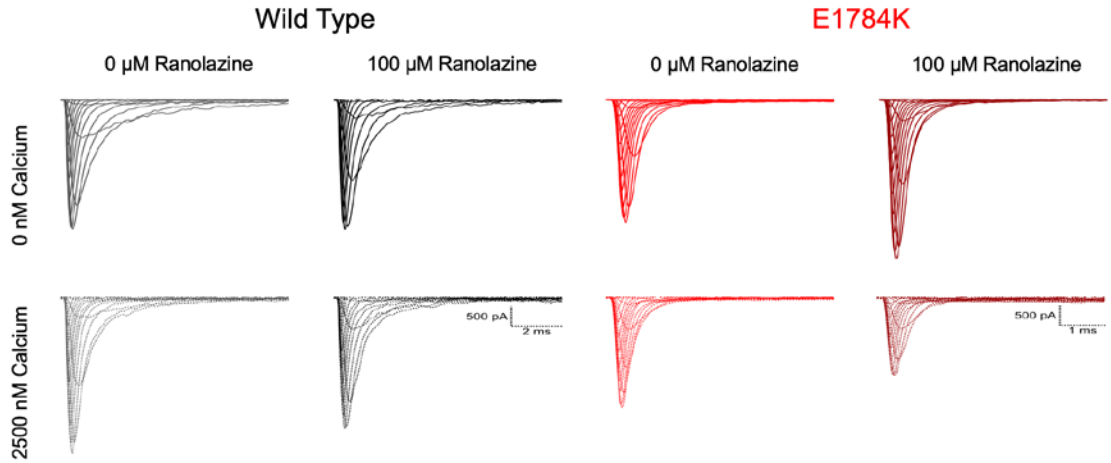


**Figure 4-3 Ranolazine effects on channel conductance.**

Top traces show raw  $I_{\text{Na}}$  traces recorded at 34 °C. Panel A shows normalized conductance plotted against the test potential (pulse protocol shown in *inset*) at 34 °C. Panel B shows the peak conductance density bar graph versus all conditions at both 22 °C and 34 °C.

**Table 4-2 Ranolazine Peak Current and Conductance Densities**

Condition	Peak I Density (pA/pF)	N	Peak GV Density (pS/pF)	N
WT - 22 °C - 0 nM Ca <sup>2+</sup> - 0 Ran	148.97 ± 35.10	7	2348.13 ± 584.87	7
WT - 22 °C - 0 nM Ca <sup>2+</sup> - 10 Ran	241.31 ± 41.80	5	3708.29 ± 580.79	5
WT - 22 °C - 0 nM Ca <sup>2+</sup> - 100 Ran	184.16 ± 40.16	5	3030.10 ± 640.76	5
WT - 22 °C - 2500 nM Ca <sup>2+</sup> - 0 Ran	302.91 ± 59.07	9	4714.99 ± 971.64	9
WT - 22 °C - 2500 nM Ca <sup>2+</sup> - 10 Ran	250.88 ± 45.34	7	4599.97 ± 788.18	7
WT - 22 °C - 2500 nM Ca <sup>2+</sup> - 100 Ran	128.74 ± 34.69	9	2088.79 ± 517.47	9
WT - 34 °C - 0 nM Ca <sup>2+</sup> - 0 Ran	354.74 ± 83.12	7	6067.75 ± 1197.96	6
WT - 34 °C - 0 nM Ca <sup>2+</sup> - 10 Ran	472.24 ± 55.47	5	7370.72 ± 654.58	7
WT - 34 °C - 0 nM Ca <sup>2+</sup> - 100 Ran	369.56 ± 81.13	8	5321.49 ± 1074.25	8
WT - 34 °C - 2500 nM Ca <sup>2+</sup> - 0 Ran	535.63 ± 70.44	6	7979.56 ± 433.11	5
WT - 34 °C - 2500 nM Ca <sup>2+</sup> - 10 Ran	447.46 ± 106.69	6	5948.51 ± 1253.7	6
WT - 34 °C - 2500 nM Ca <sup>2+</sup> - 100 Ran	599.72 ± 113.81	6	6935.36 ± 1048.34	5
EK - 22 °C - 0 nM Ca <sup>2+</sup> - 0 Ran	214.56 ± 50.18	7	3762.09 ± 835.36	7
EK - 22 °C - 0 nM Ca <sup>2+</sup> - 10 Ran	265.65 ± 51.36	8	4534.15 ± 651.10	10
EK - 22 °C - 0 nM Ca <sup>2+</sup> - 100 Ran	240.86 ± 24.43	7	3576.84 ± 301.37	7
EK - 22 °C - 2500 nM Ca <sup>2+</sup> - 0 Ran	170.41 ± 31.44	5	3660.43 ± 1006.25	6
EK - 22 °C - 2500 nM Ca <sup>2+</sup> - 10 Ran	250.36 ± 33.96	6	4562.87 ± 453.93	8
EK - 22 °C - 2500 nM Ca <sup>2+</sup> - 100 Ran	183.02 ± 44.18	5	2886.72 ± 498.80	5
EK - 34 °C - 0 nM Ca <sup>2+</sup> - 0 Ran	257.99 ± 34.07	8	3613.63 ± 524.71	9
EK - 34 °C - 0 nM Ca <sup>2+</sup> - 10 Ran	322.26 ± 47.45	6	5422.63 ± 833.24	8
EK - 34 °C - 0 nM Ca <sup>2+</sup> - 100 Ran	278.25 ± 67.75	8	4834.84 ± 766.20	7
EK - 34 °C - 2500 nM Ca <sup>2+</sup> - 0 Ran	354.25 ± 64.03	8	5587.74 ± 831.96	7
EK - 34 °C - 2500 nM Ca <sup>2+</sup> - 10 Ran	227.98 ± 41.82	5	3154.90 ± 685.41	5
EK - 34 °C - 2500 nM Ca <sup>2+</sup> - 100 Ran	212.41 ± 28.73	9	2959.51 ± 471.73	9

**Figure 4-3: A** shows normalized conductance plotted against the test potential at 34 °C. E1784K ( $p < 0.0001$ ) and elevated temperature ( $p = 0.0003$ ) depolarized the conductance midpoint ( $GV - V_{1/2}$ ). The conductance slope ( $GV - z$ ) was reduced ( $p < 0.0001$ ) in E1784K compared to WT and increased ( $p < 0.0001$ ) when temperature was elevated in both channel variants. The interaction between channel variant and temperature had no effect on  $GV - V_{1/2}$  and  $GV - z$ . Normalized conductance was unchanged in all conditions with ranolazine (**Table 4-3**).

**Table 4-3 Ranolazine Conductance and Steady-State Fast Inactivation**

Condition	GV-V <sub>1/2</sub> (mV)	GV-z	N	SSFI-V <sub>1/2</sub> (mV)	SSFI-z	N
WT - 22 °C - 0 nM Ca <sup>2+</sup> - 0 Ran	-40.45 ± 1.24	3.76 ± 0.33	7	-88.62 ± 1.99	-3.93 ± 0.26	7
WT - 22 °C - 0 nM Ca <sup>2+</sup> - 10 Ran	-45.59 ± 1.09	5.37 ± 0.29	6	-86.51 ± 1.36	-3.95 ± 0.16	7
WT - 22 °C - 0 nM Ca <sup>2+</sup> - 100 Ran	-44.13 ± 3.07	4.84 ± 0.56	5	-88.45 ± 3.18	-2.87 ± 0.11 <sup>2</sup>	6
WT - 22 °C - 2500 nM Ca <sup>2+</sup> - 0 Ran	-42.22 ± 1.16	4.08 ± 0.25	9	-91.72 ± 1.72	-3.68 ± 0.15	9
WT - 22 °C - 2500 nM Ca <sup>2+</sup> - 10 Ran	-44.40 ± 2.22	3.87 ± 0.28	7	-91.44 ± 1.63	-3.93 ± 0.18	7
WT - 22 °C - 2500 nM Ca <sup>2+</sup> - 100 Ran	-44.76 ± 2.09	4.38 ± 0.36	9	-90.94 ± 1.64	-2.20 ± 0.13 <sup>2</sup>	7
WT - 34 °C - 0 nM Ca <sup>2+</sup> - 0 Ran	-43.44 ± 2.06	6.00 ± 0.45	6	-80.31 ± 1.17	-4.72 ± 0.18	6
WT - 34 °C - 0 nM Ca <sup>2+</sup> - 10 Ran	-37.93 ± 1.97	4.95 ± 0.28	7	-82.51 ± 2.26	-4.00 ± 0.14	8
WT - 34 °C - 0 nM Ca <sup>2+</sup> - 100 Ran	-37.58 ± 2.03	4.43 ± 0.33	7	-87.30 ± 2.73	-2.82 ± 0.16 <sup>2</sup>	7
WT - 34 °C - 2500 nM Ca <sup>2+</sup> - 0 Ran	-40.62 ± 1.44	5.96 ± 0.35	6	-80.25 ± 2.30	-4.24 ± 0.08	7
WT - 34 °C - 2500 nM Ca <sup>2+</sup> - 10 Ran	-38.03 ± 3.69	5.15 ± 0.40	6	-83.18 ± 3.95	-4.00 ± 0.13	6
WT - 34 °C - 2500 nM Ca <sup>2+</sup> - 100 Ran	-43.69 ± 0.98	6.30 ± 0.48	6	-90.43 ± 2.80	-3.18 ± 0.2 <sup>2</sup>	6
EK - 22 °C - 0 nM Ca <sup>2+</sup> - 0 Ran	-35.13 ± 2.70	2.99 ± 0.27	8	-100.46 ± 1.51	-2.97 ± 0.08	8
EK - 22 °C - 0 nM Ca <sup>2+</sup> - 10 Ran	-35.83 ± 1.65	3.14 ± 0.27	10	-99.37 ± 1.61	-2.88 ± 0.08	10
EK - 22 °C - 0 nM Ca <sup>2+</sup> - 100 Ran	-36.16 ± 1.87	3.95 ± 0.17	7	-103.83 ± 2.42	-1.77 ± 0.06 <sup>2</sup>	8
EK - 22 °C - 2500 nM Ca <sup>2+</sup> - 0 Ran	-39.33 ± 2.02	3.09 ± 0.16	5	-101.30 ± 3.14	-3.07 ± 0.21	6
EK - 22 °C - 2500 nM Ca <sup>2+</sup> - 10 Ran	-34.88 ± 1.57	2.83 ± 0.15	8	-100.76 ± 1.83	-3.11 ± 0.13	8
EK - 22 °C - 2500 nM Ca <sup>2+</sup> - 100 Ran	-33.72 ± 1.52	3.02 ± 0.35	5	-106.45 ± 2.29	-2.12 ± 0.08 <sup>2</sup>	5
EK - 34 °C - 0 nM Ca <sup>2+</sup> - 0 Ran	-30.22 ± 1.27	3.68 ± 0.28	9	-91.02 ± 2.79	-3.18 ± 0.14	9
EK - 34 °C - 0 nM Ca <sup>2+</sup> - 10 Ran	-36.80 ± 1.20	4.31 ± 0.38	9	-94.20 ± 3.73	-3.14 ± 0.13	9
EK - 34 °C - 0 nM Ca <sup>2+</sup> - 100 Ran	-35.53 ± 1.18	4.11 ± 0.22	8	-105.48 ± 1.64 <sup>1</sup>	-2.07 ± 0.07 <sup>2</sup>	8
EK - 34 °C - 2500 nM Ca <sup>2+</sup> - 0 Ran	-34.74 ± 1.48	4.06 ± 0.41	8	-96.78 ± 4.70	-3.26 ± 0.12	8
EK - 34 °C - 2500 nM Ca <sup>2+</sup> - 10 Ran	-31.25 ± 2.04	3.92 ± 0.35	7	-95.01 ± 3.23	-2.94 ± 0.15	7
EK - 34 °C - 2500 nM Ca <sup>2+</sup> - 100 Ran	-32.33 ± 1.64	3.39 ± 0.15	9	-105.73 ± 2.44	-2.00 ± 0.06 <sup>2</sup>	10

<sup>1</sup>p<0.01 and <sup>2</sup>p<0.05 vs 0 μM and 10 μM Ran of same condition

#### 4.4.3. E1784K availability is decreased in ranolazine

Normalized current is plotted against membrane potential in **Figure 4-4**. E1784K hyperpolarized ( $p < 0.0001$ ) the SSFI midpoint (SSFI- $V_{1/2}$ ) compared to WT. Elevated temperature depolarized ( $p < 0.0001$ ) SSFI- $V_{1/2}$  in both WT and E1784K. At 34 °C and 0 nM cytosolic calcium, SSFI- $V_{1/2}$  in E1784K was hyperpolarized ( $p < 0.0001$ ) in 100  $\mu$ M ranolazine compared to WT (**Figure 4-4: C and Table 4-3**). This effect was not significant at 2500 nM cytosolic calcium. Analogous to the shifts on GV-z, SSFI-z was decreased in E1784K and increased with elevated temperature ( $p < 0.0001$ ). The slope was reduced in all conditions when ranolazine was increased from 10  $\mu$ M to 100  $\mu$ M ( $p < 0.05$ , **Table 4-3**).

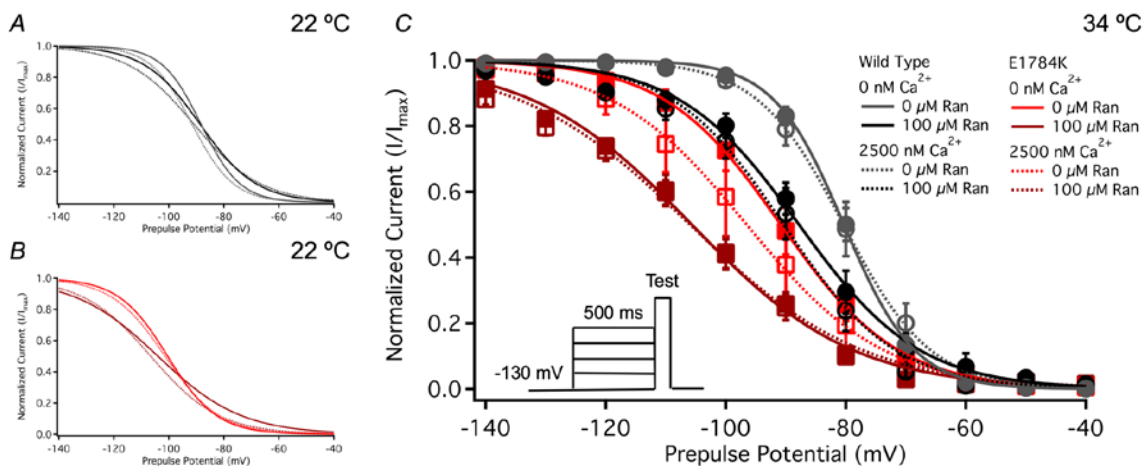


**Figure 4-4** Ranolazine effects on steady-state fast inactivation.

Panels A-B (22 °C) and C (34 °C) shows steady-state fast inactivation as normalized current plotted against the prepulse potential (pulse protocol shown in C *inset*).

#### 4.4.4. Fast inactivation onset kinetics are not altered with ranolazine

Fast inactivation onset kinetics at depolarized potentials ( $> -50$  mV) were measured from  $\tau_{on}$  of the mono-exponential fits. E1784K fast inactivation onset kinetics were accelerated regardless of temperature (**Figure 4-5: A-B**). Onset kinetics were accelerated (decreased  $\tau_{on}$ ) with elevated temperature in WT compared to E1784K ( $p < 0.01$ ). WT and E1784K onset kinetics were decelerated (increased  $\tau_{on}$ ,  $p < 0.05$ ) in ranolazine as a function of voltage and cytosolic calcium at 22 °C (values reported in **Table 4-4**). These drug effects on  $\tau_{on}$  were not significant at elevated temperature.

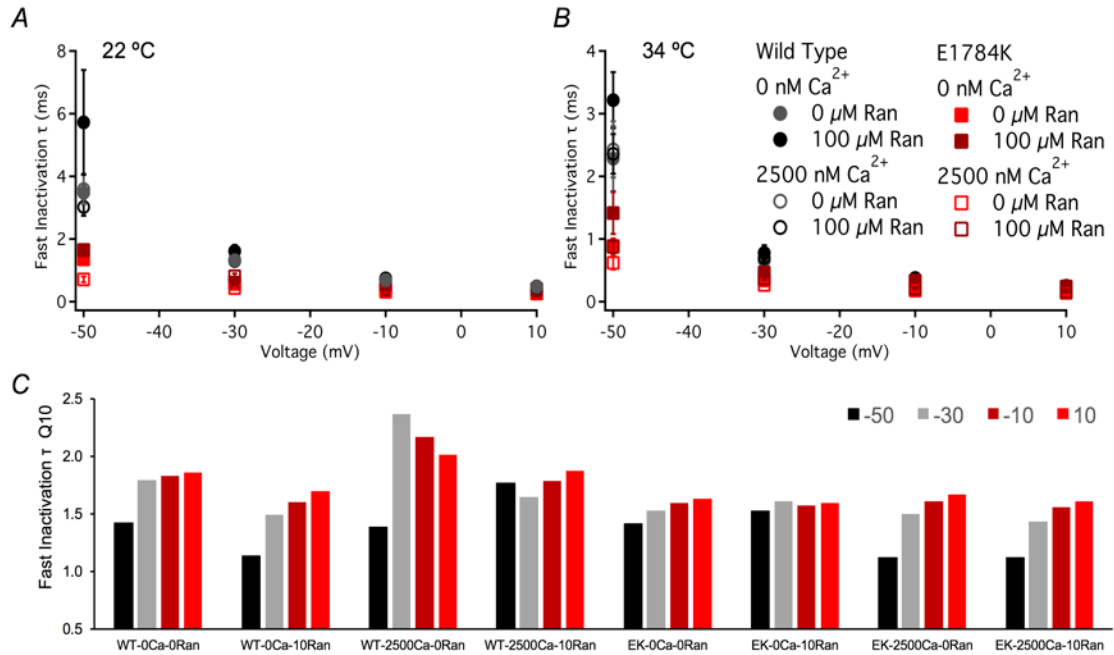


**Figure 4-5 Ranolazine effects on fast inactivation onset time constants.**

Panels A-B show the single-exponential time constants plotted against voltage. The pulse protocol is identical to that used to measure channel conductance (refer to **Methods 4.3.7.3**). Panel C includes Q<sub>10</sub> coefficient values for all conditions between -50 mV to +10 mV. Elevated cytosolic calcium seems to modulate ranolazine effects on WT Q<sub>10</sub>, as elevated cytosolic calcium heightened thermosensitivity in drug at -50 mV. E1784K thermosensitivity is dampened in elevated cytosolic at -50 mV.

**Table 4-4 Ranolazine Fast Inactivation Onset Kinetics**

Condition	-50 mV $\tau$ (ms)	-30 mV $\tau$ (ms)	-10 mV $\tau$ (ms)	+10 mV $\tau$ (ms)	N
WT - 22 °C - 0 nM Ca <sup>2+</sup> - 0 Ran	3.47 ± 0.22	1.32 ± 0.11	0.69 ± 0.07	0.48 ± 0.04	7
WT - 22 °C - 0 nM Ca <sup>2+</sup> - 10 Ran	3.28 ± 0.45	1.13 ± 0.06	0.61 ± 0.04	0.44 ± 0.03	5
WT - 22 °C - 0 nM Ca <sup>2+</sup> - 100 Ran	5.72 ± 1.67 <sup>*1</sup>	1.61 ± 0.20 <sup>*2</sup>	0.74 ± 0.06	0.46 ± 0.03	5
WT - 22 °C - 2500 nM Ca <sup>2+</sup> - 0 Ran	3.59 ± 0.49	1.34 ± 0.12	0.69 ± 0.03	0.47 ± 0.01	8
WT - 22 °C - 2500 nM Ca <sup>2+</sup> - 10 Ran	3.03 ± 0.13	1.09 ± 0.05	0.58 ± 0.01	0.42 ± 0.01	6
WT - 22 °C - 2500 nM Ca <sup>2+</sup> - 100 Ran	3.02 ± 0.28	1.30 ± 0.09	0.71 ± 0.05	0.49 ± 0.04	9
WT - 34 °C - 0 nM Ca <sup>2+</sup> - 0 Ran	2.28 ± 0.52	0.66 ± 0.07	0.34 ± 0.02	0.23 ± 0.01	5
WT - 34 °C - 0 nM Ca <sup>2+</sup> - 10 Ran	2.82 ± 0.46	0.70 ± 0.08	0.35 ± 0.04	0.23 ± 0.02	7
WT - 34 °C - 0 nM Ca <sup>2+</sup> - 100 Ran	3.22 ± 0.45	0.78 ± 0.12	0.38 ± 0.06	0.22 ± 0.02	5
WT - 34 °C - 2500 nM Ca <sup>2+</sup> - 0 Ran	2.43 ± 0.45	0.48 ± 0.04	0.27 ± 0.01	0.20 ± 0.01	6
WT - 34 °C - 2500 nM Ca <sup>2+</sup> - 10 Ran	1.53 ± 0.24	0.60 ± 0.10	0.29 ± 0.03	0.20 ± 0.02	4
WT - 34 °C - 2500 nM Ca <sup>2+</sup> - 100 Ran	2.36 ± 0.32	0.69 ± 0.08	0.38 ± 0.04	0.25 ± 0.02	6
EK - 22 °C - 0 nM Ca <sup>2+</sup> - 0 Ran	1.35 ± 0.14	0.57 ± 0.03	0.40 ± 0.02	0.33 ± 0.02	7
EK - 22 °C - 0 nM Ca <sup>2+</sup> - 10 Ran	1.46 ± 0.17	0.54 ± 0.03	0.36 ± 0.02	0.30 ± 0.02	10
EK - 22 °C - 0 nM Ca <sup>2+</sup> - 100 Ran	1.65 ± 0.16	0.61 ± 0.03	0.37 ± 0.01	0.29 ± 0.01	6
EK - 22 °C - 2500 nM Ca <sup>2+</sup> - 0 Ran	0.71 ± 0.09	0.44 ± 0.02	0.32 ± 0.01	0.26 ± 0.01	6
EK - 22 °C - 2500 nM Ca <sup>2+</sup> - 10 Ran	1.23 ± 0.09	0.54 ± 0.03	0.37 ± 0.01	0.30 ± 0.01	7
EK - 22 °C - 2500 nM Ca <sup>2+</sup> - 100 Ran	1.65 ± 0.13	0.81 ± 0.09	0.54 ± 0.06 <sup>*3</sup>	0.40 ± 0.03 <sup>*4</sup>	5
EK - 34 °C - 0 nM Ca <sup>2+</sup> - 0 Ran	0.89 ± 0.12	0.34 ± 0.02	0.23 ± 0.02	0.18 ± 0.01	9
EK - 34 °C - 0 nM Ca <sup>2+</sup> - 10 Ran	0.88 ± 0.11	0.30 ± 0.02	0.21 ± 0.01	0.17 ± 0.01	9
EK - 34 °C - 0 nM Ca <sup>2+</sup> - 100 Ran	1.41 ± 0.34	0.47 ± 0.09	0.34 ± 0.07	0.24 ± 0.05	8
EK - 34 °C - 2500 nM Ca <sup>2+</sup> - 0 Ran	0.62 ± 0.11	0.27 ± 0.02	0.18 ± 0.01	0.14 ± 0.01	9
EK - 34 °C - 2500 nM Ca <sup>2+</sup> - 10 Ran	1.08 ± 0.07	0.35 ± 0.05	0.22 ± 0.02	0.17 ± 0.01	6
EK - 34 °C - 2500 nM Ca <sup>2+</sup> - 100 Ran	0.88 ± 0.11	0.37 ± 0.02	0.21 ± 0.01	0.16 ± 0.01	8

<sup>\*1</sup> p<0.05 vs 0  $\mu$ M and 10  $\mu$ M Ran of same condition, <sup>\*2</sup> p<0.05 vs 10  $\mu$ M Ran of same condition, <sup>\*3</sup> p<0.01 and <sup>\*4</sup> p<0.05 vs 0  $\mu$ M Ran of same condition

**Figure 4-5: C** shows the Q<sub>10</sub> values at 0  $\mu$ M and 10  $\mu$ M ranolazine for all conditions. We observed high variability in the temperature coefficient at -50 mV compared to other voltages. At -50 mV, both ranolazine and cytosolic calcium mutually affect thermosensitivity in WT: Q<sub>10</sub> decreased at 0 nM cytosolic calcium and increased at 2500 nM cytosolic calcium in 10  $\mu$ M ranolazine. At more depolarized voltages than -50 mV, subtle alterations occurred in WT Q<sub>10</sub> (**Figure 4-5: C**). E1784K Q<sub>10</sub> was not sensitive to ranolazine. However, E1784K thermosensitivity was dampened in cytosolic calcium at -50 mV compared to other voltages and to WT.

#### 4.4.5. Ranolazine does not suppress thermosensitive late $I_{Na}$ in E1784K with elevated cytosolic calcium

Representative normalized late  $I_{Na}$  current traces are shown in **Figure 4-6: A-B** at 0  $\mu$ M and 100  $\mu$ M ranolazine (only 34 °C shown). Late  $I_{Na}$  percent and density are shown in **Figure 4-6: C-D** as bar graphs. Late  $I_{Na}$  percent and density in E1784K increased ( $p < 0.01$ ) by 11-fold and 7-fold, respectively, with elevated temperature at 0 nM cytosolic calcium (**Figure 4-6: D** and **Table 4-5**). This increase in late  $I_{Na}$  was almost fully attenuated in 10  $\mu$ M ranolazine. Late  $I_{Na}$  percent decreased in elevated cytosolic calcium ( $p < 0.01$ ) but there was no effect on late  $I_{Na}$  density in E1784K. Late  $I_{Na}$  percent and density in E1784K were not suppressed with ranolazine at 2500 nM cytosolic calcium (**Figure 4-6: D** and **Table 4-5**).

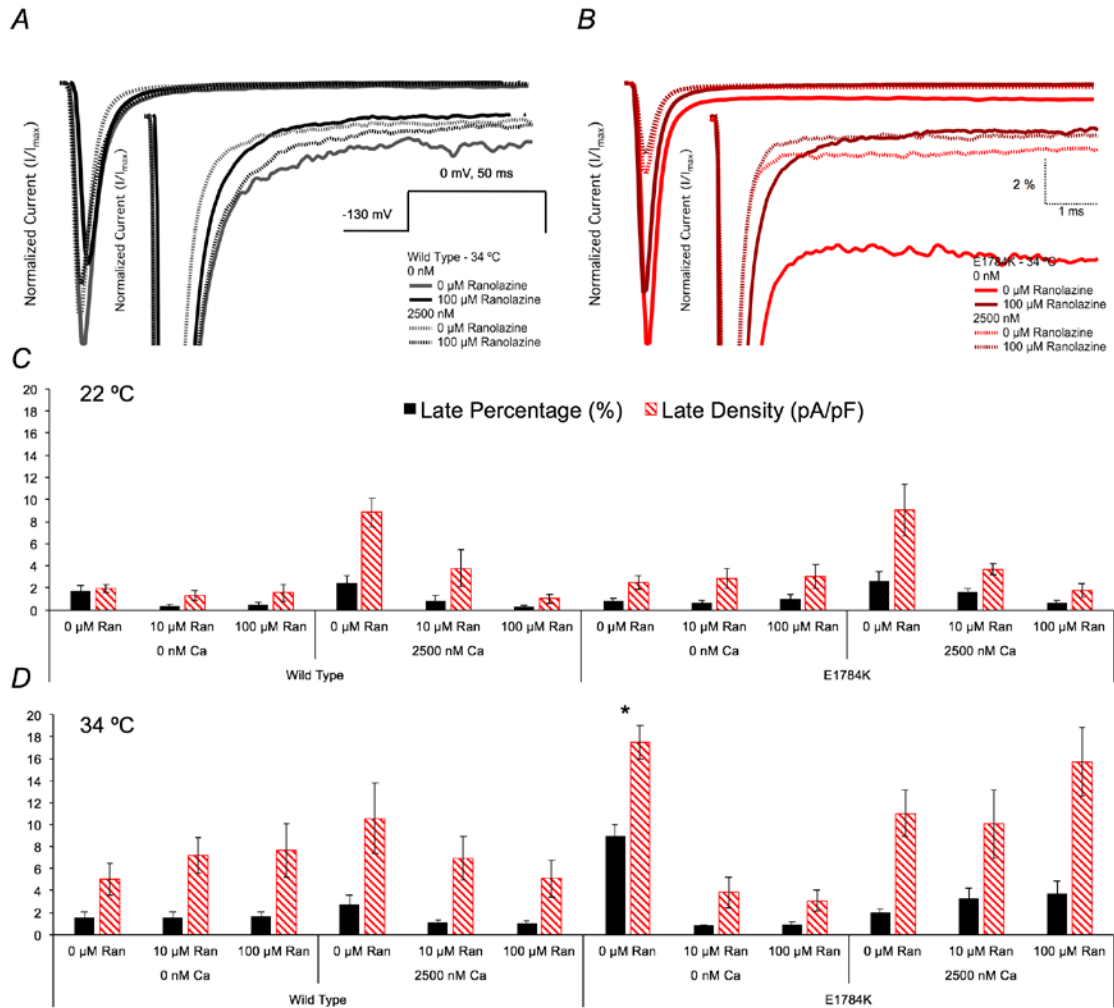


**Figure 4-6 Ranolazine effects on late  $I_{Na}$ .**

Panels A-B show normalized current traces, with emphasis on the non-inactivating, late  $I_{Na}$ , at 34 °C. The normalized late  $I_{Na}$  in E1784K is enhanced drastically by elevated temperature. Cytosolic calcium suppresses the E1784K normalized late  $I_{Na}$  (addressed in discussions). Ranolazine suppresses late  $I_{Na}$  only at 0 nM compared to 2500 nM cytosolic calcium. Panels C-D show the late  $I_{Na}$  percent and density bar graphs for all conditions at 22 °C and 34 °C, respectively.

**Table 4-5 Ranolazine Late I<sub>Na</sub>**

Condition	Late Density (pA/pF)	N	Late Percent (%)	N
WT - 22 °C - 0 nM Ca <sup>2+</sup> - 0 Ran	1.95 ± 0.34	9	1.71 ± 0.54	9
WT - 22 °C - 0 nM Ca <sup>2+</sup> - 10 Ran	1.35 ± 0.44	8	0.35 ± 0.12	8
WT - 22 °C - 0 nM Ca <sup>2+</sup> - 100 Ran	1.55 ± 0.79	6	0.45 ± 0.20	6
WT - 22 °C - 2500 nM Ca <sup>2+</sup> - 0 Ran	8.83 ± 1.33	8	2.41 ± 0.72	6
WT - 22 °C - 2500 nM Ca <sup>2+</sup> - 10 Ran	3.78 ± 1.64	8	0.80 ± 0.48	7
WT - 22 °C - 2500 nM Ca <sup>2+</sup> - 100 Ran	1.01 ± 0.38	7	0.30 ± 0.12	6
WT - 34 °C - 0 nM Ca <sup>2+</sup> - 0 Ran	5.04 ± 1.42	7	1.57 ± 0.52	9
WT - 34 °C - 0 nM Ca <sup>2+</sup> - 10 Ran	7.21 ± 1.61	8	1.54 ± 0.54	8
WT - 34 °C - 0 nM Ca <sup>2+</sup> - 100 Ran	7.66 ± 2.47	9	1.67 ± 0.42	9
WT - 34 °C - 2500 nM Ca <sup>2+</sup> - 0 Ran	10.57 ± 3.2	7	2.71 ± 0.90	9
WT - 34 °C - 2500 nM Ca <sup>2+</sup> - 10 Ran	6.95 ± 1.97	8	1.09 ± 0.26	8
WT - 34 °C - 2500 nM Ca <sup>2+</sup> - 100 Ran	5.11 ± 1.67	4	0.98 ± 0.25	5
EK - 22 °C - 0 nM Ca <sup>2+</sup> - 0 Ran	2.51 ± 0.63	9	0.85 ± 0.20	9
EK - 22 °C - 0 nM Ca <sup>2+</sup> - 10 Ran	2.86 ± 0.88	9	0.68 ± 0.21	8
EK - 22 °C - 0 nM Ca <sup>2+</sup> - 100 Ran	3.01 ± 1.08	10	1.02 ± 0.39	8
EK - 22 °C - 2500 nM Ca <sup>2+</sup> - 0 Ran	9.02 ± 2.31	5	2.64 ± 0.81	4
EK - 22 °C - 2500 nM Ca <sup>2+</sup> - 10 Ran	3.68 ± 0.51	9	1.65 ± 0.30	9
EK - 22 °C - 2500 nM Ca <sup>2+</sup> - 100 Ran	1.78 ± 0.65	8	0.61 ± 0.30	6
EK - 34 °C - 0 nM Ca <sup>2+</sup> - 0 Ran	17.47 ± 1.54 <sup>*1</sup>	6	8.97 ± 1.02 <sup>*1</sup>	6
EK - 34 °C - 0 nM Ca <sup>2+</sup> - 10 Ran	3.84 ± 1.39	4	0.86 ± 0.04	4
EK - 34 °C - 0 nM Ca <sup>2+</sup> - 100 Ran	3.09 ± 0.96	6	0.89 ± 0.22	6
EK - 34 °C - 2500 nM Ca <sup>2+</sup> - 0 Ran	11.01 ± 2.12	7	2.00 ± 0.34	9
EK - 34 °C - 2500 nM Ca <sup>2+</sup> - 10 Ran	10.05 ± 3.08	5	3.28 ± 0.93	6
EK - 34 °C - 2500 nM Ca <sup>2+</sup> - 100 Ran	15.73 ± 6.24	5	3.76 ± 1.10	4

<sup>\*1</sup> p<0.01 vs 10 μM and 100 μM Ran of same condition

#### 4.4.6. Ranolazine does not enhance UDI in E1784K with elevated cytosolic calcium

Sustained or repetitive depolarizations induce slow inactivation in Nav1.5, which was indirectly measured by the use-dependent inactivation (UDI) protocols described in the methods. Use-dependence was measured at 1 Hz and 3 Hz, mimicking resting heart rate (60 bpm) and tachycardia (180 bpm), respectively. Normalized current plotted against time for UDI measured at 1 Hz and 3 Hz are shown in **Figure 4-7** (only 34 °C shown).

UDI plateau ( $y_0$ ) was greater ( $p=0.0430$ ) at elevated temperature at both 1 Hz and 3 Hz, but the shift was larger in E1784K at 1Hz (**Table 4-6**).  $y_0$  decreased to different levels in ranolazine (reported in **Table 4-6**). At high UDI frequencies, E1784K  $y_0$  decreased in ranolazine at 34 °C compared to WT (**Figure 4-7** shows only 34 °C, **Table**

**4-6).** Our statistical results suggest that the drug effects on UDI (3 Hz) in E1784K are limited in elevated cytosolic calcium (**Table 4-6**).

UDI onset kinetics were accelerated in E1784K and elevated temperature ( $p < 0.05$ ), measured by  $\tau_1$ , at 1 Hz and 3 Hz. Onset kinetics decelerated in elevated cytosolic calcium ( $p < 0.0001$ ) at 1 Hz predominately in WT compared to E1784K. WT and E1784K  $\tau_1$  was decreased ( $p < 0.0001$ ) in ranolazine at 2500 nM cytosolic calcium and 34 °C (**Table 4-6**).  $\tau_1$  at 3 Hz was unaffected in ranolazine.  $\tau_2$  was unaffected at 1 Hz and 3 Hz in all experimental conditions.

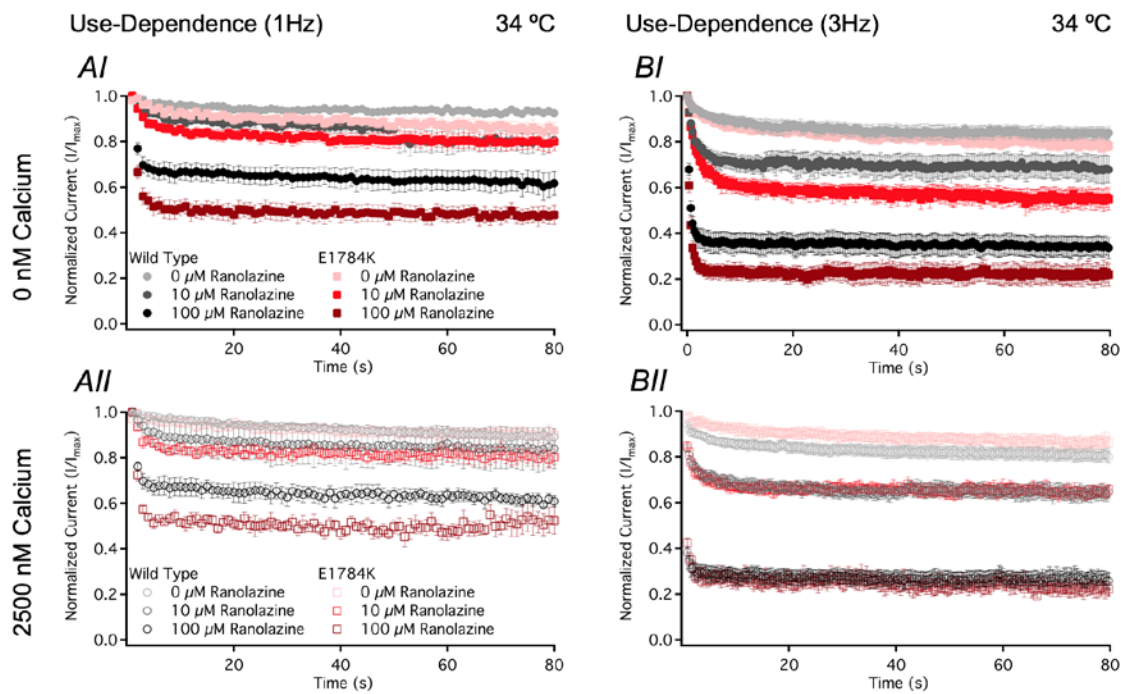


**Figure 4-7 Ranolazine effects on use-dependence.**

Panels AI-II and Panels BI-II show normalized current versus time measuring UDI at 1 Hz and 3 Hz, respectively. Insets of pulse protocols are excluded for visual clarity (refer to methods). All three drug concentrations are included in the figures to show 10  $\mu\text{M}$  ranolazine effect on UDI (3 Hz) in E1784K at 0 nM compared to 2500 nM (refer to Table 4-6 for values).

**Table 4-6 Ranolazine Use-Dependence 1Hz & 3Hz**

Condition	1 Hz - y0	1 Hz - $\tau$ 1 (s)	1 Hz - $\tau$ 2 (s)	N	3 Hz - y0	3 Hz - $\tau$ 1 (s)	3 Hz - $\tau$ 2 (s)	N
WT - 22 °C - 0 nM Ca <sup>2+</sup> - 0 Ran	0.84 ± 0.03	3.13 ± 0.88	47.88 ± 9.44	6	0.63 ± 0.04	2.03 ± 0.41	40.53 ± 5.42	7
WT - 22 °C - 0 nM Ca <sup>2+</sup> - 10 Ran	0.77 ± 0.01	2.96 ± 0.52	18.55 ± 4.50	7	0.52 ± 0.02	3.39 ± 0.62	23.00 ± 7.54	7
WT - 22 °C - 0 nM Ca <sup>2+</sup> - 100 Ran	0.44 ± 0.02 <sup>*1</sup>	2.19 ± 0.44	9.70 ± 3.31	5	0.15 ± 0.02 <sup>*1</sup>	0.92 ± 0.18	7.02 ± 4.44	4
WT - 22 °C - 2500 nM Ca <sup>2+</sup> - 0 Ran	0.81 ± 0.02	8.22 ± 2.84	114.32 ± 22.42	7	0.66 ± 0.03	1.83 ± 0.23	36.4 ± 7.98	7
WT - 22 °C - 2500 nM Ca <sup>2+</sup> - 10 Ran	0.78 ± 0.01	6.93 ± 0.94	31.93 ± 10.85	6	0.52 ± 0.02	1.19 ± 0.19	8.57 ± 0.42	5
WT - 22 °C - 2500 nM Ca <sup>2+</sup> - 100 Ran	0.35 ± 0.03 <sup>*1</sup>	1.67 ± 0.12	34.32 ± 22.87	7	0.20 ± 0.03 <sup>*1</sup>	0.69 ± 0.32	14.56 ± 13.09	3
WT - 34 °C - 0 nM Ca <sup>2+</sup> - 0 Ran	0.92 ± 0.01	4.77 ± 3.14	39.42 ± 20.36	4	0.84 ± 0.03	2.75 ± 1.00	17.73 ± 9.63	5
WT - 34 °C - 0 nM Ca <sup>2+</sup> - 10 Ran	0.76 ± 0.05	5.41 ± 3.35	62.60 ± 20.25	5	0.65 ± 0.06	0.98 ± 0.10	16.65 ± 6.29	6
WT - 34 °C - 0 nM Ca <sup>2+</sup> - 100 Ran	0.60 ± 0.06 <sup>*2</sup>	0.66 ± 0.10	43.51 ± 18.93	8	0.33 ± 0.05 <sup>*1</sup>	0.39 ± 0.08	13.99 ± 8.03	8
WT - 34 °C - 2500 nM Ca <sup>2+</sup> - 0 Ran	0.88 ± 0.03	30.10 ± 6.41 <sup>*3</sup>	59.96 ± 37.08	4	0.79 ± 0.04	1.46 ± 0.17	38.85 ± 12.19	8
WT - 34 °C - 2500 nM Ca <sup>2+</sup> - 10 Ran	0.82 ± 0.04	2.83 ± 1.02	67.05 ± 23.05	5	0.60 ± 0.03 <sup>*4</sup>	1.02 ± 0.16	17.28 ± 6.89	7
WT - 34 °C - 2500 nM Ca <sup>2+</sup> - 100 Ran	0.64 ± 0.02	0.44 ± 0.16	8.44 ± 2.77	5	0.27 ± 0.03 <sup>*1</sup>	0.41 ± 0.06	17.80 ± 9.98	5
EK - 22 °C - 0 nM Ca <sup>2+</sup> - 0 Ran	0.69 ± 0.06	3.37 ± 0.64	69.20 ± 25.09	6	0.79 ± 0.01	3.08 ± 1.61	32.65 ± 20.62	4
EK - 22 °C - 0 nM Ca <sup>2+</sup> - 10 Ran	0.57 ± 0.05	3.25 ± 0.63	64.71 ± 37.46	7	0.47 ± 0.02 <sup>*4</sup>	2.40 ± 0.37	16.28 ± 3.57	6
EK - 22 °C - 0 nM Ca <sup>2+</sup> - 100 Ran	0.27 ± 0.05 <sup>*1</sup>	1.87 ± 0.25	74.43 ± 28.56	8	0.14 ± 0.03 <sup>*1</sup>	1.00 ± 0.34	1.29 ± 0.19	4
EK - 22 °C - 2500 nM Ca <sup>2+</sup> - 0 Ran	0.73 ± 0.02	1.99 ± 1.02	31.37 ± 6.74	4	0.69 ± 0.06	3.59 ± 1.84	8.20 ± 3.73	4
EK - 22 °C - 2500 nM Ca <sup>2+</sup> - 10 Ran	0.59 ± 0.06	7.17 ± 1.35	75.52 ± 20.26	5	0.47 ± 0.04	3.38 ± 0.43	13.21 ± 1.51	5
EK - 22 °C - 2500 nM Ca <sup>2+</sup> - 100 Ran	0.24 ± 0.04 <sup>*1</sup>	2.68 ± 1.13	70.86 ± 29.29	3	0.20 ± 0.06 <sup>*2</sup>	0.82 ± 0.29	1.94 ± 0.31	3
EK - 34 °C - 0 nM Ca <sup>2+</sup> - 0 Ran	0.82 ± 0.04	6.76 ± 1.43	68.66 ± 25.39	8	0.77 ± 0.03	2.66 ± 0.45	49.11 ± 13.27	9
EK - 34 °C - 0 nM Ca <sup>2+</sup> - 10 Ran	0.77 ± 0.06	2.40 ± 0.55	78.22 ± 35.32	7	0.55 ± 0.03 <sup>*4</sup>	1.63 ± 0.32	27.16 ± 15.43	5
EK - 34 °C - 0 nM Ca <sup>2+</sup> - 100 Ran	0.47 ± 0.04 <sup>*1</sup>	0.77 ± 0.07	19.07 ± 9.49	6	0.21 ± 0.05 <sup>*1</sup>	0.40 ± 0.04	24.08 ± 18.78	5
EK - 34 °C - 2500 nM Ca <sup>2+</sup> - 0 Ran	0.87 ± 0.03	15.05 ± 3.35 <sup>*3</sup>	65.60 ± 19.19	5	0.74 ± 0.08	2.50 ± 0.65	30.82 ± 2.43	6
EK - 34 °C - 2500 nM Ca <sup>2+</sup> - 10 Ran	0.77 ± 0.04	1.77 ± 0.48	48.78 ± 22.76	5	0.63 ± 0.03	1.13 ± 0.12	6.41 ± 3.13	6
EK - 34 °C - 2500 nM Ca <sup>2+</sup> - 100 Ran	0.46 ± 0.05 <sup>*1</sup>	1.21 ± 0.20	38.24 ± 19.24	5	0.26 ± 0.03 <sup>*1</sup>	0.54 ± 0.14	6.89 ± 4.62	5

<sup>\*1</sup> p<0.0001 vs 0  $\mu$ M and 10  $\mu$ M Ran of same condition, <sup>\*2</sup> p<0.0001 vs 0  $\mu$ M Ran of same condition, <sup>\*3</sup> p<0.0001 vs 10  $\mu$ M and 100  $\mu$ M Ran of same condition, <sup>\*4</sup> p<0.0001 vs 0  $\mu$ M and 100  $\mu$ M Ran of same condition,

#### 4.4.7. E1784K-induced alternans is exacerbated with ranolazine

Biophysical data were extrapolated to physiological (37 °C) and febrile (41 °C) temperatures using a  $Q_{10}$  coefficient. Extrapolations were independently confirmed using Arrhenius relationships. Action potential (AP) traces are shown in **Figure 4-8** for simulations conducted in endocardial cells at three frequencies: 0.5 Hz (bradycardia), 1.5 Hz (sinus rhythm), and 2.5 Hz (tachycardia). At febrile temperature, simulated APs show accelerated depolarizations and repolarizations in WT compared to E1784K.

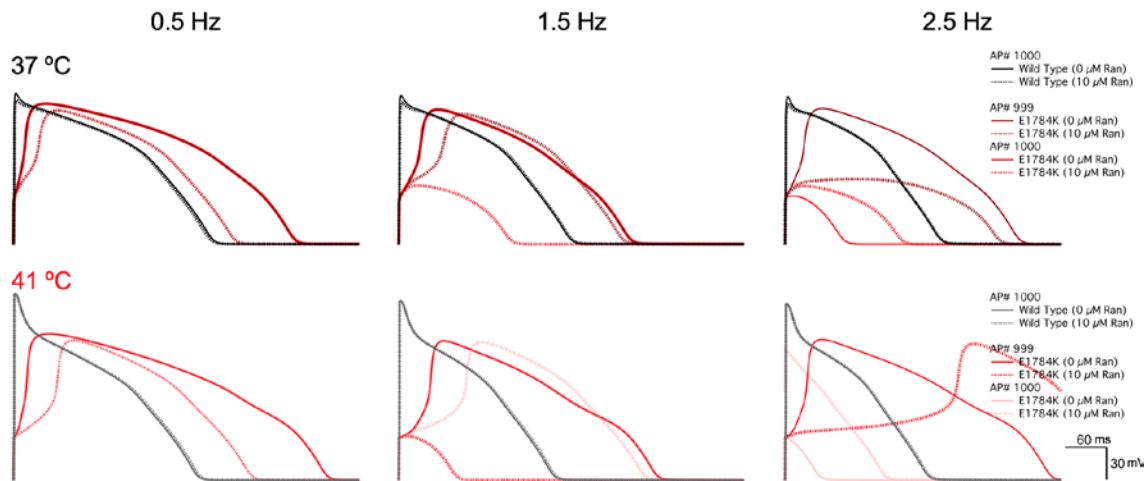


**Figure 4-8 Endocardial action potential simulations.**

AP simulations are plotted against time (*inset* is shown in bottom right corner) at 37 °C and 41 °C. The last two AP beats were plotted in E1784K to show alternans-induction. Simulations only included therapeutic concentrations of ranolazine (10  $\mu$ M).

Electrical restitution curves (ERCs) at 90 % repolarization were constructed from plotting  $APD_{90}$  against the diastolic interval as shown in **Figure 4-9: A-B** in endocardial cells. The last two beats were included in the ERCs to exemplify bifurcation and alternans-induction at critical diastolic intervals. The  $APD_{90}$  for WT follows a similar trend to previously published ERCs, typifying a relatively stable  $APD$  rate dependence (Nolasco & Dahlen, 1968; Franz, 2003; Jordan & Christini, 2004). E1784K has a higher  $APD_{90}$  in all cardiac cells, especially the mid-myocardium, compared to WT (not shown, **Figure 4-9**). At 37 °C, the mutant causes bifurcation in  $APD_{90}$ , mainly in epicardial cells, indicative of alternans (not shown); however, endocardial cells also experience alternans at febrile temperature in addition to epicardial cells (**Figure 4-9: B**). Upon drug perfusion, bifurcations were observed at higher diastolic intervals in E1784K (**Figure 4-9**). The

drug-induced bifurcations in ERCs were augmented at febrile temperature in all cardiac cells.

A linear relationship is established between the last two AP beats at each frequency step (shown in **Figure 4-9: C-D**), with no alternans. Divergence from linearity is indicative of alternans occurrence. At both 37 °C and 41 °C, WT cells had no alternans, even upon 10 μM ranolazine perfusion, showing linearity with a slope = 1 (**Figure 4-9: C-D**). In drug-free conditions, E1784K had a linear relationship at high BCLs (low frequencies), but deviated from linearity beginning at intermediate BCLs; distortion in linearity is observed at lower frequencies in epicardial cells. This relationship in E1784K is augmented with febrile temperature. The prolonged APD<sub>90</sub> in E1784K were shortened with ranolazine at very low frequencies, and alternans were quickly induced even during bradycardia, an effect exacerbated by febrile temperature.

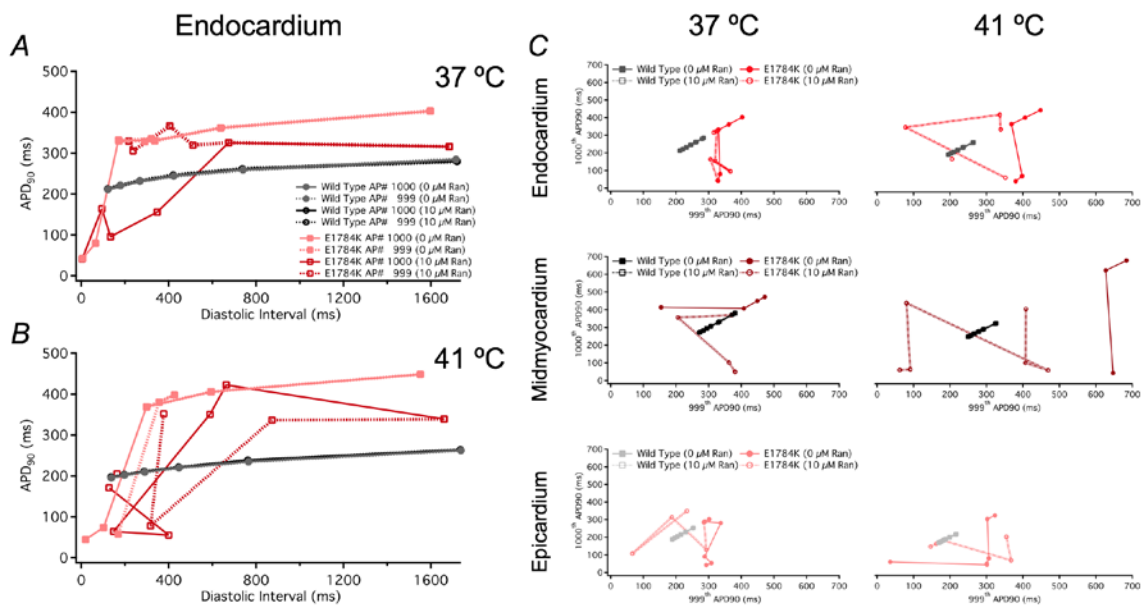


**Figure 4-9 Cardiac electrical restitution properties**

Panel A-B shows the endocardial ERC curves at 37 °C and 41 °C. Panels C shows plots of the last two AP beats to determine alternans-induction in the three myocardial cells at 37 °C and 41 °C.

## 4.5. Discussion

Our goal was to determine whether ranolazine reduced channel dysfunction in E1784K under the triggering conditions of elevated temperature and cytosolic calcium. Ranolazine did not attenuate gain-of-function in E1784K when temperature and cytosolic

calcium were elevated. Ranolazine has minimal effects on conductance in  $\text{Na}_v1.5$  (Huang et al., 2011; Sokolov et al., 2013). The drug follows the modulated receptor hypothesis, targeting the open/inactivated states at depolarized potentials, thereby suppressing late  $I_{\text{Na}}$  (Ragsdale et al., 1996). Physiological events, such as acidemia, enhance ranolazine antiarrhythmic effect by augmenting late  $I_{\text{Na}}$ , thus providing the drug with a larger open-state channel substrate to target (Jones et al., 2011; Vilin et al., 2012; Sokolov et al., 2013). In addition to physiological modulators, *SCN5a* mutations often alter voltage-dependence of the channel, which modify drug effects on  $\text{Na}_v1.5$ . To date, ranolazine has been screened against only  $\Delta\text{KPQ}$  (Fredj et al., 2006b; Moss et al., 2008), Y1767C (Huang et al., 2011), R1623Q (Rajamani et al., 2009), and D1790G (Chorin et al., 2016). Our study is the first to show the combined external triggers and *SCN5a* mutation effects on ranolazine.

Ranolazine efficacy was enhanced at elevated temperature. Similar to acidosis effects, elevated temperature increases the late open probability in E1784K (Belardinelli, 2006a; Sokolov et al., 2013). Late  $I_{\text{Na}}$  percent and density increased by 11- and 7-fold, respectively, with elevated temperature. We previously reported a 3.54-fold increase in late  $I_{\text{Na}}$  percent when temperature was elevated from 22 °C to 34 °C (Abdelsayed et al., 2015); however, we used CHOK1 cells to study E1784K thermosensitivity. The temperature coefficient ( $Q_{10}$ ) partly depends on lipid-channel interactions in the membrane, which differ between heterologous expression systems (Murray et al., 1990; Ruff, 1999). The HEK293 lipid bilayer is less viscous than CHOK1 cells as observed in our whole-cell recordings, which may justify the heightened  $Q_{10}$  in the late  $I_{\text{Na}}$  measurements. At elevated stimulation frequencies and temperature, therapeutic ranolazine decreased channel availability by increasing channel use-dependence in E1784K.

Although ranolazine efficacy appears to be increased by temperature, its efficacy appears to be dampened by the combination of both elevated temperature and cytosolic calcium. At 34 °C, E1784K late  $I_{\text{Na}}$  percent was depressed with elevated cytosolic calcium, but there was no effect on late  $I_{\text{Na}}$  density. These opposing changes in late  $I_{\text{Na}}$  percent and density may be attributed to the increased peak  $I_{\text{Na}}$  density with elevated cytosolic calcium at 34 °C. Although not significant, the shift contributes to late  $I_{\text{Na}}$  percent calculation (**Table 4-2**). Late  $I_{\text{Na}}$  in E1784K was not attenuated by ranolazine at elevated temperature and cytosolic calcium.

### 4.5.1. Drug Binding in Mutant-Trigger Context

Ranolazine action on  $\text{Na}_v1.5$  is commonly associated with the modulated receptor hypothesis (Hille, 1977). Sokolov et al. (2013) argued that the drug follows a modified form of binding, as their pharmacological analysis suggested drug-binding at hyperpolarized voltages (Sokolov et al., 2013). Ranolazine exhibits partial preference to the closed state in  $\text{Na}_v1.5$ , as suggested by the hyperpolarizing shift in SSFI observed with ranolazine. The shift mainly decreases channel availability near resting potential in cardiomyocytes. Other classic antiarrhythmics, anticonvulsants, and local anesthetics have similar effects, yet follow the modulated receptor hypothesis (Ragsdale et al., 1996; Tikhonov & Zhorov, 2017). Sokolov *et al.* (2013) also report that the drug-induced block in late  $I_{\text{Na}}$  occurs by a slow-mode recovery in slow inactivation, which is exacerbated at low pH (Sokolov et al., 2013). This effect was mildly observed in this study. However, it is difficult to correlate the drug effects in E1784K UDI to late  $I_{\text{Na}}$ , as the former had minor but significant shifts.

Ranolazine shares a very similar structure with the class 1b antiarrhythmic drug lidocaine, which, like other sodium blockers, preferentially binds to F1760 and, to a lesser extent, Y1767 in DIVS6 (Fredj et al., 2006b; Huang et al., 2011). Ranolazine has high lipophilicity and can only bind to its receptor sites by traversing the phospholipid membrane and entering the central cavity through the inner vestibule. However, lateral pores, known as fenestrations, are alternative routes for large compounds like ranolazine to access the central cavity. The fenestrations in the  $\text{Na}_v\text{Pas-Na}_v1.5$  model were unavailable for drug binding in auto-docking due to their constricted sizes (Shen et al., 2017). It would be interesting to determine whether E1784K alters fenestration size in  $\text{Na}_v1.5$ , modifying drug entry via the fenestrations.

The interaction between ranolazine and extracellular channel regions is unknown, but is unlikely due to the drug's lipophilicity; a crystal structure of the channel/drug interaction would elucidate the drug-induced modifications in gating. The newly discovered aryl sulfonamide antagonists preferentially stabilize  $\text{Na}_v1.7$  DIVS4 activation thereby stabilizing the fast inactivated state and suppressing late  $I_{\text{Na}}$  (Ahuja et al., 2015). Ranolazine may be structurally modified to include other moieties, like anionic aryl sulfonamides, for further optimizing its selectivity for targeting late versus peak  $I_{\text{Na}}$ .

#### 4.5.2. E1784K-induced Structural Rearrangements in Nav1.5 and its Impact on ranolazine

We speculate E1784K affects fast inactivation via two possible mechanisms in Nav1.5, thereby altering channel/drug interactions. **Figure 4-1** shows the channel structures discussed, as follows.

**(1)** E1784K hyperpolarizes the voltage-dependence of SSFI, thus stabilizing the interaction between the channel and the fast inactivation particle (Dumaine et al., 1996; Chandra et al., 1998; Wei et al., 1999; Deschênes et al., 2000; Makita et al., 2008a). Fast inactivation onset is correlated with DIVS4 activation, whereas channel recovery is rate limited by charge immobilization of DIVS4 (Kühn & Greeff, 1999; Capes et al., 2013). The charge reversal mutant, E1784K, may enhance the transition of DIVS4 between closed and open states, as suggested by the Peters-Ruben model (Peters et al., 2017). We postulate that this effect may be due to an electrostatic repulsion between the CTD mutant and conserved positive residues in DIVS4, given their close proximity (Shen et al., 2017). This repulsion could make the DIVS4 in E1784K more mobile, which might explain the accelerated fast inactivation onset and recovery kinetics (Makita et al., 2008a; Abdelsayed et al., 2015, 2017; Peters et al., 2017). Fast inactivation kinetics in E1784K are not enhanced by temperature. Thus, it does not seem justifiable to attribute the thermosensitive late  $I_{Na}$  in E1784K to increased recovery kinetics, which are not thermosensitive. Rather a rearrangement may occur in DIVS4, conforming the voltage sensor to a state in which conductance in E1784K is higher (Peters et al., 2017).

**(2)** E1784K alters the structure of the CTD by disrupting the native hydrophobic and electrostatic interactions holding the EF-like hand domain ( $\alpha_1$ – $\alpha_4$ ) tight with the IQ motif ( $\alpha_6$ ) (Chagot et al., 2009). Calcium sensitivity is imparted in Nav1.5 via calmodulin, which binds to the IQ motif ( $\alpha_6$ ) via its C-lobe or N-lobe depending on cytosolic calcium levels (Shah et al., 2006; Sarhan et al., 2009, 2012). During diastole or systole, calmodulin is calcified to different extents at its N-lobe (Ben-Johny et al., 2014). Calcified calmodulin has a lower affinity for the IQ motif and binds, via its C-lobe, to the DIII-DIV linker, forming a tripartite complex. This interaction is thought to prevent the DIII-DIV linker fast inactivation particle from occluding the pore, increasing channel availability near resting potential (Shah et al., 2006; Sarhan et al., 2012). With depolarized potentials, the calmodulin C-lobe stabilizes the fast inactivation particle, suppressing late

$I_{Na}$ , as in  $\Delta$ KPQ and other mixed syndrome mutants (Van Petegem et al., 2012; Potet et al., 2015; Abdelsayed et al., 2017). Some studies refute the tripartite complex formation and favor a  $Ca_v1.2$ -like regulation of inactivation in  $Na_v1.5$  (Ben-Johny et al., 2014; Pitt & Lee, 2016). In those studies, the calcium-calmodulin complex is localized to the CTD (Petegem et al., 2005; Ben-Johny & Yue, 2014). The  $Na_vPas$  structure showed intermolecular interactions between the DIII-DIV linker, CTD, and DIVS4 (Shen et al., 2017). Motoike *et al.* (2004) confirm calmodulin-independent interactions between the inter-linkers in  $Na_v1.5$ , suggesting that calmodulin acts as an auxiliary channel modifier during a calcium signal (Pitt & Lee, 2016). Calcium regulation in  $Na_v1.5$  is mediated by calmodulin since the dual EF-like hand domains in the CTD do not bind calcium (Ben-Johny et al., 2014; Pitt & Lee, 2016). In light of these structural models, we speculate that E1784K decouples both the calcium-dependent and calcium-independent interactions between the DIII-DIV linker and the CTD. Thus, E1784K inhibits calcium-dependent facilitation (CDF) and calcium-dependent inactivation (CDI) in  $Na_v1.5$ . We propose that the decoupling in the CTD caused by E1784K may create a high entropy, unstable structure. Upon a calcium signal, the calcified calmodulin has reduced affinity for the IQ motif, thus augmenting the CTD entropy (Sarhan et al., 2012).

Both mechanisms **(1)** and **(2)** may occur simultaneously in E1784K. The calcium effects in  $Na_v1.5$  are localized to the CTD. No reports have shown direct interaction between calcium-calmodulin and DIVS4, so if mechanism **(2)** occurs, it may be via an indirect effect on DIVS4.

In light of the discussed structural insights, we speculate that ranolazine can easily access the inner vestibule with non-calcified calmodulin, since the molecule binds tightly to the IQ motif. Ranolazine efficacy, however, is hampered by cytosolic calcium, suggesting an interaction between the drug and the channel at the CTD. The high entropy CTD in calcified calmodulin seems to physically hinder ranolazine from entering into the inner vestibule.

### 4.5.3. Physiological and Medical Implications

Elevated temperature and cytosolic calcium are two of many other physiological triggers that occur during exercise and are common to other pathophysiological states, such as myocardial ischemia or infarction, and heart failure (Lukas & Antzelevitch, 1996;

Rivera-Fernández et al., 2014). The majority of patients with *SCN5a* mutations show ameliorated LQT3 phenotype during exercise (Schwartz et al., 1995). Functional studies have correlated this to a stimulation frequency or calcium-induced reduction in late  $I_{Na}$  (Potet et al., 2015). However, it is clear from our study, focusing on E1784K, that the *SCN5a* mutation response to triggers can be unique (Abdelsayed et al., 2015, 2017). Thus, it is necessary to study antiarrhythmics in *SCN5a* cohorts during different physiological states as the mutant-trigger effect may determine drug efficacy.

Our AP simulations clearly show pro-arrhythmic effects of ranolazine, which are exacerbated by febrile temperatures. Electrical restitution curves clearly show a critical diastolic interval at which alternans are triggered. Our AP simulations provide evidence for ranolazine arrhythmogenicity, as it does not shorten  $APD_{90}$  in E1784K at high heart rates. At low heart rates and at body core temperature, the drug shortens  $APD_{90}$  in cardiac cells. However, with normal and elevated heart rates, the drug induces alternans, an effect exacerbated at febrile temperature. The critical diastolic intervals at which alternans are caused by the drug appear earlier (at higher BCLs) at febrile temperature.

E1784K induces alternans with higher prevalence in epicardial cells at low heart rates. This result coincides with the phase 2 re-entry phenomenon constituting the repolarization hypothesis in BrS1 (Lukas & Antzelevitch, 1996). The high  $I_{Kto}$  density, especially in the right epicardium, results in complete action potential dome failure (Di Diego et al., 1996). E1784K channels are less available for activation due to the hyperpolarized SSFI- $V_{1/2}$ . This seems to be the main mechanism behind the decrease in AP upstroke velocity in cardiac cells, especially the epicardial cells, despite the mutant and triggers-exacerbated increased late  $I_{Na}$ . Thus, E1784K expresses both gain- and loss-of-function at the electrical level in cardiac cells. However, this expressivity is finely tuned by channel switches, like temperature and cytosolic calcium.

Our previous and current data suggest exercise, and its accompanying physiological triggers, differentially affect mixed syndrome mutations, especially E1784K (Makita et al., 2008a; Abdelsayed et al., 2015; Peters et al., 2016; Abdelsayed et al., 2017). The action of different antiarrhythmics appear to differ depending on physiological state.

## **4.6. Conclusions**

Appropriate management of cardiac arrhythmias in patients with *SCN5a* mutations requires careful investigation of antiarrhythmic drug efficacy under various physiological states. Our results suggest that ranolazine may increase the susceptibility for arrhythmia development in E1784K carriers at sinus rhythm and tachycardia. The risk is augmented under febrile conditions. Although exercise is commonly associated with high heart rates, other pathophysiological states share common triggers, as in heart failure or myocardial ischemia and infarction. Other antiarrhythmics should also be screened against E1784K and other channel mutants under various physiological conditions.

## **4.7. Acknowledgments**

We thank Dr. Elizabeth M. Cherry for helping in AP simulation analysis. We are also grateful to both Mr. Colin Peters and Mr. Mohammed-Reza Ghovanloo for their valuable input and support.

## Chapter 5. General Discussion and Future Directions

### 5.1. What was the point?

My goal was to study how physiological triggers like elevated temperature and cytosolic calcium affect E1784K channel properties separately or together with ranolazine. Multiple cascades and signalling molecules are activated during exercise and pathophysiological states accompanied with elevated heart rates, such as myocardial ischemia/infarction or heart failure. Some factors may exacerbate or ameliorate the E1784K channel phenotype. I studied two factors which both exacerbate the biophysical defects caused by E1784K. The physiological and clinical implications made from the biophysical data should be treated with caution as not all channel-modifying factors were characterized. Thus, it is fair to assume that not all E1784K carriers will display similar phenotypes since genotype-channel-phenotype correlations in *SCN5a* mutations are highly complex. Furthermore, additional caveats exist in the experimental approach used in these studies which potentially obscures establishing a clear channel-phenotype relationship in E1784K. Despite these limitations, many interesting biophysical interpretations can be derived from the data presented in this thesis, which ultimately have physiological and pharmacological implications.

The functional data presented in the past three chapters all support past findings on the biophysical defects in  $\text{Na}_v1.5$  caused by E1784K. The mutant depolarizes activation (GV) and hyperpolarizes steady-state fast inactivation (SSFI) midpoints ( $V_{1/2}$ ). The mutant significantly accelerates fast inactivation kinetics at all voltages and elevates late  $I_{\text{Na}}$ . Elevated temperature affected E1784K fast inactivation voltage-dependence differently depending on the heterologous expression system: fast inactivation was destabilized in HEK293 cells (**Chapter 3**) compared to CHOK1 cells when temperature was raised from 22 °C to 34 °C. Intriguingly, elevated temperature had no impact on E1784K fast inactivation kinetics, especially near resting potential (as in **Chapter 1** with CHOK1 cells). E1784K seems to lower fast inactivation activation energy, thereby accelerating onset and recovery kinetics. Unfortunately, I could not measure activation energy directly using the Arrhenius relationship since  $\text{Na}_v$  follows a multi-activation energy profile (Schwarz, 1979; Collins & Rojas, 1982). As speculated, E1784K

dramatically lowers DIV S4 (inactivation segment) activation energy barrier, thus speeding its mobility, as supported by the Peters-Ruben 2017 model (Peters *et al.*, 2017). Additional thermal energy has minimal effects on fast inactivation kinetics, since the activation energy is substantially lowered by E1784K. The stabilized fast-inactivated state in E1784K suggests that the inactivation segments is pre-activate, thereby depleting the available E1784K pool at resting potential. Reduced channel availability leads to a decrease in the action potential (AP) upstroke velocity, as observed in the AP simulations. This effect is usually correlated with conduction abnormalities related to heart block and BrS1 (Veltmann *et al.*, 2016).

The exacerbated late  $I_{Na}$  measured in E1784K occurs at very depolarized potentials. The destabilized open fast-inactivated state in E1784K suggests that the inactivation particle (IFMT motif) has reduced affinity for its binding sites in the pore. E1784K seems to perturb the latent 'latching' role served by the C-terminal domain (CTD) in stabilizing the fast inactivation particle during open-state. Recently, the American cockroach  $Na_vPas$  structure reveals native electrostatic and van der Waals interactions between the DIII-DIV linker and the CTD. The homology model solved for  $Na_v1.5$  based on  $Na_vPas$  is shown in **Figure 5-1**. The structure does not contain any intracellular interactions between  $Na_v1.5$  and associated molecules, like calmodulin or Fibroblast Homologous Factor (FHF) (Wang *et al.*, 2012; Gabelli *et al.*, 2014; Ben-Johny *et al.*, 2015). However, the middle  $\alpha$ -helix in the DIII-DIV linker, following the IFMT motif, is a key spot for CTD interaction in  $Na_vPas$ . Multiple salt bridges are formed between the highly acidic EF-like hand domain (EFLD) in the CTD and the DIII-DIV linker positively charged residues (**Figure 5-1**). E1784 is located prior to the EFLD and is in close proximity with K1493 in the DIII-DIV linker, potentially engaging in an ionic bond (**Figure 5-1**). I speculate that E1784K disrupts the salt bridge with K1493, thus perturbing fast inactivation stability (C.H. Peters, personal communication, October 21, 2017). Many  $Na_v1.5$  mutants occur in the DIII-DIV linker and the CTD. Generalizing E1784K biophysical results to other  $Na_v1.5$  mutants is futile since most  $Na_v1.5$  mutants characterized have a unique response to external triggers (**Chapter 2**). Nevertheless, predictions on how  $Na_v1.5$  mutants affect channel behavior can be made from the  $Na_v1.5$  homology modelling included in this section (Shen *et al.*, 2017). However, the homology model is a very limited molecular depiction of the channel's highly dynamic structure.

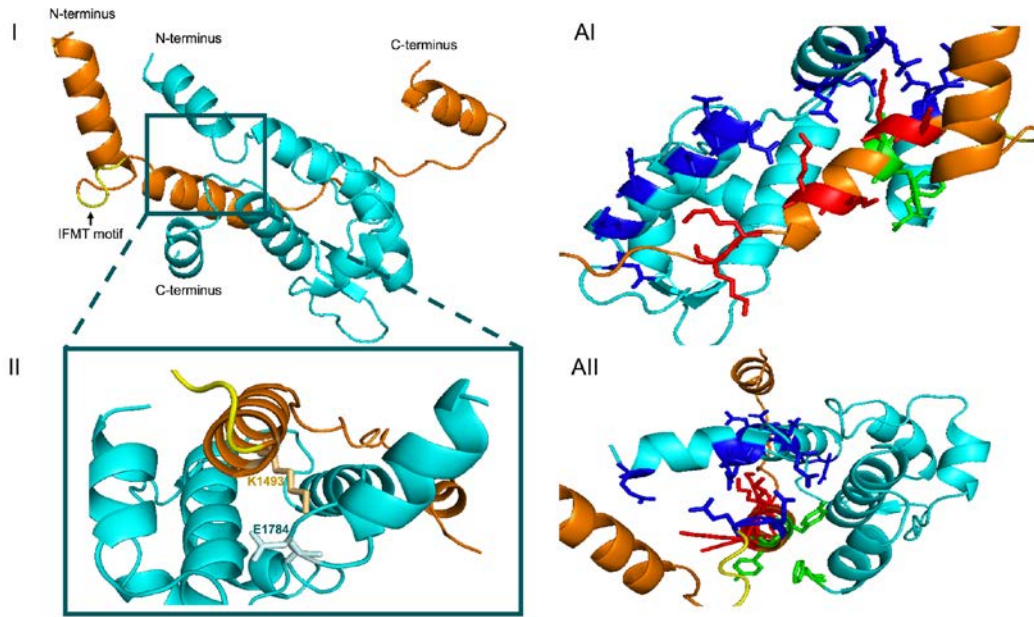


**Figure 5-1 Na<sub>v</sub>1.5-Na<sub>v</sub>Pas DIII-DIV Linker and CTD Homology Model**

Panel I shows the DIII-DIV linker (orange) and the fast inactivation particle, IFMT motif (yellow), interacting with residues in the CTD (cyan). The basis of this interaction lies in the salt bridges formed between many of the positively (red color) and negatively (blue color) charged residues found in both structures (side view in Panel AI and top view in Panel AII). Van der Waals interactions exist between Y1494, Y1495, and F1879 residues (green) as shown in the top view in Panel AII. E1784 forms a salt bridge with K1493 found in the middle helix in the DIII-DIV linker (Panel II).

E1784K is distinguished from other mutants in its ability to resist calcium-induced block of late  $I_{Na}$ , which is thought to be therapeutic in ameliorating LQT3 in exercising  $\Delta$ KPQ patients (Potet *et al.*, 2015). Disrupted CTD integrity may decrease calcium-calmodulin effects on Na<sub>v</sub>1.5. Mutants like 1795insD or Q1909R seem to strengthen the CTD integrity compared to E1784K. Elevated cytosolic calcium in 1795insD ameliorates defective fast inactivation by suppressing late  $I_{Na}$ . 1795insD is located in the EFLD- $\alpha_1$  helix in Na<sub>v</sub>1.5 CTD. Although this domain is unable to chelate calcium in Na<sub>v</sub>1.5, mutants like 1795insD introduce an additional negative residue in the EFLD. An aspartate residue in the analogous region in Na<sub>v</sub>1.4 heightens the channels sensitivity to calcium compared to Na<sub>v</sub>1.5 (Ben-Johny *et al.*, 2014). This mechanism may potentially reconfigure the Na<sub>v</sub>1.5 EFLD to operate as a functional calcium chelator, as thought to occur in Na<sub>v</sub>1.4 (Deschenes, 2002).

My data on calcium effects in Na<sub>v</sub>1.5 mutants are consistent with the tripartite complex for calcium-calmodulin regulation. Although several reports refute the interaction between calmodulin and the DIII-DIV linker, others suggest that disrupting

this inherent interaction is the underpinning for biophysical defects associated with BrS1 and LQT3 mutants (Van Petegem *et al.*, 2012; Potet *et al.*, 2015). Although calmodulin does not interact with the DIII-DIV linker in Ca<sub>v</sub>1.2, it does in Ca<sub>v</sub>1.3 (Ben-Johny *et al.*, 2014). The new NavPas structure confirms the inherent non-calmodulin based interaction between the CTD and the DIII-DIV linker (Shen *et al.*, 2017). It seems reasonable to assume that the close proximity between these two channel structures would be affected by calmodulin regulation, which binds to the CTD IQ-domain (IQD). The calcified C-lobe in calmodulin specifically binds to the DIII-DIV linker IQD nested within the central  $\alpha$ -helix. The putative binding site for the calcified C-lobe in calmodulin is a double tyrosine motif, Y1494 and Y1495, immediately downstream from K1493 (**Figure 5-2**) (Sarhan *et al.*, 2012). As speculated above, the perturbed electrostatic interaction between the CTD and the DIII-DIV linker in E1784K, may prevent calmodulin from binding to its putative binding sites in the DIII-DIV linker. These binding sites also interact closely with the CTD even in calmodulin's absence (**Figure 5-1**). Thus, E1784K seems to decouple the inactivation complex, which naturally conjugates via both calcium-dependent and calcium-independent interactions to modulate fast inactivation. In addition to distorting inter-CTD interactions, E1784K is thought to disturb intra-CTD interactions, which establish a firm anchorage for calmodulin binding and regulation. Thus, calmodulin may not be even near the inactivation complex vicinity in E1784K. Besides calmodulin binding to the CTD or the DIII-DIV linker IQD, intracellular FHF binds to the EFLD in Nav1.5, forming a ternary complex (Wang *et al.*, 2012). FHF binds to the CTD via  $\alpha$ 4,  $\alpha$ 5, and the loop between  $\alpha$ 5 and  $\beta$ 4 (Pitt & Lee, 2016). FHF determines the points of interaction between non-calcified and calcified calmodulin with the CTD (Pitt & Lee, 2016). It would seem plausible that E1784K may affect the normal FHF-mediated regulation in the CTD since it is near the EFLD. However, this observation remains to be confirmed.

The predicted instability in E1784K CTD is thought to increase the overall entropy in the intracellular milieu near the channel. The disentangled CTD in E1784K may expose the calmodulin in the binary complex along with FHF in the ternary complex to the inner vestibule, thereby affecting class I antiarrhythmic binding in Nav1.5. Alternative routes like the fenestrations allow for drugs to enter into the channel's pore (Kaczmarek & Corry, 2014); however, these drug routes may be modulated by channel type.

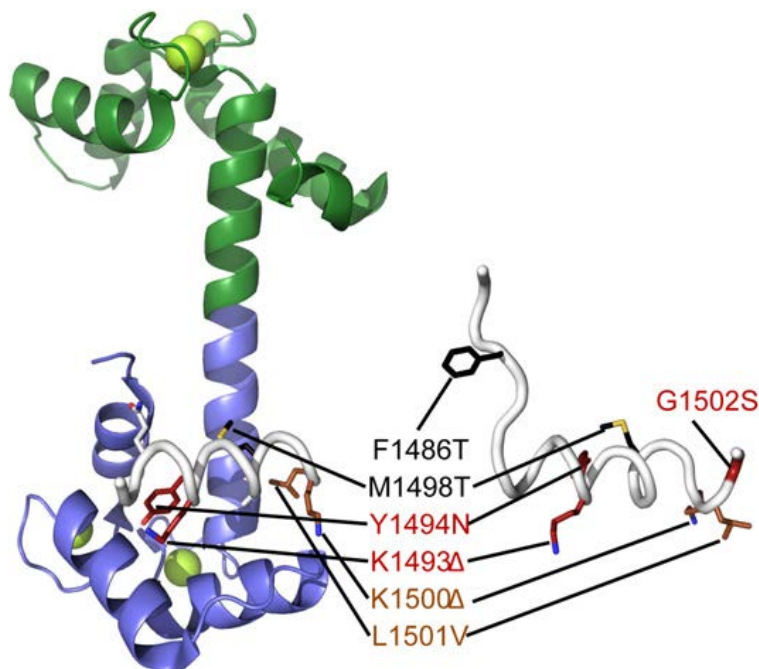


**Figure 5-2 Calmodulin C-lobe interaction with the DIII-DIV linker in Na<sub>v</sub>1.5**  
 The two EF-hand domains (N-lobe is green and C-lobe is blue) in calmodulin chelate four calcium ions (light green). The calcified C-lobe in calmodulin interacts with two Tyrosines in the DIII-DIV linker (light grey). BrS1 and LQT3 mutants are included. Reproduced from Van Petegam *et al.*, (2012).

Elevated temperature exacerbates late  $I_{Na}$  in E1784K. These thermal effects are not synergistically heightened with elevated cytosolic calcium. Rather, the interaction between temperature and calcium clearly reduces the normalized late  $I_{Na}$ , indicating a lower E1784K channel availability at open-state potentials. This reduction was owed to a decrease in peak  $I_{Na}$ . Late  $I_{Na}$  density, however, was still large in E1784K with elevated temperature and cytosolic calcium. Elevated temperatures may increase the rate by which the inactivation gate unfastens in E1784K. Inactivation gate mobility is expected to increase when there are less constraints faced from inherent CTD regulation. However, various limitations arise from the methods used in this thesis, which may undermine the above speculations.

## 5.2. Possible Limitations

### 5.2.1. Patching using Immortal cell lines

The heterologous expression systems used in this study are an important caveat. To study sodium channels *in vivo* as opposed to *in vitro* may have been more relevant to the goal of this thesis, which was to elucidate how triggers which accompany exercise affect E1784K. Native Na<sub>v</sub>1.5 in cardiac tissue are not the same as in CHOK1 and HEK293. Differences are, in part, due to lipid-membrane composition, post-translational modifications, and the intracellular protein composition of channel modifiers. Many researchers favor using native or iPSC-derived cardiomyocytes, especially when making physiological inferences as not all *in vitro* measurements are reproducible *in vivo*. For instance, the D1275N mutant displays slowed conduction velocity, atrial fibrillation, and other arrhythmias *in vivo* but displays no loss-of-function when biophysically characterized *in vitro* (Watanabe *et al.*, 2011). Other studies, however, show that Na<sub>v</sub> in heterologous expression systems are comparable to those in native cardiomyocytes, e.g. the augmented late I<sub>Na</sub> in ΔKPQ (Nuyens *et al.*, 2001; Knollmann, 2013). I chose to isolate Na<sub>v</sub>1.5 in heterologous cells since this removes the need for potentially contaminating pharmacological agents required to block other channels. However, my predictions on arrhythmogenicity may be further strengthened with current-clamp recordings from cardiomyocytes, to help understand E1784K dynamic response to increased stimulation frequency.

Another limitation in my whole-cell recordings was using fluoride ions in the intracellular solution. Although used to stabilize and maintain the giga-ohm seal, fluoride ions shift SSFI- $V_{1/2}$ . To minimize this effect, activation and fast inactivation voltage-dependences were measured immediately after intracellular solution equilibration. Fluoride is also a phosphatase inhibitor; thus, channels in the whole-cell configuration were mainly phosphorylated. Although this effect may bias the results, it may further validate the biophysical and physiological inferences.

### 5.2.2. Calcium Buffering

The cytosolic calcium buffer used was EGTA. This calcium chelator is suitable for the calcium concentrations (0  $\mu$ M – 2.5  $\mu$ M) buffered in the patch-clamp experiments.

According to Bers *et al.* (2010), selecting the appropriate calcium buffer to chelate cytosolic calcium depends on the buffer's dissociation constant ( $K_d$ ), which should lie away from the desired calcium concentration by a factor of  $10^1$  (Bers *et al.*, 2010). Following this rule, we selected EGTA, which at pH 7.4 (physiological pH) has a  $K_d \approx 67$  nM (Ben-Johny & Yue, 2014). Thus, both 500 nM and 2500 nM cytosolic calcium were strongly buffered by EGTA since these concentrations are above the  $K_d$  value. Although buffering 2500 nM cytosolic calcium lies above the range allowed by Bers *et al.* (2010), I did not consider this a significant issue for several reasons: (1) At 2500 nM cytosolic calcium, no shifts were observed in the wild-type (WT) SSFI- $V_{1/2}$ , similar to previous reports showing no SSFI- $V_{1/2}$  shifts at 0.3  $\mu$ M cytosolic calcium, also buffered with EGTA (Sarhan *et al.*, 2012). (2) Former studies using EGTA did not necessarily show calcium-induced biophysical shifts, despite surpassing the permissible concentration limit by  $10^x$ -folds ( $x=2,3,4$ ). The reported free cytosolic calcium in most studies is inaccurate given the presence of endogenous calcium in heterologous expression systems and cardiomyocytes. Past studies used EGTA and BAPTA to buffer cytosolic calcium between 1 and 10  $\mu$ M, which is well above the concentration range used in this study (Wingo *et al.*, 2004; Shah *et al.*, 2006; Potet *et al.*, 2009; Biswas *et al.*, 2009; Sarhan *et al.*, 2012). When the calcium chelator, HEDTA, is used in buffering 0  $\mu$ M to 10  $\mu$ M cytosolic calcium, no shifts are observed in WT SSFI- $V_{1/2}$  (Ben-Johny & Yue, 2014). The SSFI- $V_{1/2}$  is depolarized when cytosolic calcium is elevated from 0  $\mu$ M to 10  $\mu$ M and buffered with BAPTA, which has a relatively high affinity for calcium (low  $K_d$ ), compared to EDTA, and is supposedly super-saturated with very high calcium concentrations.

HEDTA, like EDTA (except that the former is highly soluble in water) has a  $K_d \approx 4$   $\mu$ M. HEDTA affinity for calcium far exceeds the desired concentrations I used in my experiments (500 nM and 2500 nM), making hEDTA an inappropriate chelator. No shifts in WT SSFI- $V_{1/2}$  are caused by free cytosolic calcium (10  $\mu$ M) when buffered with HEDTA (Ben-Johny *et al.*, 2014). In addition, hEDTA's affinity for calcium is very weak compared to EGTA. EGTA is highly selective for calcium. EGTA- $K_d$  for magnesium is in the millimolar range (9 mM) compared to EDTA which has a higher affinity for magnesium (2.5  $\mu$ M) (Parsons *et al.*, 1996).

BAPTA was not used in this study since it is usually used for chelating transient calcium currents, prevalent in iPSC-derived cardiomyocytes, due to its rapid forward and reverse chelation kinetics (BAPTA has a  $K_d \approx 192$  nM, similar to EGTA's). My objective

was to study the long-term cytosolic calcium effects on channel properties that take a longer time to develop, such as the non-inactivating state, underlying late  $I_{Na}$ , or the slow-inactivated state. The biophysical protocols simulated were long enough providing sufficient time for EGTA to execute its buffering effects. In addition, upon whole-cell formation, I waited 10 min to allow for the seal to stabilize and for the biophysical shifts to equilibrate with fluoride ions. Thus, allowing sufficient time for EGTA to buffer calcium. An additional culprit in this study arises from using fluoride ions, since they avidly bind to calcium ( $K_{sp} \approx 3.45 \times 10^{-11}$ ), potentially decreasing cytosolic calcium levels.

The debatable shift in SSFI- $V_{1/2}$  caused by elevated cytosolic calcium can be attributed to the inconsistencies in experimentation between patch clampers. The contemporary thought in the field leans towards the notion that calcium does not regulate fast inactivation in  $Na_v1.5$ , since recent  $Na_v1.5$ -CTD crystal structures showed a more  $Ca_v1.2$ -like mode of calcium-calmodulin regulation in  $Na_v1.5$  (Pitt & Lee, 2016) compared to the earlier models (Shah *et al.*, 2006; Sarhan *et al.*, 2012).

A major limitation in this study, which affected dynamic action potential simulations, is the inability to study  $Na_v1.5$  response to subspace calcium levels, which can rise to 10  $\mu$ M or more. Although proven to not affect WT  $Na_v1.5$ , as confirmed using photo-uncaging and calcium spillover techniques, subspace calcium can modulate mutant channel type.

Many of the mechanistic speculations on calcium effects in  $Na_v1.5$ , mediated by its association with calmodulin, require experimental validation. To test the legitimacy of the calcium-calmodulin speculations in **Chapter 2** and **Chapter 3**, the free calcium in the intracellular pipette can be replaced with barium, which weakly binds to calmodulin. The calcium effects on mixed  $Na_v1.5$  mutants can also be tested with calmodulin mutants caused by *CALM1* and *CALM2* genes, which underlie LQT15 and LQT16, respectively.

### 5.2.3. The $\beta$ 1-Subunit

The purpose of co-transfecting  $Na_v1.5$   $\alpha$  subunit with the  $\beta$ 1-subunit was to enhance channel expression in CHO-K1 and HEK293 cells. However, certain doubts may arise about whether maximal transfection efficiency is obtained. All the cells patch-clamped were glowing and expressed  $I_{Na}$ , which suggests close to 100% co-transfection

of eGFP and the Nav<sub>v</sub>1.5  $\alpha$ -subunit. I assumed that, since both the  $\alpha$ -subunit and eGFP were successfully co-transfected into the cells, the  $\beta$ 1-subunit, which was present in the mixture, is also expressed. To further confirm  $\beta$ 1-subunit co-expression, I compared my biophysical results (from **Chapter 2**) with past reports.

Vilin *et al.* (1999) compared fast and slow inactivation between skeletal (Nav<sub>v</sub>1.4) and cardiac (Nav<sub>v</sub>1.5) voltage-gated sodium channels, in which the co-expression proportion was 1:1 for  $\alpha$  and  $\beta$ 1-subunits (Vilin *et al.*, 1999).  $\beta$ 1-subunit co-expression has a minor effect on fast inactivation voltage-dependence in Nav<sub>v</sub>1.5 compared to Nav<sub>v</sub>1.4, although another study shows a depolarized shift in SSFI- $V_{1/2}$  (Maltsev *et al.*, 2009). The steady-state slow inactivation midpoint (SSSI- $V_{1/2}$ ) is negatively shifted in Nav<sub>v</sub>1.4 by the  $\beta$ 1-subunit compared to a negligible shift in Nav<sub>v</sub>1.5. Slow inactivation kinetics are accelerated by the  $\beta$ 1-subunit in Nav<sub>v</sub>1.5 near SSSI- $V_{1/2}$  potentials. In one study, TsA201 cells were co-transfected with either  $\alpha + \beta$ 1 or  $\alpha + \beta$ 2 subunits (Maltsev *et al.*, 2009). The co-transfected  $\beta$ 1-subunit results in slower sodium current decay and a larger amplitude in late  $I_{Na}$  compared to peak  $I_{Na}$ . These results were compared to the minimal shifts observed in the  $\alpha + \beta$ 2-subunits or the  $\alpha$ -subunit conditions. When co-expressed with the  $\beta$ 1-subunit in *Xenopus* Oocytes, Nav<sub>v</sub>1.5 expression is increased with no modifications in gating (Qu *et al.*, 1995). It is clear then that the heterologous expression system used impacts the interaction between Nav<sub>v</sub>1.5  $\alpha$ -subunit and  $\beta$ 1-subunit.

Since I did not perform experiments in the absence of  $\beta$ 1, I compare in **Table 5-1** the HEK 293 WT  $\alpha$ -subunit +  $\beta$ 1-subunit + eGFP results (from **Chapter 2**) to HEK 293 WT  $\alpha$ -subunit (performed with 0 nM cytosolic calcium, pH 7.4, and at room temperature) retrieved from Vilin *et al.* (2012). All differences can be attributed to the  $\beta$ 1-subunit.

**Table 5-1 Differences between  $\alpha + \beta 1$  and  $\alpha - \beta 1$  subunits**

Parameters	$\alpha + \beta 1$ (Chapter 2)	$\alpha - \beta 1$ (Vilin <i>et al.</i> , 2012)
GV- $V_{1/2}$	$-43.8 \pm 1.10$	$-32.6 \pm 2.8$
GV-z	$4.92 \pm 0.26$	$3.8 \pm 0.2$
SSFI- $V_{1/2}$	$-89.2 \pm 1.97$	$-80.6 \pm 1.3$
SSFI-z	$-3.72 \pm 0.28$	$-4.4 \pm 0.1$
SSSI- $V_{1/2}$	$-70.8 \pm 2.28$	$-71.4 \pm 3.2$
SSSI-z	$-1.34 \pm 0.07$	$1.9 \pm 0.12$
SSSI- $V_0$	$0.30 \pm 0.03$	$0.36 \pm 0.05$
Fast Inactivation $\tau_{max}^*$	65	109
SI <sub>onset</sub> $\tau_1$ (-50 mV)	$0.54 \pm 0.41$	$0.8 \pm 0.2$
SI <sub>onset</sub> $\tau_2$ (-50 mV)	$14.6 \pm 1.44$	$6.0 \pm 1.1$
SI <sub>recovery</sub> $\tau_1$ (-110 mV)	$0.04 \pm 0.02$	$0.5 \pm 0.1$
SI <sub>recovery</sub> $\tau_2$ (-110 mV)	$2.06 \pm 0.31$	$7.9 \pm 2.9$

\*this parameter is the maximum amplitude of the Gaussian distribution fit to the fast inactivation time constant versus voltage curve. GV, conductance; SSFI, steady-state fast inactivation; SSSI, steady-state slow inactivation; SI, slow inactivation

The accelerated slow inactivation kinetics observed in Vilin *et al.* (1999) coincides with the observed shifts in slow inactivation recovery (both  $\tau_1$  and  $\tau_2$ ) and onset ( $\tau_1$ ) time constants (**Table 5-1**). The negative shift in activation and fast inactivation voltage-dependences along with the enhanced fast inactivation kinetics caused by the  $\beta 1$ -subunit is comparable with the well-known shifts also caused by the  $\beta 1$ -subunit in adult rat brain type IIA, embryonic rat brain type III, and rat skeletal muscle  $Na_V$  channels (Patton *et al.*, 1994). Thus, the patch-clamp assay proved the  $\beta 1$ -subunit expression. Immunocytochemistry would not be ideal to test for the presence of the  $\beta 1$ -subunit since HEK293 cells tend to cluster and are difficult to isolate for visual assays.

Whether the temperature or cytosolic calcium effects reported in this thesis were partly due to the  $\beta 1$ -subunit is unknown; however, the  $\beta 1$ -subunit is not known to directly interact with the DIII-DIV linker and the CTD (Qu *et al.*, 1995; Chen *et al.*, 2012; Gilchrist *et al.*, 2013). The  $\beta 1$ -subunit aggravates the biophysical defects induced by the DIV S3-S4 linker  $Na_V 1.5$  mutant, T1620M: fast inactivation is destabilized and its recovery kinetics are accelerated (Makita *et al.*, 2000). The non-covalent interactions between the  $\beta 1$ -subunit and  $Na_V 1.5$  may be directly affected by this extracellular linker mutant. However, it is unknown whether the intracellular mutants studied in this thesis affect upper stream channel structures engaged with the  $\beta 1$ -subunit.

#### 5.2.4. Action Potential Modelling

The Tüsscher-Noble-Noble-Panfilov (TNNP) model used in **Chapter 2** does not show the expected E1784K-induced prolongation in APD compared to the O'Hara-Rudy (O'Rd) Model (**Chapter 3** and **Chapter 4**). The transient outward ( $I_{Kto}$ ) and slow delayed rectifier ( $I_{Ks}$ ) potassium currents in the TNNP model are approximately 11-folds and 4-folds greater than in the O'Rd model, respectively. Thus, the depolarizing current is greatly offset by the immense repolarizing current in the TNNP model. Additionally, the rapid delayed rectifier ( $I_{Kr}$ ) to slow delayed rectifier ( $I_{Ks}$ ) proportions are approximately equal in the TNNP model compared to ~9:1 ratio in the O'Rd model. Reduced  $I_{Ks}$  underlies prolonged midmyocardial action potentials in LQT3, the reason why prolonged APDs caused by  $\Delta$ KPQ, E1784K, 1795insD, and Q1909R mutants were observed in the O'Rd model (Shimizu & Antzelevitch, 1998).

The disruption of the AP waveforms is more prominent in E1784K in the O'Rd model. The elevated late  $I_{Na}$  in E1784K is high at resting potentials compared to the other mutants studied in **Chapter 2**. Although there is minimal sodium conductance at resting potentials, the normalized late  $I_{Na}$  in E1784K is high, suggesting a readily available sodium channel pool. The diastolic calcium at rest is sufficient to attenuate the late  $I_{Na}$  in other mutants with higher sensitivity to cytosolic calcium, compared to E1784K. DADs and EADs due to exacerbated late  $I_{Na}$  were observed in APs simulated with E1784K.

The reduced  $dV/dt$  in E1784K is due to decreased channel availability at resting potential, caused by the depolarized and hyperpolarized voltage-dependence of activation and fast inactivation, respectively. Previous studies show that the decrease in 1795inD upstroke velocity is caused by a channel trafficking defect (Veldkamp *et al.*, 2000a; Clancy & Rudy, 2002). Unfortunately, the absolute channel conductance was not quantified in the AP models since I did not measure channel trafficking/expression.

#### 5.2.5. Physiological and Medical Implications

To date, only one study shows that an E1784K carrier's response to exercise is like other patients with *SCN5a* mutations displaying QT shortening during exercise (Schwartz *et al.*, 1995). This result may contradict the main results presented in this

thesis showing the unique response of E1784K to physiological triggers compared to other mixed syndrome mutants. However, other factors, which were not studied, determine E1784K arrhythmogenicity at the clinical and molecular levels. At the clinical level, factors such as ethnicity, sex, and age may contribute to the differential responses exhibited by patients with *SCN5a* mutations to exercise stress testing. I previously collaborated with clinicians with access to data on the response of pediatric patients with *SCN5a* mutations to exercise stress tests: E1784K carriers had a highly variable response to exercise with a few E1784K carriers showing QT shortening during peak exercise and prolongation during recovery from exercise. In other carriers, a prolonged QT<sub>C</sub> is induced by exercise, which recovers to baseline during the recovery phase (A-E. Baruteau, personal communication, February 3, 2016).

In this thesis, my aim was to elucidate potential sources of arrhythmogenesis at the molecular level. Other factors, aside from temperature and cytosolic calcium, may determine arrhythmogenicity: various intracellular kinases are activated during heightened sympathetic stimulation, having the potential to sway E1784K channel type to loss-of-function or gain-of-function. This variability may correlate with the phenotypic heterogeneity observed in carriers. CaMKII $\delta$ c and PKA both decrease Nav1.5 availability by stabilizing the slow-inactivated state (Qu *et al.*, 1996; Herren *et al.*, 2013). Intriguingly, CaMKII $\delta$ c also augments the late I<sub>Na</sub> in Nav1.5, thereby inducing mixed channel behavior (Herren *et al.*, 2013). CaMKII $\delta$ c activation may increase risk for arrhythmias, especially with mixed syndrome Nav1.5 mutants. At high heart rates, the inherent rise in sodium channel use-dependence may be further exacerbated by these kinases in E1784K, thereby ameliorating the gain-of-function induced by temperature and cytosolic calcium factors. Thus, the E1784K channel type pendulum can be acted upon by various external forces. The effects of channel modulators on the mutants must be further examined to appropriately target the channel biophysical defects with suitable pharmacological agent(s).

Although I show that ranolazine does not suppress late I<sub>Na</sub> in E1784K, under elevated temperature and cytosolic calcium, the drug may be used to clinically screen for genotype-positive patients while exercising. It is clear that traditional provocative drugs used to unmask arrhythmias may not necessarily be provocative under different physiological states. The channel type combined with the external trigger affects how the

drug interacts with the channel. Thus, exercise stress tests and provocative drug tests can be potentially combined to fully elucidate disease entity.

Ranolazine, as suggested in **Chapter 3**, may be resisted by the high entropy CTD in E1784K due to its large size compared to other classic antiarrhythmics. Follow-up experiments using Lidocaine could test the validity of this speculation, since the drug is smaller and shares 50 % identity of ranolazine. One risk associated with screening classic antiarrhythmics against E1784K and other  $Na_v1.5$  mutants is that these drugs usually have high potency to block peak  $I_{Na}$ . Reducing sodium conductance may exacerbate biophysical defects underpinning channel loss-of-function. Thus, newer approaches in treating gain-of-function should be pursued as with the novel aryl sulfonamides, stabilizing fast inactivation extracellularly, or GS-6615 (Eleclazine), the highly selective late  $I_{Na}$  blocker (Rajamani *et al.*, 2016).

### 5.3. Conclusions and Future Directions

Mixed syndrome mutants, like E1784K, are uniquely modulated by physiological and pharmacological switches. Genotype-phenotype correlations generally constitute the basis for treatment for arrhythmias, such as in LQT3. However, it is clear from this study that the channotype-trigger interaction further complicates the intricate genotype-phenotype relationship in *SCN5a* mutation carriers. Thus, prescribing the appropriate medication for arrhythmia treatment in patients is difficult. In fact, a rigorous analysis of channotype may indicate that no suitable therapeutics currently exist for ameliorating cardiac disease. This is supported by the current focus on use of device therapy with implantable cardioverter defibrillators (ICDs). Future drug discoveries should strategically be aimed at treating both gain-of-function and loss-of-function in  $Na_v1.5$ . Although challenging, most BrS1 and LQT3 mutants display mixed channel defects, which are modulated by external factors. Unmasking these biophysical abnormalities can vary between individuals and depend on the physiological state. Thus, alternating phenotypes are observed in 1795insD carriers at different heart rates. Dividing Brugada and Long-QT syndromes as separate clinical entities may be beneficial for diagnosis but may not be the correct approach for personalized treatment. The solution then may be to administer more than one drug type for mixed syndrome patients: one targeting loss-of-function and the other for gain-of-function. However, there are currently no  $Na_v$ -selective drugs targeting loss-of-function. To minimize the risk for blocking peak  $I_{Na}$ ,

pharmaceutical companies should design drugs that target the channel extracellularly, thereby minimizing drug interaction near the channel inner vestibule and pore where most mixed syndrome mutants exist. Aryl sulfonamides have been shown to stabilize fast inactivation in Nav1.7. Developing Nav1.5-specific aryl sulfonamides will help ameliorate LQT3-related biophysical defects. Furthermore, understanding the structural gating correlates in slow inactivation is pivotal in designing drugs which target and prevent slow inactivation. Limiting slow inactivation will prevent channel loss-of-function caused by elevated frequency and other channel modifiers. Fully treating *SCN5a* mutations is an important pharmaceutical goal, and keenly inspecting *SCN5a* channel-type-trigger interactions is a first step toward precision arrhythmia management and treatment.

## References

- Abdelsayed M, Baruteau A-E, Gibbs K, Sanatani S, Krahn AD, Probst V & Ruben PC (2017). Differential calcium sensitivity in Na<sub>v</sub> 1.5 mixed syndrome mutants: Calcium and mixed syndrome mutants. *J Physiol*; DOI: 10.1113/JP274536.
- Abdelsayed M, Peters CH & Ruben PC (2015). Differential thermosensitivity in mixed syndrome cardiac sodium channel mutants. *J Physiol*; DOI: 10.1113/JP270139.
- Abriel H, Wehrens XHT, Benhorin J, Kerem B & Kass RS (2000). Molecular Pharmacology of the Sodium Channel Mutation D1790G Linked to the Long-QT Syndrome. *Circulation* **102**, 921–925.
- Ackerman MJ, Splawski I, Makielski JC, Tester DJ, Will ML, Timothy KW, Keating MT, Jones G, Chadha M, Burrow CR, Stephens JC, Xu C, Judson R & Curran ME (2004). Spectrum and prevalence of cardiac sodium channel variants among black, white, Asian, and Hispanic individuals: implications for arrhythmogenic susceptibility and Brugada/long QT syndrome genetic testing. *Heart Rhythm Off J Heart Rhythm Soc* **1**, 600–607.
- Ahern CA, Eastwood AL, Dougherty DA & Horn R (2008). Electrostatic Contributions of Aromatic Residues in the Local Anesthetic Receptor of Voltage-Gated Sodium Channels. *Circ Res* **102**, 86–94.
- Ahern CA, Payandeh J, Bosmans F & Chanda B (2016). The hitchhiker’s guide to the voltage-gated sodium channel galaxy. *J Gen Physiol* **147**, 1–24.
- Ahuja S et al. (2015). Structural basis of Nav1.7 inhibition by an isoform-selective small-molecule antagonist. *Science* **350**, aac5464-aac5464.
- Aizawa Y, Takatsuki S, Kimura T, Nishiyama N, Fukumoto K, Tanimoto Y, Tanimoto K, Miyoshi S, Suzuki M, Yokoyama Y, Chinushi M, Watanabe I, Ogawa S, Aizawa Y, Antzelevitch C & Fukuda K (2013). Ventricular fibrillation associated with complete right bundle branch block. *Heart Rhythm* **10**, 1028–1035.
- Akar FG (2002). Unique Topographical Distribution of M Cells Underlies Reentrant Mechanism of Torsade de Pointes in the Long-QT Syndrome. *Circulation* **105**, 1247–1253.
- Aman TK, Grieco-Calub TM, Chen C, Rusconi R, Slat EA, Isom LL & Raman IM (2009). Regulation of Persistent Na Current by Interactions between Subunits of Voltage-Gated Na Channels. *J Neurosci* **29**, 2027–2042.
- Amin AS, de Groot EAA, Ruijter JM, Wilde AAM & Tan HL (2009). Exercise-Induced ECG Changes in Brugada Syndrome. *Circ Arrhythm Electrophysiol* **2**, 531–539.

- Amin AS, Herfst LJ, Delisle BP, Klemens CA, Rook MB, Bezzina CR, Underkofler HAS, Holzem KM, Ruijter JM, Tan HL, January CT & Wilde AAM (2008). Fever-induced QTc prolongation and ventricular arrhythmias in individuals with type 2 congenital long QT syndrome. *J Clin Invest* **118**, 2552–2561.
- Amin AS, Klemens CA, Verkerk AO, Meregalli PG, Asghari-Roodsari A, de Bakker JMT, January CT, Wilde A a. M & Tan HL (2010a). Fever-triggered ventricular arrhythmias in Brugada syndrome and type 2 long-QT syndrome. *Neth Heart J Mon J Neth Soc Cardiol Neth Heart Found* **18**, 165–169.
- Amin AS, Tan HL & Wilde AAM (2010b). Cardiac ion channels in health and disease. *Heart Rhythm* **7**, 117–126.
- An RH, Wang XL, Kerem B, Benhorin J, Medina A, Goldmit M & Kass RS (1998). Novel LQT-3 mutation affects Na<sup>+</sup> channel activity through interactions between alpha- and beta1-subunits. *Circ Res* **83**, 141–146.
- Andreasen C, Refsgaard L, Nielsen JB, Sajadieh A, Winkel BG, Tfelt-Hansen J, Haunsø S, Holst AG, Svendsen JH & Olesen MS (2013). Mutations in genes encoding cardiac ion channels previously associated with sudden infant death syndrome (SIDS) are present with high frequency in new exome data. *Can J Cardiol* **29**, 1104–1109.
- Antzelevitch C (2001a). The Brugada syndrome: diagnostic criteria and cellular mechanisms. *Eur Heart J* **22**, 356–363.
- Antzelevitch C (2001b). Transmural dispersion of repolarization and the T wave. *Cardiovasc Res* **50**, 426–431.
- Antzelevitch C (2004). Electrophysiological Effects of Ranolazine, a Novel Antianginal Agent With Antiarrhythmic Properties. *Circulation* **110**, 904–910.
- Antzelevitch C (2005). Brugada Syndrome: Report of the Second Consensus Conference: Endorsed by the Heart Rhythm Society and the European Heart Rhythm Association. *Circulation* **111**, 659–670.
- Antzelevitch C (2007). Genetic basis of Brugada syndrome. *Heart Rhythm Off J Heart Rhythm Soc* **4**, 756–757.
- Antzelevitch C, Belardinelli L, Wu L, Fraser H, Zygmunt AC, Burashnikov A, Di Diego JM, Fish JM, Cordeiro JM, Goodrow RJ, Scornik F & Perez G (2004). Electrophysiologic properties and antiarrhythmic actions of a novel antianginal agent. *J Cardiovasc Pharmacol Ther* **9 Suppl 1**, S65-83.
- Antzelevitch C, Brugada P, Brugada J & Brugada R (2005). Brugada syndrome: from cell to bedside. *Curr Probl Cardiol* **30**, 9–54.

- Antzelevitch C, Brugada P, Brugada J, Brugada R, Shimizu W, Gussak I & Perez Riera AR (2002). Brugada Syndrome: A Decade of Progress. *Circ Res* **91**, 1114–1118.
- Antzelevitch C & Burashnikov A (2011). Overview of Basic Mechanisms of Cardiac Arrhythmia. *Card Electrophysiol Clin* **3**, 23–45.
- Antzelevitch C & Fish JM (2006). Therapy for the Brugada syndrome. *Handb Exp Pharmacol* 305–330.
- Antzelevitch C, Nesterenko V, Shryock JC, Rajamani S, Song Y & Belardinelli L (2014). The Role of Late I Na in Development of Cardiac Arrhythmias. In *Voltage Gated Sodium Channels*, ed. Ruben PC, pp. 137–168. Springer Berlin Heidelberg, Berlin, Heidelberg. Available at: [http://link.springer.com/10.1007/978-3-642-41588-3\\_7](http://link.springer.com/10.1007/978-3-642-41588-3_7) [Accessed June 16, 2015].
- Antzelevitch C & Oliva A (2006). Amplification of spatial dispersion of repolarization underlies sudden cardiac death associated with catecholaminergic polymorphic VT, long QT, short QT and Brugada syndromes. *J Intern Med* **259**, 48–58.
- Antzelevitch C & Patocskai B (2015). Brugada syndrome. Clinical, Genetic, Molecular. *Curr Probl Cardiol*. Available at: <http://www.sciencedirect.com/science/article/pii/S0146280615000961> [Accessed October 14, 2015].
- Antzelevitch C, Sun Z-Q, Zhang Z-Q & Yan G-X (1996). Cellular and ionic mechanisms underlying erythromycin-induced long QT intervals and torsade de pointes. *J Am Coll Cardiol* **28**, 1836–1848.
- Antzelevitch C, Viskin S, Shimizu W, Yan G-X, Kowey P, Zhang L, Sicouri S, Di Diego JM & Burashnikov A (2007). Does Tpeak-Tend provide an index of transmural dispersion of repolarization? *Heart Rhythm Off J Heart Rhythm Soc* **4**, 1114.
- Antzelevitch C & Yan G-X (2010). J wave syndromes. *Heart Rhythm* **7**, 549–558.
- Armstrong CM & Bezanilla F (1977). Inactivation of the sodium channel. II. Gating current experiments. *J Gen Physiol* **70**, 567–590.
- Aziz PF, Wieand TS, Ganley J, Henderson J, Patel AR, Iyer VR, Vogel RL, McBride M, Vetter VL & Shah MJ (2011). Genotype- and mutation site-specific QT adaptation during exercise, recovery, and postural changes in children with long-QT syndrome. *Circ Arrhythm Electrophysiol* **4**, 867–873.
- Baartscheer A, Schumacher CA, Belterman CNW, Coronel R & Fiolet JWT (2003). SR calcium handling and calcium after-transients in a rabbit model of heart failure. *Cardiovasc Res* **58**, 99–108.

- Bagn ris C, DeCaen PG, Hall BA, Naylor CE, Clapham DE, Kay CWM & Wallace BA (2013). Role of the C-terminal domain in the structure and function of tetrameric sodium channels. *Nat Commun*; DOI: 10.1038/ncomms3465.
- Balser JR (2002). Inherited sodium channelopathies: models for acquired arrhythmias? *Am J Physiol - Heart Circ Physiol* **282**, H1175–H1180.
- Balser JR, Nuss HB, Orias DW, Johns DC, Marban E, Tomaselli GF & Lawrence JH (1996). Local anesthetics as effectors of allosteric gating. Lidocaine effects on inactivation-deficient rat skeletal muscle Na channels. *J Clin Invest* **98**, 2874.
- Bankston JR, Sampson KJ, Kateriya S, Glaaser IW, Malito DL, Chung WK & Kass RS (2007). A novel LQT-3 mutation disrupts an inactivation gate complex with distinct rate-dependent phenotypic consequences. *Channels Austin Tex* **1**, 273–280.
- Barajas-Martinez HM, Hu D, Cordeiro JM, Wu Y, Kovacs RJ, Meltser H, Kui H, Elena B, Brugada R, Antzelevitch C & Dumaine R (2008). Lidocaine-Induced Brugada Syndrome Phenotype Linked to a Novel Double Mutation in the Cardiac Sodium Channel. *Circ Res* **103**, 396–404.
- Baroudi G, Acharfi S, Larouche C & Chahine M (2002). Expression and intracellular localization of an SCN5A double mutant R1232W/T1620M implicated in Brugada syndrome. *Circ Res* **90**, E11-16.
- Baroudi G & Chahine M (2000). Biophysical phenotypes of SCN5A mutations causing long QT and Brugada syndromes. *FEBS Lett* **487**, 224–228.
- Barra S, Provid ncia R & Nascimento J (2013). Fever outperforms flecainide test in the unmasking of type 1 Brugada syndrome electrocardiogram. *Eur Eur Pacing Arrhythm Card Electrophysiol J Work Groups Card Pacing Arrhythm Card Cell Electrophysiol Eur Soc Cardiol* **15**, 394.
- Beaufort-Krol GCM, van den Berg MP, Wilde AAM, van Tintelen JP, Viersma JW, Bezzina CR & Bink-Boelkens MTE (2005). Developmental aspects of long QT syndrome type 3 and Brugada syndrome on the basis of a single SCN5A mutation in childhood. *J Am Coll Cardiol* **46**, 331–337.
- Belardinelli L (2006a). The mechanism of ranolazine action to reduce ischemia-induced diastolic dysfunction. *Eur Heart J Suppl* **8**, A10–A13.
- Belardinelli L (2006b). Inhibition of the late sodium current as a potential cardioprotective principle: effects of the late sodium current inhibitor ranolazine. *Heart* **92**, iv6-iv14.

- Benhorin J, Taub R, Goldmit M, Kerem B, Kass RS, Windman I & Medina A (2000). Effects of Flecainide in Patients With New SCN5A Mutation : Mutation-Specific Therapy for Long-QT Syndrome? *Circulation* **101**, 1698–1706.
- Ben-Johny M et al. (2015). Towards a Unified Theory of Calmodulin Regulation (Calmodulation) of Voltage-Gated Calcium and Sodium Channels. *Curr Mol Pharmacol* **8**, 188–205.
- Ben-Johny M, Yang PS, Niu J, Yang W, Joshi-Mukherjee R & Yue DT (2014). Conservation of Ca<sup>2+</sup>/Calmodulin Regulation across Na and Ca<sup>2+</sup> Channels. *Cell* **157**, 1657–1670.
- Ben-Johny M & Yue DT (2014). Calmodulin regulation (calmodulation) of voltage-gated calcium channels. *J Gen Physiol* **143**, 679–692.
- Bennett ES (1999). Effects of channel cytoplasmic regions on the activation mechanisms of cardiac versus skeletal muscle Na(+) channels. *Biophys J* **77**, 2999–3009.
- Bennett ES (2001). Channel cytoplasmic loops alter voltage-dependent sodium channel activation in an isoform-specific manner. *J Physiol* **535**, 371–381.
- Bennett ES (2004). Channel Activation Voltage Alone Is Directly Altered in an Isoform-specific Manner by Na v1.4 and Na v1.5 Cytoplasmic Linkers. *J Membr Biol* **197**, 155–168.
- Bennett MT, Gula LJ, Klein GJ, Skanes AC, Yee R, Leong-Sit P, Chattha I, Sy R, Jones DL & Krahn AD (2014). Effect of beta-blockers on QT dynamics in the long QT syndrome: measuring the benefit. *Eur Eur Pacing Arrhythm Card Electrophysiol J Work Groups Card Pacing Arrhythm Card Cell Electrophysiol Eur Soc Cardiol* **16**, 1847–1851.
- Bers DM, Patton CW & Nuccitelli R (2010). A Practical Guide to the Preparation of Ca<sup>2+</sup> h BuVers. *Calcium Living Cells* **99**, 1.
- Bezanilla F & Armstrong CM (1977). Inactivation of the sodium channel. I. Sodium current experiments. *J Gen Physiol* **70**, 549.
- Bezzina C, Veldkamp MW, van den Berg MP, Postma AV, Rook MB, Viersma J-W, van Langen IM, Tan-Sindhunata G, Bink-Boelkens MTE, van der Hout AH, Mannens MMAM & Wilde AAM (1999). A Single Na<sup>+</sup> Channel Mutation Causing Both Long-QT and Brugada Syndromes. *Circ Res* **85**, 1206–1213.
- Biswas S, DiSilvestre D, Tian Y, Halperin VL & Tomaselli GF (2009). Calcium-Mediated Dual-Mode Regulation of Cardiac Sodium Channel Gating. *Circ Res* **104**, 870–878.

- Black D., Tran Q-K & Persechini A (2004). Monitoring the total available calmodulin concentration in intact cells over the physiological range in free Ca<sup>2+</sup>. *Cell Calcium* **35**, 415–425.
- Bordoli L, Kiefer F, Arnold K, Benkert P, Battey J & Schwede T (2008). Protein structure homology modeling using SWISS-MODEL workspace. *Nat Protoc* **4**, 1–13.
- Brackenbury WJ & Isom LL (2008). Voltage-gated Na<sup>+</sup> channels: Potential for  $\beta$  subunits as therapeutic targets. *Expert Opin Ther Targets* **12**, 1191–1203.
- Brugada P & Brugada J (1992). Right bundle branch block, persistent ST segment elevation and sudden cardiac death: a distinct clinical and electrocardiographic syndrome: a multicenter report. *J Am Coll Cardiol* **20**, 1391–1396.
- Burashnikov A, Shimizu W & Antzelevitch C (2008). Fever accentuates transmural dispersion of repolarization and facilitates development of early afterdepolarizations and torsade de pointes under long-QT Conditions. *Circ Arrhythm Electrophysiol* **1**, 202–208.
- Capes DL, Goldschen-Ohm MP, Arcisio-Miranda M, Bezanilla F & Chanda B (2013). Domain IV voltage-sensor movement is both sufficient and rate limiting for fast inactivation in sodium channels. *J Gen Physiol* **142**, 101–112.
- Carle T, Fournier E, Sternberg D, Fontaine B & Tabti N (2009). Cold-induced disruption of Na<sup>+</sup> channel slow inactivation underlies paralysis in highly thermosensitive paramyotonia: Human Nav.4 channel mutation disrupts slow inactivation at cold. *J Physiol* **587**, 1705–1714.
- Casini S, Tan H, Bhuiyan Z, Bezzina C, Barnett P, Cerbai E, Mugelli A, Wilde A & Veldkamp M (2007). Characterization of a novel SCN5A mutation associated with Brugada syndrome reveals involvement of DIIIS4–S5 linker in slow inactivation. *Cardiovasc Res* **76**, 418–429.
- Castro Hevia J, Antzelevitch C, Tornés Bárzaga F, Dorantes Sánchez M, Dorticós Balea F, Zayas Molina R, Quiñones Pérez MA & Fayad Rodríguez Y (2006). Tpeak-Tend and Tpeak-Tend Dispersion as Risk Factors for Ventricular Tachycardia/Ventricular Fibrillation in Patients With the Brugada Syndrome. *J Am Coll Cardiol* **47**, 1828–1834.
- Catterall WA (2012). Voltage-gated sodium channels at 60: structure, function and pathophysiology: Voltage-gated sodium channels. *J Physiol* **590**, 2577–2589.
- Catterall WA, Raman IM, Robinson HPC, Sejnowski TJ & Paulsen O (2012). The Hodgkin-Huxley Heritage: From Channels to Circuits. *J Neurosci* **32**, 14064–14073.

- Cha A, Ruben PC, George AL, Fujimoto E & Bezanilla F (1999). Voltage sensors in domains III and IV, but not I and II, are immobilized by Na<sup>+</sup> channel fast inactivation. *Neuron* **22**, 73–87.
- Chagot B, Potet F, Balsler JR & Chazin WJ (2009). Solution NMR Structure of the C-terminal EF-hand Domain of Human Cardiac Sodium Channel NaV1.5. *J Biol Chem* **284**, 6436–6445.
- Chandra R, Chauhan VS, Starmer CF & Grant AO (1999). beta-Adrenergic action on wild-type and KPQ mutant human cardiac Na<sup>+</sup> channels: shift in gating but no change in Ca<sup>2+</sup>:Na<sup>+</sup> selectivity. *Cardiovasc Res* **42**, 490–502.
- Chandra R, Starmer CF & Grant AO (1998). Multiple effects of KPQ deletion mutation on gating of human cardiac Na<sup>+</sup> channels expressed in mammalian cells. *Am J Physiol* **274**, H1643-1654.
- Chen C, Calhoun JD, Zhang Y, Lopez-Santiago L, Zhou N, Davis TH, Salzer JL & Isom LL (2012). Identification of the Cysteine Residue Responsible for Disulfide Linkage of Na<sup>+</sup> Channel and 2 Subunits. *J Biol Chem* **287**, 39061–39069.
- Chen J, Makiyama T, Wuriyanghai Y, Ohno S, Sasaki K, Hayano M, Harita T, Nishiuchi S, Yuta Yamamoto null, Ueyama T, Shimizu A, Horie M & Kimura T (2015). Cardiac sodium channel mutation associated with epinephrine-induced QT prolongation and sinus node dysfunction. *Heart Rhythm Off J Heart Rhythm Soc*; DOI: 10.1016/j.hrthm.2015.08.021.
- Chen Q, Kirsch GE, Zhang D, Brugada R, Brugada J, Brugada P, Potenza D, Moya A, Borggrefe M, Breithardt G, Ortiz-Lopez R, Wang Z, Antzelevitch C, O'Brien RE, Schulze-Bahr E, Keating MT, Towbin JA & Wang Q (1998). Genetic basis and molecular mechanism for idiopathic ventricular fibrillation. *Nature* **392**, 293–296.
- Chen Y, Yu FH, Surmeier DJ, Scheuer T & Catterall WA (2006). Neuromodulation of Na<sup>+</sup> Channel Slow Inactivation via cAMP-Dependent Protein Kinase and Protein Kinase C. *Neuron* **49**, 409–420.
- Choi J-S, Tyrrell L, Waxman SG & Dib-Hajj SD (2004). Functional role of the C-terminus of voltage-gated sodium channel Nav1.8. *FEBS Lett* **572**, 256–260.
- Chorin E, Hu D, Antzelevitch C, Hochstadt A, Belardinelli L, Zeltser D, Barajas-Martinez H, Rozovski U, Rosso R, Adler A, Benhorin J & Viskin S (2016). Ranolazine for Congenital Long-QT Syndrome Type III: Experimental and Long-Term Clinical Data. *Circ Arrhythm Electrophysiol*; DOI: 10.1161/CIRCEP.116.004370.
- Chugh SS, Reinier K, Teodorescu C, Evanado A, Kehr E, Al Samara M, Mariani R, Gunson K & Jui J (2008). Epidemiology of sudden cardiac death: clinical and research implications. *Prog Cardiovasc Dis* **51**, 213–228.

- Clancy CE & Rudy Y (2002). Na<sup>+</sup> channel mutation that causes both brugada and long-QT syndrome phenotypes a simulation study of mechanism. *Circulation* **105**, 1208–1213.
- Clare null, Tate null, Nobbs null & Romanos null (2000). Voltage-gated sodium channels as therapeutic targets. *Drug Discov Today* **5**, 506–520.
- Collins CA & Rojas E (1982). Temperature dependence of the sodium channel gating kinetics in the node of Ranvier. *Q J Exp Physiol* **67**, 41–55.
- Cormier JW, Rivolta I, Tateyama M, Yang A-S & Kass RS (2002). Secondary Structure of the Human Cardiac Na<sup>+</sup> Channel C Terminus: EVIDENCE FOR A ROLE OF HELICAL STRUCTURES IN MODULATION OF CHANNEL INACTIVATION. *J Biol Chem* **277**, 9233–9241.
- Czapiński P, Blaszczyk B & Czuczwar SJ (2005). Mechanisms of action of antiepileptic drugs. *Curr Top Med Chem* **5**, 3–14.
- Day CP, McComb JM & Campbell RW (1990). QT dispersion: an indication of arrhythmia risk in patients with long QT intervals. *Br Heart J* **63**, 342–344.
- DeCaen PG, Yarov-Yarovoy V, Sharp EM, Scheuer T & Catterall WA (2009). Sequential formation of ion pairs during activation of a sodium channel voltage sensor. *Proc Natl Acad Sci U S A* **106**, 22498–22503.
- Denac H, Mevissen M & Scholtysik G (2000). Structure, function and pharmacology of voltage-gated sodium channels. *Naunyn Schmiedebergs Arch Pharmacol* **362**, 453–479.
- Deo R & Albert CM (2012). Epidemiology and Genetics of Sudden Cardiac Death. *Circulation* **125**, 620–637.
- Deschenes I (2002). Isoform-Specific Modulation of Voltage-Gated Na<sup>+</sup> Channels by Calmodulin. *Circ Res* **90**, 49e–57.
- Deschênes I, Baroudi G, Berthet M, Barde I, Chalvidan T, Denjoy I, Guicheney P & Chahine M (2000). Electrophysiological characterization of SCN5A mutations causing long QT (E1784K) and Brugada (R1512W and R1432G) syndromes. *Cardiovasc Res* **46**, 55–65.
- Di Diego JM (2002). Ionic and Cellular Basis for the Predominance of the Brugada Syndrome Phenotype in Males. *Circulation* **106**, 2004–2011.
- Di Diego JM, Fish JM & Antzelevitch C (2005). Brugada syndrome and ischemia-induced ST-segment elevation. Similarities and differences. *J Electrocardiol* **38**, 14–17.

- Di Diego JM, Sun ZQ & Antzelevitch C (1996). I(to) and action potential notch are smaller in left vs. right canine ventricular epicardium. *Am J Physiol* **271**, H548-561.
- Doetzer AD, Sotomaior VS, Bubna MH & Raskin S (2011). What can be done when asymptomatic patients discover they have Brugada syndrome? A case report of Brugada syndrome. *Int J Cardiol* **150**, e96–e97.
- Dumaine R, Towbin JA, Brugada P, Vatta M, Nesterenko DV, Nesterenko VV, Brugada J, Brugada R & Antzelevitch C (1999). Ionic mechanisms responsible for the electrocardiographic phenotype of the Brugada syndrome are temperature dependent. *Circ Res* **85**, 803–809.
- Dumaine R, Wang Q, Keating MT, Hartmann HA, Schwartz PJ, Brown AM & Kirsch GE (1996). Multiple mechanisms of Na<sup>+</sup> channel–linked long-QT syndrome. *Circ Res* **78**, 916–924.
- Egri C, Vilin YY & Ruben PC (2012). A thermoprotective role of the sodium channel  $\beta$ 1 subunit is lost with the  $\beta$ 1(C121W) mutation: Na Channel  $\beta$ 1 Subunit Is Thermoprotective. *Epilepsia* **53**, 494–505.
- Elbey MA, Cil H, Onturk E & Islamoglu Y (2012). OTc prolongation and torsade de pointes ventricular tachycardia in a small dose voriconazole therapy. *Eur Rev Med Pharmacol Sci* **16**, 100–102.
- Elias CL, Xue X-H, Marshall CR, Omelchenko A, Hryshko LV & Tibbits GF (2001). Temperature dependence of cloned mammalian and salmonid cardiac Na<sup>+</sup>/Ca<sup>2+</sup> exchanger isoforms. *Am J Physiol-Cell Physiol* **281**, C993–C1000.
- El-Sayed MF, Abu-Amra E & Badr A (2012). Effect of changes in temperature on the force–frequency relationship in the heart of catfish (*Clarias gariepinus*). *J Basic Appl Zool* **65**, 274–281.
- Errington AC, Stohr T, Heers C & Lees G (2007). The Investigational Anticonvulsant Lacosamide Selectively Enhances Slow Inactivation of Voltage-Gated Sodium Channels. *Mol Pharmacol* **73**, 157–169.
- Faber GM & Rudy Y (2000). Action potential and contractility changes in [Na<sup>+</sup>]<sub>i</sub> overloaded cardiac myocytes: a simulation study. *Biophys J* **78**, 2392–2404.
- Featherstone DE, Fujimoto E & Ruben PC (1998). A defect in skeletal muscle sodium channel deactivation exacerbates hyperexcitability in human paramyotonia congenita. *J Physiol* **506**, 627–638.
- Featherstone DE, Richmond JE & Ruben PC (1996). Interaction between fast and slow inactivation in Skm1 sodium channels. *Biophys J* **71**, 3098.

- Fenichel RR, Malik M, Antzelevitch C, Sanguinetti M, Roden DM, Priori SG, Ruskin JN, Lipicky RJ, Cantilena LR & Independent Academic Task Force (2004). Drug-induced torsades de pointes and implications for drug development. *J Cardiovasc Electrophysiol* **15**, 475–495.
- Ferrier GR, Smith RH & Howlett SE (2003). Calcium sparks in mouse ventricular myocytes at physiological temperature. *Am J Physiol - Heart Circ Physiol* **285**, H1495–H1505.
- Fish JM & Antzelevitch C (2004a). Role of sodium and calcium channel block in unmasking the Brugada syndrome. *Heart Rhythm Off J Heart Rhythm Soc* **1**, 210–217.
- Fish JM & Antzelevitch C (2004b). The link between hypothermia and the Brugada syndrome. *J Cardiovasc Electrophysiol* **15**, 942.
- Francis J & Antzelevitch C (2003). Brugada-like electrocardiographic pattern. *Indian Pacing Electrophysiol J* **3**, 91–92.
- Franz MR (2003). The Electrical Restitution Curve Revisited: Steep or Flat Slope-Which is Better? *J Cardiovasc Electrophysiol* **14**, S140–S147.
- Fredj S, Lindegger N, Sampson KJ, Carmeliet P & Kass RS (2006a). Altered Na<sup>+</sup> channels promote pause-induced spontaneous diastolic activity in long QT syndrome type 3 myocytes. *Circ Res* **99**, 1225–1232.
- Fredj S, Sampson KJ, Liu H & Kass RS (2006b). Molecular basis of ranolazine block of LQT-3 mutant sodium channels: evidence for site of action. *Br J Pharmacol* **148**, 16–24.
- Frohnwieser B, Chen LQ, Schreibmayer W & Kallen RG (1997). Modulation of the human cardiac sodium channel alpha-subunit by cAMP-dependent protein kinase and the responsible sequence domain. *J Physiol* **498**, 309–318.
- Fu Y, Zhang G-Q, Hao X-M, Wu C-H, Chai Z & Wang S-Q (2005). Temperature Dependence and Thermodynamic Properties of Ca<sup>2+</sup> Sparks in Rat Cardiomyocytes. *Biophys J* **89**, 2533–2541.
- Fukuyama M, Ohno S, Makiyama T & Horie M (2016). Novel *SCN10A* variants associated with Brugada syndrome. *Europace* **18**, 905–911.
- G. S, C. L, A. B & A. B (2001). Dependence of I<sub>Ks</sub> biophysical properties on the expression system. *Pflügers Arch Eur J Physiol* **442**, 891–895.

- Gabelli SB, Boto A, Kuhns VH, Bianchet MA, Farinelli F, Aripirala S, Yoder J, Jakoncic J, Tomaselli GF & Amzel LM (2014). Regulation of the Nav1.5 cytoplasmic domain by calmodulin. *Nat Commun* **5**, 5126.
- García-Borbolla M, García-Borbolla R, Valenzuela LF & Trujillo F (2007). [Ventricular tachycardia induced by exercise testing in a patient with Brugada syndrome]. *Rev Esp Cardiol* **60**, 993–994.
- Gaudio C, Carlier E, Youssouf F, Clare JJ, Debanne D & Alcaraz G (2011). Calmodulin and calcium differentially regulate the neuronal Nav1.1 voltage-dependent sodium channel. *Biochem Biophys Res Commun* **411**, 329–334.
- Gaur N, Rudy Y & Hool L (2009). Contributions of Ion Channel Currents to Ventricular Action Potential Changes and Induction of Early Afterdepolarizations During Acute Hypoxia. *Circ Res* **105**, 1196–1203.
- Gilchrist J, Das S, Van Petegem F & Bosmans F (2013). Crystallographic insights into sodium-channel modulation by the 4 subunit. *Proc Natl Acad Sci* **110**, E5016–E5024.
- Gimeno JR, Oliva MJ, Lacunza J, Alberola AG, Sabater M, Martínez-Sánchez J, Saura D, Romero A & Valdés M (2010). Characteristics of sudden death in inherited heart disease. *Rev Esp Cardiol* **63**, 268–276.
- Glaaser IW, Bankston JR, Liu H, Tateyama M & Kass RS (2006). A carboxyl-terminal hydrophobic interface is critical to sodium channel function. Relevance to inherited disorders. *J Biol Chem* **281**, 24015–24023.
- Glaaser IW, Osteen JD, Puckerin A, Sampson KJ, Jin X & Kass RS (2012). Perturbation of sodium channel structure by an inherited Long QT Syndrome mutation. *Nat Commun* **3**, 706.
- Goldin AL (2003). Mechanisms of sodium channel inactivation. *Curr Opin Neurobiol* **13**, 284–290.
- Grant AO, Carboni MP, Neplioueva V, Starmer CF, Memmi M, Napolitano C & Priori S (2002). Long QT syndrome, Brugada syndrome, and conduction system disease are linked to a single sodium channel mutation. *J Clin Invest* **110**, 1201–1209.
- Grimster A, Segal OR & Behr ER (2008). Type I Brugada electrocardiogram pattern during the recovery phase of exercise testing. *Eur Eur Pacing Arrhythm Card Electrophysiol J Work Groups Card Pacing Arrhythm Card Cell Electrophysiol Eur Soc Cardiol* **10**, 897–898.
- Groenewegen WA, Bezzina CR, van Tintelen JP, Hoorntje TM, Mannens MMAM, Wilde AAM, Jongasma HJ & Rook MB (2003). A novel LQT3 mutation implicates the

- human cardiac sodium channel domain IVS6 in inactivation kinetics. *Cardiovasc Res* **57**, 1072–1078.
- Groome J, Lehmann-Horn F & Holzherr B (2011). Open- and closed-state fast inactivation in sodium channels: Differential effects of a site-3 anemone toxin. *Channels* **5**, 65–78.
- Groome JR, Dice MC, Fujimoto E & Ruben PC (2007). Charge Immobilization of Skeletal Muscle Na<sup>+</sup> Channels: Role of Residues in the Inactivation Linker. *Biophys J* **93**, 1519–1533.
- Groome JR, Fujimoto E & Ruben PC (2003). Negative charges in the DIII-DIV linker of human skeletal muscle Na<sup>+</sup> channels regulate deactivation gating. *J Physiol* **548**, 85–96.
- Gui J, Wang T, Trump D, Zimmer T & Lei M (2010). Mutation-specific effects of polymorphism H558R in SCN5A-related sick sinus syndrome. *J Cardiovasc Electrophysiol* **21**, 564–573.
- Hallaq H, Wang DW, Kunic JD, George AL, Wells KS & Murray KT (2012). Activation of protein kinase C alters the intracellular distribution and mobility of cardiac Na<sup>+</sup> channels. *Am J Physiol Heart Circ Physiol* **302**, H782-789.
- Hannon JP (1958). Effect of temperature on the heart rate, electrocardiogram and certain myocardial oxidations of the rat. *Circ Res* **6**, 771–778.
- Harris P & Lysitsas D (2016). Ventricular arrhythmias and sudden cardiac death. *BJA Educ* **16**, 221–229.
- Haufe V, Cordeiro J, Zimmer T, Wu Y, Schiccitano S, Benndorf K & Dumaine R (2005). Contribution of neuronal sodium channels to the cardiac fast sodium current is greater in dog heart Purkinje fibers than in ventricles. *Cardiovasc Res* **65**, 117–127.
- Haverkamp W (2000). The potential for QT prolongation and proarrhythmia by non-antiarrhythmic drugs: clinical and regulatory implications. Report on a Policy Conference of the European Society of Cardiology. *Eur Heart J* **21**, 1216–1231.
- Herren AW, Bers DM & Grandi E (2013). Post-translational modifications of the cardiac Na channel: contribution of CaMKII-dependent phosphorylation to acquired arrhythmias. *Am J Physiol Heart Circ Physiol* **305**, H431-445.
- Herzog RI, Liu C, Waxman SG & Cummins TR (2003). Calmodulin binds to the C terminus of sodium channels Nav1.4 and Nav1.6 and differentially modulates their functional properties. *J Neurosci Off J Soc Neurosci* **23**, 8261–8270.

- Hille B (1977). Local anesthetics: hydrophilic and hydrophobic pathways for the drug-receptor reaction. *J Gen Physiol* **69**, 497–515.
- Hodgkin AL & Huxley AF (1952). Currents carried by sodium and potassium ions through the membrane of the giant axon of Loligo. *J Physiol* **116**, 449–472.
- Hodgkin AL, Huxley AF & Katz B (1952). Measurement of current-voltage relations in the membrane of the giant axon of Loligo. *J Physiol* **116**, 424.
- Holzherr B, Lehmann-Horn F, Kuzmenkina E, Fan C & Jurkat-Rott K (2014). A gating model for wildtype and R1448H Nav1.4 channels in paramyotonia. *Acta Myol Myopathies Cardiomyopathies Off J Mediterr Soc Myol Ed Gaetano Conte Acad Study Striated Muscle Dis* **33**, 22–33.
- Horvath B & Bers DM (2014). The late sodium current in heart failure: pathophysiology and clinical relevance: Late sodium current in heart failure. *ESC Heart Fail* **1**, 26–40.
- Huang H, Millat G, Rodriguez-Lafrasse C, Rousson R, Kugener B, Chevalier P & Chahine M (2009). Biophysical characterization of a new SCN5A mutation S1333Y in a SIDS infant linked to long QT syndrome. *FEBS Lett* **583**, 890–896.
- Huang H, Priori SG, Napolitano C, O’Leary ME & Chahine M (2011). Y1767C, a novel SCN5A mutation, induces a persistent Na<sup>+</sup> current and potentiates ranolazine inhibition of Nav1.5 channels. *AJP Heart Circ Physiol* **300**, H288–H299.
- Huang H, Zhao J, Barrane F-Z, Champagne J & Chahine M (2006). Nav1.5/R1193Q polymorphism is associated with both long QT and Brugada syndromes. *Can J Cardiol* **22**, 309–313.
- Hund TJ, Decker KF, Kanter E, Mohler PJ, Boyden PA, Schuessler RB, Yamada KA & Rudy Y (2008). Role of activated CaMKII in abnormal calcium homeostasis and INa remodeling after myocardial infarction: Insights from mathematical modeling. *J Mol Cell Cardiol* **45**, 420–428.
- Hwang HW, Chen JJ, Lin YJ, Shieh RC, Lee MT, Hung SI, Wu JY, Chen YT, Niu DM & Hwang BT (2005). R1193Q of SCN5A, a Brugada and long QT mutation, is a common polymorphism in Han Chinese. *J Med Genet* **42**, e7; author reply e8.
- Irvine LA, Jafri MS & Winslow RL (1999). Cardiac sodium channel Markov model with temperature dependence and recovery from inactivation. *Biophys J* **76**, 1868–1885.
- Jayasuriya C & Whitman M (2011). Exercise-induced Brugada sign. *Eur Eur Pacing Arrhythm Card Electrophysiol J Work Groups Card Pacing Arrhythm Card Cell Electrophysiol Eur Soc Cardiol* **13**, 446–447.

- Jervell A & Lange-Nielsen F (1957). Congenital deaf-mutism, functional heart disease with prolongation of the Q-T interval and sudden death. *Am Heart J* **54**, 59–68.
- Johansson BW (1996). The hibernator heart—nature’s model of resistance to ventricular fibrillation. *Cardiovasc Res* **31**, 826–832.
- Jones DK, Peters CH, Tolhurst SA, Claydon TW & Ruben PC (2011). Extracellular Proton Modulation of the Cardiac Voltage-Gated Sodium Channel, NaV1.5. *Biophys J* **101**, 2147–2156.
- Jones DK & Ruben PC (2008). Biophysical defects in voltage-gated sodium channels associated with Long QT and Brugada syndromes. *Channels* **2**, 70–80.
- Jordan PN & Christini DJ (2004). Determining the effects of memory and action potential duration alternans on cardiac restitution using a constant-memory restitution protocol. *Physiol Meas* **25**, 1013–1024.
- Kaczmarek JA & Corry B (2014). Investigating the size and dynamics of voltage-gated sodium channel fenestrations: A molecular dynamics study. *Channels* **8**, 264–277.
- Kahlig KM, Lepist I, Leung K, Rajamani S & George AL (2010). Ranolazine selectively blocks persistent current evoked by epilepsy-associated NaV1.1 mutations: Ranolazine blocks NaV1.1 persistent current. *Br J Pharmacol* **161**, 1414–1426.
- Kapplinger JD et al. (2010). An international compendium of mutations in the SCN5A-encoded cardiac sodium channel in patients referred for Brugada syndrome genetic testing. *Heart Rhythm Off J Heart Rhythm Soc* **7**, 33–46.
- Keller D, Huang H, Zhao J, Frank R, Suarez V, Delacretaz E, Brink M, Osswald S, Schwick N & Chahine M (2006). A novel SCN5A mutation, F1344S, identified in a patient with Brugada syndrome and fever-induced ventricular fibrillation. *Cardiovasc Res* **70**, 521–529.
- Kim J, Ghosh S, Liu H, Tateyama M, Kass RS & Pitt GS (2004). Calmodulin Mediates Ca<sup>2+</sup> Sensitivity of Sodium Channels. *J Biol Chem* **279**, 45004–45012.
- Kirschenlohr HL, Grace AA, Vandenberg JI, Metcalfe JC & Smith GA (2000). Estimation of systolic and diastolic free intracellular Ca<sup>2+</sup> by titration of Ca<sup>2+</sup> buffering in the ferret heart. *Biochem J* **346 Pt 2**, 385–391.
- Klassen T, Davis C, Goldman A, Burgess D, Chen T, Wheeler D, McPherson J, Bourquin T, Lewis L, Villasana D, Morgan M, Muzny D, Gibbs R & Noebels J (2011). Exome Sequencing of Ion Channel Genes Reveals Complex Profiles Confounding Personal Risk Assessment in Epilepsy. *Cell* **145**, 1036–1048.

- Knollmann BC (2013). Induced Pluripotent Stem Cell-Derived Cardiomyocytes: Boutique Science or Valuable Arrhythmia Model? *Circ Res* **112**, 969–976.
- Kort AA, Capogrossi MC & Lakatta EG (1985). Frequency, amplitude, and propagation velocity of spontaneous Ca<sup>++</sup>-dependent contractile waves in intact adult rat cardiac muscle and isolated myocytes. *Circ Res* **57**, 844–855.
- Kovacic JC & Kuchar DL (2004). Brugada pattern electrocardiographic changes associated with profound electrolyte disturbance. *Pacing Clin Electrophysiol PACE* **27**, 1020–1023.
- Krishnan SC & Antzelevitch C (1993). Flecainide-induced arrhythmia in canine ventricular epicardium. Phase 2 reentry? *Circulation* **87**, 562–572.
- Kubota T, Durek T, Dang B, Finol-Urdaneta RK, Craik DJ, Kent SBH, French RJ, Bezanilla F & Correa AM (2017). Mapping of voltage sensor positions in resting and inactivated mammalian sodium channels by LRET. *Proc Natl Acad Sci* **114**, E1857–E1865.
- Kühn FJ & Greeff NG (1999). Movement of voltage sensor S4 in domain 4 is tightly coupled to sodium channel fast inactivation and gating charge immobilization. *J Gen Physiol* **114**, 167–183.
- Kukla P, Jastrzebski M, Baciór B, Gomuła P, Grodecki J & Kawecka-Jaszcz K (2007). [Variant Brugada syndrome--mild ST segment elevation in inferior leads and aborted sudden cardiac death]. *Kardiol Pol* **65**, 1494–1498.
- Kumar V, Patel N, Van Houzen N & Saini N (2013). Brugada-type electrocardiographic changes induced by fever. *Circulation* **127**, 2145–2146.
- Kwon HW, Lee SY, Kwon BS, Kim GB, Bae EJ, Kim WH, Noh CI, Cho SI & Park SS (2012). Long QT syndrome and dilated cardiomyopathy with SCN5A p.R1193Q polymorphism: cardioverter-defibrillator implantation at 27 months. *Pacing Clin Electrophysiol PACE* **35**, e243-246.
- Laslett LJ, Alagona P, Clark BA, Drozda JP, Saldivar F, Wilson SR, Poe C & Hart M (2012). The Worldwide Environment of Cardiovascular Disease: Prevalence, Diagnosis, Therapy, and Policy Issues. *J Am Coll Cardiol* **60**, S1–S49.
- Lee A, Fakler B, Kaczmarek LK & Isom LL (2014). More Than a Pore: Ion Channel Signaling Complexes. *J Neurosci* **34**, 15159–15169.
- Lee S, Goodchild SJ & Ahern CA (2012). Molecular and functional determinants of local anesthetic inhibition of NaChBac. *Channels* **6**, 403–406.

- Li HL, Galue A, Meadows L & Ragsdale DS (1999). A molecular basis for the different local anesthetic affinities of resting versus open and inactivated states of the sodium channel. *Mol Pharmacol* **55**, 134–141.
- Lipkind GM & Fozzard HA (2010). Molecular Model of Anticonvulsant Drug Binding to the Voltage-Gated Sodium Channel Inner Pore. *Mol Pharmacol* **78**, 631–638.
- Liu D-W, Gintant GA & Antzelevitch C (1993). Ionic bases for electrophysiological distinctions among epicardial, midmyocardial, and endocardial myocytes from the free wall of the canine left ventricle. *Circ Res* **72**, 671–687.
- Liu M, Yang K-C & Dudley SC (2014). Cardiac sodium channel mutations: why so many phenotypes? *Nat Rev Cardiol* **11**, 607–615.
- Livshitz LM & Rudy Y (2007). Regulation of Ca<sup>2+</sup> and electrical alternans in cardiac myocytes: role of CAMKII and repolarizing currents. *AJP Heart Circ Physiol* **292**, H2854–H2866.
- Lizotte E, Junttila MJ, Dube MP, Hong K, Benito B, DE Zutter M, Henkens S, Sarkozy A, Huikuri HV, Towbin J, Vatta M, Brugada P, Brugada J & Brugada R (2009). Genetic modulation of brugada syndrome by a common polymorphism. *J Cardiovasc Electrophysiol* **20**, 1137–1141.
- Lukas A & Antzelevitch C (1996). Phase 2 reentry as a mechanism of initiation of circus movement reentry in canine epicardium exposed to simulated ischemia. *Cardiovasc Res* **32**, 593–603.
- Makaryus JN, Verbsky J, Schwarz S & Slotwiner D (2009). Fever Associated with Gastrointestinal Shigellosis Unmasks Probable Brugada Syndrome. *Case Rep Med* **2009**, 1–3.
- Makielski JC (2006). SIDS: genetic and environmental influences may cause arrhythmia in this silent killer. *J Clin Invest* **116**, 297–299.
- Makimoto H, Nakagawa E, Takaki H, Yamada Y, Okamura H, Noda T, Satomi K, Suyama K, Aihara N, Kurita T, Kamakura S & Shimizu W (2010). Augmented ST-Segment Elevation During Recovery From Exercise Predicts Cardiac Events in Patients With Brugada Syndrome. *J Am Coll Cardiol* **56**, 1576–1584.
- Makita N, Behr E, Shimizu W, Horie M, Sunami A, Crotti L, Schulze-Bahr E, Fukuhara S, Mochizuki N, Makiyama T, Itoh H, Christiansen M, McKeown P, Miyamoto K, Kamakura S, Tsutsui H, Schwartz PJ, George AL & Roden DM (2008a). The E1784K mutation in SCN5A is associated with mixed clinical phenotype of type 3 long QT syndrome. *J Clin Invest*; DOI: 10.1172/JCI34057.

- Makita N, Mochizuki N & Tsutsui H (2008b). Absence of a trafficking defect in R1232W/T1620M, a double SCN5A mutant responsible for Brugada syndrome. *Circ J Off J Jpn Circ Soc* **72**, 1018–1019.
- Makita N, Shirai N, Wang DW, Sasaki K, George AL, Kanno M & Kitabatake A (2000). Cardiac Na<sup>+</sup> channel dysfunction in Brugada syndrome is aggravated by beta(1)-subunit. *Circulation* **101**, 54–60.
- Malhotra JD, Chen C, Rivolta I, Abriel H, Malhotra R, Mattei LN, Brosius FC, Kass RS & Isom LL (2001). Characterization of sodium channel  $\alpha$ - and  $\beta$ -subunits in rat and mouse cardiac myocytes. *Circulation* **103**, 1303–1310.
- Maltsev V & Undrovinas A (2006). A multi-modal composition of the late Na<sup>+</sup> current in human ventricular cardiomyocytes. *Cardiovasc Res* **69**, 116–127.
- Maltsev VA, Kyle JW & Undrovinas A (2009). Late Na<sup>+</sup> current produced by human cardiac Na<sup>+</sup> channel isoform Nav1.5 is modulated by its  $\beta$ 1 subunit. *J Physiol Sci* **59**, 217–225.
- Mantegazza M, Yu FH, Catterall WA & Scheuer T (2001). Role of the C-terminal domain in inactivation of brain and cardiac sodium channels. *Proc Natl Acad Sci U S A* **98**, 15348–15353.
- Marionneau C & Abriel H (2015). Regulation of the cardiac Na<sup>+</sup> channel Nav1.5 by post-translational modifications. *J Mol Cell Cardiol* **82**, 36–47.
- Marks AR (2003). Calcium and the heart: a question of life and death. *J Clin Invest* **111**, 597–600.
- Masrur S, Memon S & Thompson PD (2015). Brugada syndrome, exercise, and exercise testing. *Clin Cardiol* **38**, 323–326.
- Matteson DR & Armstrong CM (1982). Evidence for a population of sleepy sodium channels in squid axon at low temperature. *J Gen Physiol* **79**, 739–758.
- Mauerhöfer M & Bauer CK (2016). Effects of Temperature on Heteromeric Kv11.1a/1b and Kv11.3 Channels. *Biophys J* **111**, 504–523.
- McCormick KA, Isom LL, Ragsdale D, Smith D, Scheuer T & Catterall WA (1998). Molecular determinants of Na<sup>+</sup> channel function in the extracellular domain of the beta1 subunit. *J Biol Chem* **273**, 3954–3962.
- Medeiros-Domingo A, Kaku T, Tester DJ, Iturralde-Torres P, Itty A, Ye B, Valdivia C, Ueda K, Canizales-Quinteros S, Tusie-Luna MT, Makielski JC & Ackerman MJ (2007). SCN4B-Encoded Sodium Channel  $\beta$ 4 Subunit in Congenital Long-QT Syndrome. *Circulation* **116**, 134–142.

- Meggiolaro M, Zorzi A, El Maghawry M, Peruzza F, Migliore F & Pittoni GM (2013). Brugada ECG disclosed by acute malaria: is it all about fever and propofol? *J Clin Anesth* **25**, 483–487.
- Meregalli P, Wilde A & Tan H (2005). Pathophysiological mechanisms of Brugada syndrome: Depolarization disorder, repolarization disorder, or more? *Cardiovasc Res* **67**, 367–378.
- Mikkelsen RB, Reinlib L, Donowitz M & Zahniser D (1991). Hyperthermia effects on cytosolic [Ca<sup>2+</sup>]: analysis at the single cell level by digitized imaging microscopy and cell survival. *Cancer Res* **51**, 359–364.
- Millar L, Sheikh N & Sharma S (2012). Clinical and Genetic Aspects of Sudden Cardiac Death in the Practice of Sports Medicine. *Colloq Ser Genomic Mol Med* **1**, 1–162.
- Miloushev VZ, Levine JA, Arbing MA, Hunt JF, Pitt GS & Palmer AG (2009). Solution Structure of the NaV1.2 C-terminal EF-hand Domain. *J Biol Chem* **284**, 6446–6454.
- Minoura Y, Di Diego JM, Barajas-Martínez H, Zygmunt AC, Hu D, Sicouri S & Antzelevitch C (2012). Ionic and Cellular Mechanisms Underlying the Development of Acquired Brugada Syndrome in Patients Treated with Antidepressants. *J Cardiovasc Electrophysiol* **23**, 423–432.
- Modi S & Krahn AD (2011). Sudden cardiac arrest without overt heart disease. *Circulation* **123**, 2994–3008.
- Mohammadi B, Mitrovic N, Lehmann-Horn F, Dengler R & Bufler J (2003). Mechanisms of cold sensitivity of paramyotonia congenita mutation R1448H and overlap syndrome mutation M1360V. *J Physiol* **547**, 691–698.
- Mok N-S, Priori SG, Napolitano C, Chan N-Y, Chahine M & Baroudi G (2003). A newly characterized SCN5A mutation underlying Brugada syndrome unmasked by hyperthermia. *J Cardiovasc Electrophysiol* **14**, 407–411.
- Moreau A, Krahn AD, Gosselin-Badaroudine P, Klein GJ, Christé G, Vincent Y, Boutjdir M & Chahine M (2013). Sodium overload due to a persistent current that attenuates the arrhythmogenic potential of a novel LQT3 mutation. *Front Pharmacol* **4**, 126.
- Mori M, Konno T, Morii T, Nagayama K & Imoto K (2003). Regulatory interaction of sodium channel IQ-motif with calmodulin C-terminal lobe. *Biochem Biophys Res Commun* **307**, 290–296.

- Morris GM, Huey R, Lindstrom W, Sanner MF, Belew RK, Goodsell DS & Olson AJ (2009). AutoDock4 and AutoDockTools4: Automated docking with selective receptor flexibility. *J Comput Chem* **30**, 2785–2791.
- Moss AJ, Windle JR, Hall WJ, Zareba W, Robinson JL, McNitt S, Severski P, Rosero S, Daubert JP, Qi M, Cieciorca M & Manalan AS (2005). Safety and efficacy of flecainide in subjects with Long QT-3 syndrome (DeltaKPK mutation): a randomized, double-blind, placebo-controlled clinical trial. *Ann Noninvasive Electrocardiol Off J Int Soc Holter Noninvasive Electrocardiol Inc* **10**, 59–66.
- Moss AJ, Zareba W, Schwarz KQ, Rosero S, Mcnitt S & Robinson JL (2008). Ranolazine Shortens Repolarization in Patients with Sustained Inward Sodium Current Due to Type-3 Long-QT Syndrome. *J Cardiovasc Electrophysiol* **19**, 1289–1293.
- Motoike HK (2004). The Na<sup>+</sup> Channel Inactivation Gate Is a Molecular Complex: A Novel Role of the COOH-terminal Domain. *J Gen Physiol* **123**, 155–165.
- Murphy BJ, Rogers J, Perdichizzi AP, Colvin AA & Catterall WA (1996). cAMP-dependent phosphorylation of two sites in the alpha subunit of the cardiac sodium channel. *J Biol Chem* **271**, 28837–28843.
- Murray KT, Anno T, Bennett PB & Hondeghem LM (1990). Voltage clamp of the cardiac sodium current at 37 degrees C in physiologic solutions. *Biophys J* **57**, 607.
- Muslin AJ (2008). MAPK signalling in cardiovascular health and disease: molecular mechanisms and therapeutic targets. *Clin Sci Lond Engl 1979* **115**, 203–218.
- Myerburg RJ & Junttila MJ (2012). Sudden Cardiac Death Caused by Coronary Heart Disease. *Circulation* **125**, 1043–1052.
- Nagatomo T, Fan Z, Ye B, Tonkovich GS, January CT, Kyle JW & Makielski JC (1998). Temperature dependence of early and late currents in human cardiac wild-type and long Q-T DeltaKPK Na<sup>+</sup> channels. *Am J Physiol* **275**, H2016-2024.
- Nakajima T, Kaneko Y & Kurabayashi M (2015). Unveiling specific triggers and precipitating factors for fatal cardiac events in inherited arrhythmia syndromes. *Circ J Off J Jpn Circ Soc* **79**, 1185–1192.
- Nakajima T, Kaneko Y, Saito A, Irie T, Tange S, Iso T & Kurabayashi M (2011). Identification of six novel SCN5A mutations in Japanese patients with Brugada syndrome. *Int Heart J* **52**, 27–31.
- Nielsen N et al. (2013). Targeted Temperature Management at 33°C versus 36°C after Cardiac Arrest. *N Engl J Med* **369**, 2197–2206.

- Noebels J (2015). Pathway-driven discovery of epilepsy genes. *Nat Neurosci* **18**, 344–350.
- Noh CI, Song JY, Kim HS, Choi JY & Yun YS (1995). Ventricular tachycardia and exercise related syncope in children with structurally normal hearts: emphasis on repolarisation abnormality. *Br Heart J* **73**, 544–547.
- Nolan JP (2003). Therapeutic Hypothermia After Cardiac Arrest: An Advisory Statement by the Advanced Life Support Task Force of the International Liaison Committee on Resuscitation. *Circulation* **108**, 118–121.
- Nolasco JB & Dahlen RW (1968). A graphic method for the study of alternation in cardiac action potentials. *J Appl Physiol* **25**, 191–196.
- Nuss HB, Balsler JR, Orias DW, Lawrence JH, Tomaselli GF & Marban E (1996). Coupling between fast and slow inactivation revealed by analysis of a point mutation (F1304Q) in mu 1 rat skeletal muscle sodium channels. *J Physiol* **494**, 411–429.
- Nuyens D, Stengl M, Dugarmaa S, Rossenbacker T, Compennolle V, Rudy Y, Smits JF, Flameng W, Clancy CE, Moons L, Vos MA, Dewerchin M, Benndorf K, Collen D, Carmeliet E & Carmeliet P (2001). Abrupt rate accelerations or premature beats cause life-threatening arrhythmias in mice with long-QT3 syndrome. *Nat Med* **7**, 1021–1027.
- Obeyesekere MN, Klein GJ, Modi S, Leong-Sit P, Gula LJ, Yee R, Skanes AC & Krahn AD (2011). How to perform and interpret provocative testing for the diagnosis of Brugada syndrome, long-QT syndrome, and catecholaminergic polymorphic ventricular tachycardia. *Circ Arrhythm Electrophysiol* **4**, 958–964.
- O’Hara T, Virág L, Varró A & Rudy Y (2011). Simulation of the Undiseased Human Cardiac Ventricular Action Potential: Model Formulation and Experimental Validation ed. McCulloch AD. *PLoS Comput Biol* **7**, e1002061.
- O’Reilly AO, Eberhardt E, Weidner C, Alzheimer C, Wallace BA & Lampert A (2012). Bisphenol A Binds to the Local Anesthetic Receptor Site to Block the Human Cardiac Sodium Channel ed. Bondarenko VE. *PLoS ONE* **7**, e41667.
- Ozeke O, Aras D, Geyik B, Deveci B & Selcuk T (2005). Brugada-type electrocardiographic pattern induced by fever. *Indian Pacing Electrophysiol J* **5**, 146–148.
- Paavonen KJ, Swan H, Piippo K, Hokkanen L, Laitinen P, Viitasalo M, Toivonen L & Kontula K (2001). Response of the QT interval to mental and physical stress in types LQT1 and LQT2 of the long QT syndrome. *Heart Br Card Soc* **86**, 39–44.
- Parsons TD, Ellis-Davies GC & Almers W (1996). Millisecond studies of calcium-dependent exocytosis in pituitary melanotrophs: comparison of the photolabile

- calcium chelators nitrophenyl-EGTA and DM-nitrophen. *Cell Calcium* **19**, 185–192.
- Patino GA & Isom LL (2010). Electrophysiology and beyond: Multiple roles of Na<sup>+</sup> channel  $\beta$  subunits in development and disease. *Neurosci Lett* **486**, 53–59.
- Patton DE, Isom LL, Catterall WA & Goldin AL (1994). The adult rat brain beta 1 subunit modifies activation and inactivation gating of multiple sodium channel alpha subunits. *J Biol Chem* **269**, 17649–17655.
- Paul AA, Witchel HJ & Hancox JC (2002). Inhibition of the current of heterologously expressed HERG potassium channels by flecainide and comparison with quinidine, propafenone and lignocaine. *Br J Pharmacol* **136**, 717–729.
- Payandeh J, Gamal El-Din TM, Scheuer T, Zheng N & Catterall WA (2012). Crystal structure of a voltage-gated sodium channel in two potentially inactivated states. *Nature*; DOI: 10.1038/nature11077.
- Payandeh J, Scheuer T, Zheng N & Catterall WA (2011). The crystal structure of a voltage-gated sodium channel. *Nature* **475**, 353–358.
- Pelzmann B, Schaffer P, Bernhart E, Lang P, Mächler H, Rigler B & Koidl B (1998). L-type calcium current in human ventricular myocytes at a physiological temperature from children with tetralogy of Fallot. *Cardiovasc Res* **38**, 424–432.
- Peña JR & Wolska BM (2004). Troponin I phosphorylation plays an important role in the relaxant effect of beta-adrenergic stimulation in mouse hearts. *Cardiovasc Res* **61**, 756–763.
- Peng J, Cui Y-K, Yuan F-H, Yi S-D, Chen Z-M & Meng S-R (2005). [Fever and Brugada syndrome: report of 21 cases]. *1 Jun Yi Xue Xue Bao Acad J First Med Coll PLA* **25**, 432–434.
- Petegem FV, Chatelain FC & Minor, DL (2005). Insights into voltage-gated calcium channel regulation from the structure of the CaV1.2 IQ domain–Ca<sup>2+</sup>/calmodulin complex. *Nat Struct 38 Mol Biol* **12**, 1108–1115.
- Peters C, Sokolov S, Rajamani S & Ruben P (2013). Effects of the antianginal drug, ranolazine, on the brain sodium channel Na<sub>v</sub> 1.2 and its modulation by extracellular protons: Effects of ranolazine on Nav1.2 in normal and low extracellular pH. *Br J Pharmacol* **169**, 704–716.
- Peters CH, Abdelsayed M & Ruben PC (2016). Triggers for arrhythmogenesis in the Brugada and long QT 3 syndromes. *Prog Biophys Mol Biol* **120**, 77–88.

- Peters CH, Yu A, Zhu W, Silva JR & Ruben PC (2017). Depolarization of the conductance-voltage relationship in the NaV1.5 mutant, E1784K, is due to altered fast inactivation ed. Obukhov AG. *PLOS ONE* **12**, e0184605.
- Pitt G (2007). Calmodulin and CaMKII as molecular switches for cardiac ion channels. *Cardiovasc Res* **73**, 641–647.
- Pitt GS (2009). Channeling a New Focus for Heart Failure: Insights Into Ion Channels: *J Cardiovasc Pharmacol* **54**, 95–97.
- Pitt GS & Lee S-Y (2016). Current view on regulation of voltage-gated sodium channels by calcium and auxiliary proteins. *Protein Sci*; DOI: 10.1002/pro.2960.
- Poelzing S, Forleo C, Samodell M, Dudash L, Sorrentino S, Anaclerio M, Troccoli R, Iacoviello M, Romito R, Guida P, Chahine M, Pitzalis M & Deschênes I (2006). SCN5A polymorphism restores trafficking of a Brugada syndrome mutation on a separate gene. *Circulation* **114**, 368–376.
- Polderman KH (2013). Of ions and temperature: the complicated interplay of temperature, fluids, and electrolytes on myocardial function. *Crit Care Lond Engl* **17**, 1018.
- Postema PG, Van den Berg M, Van Tintelen JP, Van den Heuvel F, Grundeken M, Hofman N, Van der Roest WP, Nannenbergh EA, Krapels IPC, Bezzina CR & Wilde A (2009). Founder mutations in the Netherlands: SCN5a 1795insD, the first described arrhythmia overlap syndrome and one of the largest and best characterised families worldwide. *Neth Heart J Mon J Neth Soc Cardiol Neth Heart Found* **17**, 422–428.
- Potet F, Beckermann TM, Kunic JD & George AL (2015). Intracellular Calcium Attenuates Late Current Conducted by Mutant Human Cardiac Sodium Channels. *Circ Arrhythm Electrophysiol*; DOI: 10.1161/CIRCEP.115.002760.
- Potet F, Chagot B, Angheliescu M, Viswanathan PC, Stepanovic SZ, Kupersmidt S, Chazin WJ & Balsler JR (2009). Functional Interactions between Distinct Sodium Channel Cytoplasmic Domains through the Action of Calmodulin. *J Biol Chem* **284**, 8846–8854.
- Priori SG, Napolitano C, Giordano U, Collisani G & Memmi M (2000). Brugada syndrome and sudden cardiac death in children. *The Lancet* **355**, 808–809.
- Priori SG, Wilde AA, Horie M, Cho Y, Behr ER, Berul C, Blom N, Brugada J, Chiang C-E, Huikuri H, Kannankeril P, Krahn A, Leenhardt A, Moss A, Schwartz PJ, Shimizu W, Tomaselli G & Tracy C (2013). HRS/EHRA/APHRS Expert Consensus Statement on the Diagnosis and Management of Patients with Inherited Primary Arrhythmia Syndromes. *Heart Rhythm* **10**, 1932–1963.

- Proud C (1994). Protein phosphorylation: A practical approach. *Trends Biochem Sci* **19**, 263–264.
- Qiu X, Liu W, Hu D, Sun Y, Li L & Li C (2009). Patient with obstructive sleep apnea-hypopnea syndrome and SCN5A mutation (R1193Q polymorphism) associated with Brugada type 2 electrocardiographic pattern. *J Electrocardiol* **42**, 250–253.
- Qu Y, Isom LL, Westenbroek RE, Rogers JC, Tanada TN, McCormick KA, Scheuer T & Catterall WA (1995). Modulation of cardiac Na<sup>+</sup> channel expression in *Xenopus* oocytes by beta 1 subunits. *J Biol Chem* **270**, 25696–25701.
- Qu Y, Karnabi E, Chahine M, Vassalle M & Boutjdir M (2007). Expression of skeletal muscle NaV1.4 Na channel isoform in canine cardiac Purkinje myocytes. *Biochem Biophys Res Commun* **355**, 28–33.
- Qu Y, Rogers JC, Tanada TN, Catterall WA & Scheuer T (1996). Phosphorylation of S1505 in the cardiac Na<sup>+</sup> channel inactivation gate is required for modulation by protein kinase C. *J Gen Physiol* **108**, 375–379.
- Quandt FN (1987). Burst kinetics of sodium channels which lack fast inactivation in mouse neuroblastoma cells. *J Physiol* **392**, 563–585.
- Radzicki D, Yau H-J, Pollema-Mays SL, Mlsna L, Cho K, Koh S & Martina M (2013). Temperature-Sensitive Cav1.2 Calcium Channels Support Intrinsic Firing of Pyramidal Neurons and Provide a Target for the Treatment of Febrile Seizures. *J Neurosci* **33**, 9920–9931.
- Ragsdale DS & Avoli M (1998). Sodium channels as molecular targets for antiepileptic drugs. *Brain Res Brain Res Rev* **26**, 16–28.
- Ragsdale DS, McPhee JC, Scheuer T & Catterall WA (1996). Common molecular determinants of local anesthetic, antiarrhythmic, and anticonvulsant block of voltage-gated Na<sup>+</sup> channels. *Proc Natl Acad Sci U S A* **93**, 9270–9275.
- Rajamani S, El-Bizri N, Shryock JC, Makielski JC & Belardinelli L (2009). Use-dependent block of cardiac late Na<sup>(+)</sup> current by ranolazine. *Heart Rhythm Off J Heart Rhythm Soc* **6**, 1625–1631.
- Rajamani S, Liu G, El-Bizri N, Guo D, Li C, Chen X-L, Kahlig KM, Mollova N, Elzein E, Zablocki J & Belardinelli L (2016). The novel late Na<sup>+</sup> current inhibitor, GS-6615 (eleclazine) and its anti-arrhythmic effects in rabbit isolated heart preparations: Cardiac late I<sub>Na</sub> inhibitor. *Br J Pharmacol* **173**, 3088–3098.
- Remme CA, Verkerk AO, Hoogaars WMH, Aanhaanen WTJ, Scicluna BP, Annink C, den Hoff MJB, Wilde AAM, Veen TAB, Veldkamp MW, Bakker JMT, Christoffels VM & Bezzina CR (2009). The cardiac sodium channel displays differential distribution

- in the conduction system and transmural heterogeneity in the murine ventricular myocardium. *Basic Res Cardiol* **104**, 511–522.
- Remme CA, Verkerk AO, Nuyens D, van Ginneken ACG, van Brunschot S, Belterman CNW, Wilders R, van Roon MA, Tan HL, Wilde AAM, Carmeliet P, de Bakker JMT, Veldkamp MW & Bezzina CR (2006). Overlap syndrome of cardiac sodium channel disease in mice carrying the equivalent mutation of human SCN5A-1795insD. *Circulation* **114**, 2584–2594.
- Richmond JE, Featherstone DE, Hartmann HA & Ruben PC (1998). Slow inactivation in human cardiac sodium channels. *Biophys J* **74**, 2945–2952.
- Richmond JE, Featherstone DE & Ruben PC (1997). Human Na<sup>+</sup> channel fast and slow inactivation in paramyotonia congenita mutants expressed in *Xenopus laevis* oocytes. *J Physiol* **499**, 589–600.
- Rivera-Fernández R, Arias-Verdú MD, García-Paredes T, Delgado-Rodríguez M, Arboleda-Sánchez JA, Aguilar-Alonso E, Quesada-García G & Vera-Almazán A (2014). Prolonged QT interval in ST-elevation myocardial infarction and mortality: new prognostic scale with QT, Killip and age. *J Cardiovasc Med Hagerstown Md*; DOI: 10.2459/JCM.0000000000000015.
- Rivolta I (2001). Inherited Brugada and Long QT-3 Syndrome Mutations of a Single Residue of the Cardiac Sodium Channel Confer Distinct Channel and Clinical Phenotypes. *J Biol Chem* **276**, 30623–30630.
- Ruben PC, Starkus JG & Rayner M (1992). Steady-state availability of sodium channels. Interactions between activation and slow inactivation. *Biophys J* **61**, 941.
- Ruff RL (1999). Effects of temperature on slow and fast inactivation of rat skeletal muscle Na<sup>(+)</sup> channels. *Am J Physiol* **277**, C937-947.
- Salinski EP & WorriLOW CC (2014). ST-segment elevation myocardial infarction vs. hypothermia-induced electrocardiographic changes: a case report and brief review of the literature. *J Emerg Med* **46**, e107-111.
- Santarelli VP, Eastwood AL, Dougherty DA, Horn R & Ahern CA (2007). A Cation-Interaction Discriminates among Sodium Channels That Are Either Sensitive or Resistant to Tetrodotoxin Block. *J Biol Chem* **282**, 8044–8051.
- Sarhan MF, Tung C-C, Van Petegem F & Ahern CA (2012). Crystallographic basis for calcium regulation of sodium channels. *Proc Natl Acad Sci* **109**, 3558–3563.
- Sarhan MF, Van Petegem F & Ahern CA (2009). A Double Tyrosine Motif in the Cardiac Sodium Channel Domain III-IV Linker Couples Calcium-dependent Calmodulin Binding to Inactivation Gating. *J Biol Chem* **284**, 33265–33274.

- Scheuer T (2011). Regulation of sodium channel activity by phosphorylation. *Semin Cell Dev Biol* **22**, 160–165.
- Schwartz PJ et al. (2001). Genotype-phenotype correlation in the long-QT syndrome: gene-specific triggers for life-threatening arrhythmias. *Circulation* **103**, 89–95.
- Schwartz PJ, Priori SG, Dumaine R, Napolitano C, Antzelevitch C, Stramba-Badiale M, Richard TA, Berti MR & Bloise R (2000). A molecular link between the sudden infant death syndrome and the long-QT syndrome. *N Engl J Med* **343**, 262–267.
- Schwartz PJ, Priori SG, Locati EH, Napolitano C, Cantù F, Towbin JA, Keating MT, Hammoude H, Brown AM & Chen LS (1995). Long QT syndrome patients with mutations of the SCN5A and HERG genes have differential responses to Na<sup>+</sup> channel blockade and to increases in heart rate. Implications for gene-specific therapy. *Circulation* **92**, 3381–3386.
- Schwartz PJ & Wolf S (1978). QT interval prolongation as predictor of sudden death in patients with myocardial infarction. *Circulation* **57**, 1074–1077.
- Schwarz W (1979). Temperature experiments on nerve and muscle membranes of frogs. Indications for a phase transition. *Pflugers Arch* **382**, 27–34.
- Serletis-Bizios A, Azevedo ER & Singh SM (2009). Unmasking of Brugada syndrome during a febrile episode. *Can J Cardiol* **25**, 239.
- Shah VN, Wingo TL, Weiss KL, Williams CK, Balsler JR & Chazin WJ (2006). Calcium-dependent regulation of the voltage-gated sodium channel hH1: intrinsic and extrinsic sensors use a common molecular switch. *Proc Natl Acad Sci U S A* **103**, 3592–3597.
- Sheets MF, Fozzard HA, Lipkind GM & Hanck DA (2010). Sodium Channel Molecular Conformations and Antiarrhythmic Drug Affinity. *Trends Cardiovasc Med* **20**, 16–21.
- Sheets MF & Hanck DA (2007). Outward stabilization of the S4 segments in domains III and IV enhances lidocaine block of sodium channels: Stabilization of S4 segments. *J Physiol* **582**, 317–334.
- Shen H, Zhou Q, Pan X, Li Z, Wu J & Yan N (2017). Structure of a eukaryotic voltage-gated sodium channel at near-atomic resolution. *Science* **355**, eaal4326.
- Shimizu W, Aiba T & Antzelevitch C (2005). Specific therapy based on the genotype and cellular mechanism in inherited cardiac arrhythmias. Long QT syndrome and Brugada syndrome. *Curr Pharm Des* **11**, 1561–1572.

- Shimizu W & Antzelevitch C (1998). Cellular Basis for the ECG Features of the LQT1 Form of the Long-QT Syndrome Effects of  $\beta$ -Adrenergic Agonists and Antagonists and Sodium Channel Blockers on Transmural Dispersion of Repolarization and Torsade de Pointes. *Circulation* **98**, 2314–2322.
- Shimizu W & Antzelevitch C (1999). Cellular and ionic basis for T-wave alternans under long-QT conditions. *Circulation* **99**, 1499–1507.
- Shimizu W & Antzelevitch C (2000). Differential effects of beta-adrenergic agonists and antagonists in LQT1, LQT2 and LQT3 models of the long QT syndrome. *J Am Coll Cardiol* **35**, 778–786.
- Shimizu W, Matsuo K, Kokubo Y, Satomi K, Kurita T, Noda T, Nagaya N, Suyama K, Aihara N, Kamakura S, Inamoto N, Akahoshi M & Tomoike H (2007). Sex hormone and gender difference--role of testosterone on male predominance in Brugada syndrome. *J Cardiovasc Electrophysiol* **18**, 415–421.
- Shutt RH & Howlett SE (2008). Hypothermia increases the gain of excitation-contraction coupling in guinea pig ventricular myocytes. *AJP Cell Physiol* **295**, C692–C700.
- Sicouri S, Timothy KW, Zygmunt AC, Glass A, Goodrow RJ, Belardinelli L & Antzelevitch C (2007). Cellular basis for the electrocardiographic and arrhythmic manifestations of Timothy syndrome: effects of ranolazine. *Heart Rhythm Off J Heart Rhythm Soc* **4**, 638–647.
- Sieira J, Dendramis G & Brugada P (2016). Pathogenesis and management of Brugada syndrome. *Nat Rev Cardiol* **13**, 744–756.
- da Silva EF, Oliveira VH, Sorenson MM, Barrabin H & Scofano HM (2002). Converting troponin C into calmodulin: effects of mutations in the central helix and of changes in temperature. *Int J Biochem Cell Biol* **34**, 657–667.
- Silva JR & Goldstein SA (2013a). Voltage-sensor movements describe slow inactivation of voltage-gated sodium channels II: A periodic paralysis mutation in NaV1.4 (L689I). *J Gen Physiol* **141**, 323–334.
- Silva JR & Goldstein SAN (2013b). Voltage-sensor movements describe slow inactivation of voltage-gated sodium channels I: Wild-type skeletal muscle NaV1.4. *J Gen Physiol* **141**, 309–321.
- Skinner JR (2005). Near-miss SIDS due to Brugada syndrome. *Arch Dis Child* **90**, 528–529.
- Smeets JL, Allessie MA, Lammers WJ, Bonke FI & Hollen J (1986). The wavelength of the cardiac impulse and reentrant arrhythmias in isolated rabbit atrium. The role of heart rate, autonomic transmitters, temperature, and potassium. *Circ Res* **58**, 96–108.

- Sokolov S, Peters CH, Rajamani S & Ruben PC (2013). Proton-dependent inhibition of the cardiac sodium channel Nav1.5 by ranolazine. *Front Pharmacol*; DOI: 10.3389/fphar.2013.00078.
- Somers VK, Dyken ME, Mark AL & Abboud FM (1993). Sympathetic-nerve activity during sleep in normal subjects. *N Engl J Med* **328**, 303–307.
- Song LS, Wang SQ, Xiao RP, Spurgeon H, Lakatta EG & Cheng H (2001). beta-Adrenergic stimulation synchronizes intracellular Ca(2+) release during excitation-contraction coupling in cardiac myocytes. *Circ Res* **88**, 794–801.
- Sossalla S, Wagner S, Rasenack ECL, Ruff H, Weber SL, Schöndube FA, Tirilomis T, Tenderich G, Hasenfuss G, Belardinelli L & Maier LS (2008). Ranolazine improves diastolic dysfunction in isolated myocardium from failing human hearts — Role of late sodium current and intracellular ion accumulation. *J Mol Cell Cardiol* **45**, 32–43.
- Splawski I, Shen J, Timothy KW, Lehmann MH, Priori S, Robinson JL, Moss AJ, Schwartz PJ, Towbin JA, Vincent GM & Keating MT (2000). Spectrum of mutations in long-QT syndrome genes. KVLQT1, HERG, SCN5A, KCNE1, and KCNE2. *Circulation* **102**, 1178–1185.
- Starkus JG, Rayner MD, Fleig A & Ruben PC (1993). Fast and slow inactivation of sodium channels: effects of photodynamic modification by methylene blue. *Biophys J* **65**, 715.
- Steenbergen C, Murphy E, Levy L & London RE (1987). Elevation in cytosolic free calcium concentration early in myocardial ischemia in perfused rat heart. *Circ Res* **60**, 700–707.
- Sumitomo N (2014). E1784K mutation in SCN5A and overlap syndrome. *Circ J Off J Jpn Circ Soc* **78**, 1839–1840.
- Sun A, Xu L, Wang S, Wang K, Huang W, Wang Y, Zou Y & Ge J (2008). SCN5A R1193Q polymorphism associated with progressive cardiac conduction defects and long QT syndrome in a Chinese family. *J Med Genet* **45**, 127–128.
- Sun AY, Koontz JI, Shah SH, Piccini JP, Nilsson KR, Craig D, Haynes C, Gregory SG, Hranitzky PM & Pitt GS (2011). The S1103Y cardiac sodium channel variant is associated with ICD events in African Americans with heart failure and reduced ejection fraction. *Circ Cardiovasc Genet* CIRCGENETICS–110.
- Takahashi K, Shimizu W, Miyake A, Nabeshima T, Nakayashiro M & Ganaha H (2014). High prevalence of the SCN5A E1784K mutation in school children with long QT syndrome living on the Okinawa islands. *Circ J Off J Jpn Circ Soc* **78**, 1974–1979.

- Takenaka K, Ai T, Shimizu W, Kobori A, Ninomiya T, Otani H, Kubota T, Takaki H, Kamakura S & Horie M (2003). Exercise stress test amplifies genotype-phenotype correlation in the LQT1 and LQT2 forms of the long-QT syndrome. *Circulation* **107**, 838–844.
- Tan B-H, Valdivia CR, Song C & Makielski JC (2006). Partial expression defect for the SCN5A missense mutation G1406R depends on splice variant background Q1077 and rescue by mexiletine. *Am J Physiol Heart Circ Physiol* **291**, H1822-1828.
- Tan HL, Kupersmidt S, Zhang R, Stepanovic S, Roden DM, Wilde AAM, Anderson ME & Balsler JR (2002). A calcium sensor in the sodium channel modulates cardiac excitability. *Nature* **415**, 442–447.
- Tateyama M, Rivolta I, Clancy CE & Kass RS (2003). Modulation of cardiac sodium channel gating by protein kinase A can be altered by disease-linked mutation. *J Biol Chem* **278**, 46718–46726.
- Tester DJ, Will ML, Haglund CM & Ackerman MJ (2005). Compendium of cardiac channel mutations in 541 consecutive unrelated patients referred for long QT syndrome genetic testing. *Heart Rhythm* **2**, 507–517.
- Tikhonov DB & Zhorov BS (2017). Mechanism of sodium channel block by local anesthetics, antiarrhythmics, and anticonvulsants. *J Gen Physiol* **149**, 465–481.
- Tomita M, Kitazawa H, Sato M, Okabe M, Antzelevitch C & Aizawa Y (2012). A complete right bundle-branch block masking Brugada syndrome. *J Electrocardiol* **45**, 780–782.
- Trinder J, Kleiman J, Carrington M, Smith S, Breen S, Tan N & Kim Y (2001). Autonomic activity during human sleep as a function of time and sleep stage. *J Sleep Res* **10**, 253–264.
- Trip J, Faber CG, Ginjaar HB, Engelen BGM & Drost G (2007). Warm-up phenomenon in myotonia associated with the V445M sodium channel mutation. *J Neurol* **254**, 257–258.
- ten Tusscher KHWJ (2003). A model for human ventricular tissue. *AJP Heart Circ Physiol* **286**, H1573–H1589.
- ten Tusscher KHWJ (2006). Alternans and spiral breakup in a human ventricular tissue model. *AJP Heart Circ Physiol* **291**, H1088–H1100.
- ten Tusscher KHWJ, Noble D, Noble PJ & Panfilov AV (2004). A model for human ventricular tissue. *Am J Physiol Heart Circ Physiol* **286**, H1573-1589.

- Ulbricht W (2005). Sodium Channel Inactivation: Molecular Determinants and Modulation. *Physiol Rev* **85**, 1271–1301.
- Valdivia CR, Ackerman MJ, Tester DJ, Wada T, McCormack J, Ye B & Makielski JC (2002). A novel SCN5A arrhythmia mutation, M1766L, with expression defect rescued by mexiletine. *Cardiovasc Res* **55**, 279–289.
- Van Petegem F, Lobo PA & Ahern CA (2012). Seeing the Forest through the Trees: towards a Unified View on Physiological Calcium Regulation of Voltage-Gated Sodium Channels. *Biophys J* **103**, 2243–2251.
- Veldkamp MW, Viswanathan PC, Bezzina C, Baartscheer A, Wilde AA & Balsler JR (2000a). UltraRapid Communication. *Circ Res* **86**, e91–e97.
- Veldkamp MW, Viswanathan PC, Bezzina C, Baartscheer A, Wilde AAM & Balsler JR (2000b). Two Distinct Congenital Arrhythmias Evoked by a Multidysfunctional Na<sup>+</sup> Channel. *Circ Res* **86**, e91–e97.
- Veldkamp MW, Wilders R, Baartscheer A, Zegers JG, Bezzina CR & Wilde AAM (2003). Contribution of sodium channel mutations to bradycardia and sinus node dysfunction in LQT3 families. *Circ Res* **92**, 976–983.
- Veltmann C, Barajas-Martinez H, Wolpert C, Borggrefe M, Schimpf R, Pfeiffer R, Cáceres G, Burashnikov E, Antzelevitch C & Hu D (2016). Further Insights in the Most Common SCN5A Mutation Causing Overlapping Phenotype of Long QT Syndrome, Brugada Syndrome, and Conduction Defect. *J Am Heart Assoc* **5**, e003379.
- Vilin YY, Fujimoto E & Ruben PC (2001). A single residue differentiates between human cardiac and skeletal muscle Na<sup>+</sup> channel slow inactivation. *Biophys J* **80**, 2221–2230.
- Vilin YY, Makita N, George AL & Ruben PC (1999). Structural determinants of slow inactivation in human cardiac and skeletal muscle sodium channels. *Biophys J* **77**, 1384–1393.
- Vilin YY, Peters CH & Ruben PC (2012). Acidosis Differentially Modulates Inactivation in NaV1.2, NaV1.4, and NaV1.5 Channels. *Front Pharmacol*; DOI: 10.3389/fphar.2012.00109.
- Viswanathan PC, Bezzina CR, George AL, Roden DM, Wilde AAM & Balsler JR (2001). Gating-Dependent Mechanisms for Flecainide Action in SCN5A-Linked Arrhythmia Syndromes. *Circulation* **104**, 1200–1205.
- Wagner S, Dybkova N, Rasenack ECL, Jacobshagen C, Fabritz L, Kirchhof P, Maier SKG, Zhang T, Hasenfuss G, Brown JH, Bers DM & Maier LS (2006). Ca<sup>2+</sup>/calmodulin-

- dependent protein kinase II regulates cardiac Na<sup>+</sup> channels. *J Clin Invest* **116**, 3127–3138.
- Wakita R, Watanabe I, Okumura Y, Yamada T, Takagi Y, Kofune T, Okubo K, Masaki R, Sugimura H, Oshikawa N, Saito S, Ozawa Y & Kanmatsuse K (2004). Brugada-like electrocardiographic pattern unmasked by fever. *Jpn Heart J* **45**, 163–167.
- Walker J, Calkins H & Nazarian S (2010). Evaluation of cardiac arrhythmia among athletes. *Am J Med* **123**, 1075–1081.
- Wang C, Chung BC, Yan H, Lee S-Y & Pitt GS (2012). Crystal Structure of the Ternary Complex of a NaV C-Terminal Domain, a Fibroblast Growth Factor Homologous Factor, and Calmodulin. *Structure* **20**, 1167–1176.
- Wang C, Chung BC, Yan H, Wang H-G, Lee S-Y & Pitt GS (2014). Structural analyses of Ca<sup>2+</sup>/CaM interaction with NaV channel C-termini reveal mechanisms of calcium-dependent regulation. *Nat Commun* **5**, 4896.
- Wang DW, Desai RR, Crotti L, Arnestad M, Insolia R, Pedrazzini M, Ferrandi C, Vege A, Rognum T, Schwartz PJ & George AL (2007). Cardiac sodium channel dysfunction in sudden infant death syndrome. *Circulation* **115**, 368–376.
- Wang DW, Makita N, Kitabatake A, Balsler JR & George AL (2000). Enhanced Na<sup>+</sup> channel intermediate inactivation in Brugada syndrome. *Circ Res* **87**, e37–e43.
- Wang Q (2004). The common SCN5A mutation R1193Q causes LQTS-type electrophysiological alterations of the cardiac sodium channel. *J Med Genet* **41**, e66–e66.
- Watanabe H, Yang T, Stroud DM, Lowe JS, Harris L, Atack TC, Wang DW, Hipkens SB, Leake B, Hall L, Kupersmidt S, Chopra N, Magnuson MA, Tanabe N, Knollmann BC, George AL & Roden DM (2011). Striking In vivo phenotype of a disease-associated human SCN5A mutation producing minimal changes in vitro. *Circulation* **124**, 1001–1011.
- Webb JR (2009). *Slow Inactivation of Sodium Channels: Structural Clues and Disease Associations* (thesis). Available at: <https://utswmed-ir.tdl.org/utswmed-ir/handle/2152.5/453> [Accessed November 22, 2016].
- Wei J, Wang DW, Alings M, Fish F, Wathen M, Roden DM & George AL (1999). Congenital Long-QT Syndrome Caused by a Novel Mutation in a Conserved Acidic Domain of the Cardiac Na<sup>+</sup> Channel. *Circulation* **99**, 3165–3171.
- Wilde AAM (2002). Proposed Diagnostic Criteria for the Brugada Syndrome: Consensus Report. *Circulation* **106**, 2514–2519.

- Wilde AAM, Postema PG, Di Diego JM, Viskin S, Morita H, Fish JM & Antzelevitch C (2010). The pathophysiological mechanism underlying Brugada syndrome. *J Mol Cell Cardiol* **49**, 543–553.
- Wingo TL, Shah VN, Anderson ME, Lybrand TP, Chazin WJ & Balsler JR (2004). An EF-hand in the sodium channel couples intracellular calcium to cardiac excitability. *Nat Struct Mol Biol* **11**, 219–225.
- Wu L, Rajamani S, Shryock JC, Li H, Ruskin J, Antzelevitch C & Belardinelli L (2008). Augmentation of late sodium current unmasks the proarrhythmic effects of amiodarone. *Cardiovasc Res* **77**, 481–488.
- Xia L, Zhang Y, Zhang H, Wei Q, Liu F & Crozier S (2006). Simulation of Brugada syndrome using cellular and three-dimensional whole-heart modeling approaches. *Physiol Meas* **27**, 1125–1142.
- Yan G-X & Antzelevitch C (1998). Cellular basis for the normal T wave and the electrocardiographic manifestations of the long-QT syndrome. *Circulation* **98**, 1928–1936.
- Yan G-X & Antzelevitch C (1999). Cellular basis for the Brugada syndrome and other mechanisms of arrhythmogenesis associated with ST-segment elevation. *Circulation* **100**, 1660–1666.
- Yan H, Wang C, Marx SO & Pitt GS (2017a). Calmodulin limits pathogenic Na<sup>+</sup> channel persistent current. *J Gen Physiol* **149**, 277–293.
- Yan Z, Zhou Q, Wang L, Wu J, Zhao Y, Huang G, Peng W, Shen H, Lei J & Yan N (2017b). Structure of the Na<sup>v</sup> 1.4-β1 Complex from Electric Eel. *Cell* **170**, 470–482.e11.
- Yang F & Zheng J (2014). High temperature sensitivity is intrinsic to voltage-gated potassium channels. *eLife* **3**, e03255.
- Yang N & Horn R (1995). Evidence for voltage-dependent S4 movement in sodium channels. *Neuron* **15**, 213–218.
- Yang Y-C, Huang C-S & Kuo C-C (2010). Lidocaine, carbamazepine, and imipramine have partially overlapping binding sites and additive inhibitory effect on neuronal Na<sup>+</sup> channels. *Anesthesiology* **113**, 160–174.
- Yarov-Yarovoy V, DeCaen PG, Westenbroek RE, Pan C-Y, Scheuer T, Baker D & Catterall WA (2012). Structural basis for gating charge movement in the voltage sensor of a sodium channel. *Proc Natl Acad Sci* **109**, E93–E102.

- Yu J, Hu J, Zhou H, Liu X, Cao Q, Shen Y, Ma J, Zhou S, Liu X, Li J, Chen Q, Cheng X & Hong K (2013). [SCN5A mutation in patients with Brugada electrocardiographic pattern induced by fever]. *Zhonghua Xin Xue Guan Bing Za Zhi* **41**, 1010–1014.
- Yuasa S, Sato M, Kitazawa H, Okabe M, Komatsu Y, Koshikawa T, Miyajima S & Aizawa Y (2014). Brugada syndrome and idiopathic left ventricular tachycardia unmasked by exercise and a class Ic drug. *J Electrocardiol* **47**, 721–724.
- Zhang X, Ren W, DeCaen P, Yan C, Tao X, Tang L, Wang J, Hasegawa K, Kumasaka T, He J, Wang J, Clapham DE & Yan N (2012). Crystal structure of an orthologue of the NaChBac voltage-gated sodium channel. *Nature*; DOI: 10.1038/nature11054.
- Zhou Y, Wang J, Li X & Wang Y (2013). ST-T-wave alternans in Brugada electrocardiogram type I pattern during the resolution of febrile states. *Cardiovasc J Afr* **24**, e1-3.
- Zhu Y, Kyle JW & Lee PJ (2006). Flecainide sensitivity of a Na channel long QT mutation shows an open-channel blocking mechanism for use-dependent block. *Am J Physiol Heart Circ Physiol* **291**, H29-37.
- Zimmer T, Haufe V & Blechschmidt S (2014). Voltage-gated sodium channels in the mammalian heart. *Glob Cardiol Sci Pract* **2014**, 58.
- Zipes DP & Wellens HJJ (1998). Sudden Cardiac Death. *Circulation* **98**, 2334–2351.
- Zygmunt AC, Eddlestone GT, Thomas GP, Nesterenko VV & Antzelevitch C (2001). Larger late sodium conductance in M cells contributes to electrical heterogeneity in canine ventricle. *Am J Physiol-Heart Circ Physiol* **281**, H689–H697.